

Manipulating Energy Levels in Organic Solar Cell Materials

Jordan Shaikh

Supervised by Dr Tracey M. Clarke

University College London

Department of Chemistry

*This thesis is submitted to University College London for
the degree of Doctor of Philosophy*

December 2020

Declaration

I, Jordan Shaikh confirm the work presented in this thesis is my own. Where information has been derived from other sources, I confirm that this has been indicated in the thesis:

Abstract

Organic solar cells offer the prospect of an entire new class of renewable energy resource. This thesis aims at addressing the issue of triplet state formation in these devices, which can contribute to both a reduction in device efficiency and operational lifetime. Furthermore, triplet states can be exploited to enhance device efficiency via photophysical processes such as triplet-triplet annihilation upconversion and thermally activated delayed fluorescence. Transient absorption spectroscopy on a timescale of ps-ms is employed as the primary investigative technique throughout this thesis.

In chapter 3 we explore the dynamics of a prototypical small molecule DPP/fullerene system, which was found to elegantly demonstrate the issue of triplet state formation stemming from recombination. It was found that ultrafast spin mixing, followed by subsequent geminate recombination yielded the donor-triplet exciton, the lowest energy state of the system.

In chapters 4 and 5 novel polymeric materials were investigated, which were designed with the intention of manipulating/harvesting triplet states such that they no longer constitute a loss mechanism. In chapter 4 a zinc porphyrin-F8BT hybrid copolymer solution, F8BT-HAPAPP, was found to undergo a dual energy-transfer mechanism, whereby the fate of each photogenerated F8BT singlet exciton was found to depend upon its distance from the porphyrin unit. Intriguingly, the F8BT-HAPAPP triplets generated were found to possess a lifetime intermediate between the two pristine materials.

In chapter 5 a donor-orthogonal acceptor low band-gap polymer, Thiro, was found to exhibit facile triplet formation on a <200 fs timescale. This rapid triplet population was thought to derive from a spin-orbit charge transfer interaction, afforded by CT states deriving from the perpendicular substituted spirobifluorene groups. Most peculiarly, free charge formation was observed in both the solution and pristine Thiro film, as evidenced via the observation of a radical cation in the μ s-TA spectra. This assignment was further validated via comparison with a Thiro:PC₆₀BM μ s-TA spectrum, which is the first time a D-oA conjugated polymer has been investigated in a bulk heterojunction.

Impact Statement

Anthropogenic climate change is the main issue facing mankind in the 21st century, which necessitates a shift away from fossil fuels and towards renewable energy sources. A key technology driving this transition has been that of photovoltaic ("solar") energy. Organic solar cells (alternatively referred to as plastic solar cells) are a new promising class of photovoltaic device, which differ fundamentally from their inorganic counterparts. Whereas traditional photovoltaic cells are overwhelmingly made from silicon, organic solar cells are typically comprised of polymeric ('plastic') materials, allowing them to be built thin and mechanically flexible. These polymeric materials also possess physical properties that allows for solution processing to be viable, offering the prospect of low-cost and large-scale production of solar cells via roll-to-roll technology. Nonetheless, fundamental issues relating to stability and device efficiency are still present and must be addressed if organic solar cells are to compete with the existing energy regime.

One of the main processes that contributes to a reduction in both stability and efficiency of OSCs is the formation of excited states known as "triplets". Transient absorption spectroscopy is used throughout this thesis to elucidate the photophysics of novel polymeric materials designed such that triplet states no longer constitute a loss process.

The research presented in thesis represents significant first attempts at implementing "triplet manipulation" into systems which reflect OSC materials. As such, the findings of this thesis provide a foundation for further studies into more efficient materials, thus allowing for OSC devices to become more competitive in the energy market. It should also be noted that while this thesis discusses its findings in the context of organic solar cells, its conclusions can be applied to the wider field of organic electronics.

Table of Contents

Declaration.....	i
Abstract.....	ii
Impact Statement.....	iii
Table of Contents.....	iv
List of Figures.....	viii
List of Tables.....	xxiv
Acronyms and Abbreviations.....	xxv
Acknowledgements.....	xxvii
Publications.....	xxviii

Chapter 1

1 Introduction and Overview

1.1 Motivation and Overview.....	1
1.2 Historical Context.....	3
1.3 Electronic Structure of Inorganic and Organic Semiconductors.....	6
1.4 Exciton formation in Solar cells.....	8
1.5 Mechanisms of Exciton Diffusion.....	10
1.5.1 Förster Resonance Energy Transfer (FRET).....	11
1.5.2 Dexter Energy Transfer.....	13
1.5.3 Triplet Diffusion.....	14
1.6 Exciton Dissociation.....	15
1.6.1 Marcus Theory of Electron Transfer.....	15
1.6.2 The Charge Transfer State.....	17
1.7 Charge Recombination.....	20
1.7.1 Geminate Recombination and Onsager Theory.....	20
1.7.2 Bimolecular Recombination.....	21
1.8 Spin States in Organic Semiconductors.....	24
1.8.1 Singlet-Triplet Energy Gap – Role of the exchange energy.....	25

1.8.2 Intersystem Crossing, Spin-orbit Coupling and the Heavy Atom Effect.....	27
1.9 Aims of this Thesis.....	29
1.10 Bibliography.....	30

Chapter 2

2 Experimental Techniques

2.1 Materials Investigated in this Thesis.....	40
2.2 Sample Preparation.....	41
2.3 Steady State UV-Vis Spectroscopy.....	42
2.4 Photoluminescence (PL) Spectroscopy.....	43
2.5 Quantum Yields.....	45
2.6 Transient Absorption Spectroscopy (TAS).....	45
2.6.1 TAS with Nanosecond-Microsecond Resolution (μ s-TAS).....	47
2.6.2 TAS with Picosecond Resolution (ps-TAS).....	51
2.6.3 TAS Data Analysis in the ns-ms Regime.....	53
2.6.4 TAS Data Analysis in the ps-ns Regime.....	57
2.6.5 TAS Data Processing and General Analysis.....	60
2.7 Bibliography.....	61

Chapter 3

3 Exploring the Photophysics of a Small Molecule DPP/Fullerene System

3.1 Outline.....	63
3.2 Introduction.....	64
3.3 Experimental.....	65
3.4 Ground State Absorbance, Fluorescence and Atomic Force Microscopy (AFM).....	66
3.5 Picosecond Transient Absorption Spectroscopy.....	68
3.6 Microsecond Transient Absorption Spectroscopy.....	79

3.7 Time-resolved electron paramagnetic resonance spectroscopy (TR-EPR).....	84
3.8 Discussion.....	86
3.9 Conclusion.....	88
3.10 Bibliography.....	88

Chapter 4

4 Investigation into Energy-Transfer Pathways in a Zinc Porphyrin/F8BT Hybrid Polymer

4.1 Outline.....	93
4.2 Introduction.....	94
4.3 Experimental.....	101
4.4 Ground State Absorbance and Fluorescence.....	102
4.5 Picosecond Transient Absorption Spectroscopy.....	106
4.6 Microsecond Transient Absorption Spectroscopy.....	118
4.7 A note on Oxygen sensitivity and reproducibility.....	130
4.8 Discussion.....	131
4.9 Conclusion.....	138
4.10 Bibliography.....	139

Chapter 5

5 Investigating the Impact of a Donor-orthogonal Acceptor Architecture on Reducing the Singlet-Triplet Energy Splitting in a Low-band Gap Polymer

5.1 Outline.....	143
5.2 Introduction.....	144
5.3 Experimental.....	148
5.4 Ground State Absorbance.....	149
5.5 Fluorescence.....	151
5.6 Time-Correlated Single Photon Counting.....	152

5.7 Time-Resolved Photoluminescence Spectroscopy (ICCD).....	154
5.8 Picosecond Transient Absorption Spectroscopy.....	157
5.9 Microsecond Transient Absorption Spectroscopy.....	167
5.10 Discussion.....	180
5.11 Conclusion.....	188
5.12 Bibliography.....	189

Chapter 6

6 Conclusions and Future Work

6.1 Conclusions.....	194
6.2 Future Work.....	195

List of Figures

- Figure 1.1** Schematic representation of **a)** localised Frenkel exciton, typically found in low dielectric medium organic semiconductor materials **b)** non-localised Wannier-Mott exciton, typically found in high dielectric medium inorganic semiconductors, such as silicon.....3
- Figure 1.2** Schematic representation of electron donor (D) and acceptor (A) materials arranged in **a)** a heterojunction bilayer structure **b)** an ideal interpenetrating bulk heterojunction (BHJ) structure. In the bilayer, excitons not generated within the diffusion length of the donor/acceptor interface will recombine. In the BHJ, nanoscale phase separation increases the surface area between the donor and acceptor, therefore increasing the chance exciton reach the interface.....5
- Figure 1.3** Orbital energy diagram illustrating the effect of energetic disorder when transitioning from **a)** a discrete polymer chain to **b)** a cluster of polymer chains, such as when aggregated in a concentrated solution to **c)** bulk polymer, such as when in a thin film and DOS is the density of states. d) a semiconducting crystal, where VB is the valence band, CB is the conduction band and E_g is the energy of the bandgap. It is noted that in **a)** a single energy level is represented for simplicity, but in reality, will possess a distribution of energies due to variations in conjugation length, defects and conformation.....6
- Figure 1.4** Schematic representation of conjugation in polyacetylene. Overlapping Pz orbitals results in an extended π -conjugated network across the backbone of the polymer.....7
- Figure 1.5.** Orbital energy diagram illustrating the formation of a coulombically bound electron-hole pair known as an exciton. The dashed line enclosing the positive and negative charges schematically represents the coulombic attraction that must be overcome to achieve charge dissociation. The density of states (DOS) reflects the disordered nature of organic materials and indicates that the energy of the exciton may extend into the bandgap.....8
- Figure 1.6** Schematic representation of the mechanisms involved in **a)** Förster resonance energy transfer and **b)** Dexter energy transfer. The Förster mechanism is a dipole-dipole interaction whereas Dexter involves electron exchange. In the case of Dexter energy transfer, electron exchange must obey the laws of spin conservation.....11

Figure 1.7 Parabolic potential energy surfaces of an electron transfer reaction from an excited donor, D^* , to an acceptor, A . The $^1D^*$ infers a photogenerated singlet state on the donor. ΔG^0 is the driving force for electron transfer and is the energy difference between the two surfaces minima. ΔG^\ddagger is the activation energy, which is determined from the difference in energy between the reactants ($^1D^*/A$) minimum and the point of intersection between the two surfaces. λ is the reorganisation energy. **a)** represents the case for isoenergetic electron transfer, **b)** represents the normal region for electron transfer, **c)** represents the barrierless region for electron transfer and **d)** represents the inverted region for electron transfer. The y-axis is the free energy and the x-axis is the reaction coordinate, which have been omitted....**15**

Figure 1.8 Schematic for the process of charge dissociation in a bulk heterojunction solar cell: **i)** The bulk heterojunction device architecture **ii)** The process of exciton diffusion to the donor/acceptor interface **iii)** The CT state, illustrating the electron-hole pair being bound across the interface **iv)** The charge separated state, where charges have escaped their mutual coulombic field.....**17**

Figure 1.9 Orbital energy diagram illustrating the formation of an interfacial charge transfer (CT) state. In a CT state the electron-hole pair is bound across the interface, with the hole being located on the HOMO of the donor and the electron being located on the LUMO of the acceptor. The dashed line enclosing the positive and negative charges schematically represents the coulombic attraction still present in a CT state. IP and EA are the ionisation potential and electron affinity respectively. E_B^{EXC} and E_B^{CT} are the binding energies for the exciton and charge transfer states respectively.....**19**

Figure 1.10 Simplified state diagram for the process of charge photogeneration and recombination. **i)** Initial exciton formation by photon absorption. **ii)** Non-radiative and radiative relaxation of the singlet exciton to the ground state. **iii)** Intersystem crossing to yield a triplet exciton. **iv)** Electron transfer to yield a charge transfer state (CT). **v)** Charge separation to yield a charge separated state (CS). **vi)** Free charge carrier diffusion and extraction at electrodes. **vii)** Bimolecular recombination of free charges to form both 1CT and 3CT states. **viii)** Non-radiative and radiative bimolecular recombination from the CT state to the ground state. **ix)** Bimolecular recombination from the 3CT state to the triplet exciton. **x)** Non-radiative and radiative triplet relaxation of the triplet exciton to the ground state.....**20**

Figure 1.11 Energy diagram showing the difference in energy of S_1 and T_1 is given by ΔE_{ST} which is equal to $2J$	25
Figure 1.12 Structure of an approximate bromobenzene π - π^* generated after excitation. X denotes a π or π^* electron.....	28
Figure 2.1 Structures of the materials used in this thesis.....	41
Figure 2.2 A general scheme for a μ s TAS experimental setup used in this thesis. The change in the optical density (relative to the ground state absorbance) after excitation may be plotted as a function of probe wavelength, λ , yielding a transient absorption spectrum.....	48
Figure 2.3 Picture of the μ s-TAS experimental setup used in this thesis. The OPO is located inside the black shroud with the laser outlet. The optical transient detectors are located after the monochromator.....	49
Figure 2.4 Pictures of a) The infrared transient detector containing an Ingas PIN photodiode with a spectral range of 700-1700 nm, b) The visible transient detector containing an Si PIN photodiode with a spectral range of 320-1060 nm.....	50
Figure 2.5 Picture of a Costronics transient amplifier and filtering box. The background (DC) light level is observed on the LCD screen.....	51
Figure 2.6 Microsecond transient absorption decay kinetics of F8BT chlorobenzene solution (68 μ g/mL). Bubbling O_2 through the solution results in a complete quenching of the signal. The sample was re-degassed to check that the initial signal was recoverable.....	54
Figure 2.7 ps-TA spectrum of a pristine Thiro film at 1 ps (taken from chapter 5), illustrating multiple signal components that may comprise the spectrum. Obtained with an excitation wavelength of 520 nm. i) The laser 'spike' can be observed at 520 nm. ii) The ground state bleach corresponds to depletion of the ground state and results in a negative ΔOD signal. iii) Stimulated emission can also result in a negative ΔOD signal and can be found spectrally situated in the area of emission. iv) The visible and infrared light probes do encompass the entire spectrum, and results in a ~ 100 nm spectral dead zone (represented by the grey dashed vertical lines in figure 7 v) . Excited state absorption results in a positive ΔOD , but it is important to note that the obtained signals may represent contributions from different species.....	58

Figure 2.8 An example of excitation energy dependant ps-TA kinetics for F8BT solution.....	58
Figure 3.1 The basic diketopyrrolopyrrole, DPP, moiety used in small molecules and polymers.....	64
Figure 3.2 Structure of small molecule 2,5-bis(2-hexyldecyl)-3,6-di(thiophen-2-yl)-2,5-dihydropyrrolo[3,4-c]pyrrole-1,4-dione, TDPP.....	65
Figure 3.3 Normalised ground state absorbance spectra of a pristine TDPP film, TDPP:PC ₆₀ BM (1:2) and TDPP:PC ₆₀ BM blend films and normalised photoluminescence spectrum of a pristine TDPP film. Pristine TDPP film photoluminescence spectrum was collected with an excitation wavelength of 510 nm. Spectra have been normalised to their respective peak maxima.....	66
Figure 3.4 AFM images for a) pristine TDPP, b) TDPP:PC ₆₀ BM (1:2) and c) TDPP:PC ₇₀ BM films. AFM images were collected by Caroline Nowicka-Dyag.....	67
Figure 3.5 Photoluminescence spectra of a pristine TDPP thin film and TDPP:PC ₆₀ BM/PC ₇₀ BM (1:2 by weight) blend films. Spectra were obtained with an excitation wavelength of 510 nm and the data has been corrected for the absorbance at the exciting wavelength.....	68
Figure 3.6 Picosecond transient absorption spectrum of a pristine TDPP thin film. The film was excited at 510 nm with an excitation density of 2.7 $\mu\text{J cm}^{-2}$	68
Figure 3.7 Picosecond transient absorption decay kinetics of a pristine TDPP thin film. Sample was excited with a pump wavelength 510 nm, with an excitation density of 11 $\mu\text{J cm}^{-2}$. Kinetics were obtained through averaging the kinetic data in the spectral regions of 800-810 nm, 850-1000 nm and 1590-1600 nm.....	69
Figure 3.8 Normalised picosecond transient absorption decay kinetics of a pristine TDPP thin film. Obtained with a pump wavelength of 510 nm and at a probe wavelength (where the kinetic data has been averaged in the spectral range) of a) 800-810 nm and b) 1590-1600 nm. Both the transitions at 800-810 nm and 1590-1600 nm exhibit near-identical decays, exhibiting the same excitation dependence.....	71

Figure 3.9 Picosecond transient absorption spectrum of a TDPP:PC ₆₀ BM (1:2 by weight) thin film. Sample was excited with a pump wavelength of 510 nm, with an excitation density of 2.7 μJ cm ⁻²	72
Figure 3.10 Picosecond transient absorption decay kinetics of a TDPP:PC ₆₀ BM (1:2 by weight) thin film. Sample was excited with a pump wavelength of 510 nm, with an excitation density of 11 μJ cm ⁻² . Kinetics were obtained through averaging the kinetic data in the spectral regions of 800-810 nm, 860-870 nm, 1110-1150 nm and 1590-1600 m.....	72
Figure 3.11 Normalised picosecond transient absorption decay kinetics of TDPP:PC ₆₀ BM (1:2 by weight) thin film. Obtained with a pump wavelength of 510 nm and at a probe wavelength (where the kinetic data has been averaged in the spectral range of a) 800-810 nm, b) 860-870 nm and c) 1100-1150 nm.....	73
Figure 3.12 Picosecond transient absorption spectrum of a TDPP:PC ₇₀ BM (1:2 by weight) thin film. The film was excited at 510 nm with an excitation density of 2.7 μJ cm ⁻²	75
Figure 3.13 Picosecond transient absorption decay kinetics of a TDPP:PC ₇₀ BM (1:2 by weight) thin film. The film was excited at 510 nm with an excitation density of 11 μJ cm ⁻² . Kinetics were obtained through averaging in the wavelength regions 860-870 nm and 1250-1300 nm.....	76
Figure 3.14 Normalised picosecond transient absorption decay kinetics of TDPP:PC ₇₀ BM (1:2 by weight) thin film. Obtained with a pump wavelength of 510 nm and at a probe wavelength (where the kinetic data has been averaged in the spectral range) of a) 800-810 nm, b) 860-870 nm and c) 1250-1150 nm.	77
Figure 3.15 Microsecond transient absorption spectrum of a pristine TDPP thin film. The film was excited at 500 nm with an excitation density of 128 μJ cm ⁻² . No spectral response is observed, illustrating that no long-lived species (triplets or polarons) are generated.....	79
Figure 3.16 Normalised microsecond transient absorption spectrum of a TDPP:PC ₆₀ BM (1:2 by weight) thin film. The film was excited at 500 nm with an excitation density of 36 μJ cm ⁻² . Inset: Normalised ps-TA and μs-TA spectra of TDPP:PC ₆₀ BM (1:2 by weight) thin film. Films have been normalised to their respective peak maxima at times of 6 ns and 1 μs respectively.....	79

Figure 3.17 <i>Microsecond transient absorption kinetics of a TDPP:PC₆₀BM 1:2 by weight film. Obtained with a pump wavelength of 510 nm and a probe wavelength of 875 nm.....</i>	80
Figure 3.18 <i>Microsecond transient absorption spectrum of a TDPP:PC₇₀BM (1:2 by weight) thin film. The film was excited at 510 nm with an excitation density of 36 $\mu\text{J cm}^{-2}$.....</i>	81
Figure 3.19 <i>Microsecond transient absorption kinetics of a TDPP:PC₇₀BM 1:2 by weight film. Obtained with a pump wavelength of 510 nm and a probe wavelength of 880 nm.....</i>	82
Figure 3.20 <i>Microsecond transient absorption kinetics of a) TDPP:PC₆₀BM 1:2 by weight film and b) TDPP:PC₇₀BM 1:2 by weight film. Obtained with a pump wavelength of 510 nm, a probe wavelength of 875 nm and an excitation density of 11 $\mu\text{J cm}^{-2}$. The measurement was carried out in both Ar and O₂ atmospheres, illustrating an O₂ independent decay for both blend films.....</i>	83
Figure 3.21 a) <i>50 K TR-EPR spectrum of PC₇₀BM (blue line) in toluene solution recorded after 300-500 ns after excitation. Data was collected by Dr Enrico Salvadori.</i>	85
Figure 3.22 <i>State diagram for the proposed model of TDDP triplet generation in TDPP:fullerene film. For the lifetimes given a) is for the blend containing PC₆₀BM and b) for PC₇₀BM.....</i>	86
Figure 4.1 <i>Normalised AM1.5 solar emission spectrum overlaid with the normalised absorbance spectra of P3HT thin film and chlorobenzene solutions of F8BT-HAPAPP and HAPAPP.....</i>	95
Figure 4.2 <i>Schematic representation of the general case of triplet-triplet annihilation upconversion. Note: the presence of a second molecule has been omitted for simplicity.....</i>	96
Figure 4.3 <i>Schematic representation of sensitised triplet-triplet annihilation upconversion and resulting charge separation. The presence of the acceptor molecule quenches the 'delayed' fluorescence. Note: the presence of a second sensitised molecule has been omitted for simplicity.....</i>	97
Figure 4.4 <i>Schematic representation of the electron exchange mechanism of TTA to yield a singlet excited state and singlet ground state.....</i>	98

Figure 4.5 Structures of the polymer F8BT, the isolated porphyrin HAPAPP and porphyrin containing polymer, F8BT-HAPAPP.....	100
Figure 4.6 Normalised ground state absorption spectra of F8BT, F8BT-HAPAPP and HAPAPP in chlorobenzene solution. The inset enhances the spectral area of the Q-bands observed in HAPAPP and F8BT-HAPAPP. Pristine F8BT exhibits negligible absorption in the red and near infrared.....	102
Figure 4.7 Steady state fluorescence spectra of F8BT, F8BT-HAPAPP and HAPAPP, in chlorobenzene solution (3.4 $\mu\text{g}/\text{mL}$) with an excitation wavelength of 450 nm. F8BT-HAPAPP was also excited at the porphyrin Q-band with 650 nm. F8BT and F8BT-HAPAPP exhibit near identical fluorescence spectra under the same excitation conditions.....	103
Figure 4.8 Excitation and emission spectra of F8BT-HAPAPP in chlorobenzene solution. The lack of upconverted (anti-Stokes) fluorescence, can be seen when exciting the porphyrin Q-band with 650 nm, and probing for the fluorescence of F8BT at 550 nm. Emission and excitation spectra were corrected for instrument response.....	104
Figure 4.9 Picosecond transient absorption spectra of chlorobenzene solutions a) F8BT b) F8BT-HAPAPP excited at 518 nm with an excitation energy of 23 $\mu\text{J cm}^{-2}$. Samples were degassed with argon for 30 min. Solution concentrations were 3.4 mg/mL for both F8BT and F8BT-HAPAPP.....	107
Figure 4.10 Picosecond transient absorption decay kinetics of pristine F8BT chlorobenzene solution (3.4 mg/mL) obtained with an excitation wavelength of 518 nm. Kinetics traces of the stimulated emission and singlet decay were obtained via averaging the regions of 550-600 nm and 900-1000 nm respectively. Kinetics have been normalised at 1 ps to illustrate the similarity of the F8BT stimulated emission and singlet decay.....	108
Figure 4.11 Picosecond transient absorption decay kinetics of neat F8BT chlorobenzene solution (3.4 mg/mL) obtained with an excitation wavelength of 518 nm. Kinetics were obtained through averaging decays in the wavelength region of 900-1000 nm. Sample was degassed with argon. The red lines are monoexponential fits. Inset: The transient signal amplitude at 1 ps as a function of energy density, illustrating the linear signal response.....	109

Figure 4.12 Picosecond transient absorption spectra of chlorobenzene solutions **a)** HAPAPP **b)** F8BT-HAPAPP excited at 650 nm with an excitation energy of $23 \mu\text{J cm}^{-2}$. Samples were degassed with argon for 30 min. Solution concentrations were $34 \mu\text{g/mL}$ for HAPAPP and 3.4 mg/mL for F8BT-HAPAPP.....110

Figure 4.13 Picosecond transient absorption decay kinetics of pristine HAPAPP chlorobenzene solution ($34 \mu\text{g/mL}$) obtained with an excitation wavelength of 650 nm. Kinetics were obtained through averaging the decays from averaging decays in the wavelength region of 480-485 nm. Sample was degassed with argon. Inset shows the transient signal amplitude at 1 ps as a function of energy density, illustrating the linear signal response.....111

Figure 4.14 Picosecond transient absorption decay kinetics of pristine HAPAPP chlorobenzene solution ($34 \mu\text{g/mL}$) obtained with an excitation wavelength of 650 nm and an excitation energy of $23 \mu\text{J cm}^{-2}$. Kinetics were obtained through averaging in the probe wavelength regions of 600-610 nm and 480-485 nm.....112

Figure 4.15 Picosecond transient absorption decay kinetics of F8BT-HAPAPP chlorobenzene solution (3.4 mg/mL) obtained with an excitation wavelength of 650 nm. Kinetics were obtained through averaging the decays in the wavelength region of 900-1000 nm. Sample was degassed with argon. Inset shows the transient signal amplitude at 1 ps as a function of energy density, illustrating the linear signal response.....113

Figure 4.16 Normalised picosecond transient absorption spectra take at 1 ps of F8BT and F8BT-HAPAPP chlorobenzene solution (3.4 mg/mL) obtained with an excitation wavelength of 518 nm ($23 \mu\text{J cm}^{-2}$). Spectra have been normalised to their respective peak maxim.....114

Figure 4.17 Kinetic decays of F8BT and F8BT-HAPAPP, excited with a pump wavelength of 518 nm. Kinetic decays obtained from averaging the probe wavelengths 900-1000 nm. Decays have been normalised to 1 ps to illustrate the additional decay phase present in F8BT-HAPAPP.....115

Figure 4.18 Picosecond transient absorption decay kinetics of F8BT-HAPAPP in chlorobenzene solution (3.4 mg/mL) obtained with an excitation wavelength of 518 nm. Kinetics were obtained through averaging decays in the wavelength region of 900-1000 nm. Sample was degassed with argon. Inset: the transient

signal amplitude at 1 ps as a function of energy density, illustrating the linear signal response.....116

Figure 4.19 Microsecond transient absorption spectrum of neat F8BT chlorobenzene solution (68 $\mu\text{g}/\text{mL}$) excited with a pump wavelength of 460 nm and 650 nm. Obtained with excitation densities of 16 and 25 $\mu\text{J cm}^{-2}$ for 460 and 650 nm respectively. Solution was degassed via three cycles of freeze pump thawing and placed under an N_2 atmosphere.....118

Figure 4.20 Microsecond transient absorption decay kinetics of F8BT chlorobenzene solution (68 $\mu\text{g}/\text{mL}$) under nitrogen, oxygen and nitrogen restored atmospheres, at a probe wavelength of 800 nm. Obtained with a pump wavelength of 460 nm with an excitation density of 12.2 $\mu\text{J cm}^{-2}$. Bubbling O_2 through the solution results in a complete quenching of the signal, illustrating the presence of a highly oxygen sensitive species, most likely to be that of a triplet.....119

Figure 4.21 Microsecond transient absorption decay kinetics of F8BT chlorobenzene solution (68 $\mu\text{g}/\text{mL}$), excited with a pump wavelength of 460 nm and probe wavelength of 800 nm. Solution was degassed via three cycles of freeze pump thawing and placed under an N_2 atmosphere. **Inset:** the transient signal amplitude at 1 μs as a function of energy density, illustrating the linear signal response.....120

Figure 4.22 Microsecond transient absorption spectrum of neat HAPAPP chlorobenzene solution (32 $\mu\text{g}/\text{mL}$) excited with a pump wavelength of 640 nm. Obtained with an excitation energy of 10 $\mu\text{J cm}^{-2}$121

Figure 4.23 Normalised microsecond transient absorption decay kinetics of neat HAPAPP chlorobenzene solution (32 $\mu\text{g}/\text{mL}$) excited with a pump wavelength of 640 nm. Probe wavelengths of 800 and 1060 nm were used.....121

Figure 4.24 Microsecond transient absorption decay kinetics of neat HAPAPP chlorobenzene solution (32 $\mu\text{g}/\text{mL}$) excited with a pump wavelength of 640 nm and probe wavelength of 800 nm.....122

Figure 4.25 Microsecond transient absorption spectrum of F8BT-HAPAPP chlorobenzene solution (0.65 mg/mL) excited with a pump wavelength of 650 nm. Obtained with an excitation energy of 15 $\mu\text{J cm}^{-2}$. **Inset:** the same spectral

data normalised to the peak maxima, demonstrating the absence of spectral evolution.....123

Figure 4.26 *Microsecond transient absorption decay kinetics of F8BT-HAPAPP chlorobenzene solution (0.65 mg/mL) excited with a pump wavelength of 650 nm and probe wavelength of 800 nm. Inset: the transient signal amplitude at 1 μ s as a function of excitation density, illustrating a linear signal response.....123*

Figure 4.27 *Microsecond transient absorption spectra of F8BT and F8BT-HAPAPP taken at 1 μ s. F8BT-HAPAPP was selectively excited with a pump wavelength of 518 and 650 nm, corresponding to excitation of F8BT or HAPAPP respectively. The inset enhances the region of 950-1350 nm for F8BT-HAPAPP, illustrating the characteristic porphyrin triplet peak present regardless of excitation of F8BT or the Q-band.....125*

Figure 4.28 *Microsecond transient absorption spectrum of F8BT-HAPAPP chlorobenzene solution (0.65 mg/mL) excited with a pump wavelength of 518 nm. Obtained with an excitation energy of 21 μ J cm⁻². Inset: the same spectral data normalised to the peak maxima, demonstrating the presence of spectral evolution.....125*

Figure 4.29 *Microsecond transient absorption spectra of F8BT and F8BT-HAPAPP. F8BT-HAPAPP was selectively excited with a pump wavelength of 518 and 650 nm, corresponding to excitation of the F8BT or HAPAPP respectively. Spectra have been normalised to their respective peak maxima. For F8BT-HAPAPP spectra are taken at 2 and 100 μ s to illustrate the spectral evolution from the F8BT triplet to that of the porphyrin, HAPAPP, triplet.....126*

Figure 4.30 *Microsecond transient absorption decay kinetics of F8BT-HAPAPP, probed at 800 nm. Obtained using a pump wavelength of 650 nm, with excitation densities ranging from 6– 15 μ J cm⁻².....127*

Figure 4.31 *Normalised signal amplitudes obtained from the kinetic decays of F8BT-HAPAPP chlorobenzene solution (0.65 mg/mL) excited with a pump wavelength of 518 nm. Signal amplitudes were taken at 1.2 and 120 μ s corresponding to the decay of the fast and slow phases respectively.....129*

Figure 4.32 *Microsecond transient absorption decay kinetics of F8BT-HAPAPP, probed at 800 nm. Obtained using a pump wavelength of 518 nm, with excitation density of 7 μ J cm⁻².....129*

- Figure 4.33** *Microsecond transient absorption decay kinetics of F8BT-HAPAPP, probed at 800 nm and illustrating the difference in kinetics obtained from degassing via bubbling with N₂ or using a freeze pump thaw technique. Obtained using a pump wavelength of 518 nm, with excitation density of 7 μJ cm⁻².....130*
- Figure 4.34** *State diagram for the proposed photophysical mechanism of F8BT-HAPAPP and the controls F8BT and HAPAPP in chlorobenzene solution. The figure is not to scale. The green colour denotes excitation of the F8BT backbone of F8BT-HAPAPP with 518 nm, whereas the red colour denotes excitation of the porphyrin moieties with 650 nm. Internal conversion is omitted.....131*
- Figure 4.35** *Microsecond transient absorption spectra of F8BT-HAPAPP chlorobenzene solution, excited with pump wavelengths of 518 and 650 nm. Spectra are taken at 100 μs and have been normalised to the number of photons absorbed. The porphyrin triplet peak at 800 nm when exciting at 518 nm is 25% of the value of that obtained when exciting at 650 nm.....132*
- Figure 4.36** *Schematic representation of a) Singlet energy transfer (SET) from the initially excited F8BT, to that of the porphyrin HAPAPP. F8BT moieties excited near the porphyrin may undergo rapid SET and subsequent IC/ISC. Those F8BT moieties excited beyond the diffusion distance of the porphyrin may undergo the standard photophysics of the control F8BT. b) Triplet energy transfer (TET) from F8BT triplets formed from ISC, to that of the porphyrin HAPAPP. ¹F8BT* states initially excited may undergo ISC to yield the ³F8BT* state. The long lifetime of the ³F8BT* permits diffusion towards the porphyrin with subsequent TET.....135*
- Figure 4.37** *Molecular orbitals of a F8BT-HAPAPP model and HAPAPP calculated using a B3LYP/6-31G(d). Note that the LUMO +1 and LUMO +2 of F8BT-HAPAPP are isoenergetic and identical except for inversion of the wavefunction phase symmetry. Results provided by Dr Tracey Clarke.....137*
- Figure 5.1** *Schematic representation of a donor-acceptor (D-A) and a donor-orthogonal acceptor (D-oA) conjugated polymer. The blue and red rectangles represent donor and acceptor units respectively.....145*
- Figure 5.2** *Structures of the donor-orthogonal acceptor conjugated polymers SFCN and ASFCN. Note the substituted spiro moiety located orthogonal to the*

backbone in SFCN and ASFCN. S_{LO} and T_{LO} represent local singlet and triplet states respectively.....146

Figure 5.3 Structures of the donor-orthogonal acceptor conjugated polymer Thiro and its monomeric derivatives, CPDT-C16 and M-Thiro. Note the substituted spiro moiety located orthogonal to the CPDT backbone on Thiro.147

Figure 5.4 Normalised ground state absorbance spectra of pristine Thiro in chlorobenzene solution (50 $\mu\text{g/mL}$) and thin film, including its monomeric constituents mThiro and CPDT-C16 in chlorobenzene solution (10 $\mu\text{g/mL}$). Spectra have been normalised to their respective peak maxima.....149

Figure 5.5 Normalised ground state photoluminescence spectra of pristine Thiro in chlorobenzene solution (50 $\mu\text{g/mL}$) and thin film. Spectra were obtained with an excitation wavelength of 532 nm and have been normalised to their respective peak maxima.....151

Figure 5.6 Time-correlated single photon counting obtained for pristine Thiro in chlorobenzene solution (50 $\mu\text{g/mL}$). Obtained with a pump wavelength of 467 nm and carried out under and N_2 atmosphere. Inset: The same spectral data normalised to the peak maxima, illustrating the presence of a long-lived transition to the red of the main emission. The black arrow demonstrates the spectral evolution over time. Data collected at Imperial College London... 152

Figure 5.7 Time-correlated single photon counting obtained for a) pristine Thiro in chlorobenzene solution (50 $\mu\text{g/mL}$) and b) pristine Thiro thin film. Obtained with an excitation wavelength of 445 nm and at probe wavelengths of a) 680 and b) 800 nm. IRF is the instrument response function and yields a temporal resolution of ~ 5 ns. Data collected at UCL.....153

Figure 5.8 Time-resolved emission spectra of pristine Thiro solution (50 $\mu\text{g/mL}$) and b) the same spectral data normalised. Obtained with a ICCD camera, using an excitation wavelength of 525 nm at a power of 10 μW . A 550 nm long pass filter was used. Data collected at Cambridge University with the aid of Saul Jones and Bluebell Drummond. For b), the data from 45-70 ns has been smoothed via adjacent averaging.....154

Figure 5.9 Photoluminescence decay kinetics of pristine thiro solution. Obtained with an excitation wavelength of 525 nm, at a power of 10 μW155

Figure 5.10 <i>Time-resolved emission spectra of pristine Thiro thin film. Obtained with an excitation wavelength of 525 nm, at a power of 10 μW. A 550 nm long pass filter was used.....</i>	156
Figure 5.11 <i>Picosecond transient absorption spectrum of Thiro in chlorobenzene solution (50 μg/mL), excited with a pump wavelength of 520 nm and an excitation density of 50 μJ cm⁻². Spectrum has been corrected for the absorbance at the exciting wavelength.....</i>	157
Figure 5.12 <i>Normalised picosecond transient absorption, ground state absorbance and steady state photoluminescence spectra of a) pristine Thiro solution b) pristine Thiro film. Spectra have been normalised to their respective peak maxima.....</i>	158
Figure 5.13 <i>Normalised picosecond transient absorption decay kinetics of Thiro solution excited with a pump wavelength of 520 nm and excitation energies of 5 and 50 μJ cm⁻². Dynamics were averaged using the decay data in the range of 1200-1300 nm.....</i>	159
Figure 5.14 <i>Kinetics obtained by global analysis of the picosecond transient absorption data of Thiro in chlorobenzene solution (50 μg/mL). Excited with a pump wavelength of 520 nm and an excitation density of 50 μJ cm⁻². Inset: the spectral components obtained from global analysis of the same data used to obtain the kinetics.....</i>	160
Figure 5.15 <i>Normalised excitation dependant kinetics obtained by global analysis of the picosecond transient absorption data of Thiro in chlorobenzene solution (50 μg/mL). The kinetic decays correspond to the different spectral components at a) 1300, b) 950 nm and c) 1100 nm. Data was obtained with a pump wavelength of 520 nm and an excitation density range of 5-50 μJ cm⁻².</i>	161
Figure 5.16 <i>ps transient absorption spectrum of Thiro thin film, excited with a pump wavelength of 520 nm an excitation density of 50 μJ cm⁻². Spectrum has been corrected for the absorbance at the exciting wavelength.....</i>	162
Figure 5.17 <i>Normalised ps transient absorption spectrum of Thiro thin film and chlorobenzene solution. Obtained with a pump wavelength of 520 nm, at an excitation density of 50 μJ cm⁻². Spectra taken at 6 ns.....</i>	163

Figure 5.18 Kinetics obtained by global analysis of the picosecond transient absorption data of a pristine Thiro film. Excited with a pump wavelength of 520 nm and an excitation density of 50 $\mu\text{J cm}^{-2}$). **Inset:** the normalised spectral components obtained from global analysis of the same data used to obtain the kinetics.....164

Figure 5.19 Kinetics obtained by global analysis of the picosecond transient absorption data of pristine Thiro in chlorobenzene solution and its thin film. Excited with a pump wavelength of 520 nm and an excitation density of 51 $\mu\text{J cm}^{-2}$165

Figure 5.20 a) Microsecond transient absorption spectrum of Thiro in chlorobenzene solution (50 $\mu\text{g/mL}$). Obtained with an excitation wavelength of 532 nm and an excitation density of 40 $\mu\text{J cm}^{-2}$. **b)** The same spectral data normalised to 900 nm, illustrating the presence of a new species at later time scales.....167

Figure 5.21 Microsecond transient absorption kinetics of pristine Thiro in chlorobenzene solution (50 $\mu\text{g/mL}$). Obtained with a pump wavelength of 532 nm and a probe wavelength of 980 nm.....168

Figure 5.22 Microsecond transient absorption kinetics of neat Thiro in chlorobenzene solution (50 $\mu\text{g/mL}$). Obtained with an excitation wavelength of 532 nm and a probe wavelength of 980 nm. Decays have been obtained via subtracting a fitted power-law decay ($A\tau^a$) from the overall decay data.....170

Figure 5.23 a) Excitation density dependant kinetics of a pristine Thiro solution (50 $\mu\text{g/mL}$), **b)** pristine Thiro thin film. Obtained with an excitation wavelength of 532 nm and at a probe wavelength of 980 nm. The normalised signal amplitude at 1 and 100 μs is shown as a function of excitation energy, where the ΔOD at 1 μs for both the solution and film has had the contribution from the slow phase subtracted from it.....171

Figure 5.24 Microsecond transient absorption kinetics of pristine Thiro in chlorobenzene solution (50 $\mu\text{g/mL}$), excited with an excitation wavelength of 532 nm and at an excitation density of 20 $\mu\text{J cm}^{-2}$. The initial solution was degassed for 1h with N_2 . The solution was then bubbled with O_2 for 30 min, and then restored with N_2 by degassing for 1 h. **Inset:** the kinetic decays with the contribution from the long-lived decay removed.....172

Figure 5.25 a) Microsecond transient absorption spectrum of a pristine Thiro thin film. Obtained with an excitation wavelength of 530 nm and at an excitation density of $14 \mu\text{J cm}^{-2}$. **b)** The same spectral data normalised to 960 nm, illustrating the presence of a long-lived species at later time scales.....173

Figure 5.26 Microsecond transient absorption kinetics of pristine Thiro thin film. Obtained with a pump wavelength of 532 nm and a probe wavelength of 980 nm. Excitation energy $14 \mu\text{J cm}^{-2}$. * During the N_2 restored measurement, the power output of the laser was found to decrease, resulting in a perceived reduction in ΔOD . The normalised kinetics of the initial and restored N_2 atmospheres are provided in the inset and illustrate near identical decays.174

Figure 5.27 Microsecond transient absorption kinetics of a pristine Thiro thin film. Obtained with a pump wavelength of 532 nm and a probe wavelength of 980 nm.....174

Figure 5.28 Normalised microsecond transient absorption kinetics of pristine Thiro thin film. Obtained with a pump wavelength of 532 nm and at a probe wavelength of 980 nm. Decays have been obtained via subtracting a fitted power-law decay (At^α) from the overall decay data.....175

Figure 5.29 a) Microsecond transient absorption spectrum of a Thiro:PC₆₀BM 1:1 thin film. Obtained with an excitation wavelength of 530 nm and at an excitation density of $16 \mu\text{J cm}^{-2}$. **Inset:** Microsecond transient absorption kinetics of a Thiro:PC₆₀BM 1:1 thin film under N_2 and O_2 atmospheres, illustrating an O_2 independent decay. Obtained with a pump wavelength of 530 nm, an excitation density of $18 \mu\text{J cm}^{-2}$ and at a probe wavelength of 1020 nm. **b)** The same spectral data presented in **a)** normalised to 1020 nm, illustrating that new species appear at later time scales.....177

Figure 5.30 Normalised microsecond transient absorption spectra of pristine Thiro in chlorobenzene solution (50 $\mu\text{g/mL}$), pristine Thiro thin film and a Thiro:PC₆₀BM 1:1 blend. All spectra have been normalised to their respective peak maxima. At 1 μs both the pristine solution and thin film exhibit triplet transitions at 900 and 980 nm respectively.....178

Figure 5.31 Microsecond transient absorption kinetics of a Thiro:PC₆₀BM (1:1) film. Obtained with an excitation wavelength of 530 nm and at a probe wavelength of 1020 nm.....179

Figure 5.32 *Microsecond transient absorption kinetics of a Thiro:PC₆₀BM (1:1) film. Obtained with an excitation wavelength of 530 nm and at a probe wavelength of 1020 nm. The normalised signal amplitude at 0.6 and 100 μs is shown as a function of excitation energy, where the ΔOD at 0.6 μs has had the contribution from the slow phase subtracted from it.....179*

Figure 5.33 *Schematic energy diagram for Thiro and density difference plots for the B₁ (S₂(LE) and T₁(LE)) and B₂ (S₁(CT) and T₃(CT)) symmetry states. Energies displayed were calculated by Dr Tom Penfold (Newcastle university) using a dimeric unit of the Thiro Polymer, in conjunction with a CAM-B3LYP methodology with a def2-TZVP basis set. Diagram is not to scale.....182*

Figure 5.34 *Normalised microsecond transient absorption kinetics of pristine Thiro solution (50 μg/mL), pristine Thiro film and a Thiro:PC₆₀BM 1:1 blend film. The decay data has been normalised to the number of photons absorbed at the exciting wavelength.....185*

List of Tables

Table 4.1 Spin statistics for the interaction of two triplet states. The type 1 interaction permits spin conservation.....	98
Table 4.2 Photophysical parameters obtained for F8BT-HAPAPP and its control samples F8BT and HAPAPP. F8BT-HAPAPP was selectively excited at 400 and 645 nm, corresponding to exciting of the F8BT backbone and porphyrin Q-band respectively.....	105
Table 4.3 Fitting results of F8BT-HAPAPP chlorobenzene solution (3.2 mg/mL) excited with 518 nm. Decays were obtained by averaging the region 900-1000 nm. Decays were obtained from fits with a biexponential function shown in equation 4.1.....	117
Table 4.4 Fitting results of F8BT chlorobenzene solution (68 µg/mL) excited with 460 nm and a probe wavelength of 800 nm. Decays were obtained from fits with a biexponential function shown in equation 4.1.....	120
Table 4.5 Selected TD-DFT results for HAPAPP and an F8BT-Model using B3LYP/6-31G(d). Results provided by Dr Tracey Clarke.....	138
Table 5.1 Spin orbit couple matrix elements between the excited states calculated by Dr Tom Penfold (Newcastle university) with TDDFT using by using quasi-degenerate perturbation theory.....	183

Acronyms and Abbreviations

BR – *Bimolecular recombination*

CB – *Chlorobenzene*

CT – *Charge transfer*

DOS – *Density of states*

EQE - *External quantum efficiency*

FC – *Franck-Condon*

FRET - *Förster resonance energy transfer*

FWHM – *Full width at half maximum*

GR – *Geminate recombination*

HFI – *Hyper fine interaction*

IC - *Internal conversion*

ICCD – *Intensified charge coupled device*

IQE – *Internal quantum efficiency*

IRF – *Instrument response function*

ISC - *Intersystem crossing*

NIR – *Near infrared*

NFA – *Non-fullerene acceptor*

OD – *Optical density*

o-DCB – *Ortho dichlorobenzene*

OLED – *Organic light emitting diode*

OSC – *Organic solar cell*

PL – *Photoluminescence*

PV – *Photovoltaic*

QY – *Quantum yield*

RT – *Room temperature*

SF – *Singlet fission*

SOC - *Spin orbit coupling*

SOCT – *Spin-orbit charge transfer*

Si-PV – *Silicon photovoltaics*

TADF - *Thermally activated delayed fluorescence*

TAS – *Transient absorption spectroscopy*

TC-SPC – *Time correlated singlet photon counting*

TTA – *Triplet-triplet annihilation*

TTA-UC – *Triplet-triplet annihilation upconversion*

TR-EPR – *Transient electron paramagnetic resonance*

ZFS – *Zero field splitting*

Acknowledgements

This PhD would not have been possible without being provided with equal parts grinding criticism and unmatched wisdom by my supervisor Dr Tracey Clarke. I will forever be grateful for the trust and guidance she gave to me.

To all those in our group past and present who have helped me along the way. To Nathaniel Luke who shared dungeons deep and foul and has moved on to pastures anew. To Dr Jose Beloqui whose eccentric personality acts as a bulwark against the Spanish cultural catastrophe that is the Sagrada Familiar. To Jun Jun for her constant look of bemusement. To Caroline for wasting the N₂.

To Dr Hugo Bronstein and his crew for endeavouring to impede the progress of my PhD by providing me with extremely small quantities of master-crafted materials. To Dr Caroline Knapp and her tribe for showing me what a real oxygen free atmosphere is. To Professor Helen Fielding, Mike, Joe, Jamie and Alice, who provided such warmth and hospitality. To Professor James Durrant and his group, who generously lent their expensive equipment and invaluable time. To Dr Allesandro Minotto for aiding me when he did not need to. To all those not mentioned who have helped me on my journey.

To all my friends who I had to say no to when I wanted to say yes. To the chicken dinner hunters and pint-smiths. To squash warlords and trainers of men.

To my family who are the reason I am here.

It's been a long and winding road, but what a blast it was!

List of Publications

Published

1. E. Salvadori, L. Luke, **J. Shaikh**, A. Leventis, H. Bronstein, C. W. Kay and T. M. Clarke, *J. Mater. Chem. A*, 2017, **5**, 24335-24343. "Ultra-fast spin-mixing in a diketopyrrolopyrrole monomer/fullerene blend charge transfer state".
2. **J. Shaikh**, D. M. E. Freeman, H. Bronstein and T. M. Clarke, *J. Phys. Chem. C*, 2018, **122**, 23950-23958. "Energy-Transfer Pathways and Triplet Lifetime Manipulation in a Zinc Porphyrin/F8BT Hybrid Polymer".
3. **J. Shaikh**, D. G. Congrave, A. Forster, A. Minotto, F. Cacialli, T. J. H. Hele, T. J. Pemfold, H. Bronstein and T. M. Clarke. *Chem. Sci.*, 2021, Advance Article, DOI: 10.1039/D1SC00919B. "Intrinsic photogeneration of long-lived charges in a donor-orthogonal acceptor conjugated polymer".

Chapter 1

Introduction and Overview

1.1 Motivation and Overview

Energy security has become one of the preeminent problems facing humanity in the 21st century. An overreliance on primary fossil fuel sources has led to anthropological climate change, with the International Panel on Climate Change (IPCC) recently stating that the global average temperature should not exceed 1.5 °C above pre-industrial levels to mitigate the worst of these effects.¹ In addition to this, the finite nature of fossil fuels in conjunction with an increased energy demand from developing nations has driven the need to develop and use renewable energy. For example, the UK seeks to deliver 15% of its total energy consumption from renewable energy sources by 2020.² The most abundant renewable resource available on Earth is that of solar energy, with it receiving 120 000 TW of electromagnetic radiation from the Sun. This vast quantity of energy dwarf's mankind's current needs. It is thought that covering just 0.16 % of Earth's land mass with 10 % efficient solar-conversion systems would provide 20 TW of power, more than enough to meet mankind's energy needs.³ Photovoltaic (PV) cells (colloquially known as solar cells) provide a means to harvest this near unlimited energy reserve. Since Edmund Becquerel's discovery of the photovoltaic effect in 1839,⁴ researchers have made great strides in the area of photovoltaics. A photovoltaic cell is an electrical device that allows for the conversion of light directly into electrical energy, via the photovoltaic effect. The photovoltaic effect is the generation of a potential difference in a material, when it is exposed to light. The most commonly known photovoltaic cells derive from a class known as 'inorganic' solar cells. These inorganic solar cells are made predominantly from semiconducting materials, such as silicon, gallium arsenide, cadmium telluride, or copper germanium selenide.⁵ The first inorganic photovoltaic device was that of silicon in 1954, exhibiting a photoconversion efficiency of 6%.⁶ These silicon devices have now matured to exhibit efficiencies of up to 26.7%.⁷ Photovoltaics have exhibited rapid growth in recent years, with 2018 yielding a 25% increase in commercial energy capacity compared to the previous year. Regardless of this, photovoltaics accounted for just 2.6% of global electricity generated, with it expected to increase to 4% by 2023 according to the International Energy Agency (IEA).⁸

Silicon solar cells are a mature technology, and with sharp cost reductions globally over the last decade (>85% for the period of 2009-2019)⁹ they are now among the

Chapter 1

cheapest forms of energy available.¹⁰ Nonetheless, silicon solar cells are not without drawbacks. One such disadvantage is that Si-PV production requires the use of molten elemental silicon, requiring temperatures in excess of 1400 °C, leading to both wider emission concerns and setting of a lower limit for their production cost.¹¹ Furthermore, silicon solar cells in general display poor mechanical flexibility, resulting in rigid and often heavy devices, thus limiting their installation potential. A possible alternative to traditional silicon photovoltaics is that of organic solar cells, which are solar cells typically comprised of π -conjugated polymeric materials. The organic nature of these materials makes low-temperature solution processing viable, offering the prospect for low-cost and large-scale production of solar cells via roll-to-roll printing technology.^{12,13} This is in stark contrast to the energy intensive production techniques of silicon solar cells. In addition, the polymeric nature of many of these materials results in relatively low-weight thin films, which also exhibit mechanical flexibility, thus opening up the potential for flexible electronics (such as textile compatible solar cells).¹⁴ In addition, the narrow band-gaps possessed by some conjugated materials may result in semi-transparent devices, thus allowing for integration of solar cell devices into window panes, skylight and building facades – areas hitherto unreachable by traditional Si-PV.¹⁵ Despite the fact that organic solar cells are similar in nature to organic light emitting diodes (OLEDs) they have only realised limited commercialisation.¹⁶ Fundamental issues relating to stability and device efficiency must be addressed before OSCs can compete with the existing energy regime.^{17,18,19,20}

1.2 Historical Context

The ultimate aim of a photovoltaic cell is to absorb radiation and generate electrical work. This is achieved by using a semiconductor which absorbs photons of light, generating free charge carrier species. These generated free charges are then sent to the electrodes via a built-in spatial asymmetry. Under open circuit voltage conditions, this results in the formation of a photovoltage, whilst at short circuit a photocurrent is generated. When a load is connected to the external circuit, the PV cell yields both current and voltage, with the capability to do electrical work.²¹

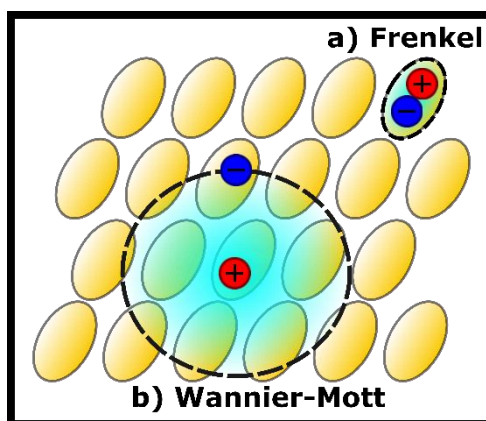


Figure 1.1 Schematic representation of **a)** localised Frenkel exciton, typically found in low dielectric medium organic semiconductor materials **b)** non-localised Wannier-Mott exciton, typically found in high dielectric medium inorganic semiconductors, such as silicon.

Organic solar cells possess a fundamentally different photogeneration mechanism when compared to their inorganic counterparts. The primary photoexcitation in an OSC is that of a coulombically bound electron-hole pair, known as a 'Frenkel' exciton (as opposed to a non-localised Wannier-Mott exciton), which needs to be subsequently dissociated to yield a free charge carrier.²² A simplified depiction of the difference between Frenkel and Wannier-Mott excitons is shown in figure 1.1. Organic solar cells are based upon a charge-transfer mechanism that occurs at the interface between the predominant light absorbing component, the electron donor (D) and an electron acceptor (A).²³ This interface can be considered analogous to an inorganic p-n junction, where the electron donor is the p-type material and the electron acceptor is the n-type. The difference in electron affinity between the donor and acceptor materials creates a driving force at the interface, that can allow for charge separation of the photogenerated excitons.²⁴

Chapter 1

In 1977 Alan J. Heeger, Alan G. MacDiarmid and Hideki Shirakawa demonstrated that doping polyacetylene with iodine resulted in an increase in conductivity by 12 orders of magnitude.²⁵ This discovery would earn them the Nobel prize in chemistry in 2000 and would usher in a revolution in the field of organic semiconductor materials. The first efficient organic photovoltaic device would be developed shortly thereafter by Ching W. Tang in 1986, exhibiting a modest photoconversion efficiency (PCE) of 1%.²⁶ This was achieved via the use of an electron donating copper phthalocyanine (CuPc) coupled with an electron accepting perylene derivative, with both materials orientated in a bilayer structure to create a donor-acceptor junction (schematically shown in figure 1.2 a)). The next significant milestone would be made by Heeger, who observed ultrafast electron transfer from the conjugated polymer MEH-PPV to C₆₀.²⁷ Although these polymer/fullerene bilayer devices would only yield a PCE of 0.1%, it would nonetheless lead to fullerene derivatives becoming the universal electron acceptor in OSCs. The next major leap in the field of OSC design came with the advent of the bulk heterojunction (BHJ) concept (schematically shown in figure 1.2 b)). It was known that the small diffusion distance (<10 nm) of excitons was approximately a factor of 10 smaller than the optical absorption depth, which contributed to initial bilayer devices exhibiting poor photoconversion efficiencies, as excitons not generated within the diffusion distance of the donor/acceptor interface would recombine. A bulk heterojunction structure alleviates this issue by using a bicontinuous interpenetrating network, which is made by blending the donor and acceptor materials together (with the term 'blend' referring to a mixture of donor and acceptor materials). This increases the interfacial surface area of the donor acceptor junction, thereby solving the problem of limited exciton diffusion by reducing the distance excitons need to travel to the interface, while simultaneously still maintaining a conducting pathway to the electrodes.²⁸

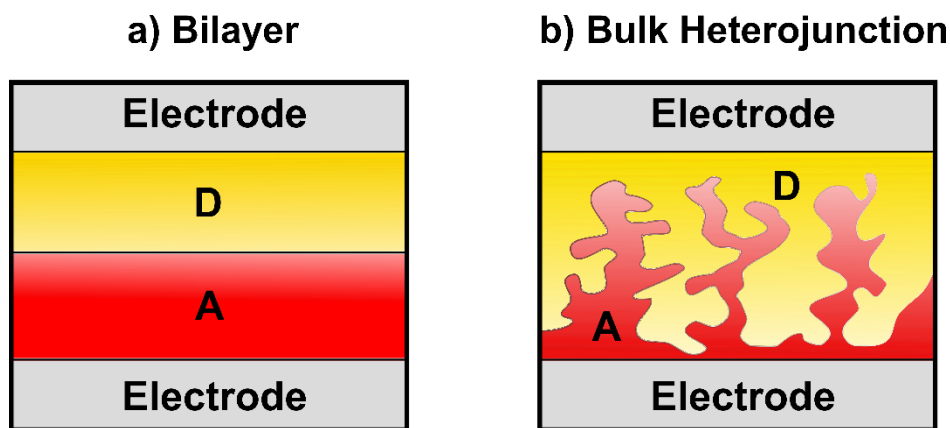


Figure 1.2 Schematic representation of electron donor (D) and acceptor (A) materials arranged in **a)** a heterojunction bilayer structure **b)** an ideal interpenetrating bulk heterojunction (BHJ) structure. In the bilayer, excitons not generated within the diffusion length of the donor/acceptor interface will recombine. In the BHJ, nanoscale phase separation increases the surface area between the donor and acceptor, therefore increasing the chance exciton reach the interface.

In recent years, the field of organic solar cells has made massive strides in improving the efficiency of devices, which in part can be attributed to the development of non-fullerene acceptor (NFA) materials. NFAs are more synthetically versatile relative to fullerene acceptors and concomitantly their electronic properties are more readily tuneable. NFAs in conjunction with an increased understanding of recombination losses and morphological control have allowed device efficiencies of 18.2% for single junction and 17.3% for tandem cells to be attained.^{29,30} While these values represent significant milestones for the development of OSCs they still pale in comparison to the efficiency of state of the art Si-PV.³¹ As such, more research into the fundamental mechanisms that govern loss processes in OSCs are needed. Furthermore, as OSCs approach higher PCEs, they still are fundamentally limited by the thermodynamic bottleneck proposed by Shockley and Quessier, which restricts the photoconversion efficiency of single-junction solar cells to 33.7%.^{32,33} New materials must be designed and studied with overcoming this barrier in mind to help herald in the era of so-called third generation solar cells.³⁴

1.3 Electronic Structure of Inorganic and Organic Semiconductors

When two atoms are brought together in a molecule, two atomic orbitals combine to yield two molecular orbitals that are lower and higher in energy than their original atomic energy levels. These new molecular orbitals are termed bonding and anti-bonding orbitals respectively. When a large number of atoms are brought close together in a solid, their atomic orbitals split into a vast number of energy levels. This has the effect of the energy levels becoming closer in energy to one another until they lose their discrete character and effectively become a continuum of states referred to as a 'band'. The highest occupied band, where the valence electrons are found, is termed the valence band. The lowest unoccupied band is termed the conduction band. If the conduction band is found to overlap energetically with the valence band the solid will possess metallic character, with the ability to conduct both heat and electricity. If there is an energetic gap between the valence and conduction band that is in the range of 0.5 to 3 eV, then the solid is said to be a semi-conductor (shown schematically in figure 1.3 d).

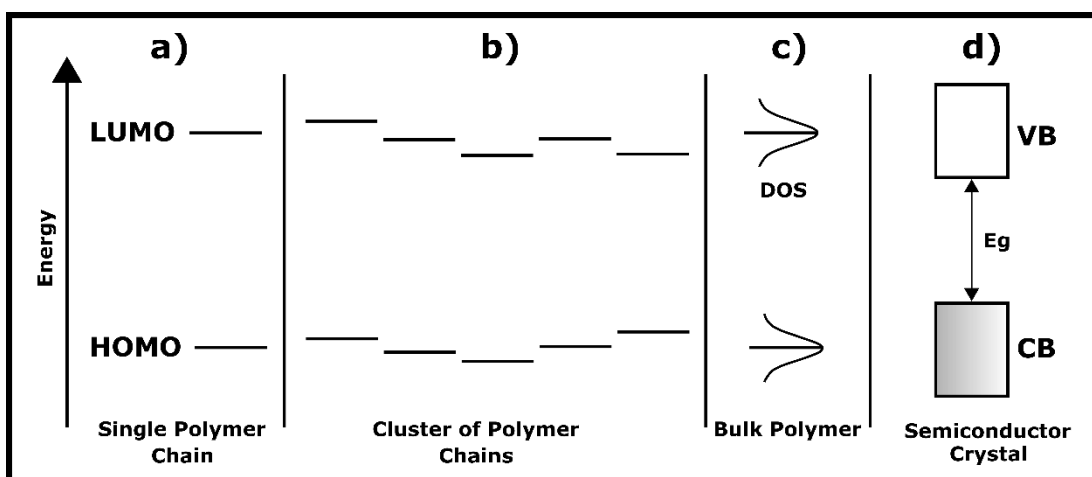


Figure 1.3 Orbital energy diagram illustrating the effect of energetic disorder when transitioning from **a)** a discrete polymer chain to **b)** a cluster of polymer chains, such as when aggregated in a concentrated solution to **c)** bulk polymer, such as when in a thin film and DOS is the density of states. **d)** a semiconducting crystal, where VB is the valence band, CB is the conduction band and E_g is the energy of the bandgap. It is noted that in **a)** a single energy level is represented for simplicity, but will possess a distribution of energies due to variations in conjugation length, defects and conformation.

Chapter 1

The energy separation between the valence and conduction bands is known as the bandgap. An electron may be promoted from the valence band to the conduction band via means of thermal energy or a photon that is greater in energy than the band gap. When a valence electron is promoted to the conduction band, a positively charged vacancy is created in the valence band, which is known as a hole. Both the newly freed conduction band electron and positive hole are able to travel and transport charge. The conductive behaviour that arises from the absorption of light is known as photoconductivity.

Unlike inorganic crystals, the electronic properties of organic semiconducting materials, such as small molecules and polymers stem from their conjugated π -system. The conjugated π -system affords the ability for electrons to be delocalised across the system, allowing for the flow of charge. This conjugated system arises from sp^2 -hybridisation of carbon atoms, which yields a series of overlapping p_z orbitals, as shown schematically in figure 1.4. These overlapping p_z orbitals result in the formation of alternating π -molecular orbitals, which are split into lower energy bonding π -orbitals and higher energy anti-bonding π^* -orbitals. The π -orbital will therefore be the highest occupied molecular orbital (HOMO), corresponding to the top of the valence band in inorganic semiconductors. Conversely, the π^* -orbital will be the lowest unoccupied molecular orbital (LUMO), corresponding to the bottom of the conduction band in inorganic semiconductors. Thus, HOMO to LUMO transitions in organic semiconductors can be considered analogous to transitions between the valence and conduction band, with the energy difference between the HOMO and LUMO being approximated as the band gap.³⁵

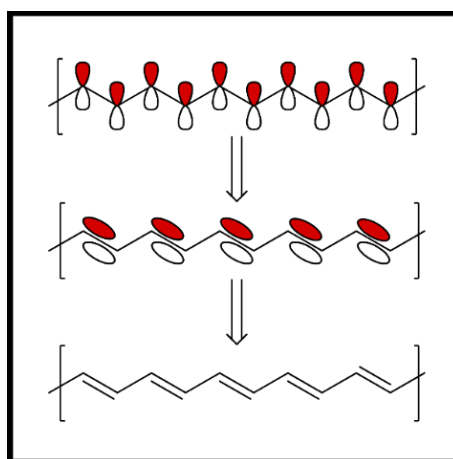


Figure 1.4 Schematic representation of conjugation in polyacetylene. Overlapping P_z orbitals results in an extended π -conjugated network across the backbone of the polymer.

Chapter 1

An important feature inherent to polymeric materials is the presence of significant energetic and morphological disorder (schematically presented in figure 1.3). The conjugated network is not likely to be maintained over the entire backbone, instead extending over a small chain segment. This inability to maintain long-range order is the result of kinks, chemical defects and torsion around single covalent bonds, found on the polymer backbone. This therefore leads to a range of conjugation lengths, and consequently a distribution of energies (energetic disorder). This energetic disorder is characterised as a gaussian distribution of energy states for the HOMO and LUMO (as shown in figure 1.3 c),³⁶ and as such plays an important role in dictating the transport properties of the material. When in the solid phase, morphological disorder is also present, stemming from different molecular conformations present in the film, as well as interchain interactions between polymer chain segments resulting in different chemical environments.

1.4 Exciton formation in Solar cells

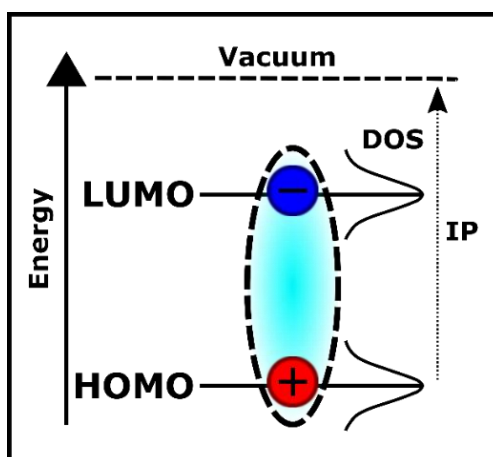


Figure 1.5 Orbital energy diagram illustrating the formation of a coulombically bound electron-hole pair known as an exciton. The dashed line enclosing the positive and negative charges schematically represents the coulombic attraction that must be overcome to achieve charge dissociation. The density of states (DOS) reflects the disordered nature of organic materials and indicates that the energy of the exciton may extend into the bandgap.

A solar cell operates by absorbing incident solar radiation to generate freely dissociated charge species. These free charges may then be subsequently sent around a circuit and used to generate electrical power. In an inorganic solar cell initial absorption of an incident photon of energy equal to or greater than the bandgap results in an electronic transition, from the occupied valence band to the unoccupied conduction band of the crystal. This results in the formation of a positively charged

Chapter 1

hole in the valence band and a negatively charged electron located in the conduction band, which are free to dissociate from one another at room temperature. Organic solar cells differ from this, in that initial solar excitation of the HOMO of the donor molecule to its LUMO does not result in the formation of free charge carriers (i.e. unbound electrons and holes). The initial species generated are subject to a strong mutual Coulombic interaction, resulting in an electrostatically bound singlet 'excitonic state', where the negative electron is localised on the LUMO and the positive hole on the HOMO (schematically shown in figure 1.5).²³ The degree of this Coulombic interaction, V , is derived from the electric charge e , permittivity of vacuum ϵ_0 , the dielectric constant of the medium ϵ_r and the distance between the electron-hole pair separation r , as shown in equation 1.1.

$$V = \frac{e^2}{4\pi\epsilon_r\epsilon_0r} \quad \text{Eqn. 1.1}$$

In standard inorganic solar cells this mutual coulombic attraction is easy to overcome due to their relatively large dielectric constants (for example silicon $\epsilon_r = 11.68$).³⁷ Furthermore, inorganic materials possess strong interatomic electronic interactions, resulting in a more delocalised wave function, which manifests itself as a larger electron-hole separation distance, r . These properties result in inorganic materials possessing electron-hole pairs with a small exciton binding energy, which can overcome their mutual coulombic attraction at room temperature and dissociate into free charges.

The molecular materials utilised in organic solar cells, in contrast to their inorganic counterparts possess significantly smaller dielectric constants ($\epsilon_r \sim 2-4$). Additionally, due to their weaker, non-covalent electronic interactions between molecules, the electron's wave function is found to be spatially confined. Both of these factors give rise to a strong coulombic interaction between the electron and hole, typically an order of magnitude greater than the thermal energy available at room temperature. This means at RT the main photogenerated product of organic semiconductor materials is that of bound electron-hole pairs.

These bound excitons are split through 'blending' of the electron donor material with an electron-deficient acceptor molecule. The donor and acceptor materials are chosen such that an energetic offset between the donor HOMO and acceptor LUMO exists, to create a driving force, $-\Delta G_{CS}$, for charge separation.^{23,38,24}

1.5 Mechanisms of Exciton Diffusion

When a donor-acceptor blend is excited, excitons are statistically more likely to be generated in the bulk as opposed to at the D/A interface. This has the consequence of bulk generated excitons needing to diffuse to the acceptor at the interface to allow for charge separation. The exciton diffusion distance is therefore an important parameter when determining the efficiency of an organic photovoltaic device. This is because if an exciton cannot diffuse to an interface within its lifetime, it will undergo radiative and non-radiative decay, with that energy being lost and not contributing to device photocurrent. As such, long diffusion distances are highly desirable, as shown by Terao et al who demonstrated a linear J_{sc} dependence on increasing exciton diffusion length in a series of metal phthalocyanines blended with PC₆₀BM.³⁹

The exciton diffusion distance in fluorescent materials can be determined from steady state or time-resolved photoluminescence techniques by measuring the fluorescence of an organic material, in the absence and presence of an exciton quencher (which is typically a fullerene).⁴⁰ Organic polymeric materials used in solar cells are usually found to possess singlet exciton lifetimes of <1 ns,^{41,42} which results in a relatively small diffusion distance of <10 nm.^{43,44,45} The most efficient devices will therefore have domain sizes on the order of this diffusion length to prevent competition with relaxation to the ground state. It should be noted, however, that if the domain sizes become too small, free charge recombination can become significant, negatively impacting charge collection.⁴⁶ Exciton diffusion is thought to proceed via energy migration (i.e. through identical chromophores) and follow either Förster or Dexter mechanisms (figure 1.6). Each of these energy transfer mechanisms will be discussed briefly.

1.5.1 Förster Resonance Energy Transfer (FRET)

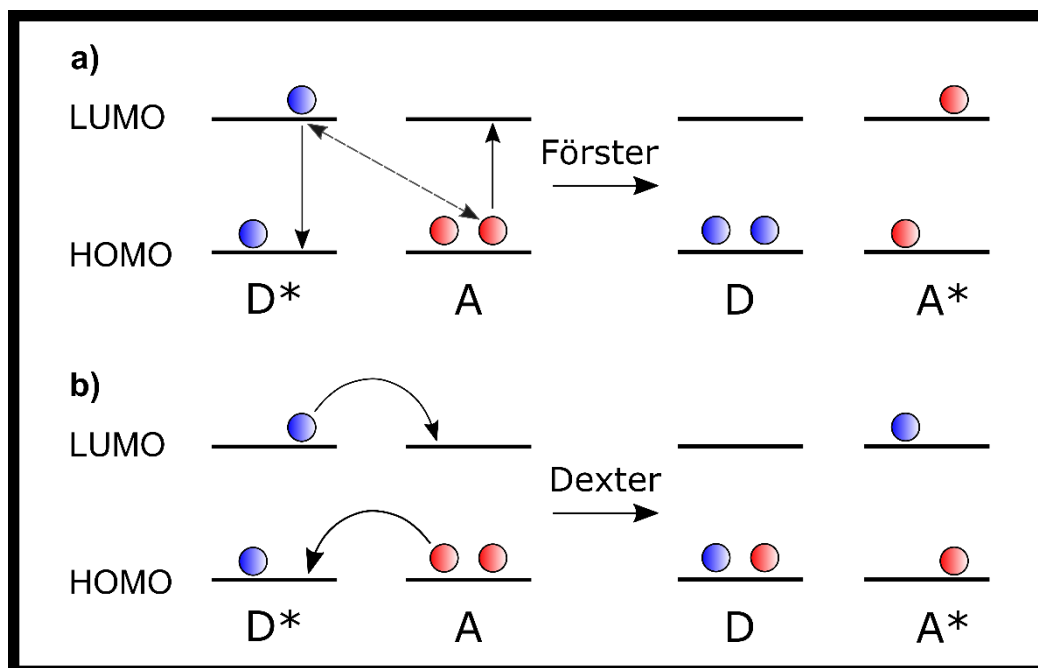


Figure 1.6 Schematic representation of the mechanisms involved in **a)** Förster resonance energy transfer and **b)** Dexter energy transfer. The Förster mechanism is a dipole-dipole interaction whereas Dexter involves electron exchange. In the case of Dexter energy transfer, electron exchange must obey the laws of spin conservation.

Förster resonance energy transfer (FRET) is a long range, through-space process, that is mediated via coulombic coupling between the exciton dipole moments of the donor and acceptor species (schematically shown in figure 1.6 a). It should be noted that, for conjugated polymers, the donor and acceptor may reside on the same polymer chain (intramolecular energy transfer) or a different one altogether (intermolecular energy transfer). The efficiency of the FRET process is found to strongly depend upon the degree of overlap between the emission spectrum of the donor species and the absorption spectrum of the acceptor species (hence the term “resonance”). FRET interactions distances are typically found to be in the range of 1-5 nm,⁴⁷ thus allowing for energy transfer on a scale much greater than molecular diameters. The rate of Förster energy transfer, k_f , is given by equation 1.2.

$$k_f = \frac{1}{\tau_D} \left(\frac{R_0}{r} \right)^6 \quad \text{Eqn. 1.2}$$

Where r is the distance between the donor and acceptor, τ_D is the lifetime of the donor in the absence of the acceptor, and R_0 is the Förster critical radius, which is the distance at which energy transfer has 50% efficiency. This observed r^{-6} dependence

in equation 1.2 is a characteristic hallmark of FRET, allowing it to be easily distinguished from other forms of energy transfer. The Förster radius itself is given by equation 1.3.

$$R_0^6 = \frac{9\Phi_{PL}k^2}{128\pi^5n^4}J_F \quad \text{Eqn. 1.3}$$

Where Φ_{PL} is the photoluminescence quantum yield, k is an orientation factor to allow for the directional nature of the dipole-dipole interaction, n is the refractive index, and J_F is the Förster overlap integral between the photoluminescence spectrum of the donor and the absorption spectrum of the acceptor. The Förster mechanism is thought to be the predominant method for which singlet excitons diffuse through an organic semiconductor. Triplet excitons on the other hand are spin forbidden from undergoing the interaction, as each transfer step would require a change in spin.⁴⁷ However, provided the donor exhibits a high phosphorescence quantum yield, triplets may also undergo FRET.⁴⁸ It should be noted however, that most organic conjugated materials used in organic solar cells possess weak spin-orbit interactions, and consequently do not possess the ability to undergo triplet exciton FRET.⁴⁹

Förster theory has been successfully used to determine the diffusion length of small molecules,^{50,51,52} but has been less successful when applied to polymeric materials. The energetic, spatial and orientational disorder inherent to polymeric materials plays an additional role in exciton diffusion dynamics. A disordered material will possess a gaussian distribution of excitonic energy states. Upon initial photogeneration, an exciton will undergo downhill energy migration to sites of lower energy on a timescale of ps-ns.^{53,54,55} This energy migration process can manifest itself spectroscopically as a bathochromic shift in the PL spectrum over time, until thermal equilibrium is reached.⁵⁶ In addition to this spectral shift, polymers have also been observed to exhibit a temperature dependence for exciton diffusion. At room temperature MDMO-PPV possesses two distinct exciton diffusion regimes, an initial temperature independent diffusion, followed by a thermally activated one.⁵³ When the polymer is cooled from room temperature to ~150 K, activated diffusion becomes significantly less important, resulting in a decreased exciton diffusion length and diffusion coefficient. Reducing the temperature <150 K effectively switches off the activated diffusion mechanism, such that the diffusion length and coefficient become temperature independent. It should be noted that the observed temperature dependence cannot be fully explained by equation 1.3, as there is no explicit temperature term in the expression. Both the parameters Φ_{PL} and J_F however, are affected by temperature to some degree. Φ_{PL} is expected to increase as temperature

is reduced, as non-radiative decay channels are deactivated. This increase in Φ_{PL} will be counteracted by the expected decrease in the value of J_{F} from a reduction in thermal spectral broadening. The observed temperature dependence on exciton diffusion is thought to be a function of the intermolecular separation, d , between excitonic sites involved in the energy hopping process. If thermal equilibrium is established during the lifetime of the exciton, then the distance between the excitonic sites at that energy level will be given by equation 1.4:

$$d_{eqb} = [n_{eqb}]^{\frac{1}{3}} = \left[N_0 e^{\left(\frac{-\sigma^2}{2(kT)^2} \right)} \right]^{\frac{1}{3}} \quad \text{Eqn. 1.4}$$

Where n_{eqb} is the density of states at equilibrium, N_0 is the total density of available excitonic states ($\sim 10^{21} \text{ cm}^{-3}$ for organic semiconductors) and σ is the energetic disorder. When the temperature of MDMO-PPV is reduced below 150 K, the distance between the donor and acceptor sites becomes greater than the range of Förster energy transfer (i.e. $>1\text{-}5 \text{ nm}$).

1.5.2 Dexter Energy Transfer

In contrast to FRET, Dexter energy transfer is a short-range collisional process, requiring physical overlap of the donor and acceptor orbitals.⁵⁷ This has the effect of leading to interaction ranges on the order of $<1 \text{ nm}$, which is less than the $1\text{-}5 \text{ nm}$ observed for FRET. Dexter energy transfer is considered to involve a two-electron transfer process, with an excited electron in the donor LUMO being transferred to the LUMO of the acceptor, whilst simultaneously a ground state electron in the acceptor's HOMO is transferred to the HOMO of the donor (schematically represented in figure 1.6 b). For singlet excitons, FRET is thought to outcompete Dexter energy transfer. As previously mentioned, triplet exciton diffusion via FRET is spin forbidden, as each transfer step would require a change in spin. Dexter energy transfer on the other hand, involves no net change in spin, due to it involving the transfer of two electrons and as such is thought to be the predominant mechanism via which triplet excitons diffuse.^{58,59} The overlap between orbitals is found to decrease exponentially as the separation distance between the donor and acceptor increases. In turn, as the magnitude of the electron exchange involved in energy transfer depends upon the degree of orbital overlap, so too will the rate of Dexter energy transfer, k_{ED} as shown in equation 1.5.

$$k_{\text{ED}} = K J_{\text{D}} e^{\left(\frac{-2r}{L} \right)} \quad \text{Eqn. 1.5}$$

Where r is the separation distance between the donor and acceptor, K is a parameter related to specific orbital interactions, L is the sum of the Van der Waals radii of the donor and acceptor and J_D is the Dexter overlap integral between the photoluminescence spectrum of the donor and the absorption spectrum of the acceptor.

1.5.3 Triplet Exciton Diffusion

Triplet exciton species are conjectured to possess larger diffusion lengths than their singlet counterparts, predominantly as a consequence of their much longer lifetimes. Historically, considerably less attention has been given to triplet excitons, owing to the fact that they are indirectly generated and are not the primary species in the charge generation process. This has led to relatively few reports of the triplet diffusion length in the literature. In some circumstances triplet diffusion lengths have been reported to be as low as 10-20 nm, which is of the same order of magnitude as that of singlet diffusion, thus indicating that long triplet lifetimes may be of less relevance in determining the diffusion distance.^{60,61,62,63} In contrast, triplet exciton diffusion lengths have been found to be on the order of μm s for some molecular crystals, such as, anthracene, pyrene, tetracene and rubrene.^{64, 65,66,67} The triplet exciton diffusion length has also been determined for some conjugated polymers, such as a ladder type polymer, PhLPPP, which was found to have a triplet diffusion length of 1.7-3.9 μm .⁶⁸ Additionally, Wallikewitz et al demonstrated that F8BT (this polymer will be discussed in chapter 4) possessed a triplet exciton diffusion distance of 178 nm, much greater than the 8 nm found for the singlet exciton.^{69,56}

Recently, a renewed emphasis on research into triplet exciton diffusion dynamics has been driven by a desire to exploit their photophysics to increase the efficiency of OSC devices. Photophysical processes such as, singlet fission, thermally activated delayed fluorescence and triplet-triplet annihilation are all thought to be able to enhance OSC device efficiency via incorporation of triplet excitons into the charge generation process.^{70,71,72} For the case of singlet fission, SF, an excited singlet state is split into two triplet states, with each triplet possessing half the original singlet state energy.⁷³ Both of these triplet states are initially coupled into an overall singlet state, thus conserving spin and allowing for triplet formation on the sub-100 fs timescale.⁷³ This ability to split one exciton into two, allows for internal quantum efficiencies approaching 200% and in theory permits the doubling of device photocurrent.^{74,75,76} SF has already been shown to be successful in increasing OSC photocurrent,⁷⁴ however, the mechanism via which SF proceeds is still debated. SF has been observed in both solid films and aggregated solutions,^{77,78} however, the relationship

between the intermolecular geometry, SF rate and yield is not yet fully established, inhibiting the rational design of new SF materials. It has been shown that in some cases the formation of a triplet pair state, $^1(\text{TT})$, precedes the formation of free triplets and as such must act as an intermediate in the SF process.^{77,79,80} It has also been shown that additional spatially separated triplet pairs may play an additional role in the 'free' triplet formation process, however, direct optical observation of these states is difficult.^{81,82,80} It should also be noted that in aggregated carotenoid solutions, direct free triplet formation from SF was observed to proceed without the observation of a $^1(\text{TT})$ intermediate.⁷⁸ One of the main challenges in applying SF to OSC devices is that the SF triplet excitons formed are half the initial energy of the singlet state. This therefore places stringent requirements on the donor material, which must be able to accept these relatively energetically low SF excitons and most importantly, dissociate them at donor/acceptor interface.

1.6 Exciton Dissociation

1.6.1 Marcus Theory of Electron Transfer

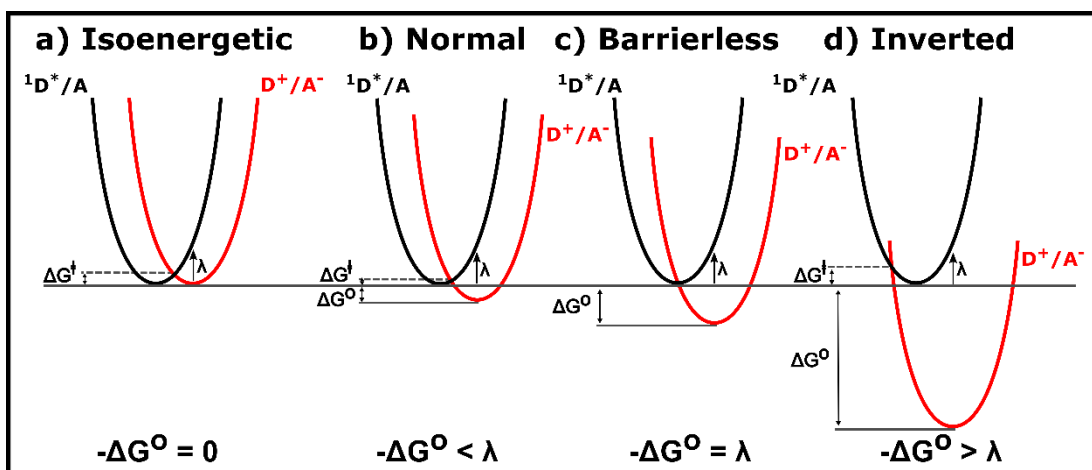


Figure 1.7 Parabolic potential energy surfaces of an electron transfer reaction from an excited donor, D^* , to an acceptor, A . The $^1D^*$ infers a photogenerated singlet state on the donor. ΔG^0 is the driving force for electron transfer and is the energy difference between the two surfaces minima. ΔG^\ddagger is the activation energy, which is determined from the difference in energy between the reactants ($^1D^*/A$) minimum and the point of intersection between the two surfaces. λ is the reorganisation energy. **a)** represents the case for isoenergetic electron transfer, **b)** represents the normal region for electron transfer, **c)** represents the barrierless region for electron transfer and **d)** represents the inverted region for electron transfer. The y-axis is the free energy and the x-axis is the reaction coordinate, which have been omitted.

Chapter 1

An exciton may be directly photogenerated at, or diffuse to a donor-acceptor interface, where the electron in the exciton may undergo an electron transfer reaction to the acceptor molecule. Marcus theory of non-adiabatic electron transfer is often invoked to describe the process of electron transfer at the interface. Marcus theory considers that the reactant and product potential energy surfaces as two simple intersecting parabolas (harmonic oscillator approximation), with the reaction coordinate corresponding to a change in the nuclear geometry.⁸³

The Frank Condon (FC) principle states that electronic transitions are much more rapid relative to the change in nuclear configuration, such that electron transfer can be considered to take place in the presence of a fixed nuclear framework. As such, electron transfer must take place at an intersection to account for both conservation of energy and the FC principle. At this intersection point, both the initial and final states will possess the same molecular geometry and potential. Isoenergetic electron transfer can therefore occur if the geometry of the reactant is brought to this intersection via vibrational motion. Electron transfer will therefore have an associated activation energy, ΔG^\ddagger , which is a function of the Gibbs free energy, ΔG° (the thermodynamic driving force), and the reorganisation energy, λ , as shown in equation 1.6.

$$\Delta G^\ddagger = \frac{(\lambda + \Delta G^\circ)^2}{4\lambda} \quad \text{Eqn. 1.6}$$

The reorganisation energy can be considered to be an additional activation barrier, corresponding to the energy required to allow the reactant and its surrounding medium to adopt the equilibrium geometry. This thermal vertical transition can be considered equivalent to the absorption of a photon, i.e. $\lambda = h\nu$.

Marcus theory was derived under the assumption that only a weak electronic interaction between the reactants is necessary for electron transfer to take place. As such, the rate of electron transfer, k_{et} , can be formulated in terms of Fermi's golden rule, as seen in equation 1.7.

$$k_{et} = \frac{2\pi}{\hbar\sqrt{4\pi\lambda k_B T}} V^2 e^{-\frac{(\lambda + \Delta G^\circ)^2}{4\lambda k_B T}} \quad \text{Eqn. 1.7}$$

Where V is the electronic coupling between the donor and acceptor wavefunctions, which depends upon the degree of their overlap. Therefore, under the weak interaction, V , will display an exponential dependence on the distance between the donor and acceptor species. k_B is the Boltzmann constant and T is the temperature.

From equations 1.6 and 1.7, several important predictions regarding the rate of electron transfer can be ascertained. The first is that k_{et} will be found to increase with increasing $-\Delta G^\circ$ (provided $-\Delta G^\circ < \lambda$), until $-\Delta G^\circ = \lambda$ is reached. This regime is known as the “normal” region for electron transfer and is shown in figure 1.7 a) and d). The point at which $-\Delta G^\circ = \lambda$ will be a barrierless region, as $\Delta G^\ddagger = 0$ and consequently k_{et} will be at its maximum. From this point, further increases to the free energy, such that $-\Delta G^\circ > \lambda$, results in the activation barrier reappearing, and a decrease in k_{et} is observed. This is known as the “inverted” region and has been observed experimentally in solution.^{84,85,86,87} Marcus type behaviour is best observed on a plot of $\ln k_{et}$ against $-\Delta G^\circ$, manifesting itself as a downward parabola, exhibiting a maximum at the barrierless region (i.e. $-\Delta G^\circ = \lambda$). In addition to solution studies, the Marcus inverted region has also been observed for a conjugated polymer/fullerene film.⁸⁸ In this study, the relative yield of charge generation was measured via time-resolved microwave conductivity, as a function of the driving force for charge generation, ΔG° , which was calculated according to previous literature methods.^{89,90} It was found that the data yielded a downward parabola, with continual increases in ΔG° leading to a reduction in charge generation. The presence of the Marcus “inverted” region was thought to be the result of charge transfer not being limited via diffusion, which is in agreement with the observation of ultrafast electron transfer.^{91,92}

1.6.2 The Charge Transfer State

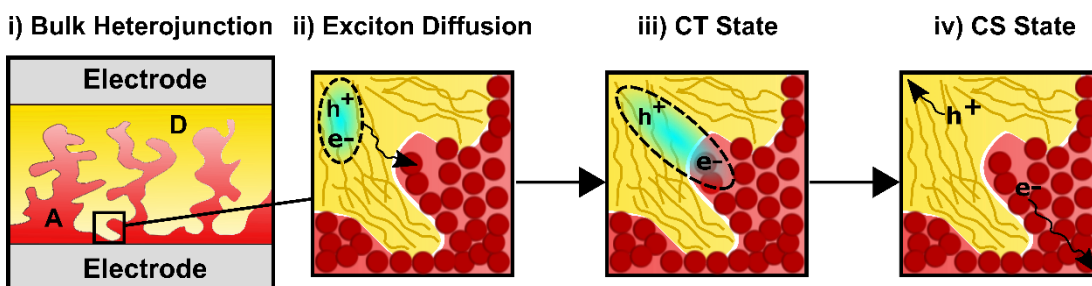


Figure 1.8 Schematic for the process of charge dissociation in a bulk heterojunction solar cell: **i)** The bulk heterojunction device architecture **ii)** The process of exciton diffusion to the donor/acceptor interface **iii)** The CT state, illustrating the electron-hole pair being bound across the interface **iv)** The charge separated state, where charges have escaped their mutual coulombic field.

The prevailing hypothesis is that when a donor exciton diffuses to the donor/acceptor interface, (or is directly generated at it) it will be quenched by the acceptor molecule via an electron transfer reaction. This results in the formation of a new intermediate species termed a charge transfer (CT) state, which has been demonstrated to play a

Chapter 1

crucial role in both free charge generation and recombination.⁹³ It is for this reason that the necessary formation of the CT state can be considered analogous to an indirect bandgap, such as that exhibited by silicon. This process of exciton diffusion CT state formation and subsequent charge separation is schematically shown in figure 1.8. A CT state is a coulombically bound electron-hole pair (schematically shown in figure 1.9), whereby the newly transferred electron is located on the LUMO of the acceptor and the hole is located on the HOMO of the donor. As the electron and hole are now located on separate adjacent species, they are afforded a greater degree of spatial separation relative to the initial photogenerated exciton. Nonetheless, CT states are still believed to be subject to a significant coulombic interaction, believed to be in the range of 0.1-0.5 eV.^{94,95} This binding energy may pose a substantial barrier to charge dissociation (~25 meV) at room temperature and predicts that geminate recombination (this will be discussed in more detail in section 1.7.1) should be a major loss mechanism. The observation of near unity photoconversion efficiencies for some bulk heterojunction solar cells,^{96,97} however, contradicts this severely. This calls into question the validity of these CT binding energies, indeed, the separation distance is thought to be of the same order of magnitude as the size of the molecular orbitals involved in the transition (0.5 – 1 nm). However, electron-hole separation distances have been reported to be in some cases 3-5 nm,^{98,99} which is greater than the expected molecular distances (< 1nm). These longer separation distances may also account for the observation of a weak temperature dependence for charge dissociation, with lower than expected activation energies of 30 meV.^{100,101,102} Although CT states are predominantly formed indirectly from an exciton, there is also evidence of direct CT state absorbance from the donor ground state via sub bandgap excitation.^{103,104,105} However, this ground state interaction is expected to be weak, owing to the low absorption coefficients exhibited by CT states.¹⁰⁶

The exact mechanism by which CT states dissociate is currently strongly debated in the literature. The main point of contention is whether charge dissociation proceeds via vibrationally excited 'hot', or thermally relaxed 'cold' CT states. In the case of 'hot' CT states, the initial energy is thought to be used to overcome the mutual coulombic field by accessing excited delocalised band states.^{107,108,109} These states are suggested to afford an increased electron hole separation distance, which allows for the otherwise dominant coulombic interaction to be overcome. This argument invokes an Onsager type treatment (see reference ²³ for more details), and to some extent can rationalise the lower than expected charge separation activation energies.

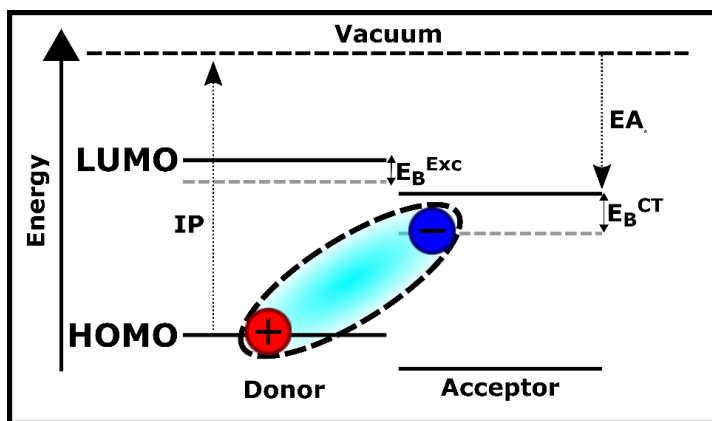


Figure 1.9 Orbital energy diagram illustrating the formation of an interfacial charge transfer (CT) state. In a CT state the electron-hole pair is bound across the interface, with the hole being located on the HOMO of the donor and the electron being located on the LUMO of the acceptor. The dashed line enclosing the positive and negative charges schematically represents the coulombic attraction still present in a CT state. IP and EA are the ionisation potential and electron affinity respectively. E_B^{Exc} and E_B^{CT} are the binding energies for the exciton and charge transfer states respectively.

There is also a plethora of evidence for the countervailing argument of charge separation predominantly occurring from “cold” CT states.^{95,99,110} It has been shown that for MEH-PPV:PCBM blends, the probability of the CT state dissociating is independent of whether it was generated “hot” with additional vibrational energy, or generated cold, through directly exciting the CT manifold to yield the thermally relaxed CT state (CT₁).¹¹⁰ This suggests that excess energy is not necessarily required for charge separation and most importantly the main dissociating species is that of the relaxed, localised CT₁ state, in contrast to a more separated electron-hole pair. Although many studies agree with charge separation occurring predominantly via relaxed CT states, there is less consensus on the role of the energetic driving force ($E_{gap} - E_{CT}$). For example, a milestone study by Durrant et al. elegantly demonstrated that for a series of polythiophenes possessing different ionisation energies and blended with the same PC₆₀BM acceptor, a clear correlation between the yield of free charges and the energetic driving force could be made.⁸⁹ It was found that even a modest increase of 200 meV to the driving force could result in a 2 order of magnitude increase in the yield of charge separation. An additional study involving Si-PCPDTBT, found that replacing PCBM with progressively higher fullerene adducts (which reduced the driving force), resulted in a reduction in the yield of free charges.⁹⁵ It was also found that the morphology of the film did not change upon alteration of the fullerene and as such the origin of the reduction in charge generation could be

attributed to a change in the CT state energy. A further study by Jakowetz et al showed that while altering the driving force did have an effect on the rate of charge generation, changing the size of the fullerene aggregates by increasing fullerene content had more of an impact.¹¹¹ This is consistent with other studies which also observed that the presence of fullerene crystallites aided charge dissociation.^{98,99,112} In one such study, annealing a P3HT:PC₆₀BM blend resulted in a reduction in the activation energy of charge separation, from 25 to 9 meV.¹⁰² It is suggested that the presence of these ordered fullerene domains might impart an additional entropic gain, as fullerene clusters possess a greater density of states, and in turn, allow electrons to bypass localised CT states.¹¹³

1.7 Charge Recombination

1.7.1 Geminate Recombination

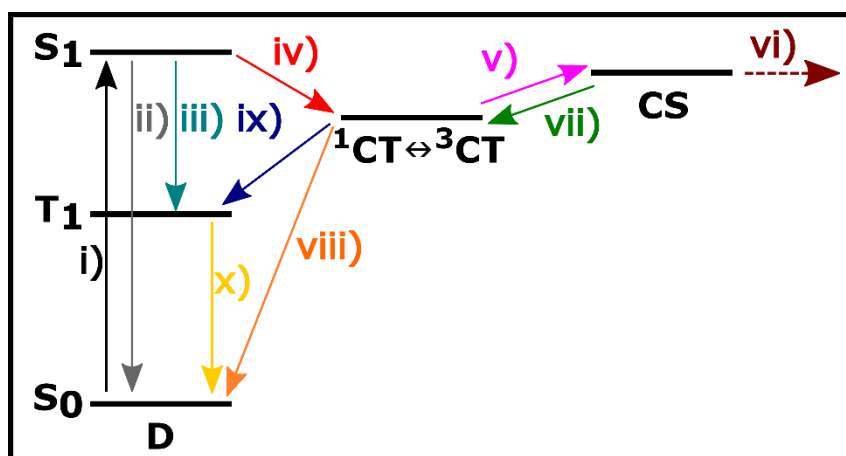


Figure 1.10 Simplified state diagram for the process of charge photogeneration and recombination. **i)** Initial exciton formation by photon absorption. **ii)** Non-radiative and radiative relaxation of the singlet exciton to the ground state. **iii)** Intersystem crossing to yield a triplet exciton. **iv)** Electron transfer to yield a charge transfer state (CT). **v)** Charge separation to yield a charge separated state (CS). **vi)** Free charge carrier diffusion and extraction at electrodes. **vii)** Bimolecular recombination of free charges to form both ¹CT and ³CT states. **viii)** Non-radiative and radiative bimolecular recombination from the CT state to the ground state. **ix)** Bimolecular recombination from the ³CT state to the triplet exciton. **x)** Non-radiative and radiative triplet relaxation of the triplet exciton to the ground state. If both ix) and viii) occur prior to charge separation, i.e. pathway v), then recombination will be geminate.

Chapter 1

As described previously, in order for a CT state to dissociate to free charges, it must overcome its coulombic binding energy. If the CT state is unable to overcome this barrier it will undergo geminate recombination, which can constitute a significant loss mechanism in OSC devices.^{114,115} Geminate recombination involves the recombination of an electron and hole that originated from the same exciton (schematically shown in figure 1.10), and is found to occur on relatively fast timescales of tens of ps up to hundreds of ns.^{116,117,118,89} Typically geminate recombination is used to refer to recombination of a bound electron and hole in a CT state. However, geminate recombination can also arise from free charges that manage to escape their mutual coulombic field but, remain spatially confined due to the physical size of their respective domains.¹¹⁸ This results in recombination between the electron and original hole being the only possible relaxation pathway. It is also worth noting that triplet species in singlet fission materials such as TIPS-tetracene have also been observed to recombine geminately and as such geminate behaviour cannot just be ascribed to the recombination of an electron and hole.^{77,119} In all of these cases recombination will be a monomolecular decay process that is independent of the excitation energy used, provided that it is of sufficiently low intensity as to not incur annihilation effects.²³

In geminate recombination, the CT state has several potential decay pathways. One pathway involves non-radiative or radiative decay to the singlet ground state (figure 1.10 (vi) , with the radiative decay being characterised by a red-shifted emission relative to the neat donor.¹²⁰ A second pathway involves CT state mediated spin-mixing ($^1\text{CT} \rightarrow ^3\text{CT}$), followed by subsequent back-transfer to yield the donor triplet exciton (figure 1.10 (vii) or acceptor triplet exciton, which has been observed for both fullerene and non-fullerene acceptor systems.^{121,122} It should be noted that triplet exciton back-transfer is only possible if the donor triplet state energy is less than that of the CT state (<0.1 eV), which for polymeric materials is likely to be the case due to the singlet-triplet energy splitting being ~ 0.7 eV.^{123,124}

1.7.2 Bimolecular Recombination

In contrast to geminate recombination, bimolecular recombination takes place between free charges that did not originate from the same CT state. For optimised systems which exhibit high quantum efficiencies, geminate recombination is considered to be negligible, as such bimolecular recombination is thought to be the predominant loss mechanism in the most efficient OSC devices.^{125,126}

Chapter 1

Bimolecular recombination can be formulated in terms of Langevin theory. In Langevin type recombination, the rate of recombination is dictated by the time taken for free electrons and holes to diffuse to within the coulomb capture radius (r_c) of one another. As such, Langevin recombination will depend upon the concentration of electrons and holes (n and p respectively) and their relative mobility. Bimolecular recombination can be expressed in terms of this Langevin formalism, as shown in equation 1.8.

$$R = k(np - n_i p_i) \approx kn^2 \quad \text{Eqn. 1.8}$$

$$k = \frac{e\mu}{\epsilon_0 \epsilon_r} \quad \text{Eqn. 1.9}$$

Where R is the recombination rate and n_i and p_i are the intrinsic charge carrier concentrations for electrons and holes respectively. In OSCs, both n_i and p_i are expected to be negligible relative to n and p and so equation 1.8 can be simplified. In addition, it can be assumed that the concentration of holes is equal to the concentration of electrons (i.e. $n = p$). k is the recombination rate constant, which exhibits a dependence on the charge mobility, as shown in equation 1.9.

Curiously, Langevin theory is often found to overestimate the recombination rate by up to several orders of magnitude.^{127,128,129,130} This empirical observation has led to the inclusion of an additional parameter, ζ ,¹³¹ as shown in equation 1.10.

$$k_{bi} = \zeta \frac{e\mu}{\epsilon_0 \epsilon_r} \quad \text{Eqn. 1.10}$$

The term, ζ , is commonly referred to as the Langevin reduction factor, with polymer:fullerene systems displaying values in the range of 0.01-1.¹³¹ The origin of this reduction in the bimolecular rate coefficient is currently not yet fully understood, but initial studies have indicated that it may be a consequence of film morphology.¹³² For example, annealed P3HT:PC₆₀BM blends are found to exhibit bimolecular recombination coefficients that are 3-4 orders of magnitude lower than what the Langevin model would predict.^{127,133} In contrast, both non-annealed and regiorandom P3HT:PC₆₀BM blends are found to show normal Langevin-type behaviour.^{134,127} This disparity in bimolecular recombination behaviour has been ascribed to the differences in morphology, with annealed P3HT:PCBM exhibiting greater phase segregation and crystallinity than its non-annealed counterpart.¹³⁵ It should be noted however, that some literature suggests that the origin of non-Langevin recombination may be more complex than a simple morphological argument, or that structural features integral to suppressing recombination are beyond the resolution of current instrumentation.¹²⁸

Chapter 1

An important factor that needs to be taken into account when discussing bimolecular recombination is that it takes place at the donor/acceptor interface. This infers that bimolecular recombination, like that of geminate recombination must take place via a CT state. Indeed, this has been shown via electroluminescence measurements, where injected charges are observed to undergo radiative recombination from the CT state.^{136,137} In bimolecular recombination, free electron and hole capture events may lead to the formation of CT states with either singlet or triplet spin character (^1CT or ^3CT) and is schematically shown in figure 10 (v).¹²¹ When ^1CT states are formed from recombination at the interface they may relax radiatively or non-radiatively back to the ground state. ^3CT states on the other hand are spin forbidden from undergoing relaxation to the singlet ground state, however, recombination to the donor or acceptor triplet exciton is spin allowed.⁴⁹ The T_1 state of the donor material is often found to be lower in energy than the ^3CT state,¹²³ which results in relaxation to bound triplet excitons being energetically favourable. This triplet recombination channel is thought to be a main loss pathway, accounting in some cases for up to 90% of observed recombination.¹³⁸ As such, suppressing this triplet recombination channel should enhance OSC efficiency.

The idea has also been posed that if recombination occurs via a CT state, it must also be subject to the same mechanisms that prevent geminate recombination and allow for efficient charge separation.¹³¹ It been observed that CT states formed from bimolecular recombination, can in some instances re-dissociate to form free charges again.¹³⁹ Rao et al demonstrated that for PIDT-PhanQ:PC₆₀BM (1:3) blends, bimolecular recombination to the triplet exciton channel could effectively be turned off, thereby potentially increasing device performance.¹⁴⁰ It was observed via transient absorption spectroscopy that CT states formed upon recombination could re-dissociate to free charges at room temperature, thus outcompeting relaxation to the neutral triplet exciton.¹⁴⁰ In stark contrast, blends containing ICMA and ICBA resulted in CT mediated triplet exciton formation. It was rationalised that the difference in recombination behaviour was unlikely to arise from energetics, owing to the small energy difference of 50 meV between the CT states of PC₆₀BM and ICMA.

It was suggested that the CT states observed in the PC₆₀BM blend were 'weakly' bound as a consequence of being delocalised into aggregated, well-ordered fullerene domains, which has the effect of increasing the electron-hole separation and reducing the CT binding energy.¹⁴¹ These aggregated domains were shown to be much smaller in the higher fullerene adduct blends, indicating a more localised wavefunction and thus accounting for a more strongly bound CT state. Complimentary evidence for this

comes from Nuzzo et al, who found that adding 1, 8- diodooctane (DIO) to PCPDTBT:PCBM induced the formation of fullerene aggregates, with an accompanying suppression of recombination to triplet excitons.¹⁴² The idea of delocalised CT states contributing to bimolecular recombination suppression, is in essence the same argument that has been invoked for suppressing geminate recombination,^{99,109} and may help to explain the presence of non-Langevin behaviour.^{131,143}

1.8 Spin States in Organic Semiconductors

Electron spin plays an integral role in the photophysics of organic solar cells and as such will be briefly discussed. In quantum mechanics, spin is the result of the electron's angular momentum, which is a fundamental property alongside that of its mass and charge. A classical model for angular momentum is often invoked, whereby a rotating sphere is used to describe electron spin. It should be noted however, that spin is fundamentally a quantum mechanical phenomenon with no corresponding classical analogue.

One of the features of quantum mechanics is that angular momentum is quantised, allowing only certain spatial orientations. The total spin angular momentum, S , is the sum of the spin quantum numbers, with each frontier electron possessing a spin of $1/2$. The multiplicity, M , of a given state of spin angular momentum is the number of quantum mechanically allowed orientations of spin of magnitude S in a magnetic field. M may be determined from S using equation 1.11.

$$M = 2S + 1 \qquad \text{Eqn. 1.11}$$

Each possible orientation is given a spin orientation quantum number, M_s . When discussing organic photochemistry multiplicities for single electrons and two coupled electrons are of most interest to us. For a single electron (such as a spin unpaired radical) the spin quantum number is $1/2$ and consequently the total number of allowed spin orientations in space are $M = (2(1/2)+1) = 2$. As there are two allowed orientations in a magnetic field (corresponding to $M_s = +1/2$ and $M_s = -1/2$), the $S = 1/2$ state is referred to as that of a "doublet".

Most of the time in organic photochemistry however, we are dealing with coupled electron spins that occupy two separate orbitals (such as after excitation). In the case where the spin vectors are antiparallel ($\uparrow\downarrow$), there is a cancellation of the net spin angular momentum of each of the spin vectors, resulting in zero angular momentum. The multiplicity of this state is therefore $M = (2(0)+1) = 1$ and so the $S = 0$ state is termed a "singlet". In the case where the spin vectors are parallel ($\uparrow\uparrow$) and not

colinear, the vectors will add vectorially to result in a total spin angular momentum of $S = 1$, with a corresponding multiplicity of $M = (2(1)+1) = 3$. There will therefore be three possible spin orientations allowed in a magnetic field (corresponding to $M_s = +1$, $M_s = 0$ and $M_s = -1$), with the $S = 1$ state being referred to as a 'triplet'.

For organic molecules the ground state is typically found to be that of a singlet. This is because most organic molecules in their ground state possess two electrons in each orbital, and the Pauli exclusion principle states that two electrons in the same orbital must have opposite spin integer. In the case where an organic molecule is excited, an electron will be promoted to a higher energy LUMO orbital, whereas another will reside in the initial HOMO. As these electrons now reside in different orbitals, they are no longer subject to the demands of the Pauli exclusion principle, and consequently may possess different spins. Excited states can therefore be either singlet or triplet spin states.

1.8.1 Singlet-Triplet Energy Gap – Role of the exchange energy

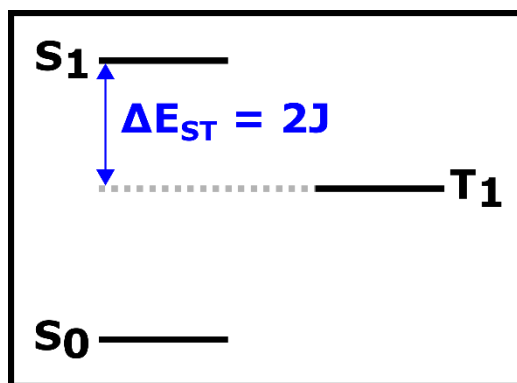


Figure 1.11 Energy diagram showing the difference in energy of S_1 and T_1 is given by ΔE_{ST} which is equal to $2J$.

In OSCs, the energy difference between the first singlet and triplet states (also known as the singlet-triplet energy splitting), ΔE_{ST} , is an important physical property that must be considered and is of relevance to all results chapters discussed in this thesis. Certain photophysical processes, such as triplet-triplet annihilation, thermally activated delayed fluorescence and singlet fission depend upon the magnitude of this E_{ST} splitting.^{144,145,146} In direct reference to organic solar cell blends, if the donor material possesses a T_1 energy level lower than that of the CT state, it can act as a recombination pathway for the electron-hole pair forming the CT state (see section 1.7.2 for more details), thereby preventing charge dissociation and limiting the efficiency of the device.¹⁴⁷ The singlet and triplet state energies, E_{S1} and E_{T1} , are determined from equations 1.12 and 1.13, respectively:

Chapter 1

$$E_{S_1} = E_{\text{GAP}} + K + J \quad \text{Eqn. 1.12}$$

$$E_{T_1} = E_{\text{GAP}} + K - J \quad \text{Eqn. 1.13}$$

Where E_{GAP} is the energy difference between the HOMO and the LUMO, K is the coulomb interaction integral, which is a first order correction for classical electron-electron correlation and J is the electron exchange energy, the first-order quantum mechanical correction needed to account for the electron-electron repulsion felt as a consequence of the Pauli exclusion principle. Both corrections involve negative-negative electron charge interactions that lead to repulsion, and as such both K and J are mathematically defined as positive values. The coulomb interaction integral is found to raise the energy of both the singlet and triplet states, whereas the electron exchange energy only raises the energy of the singlet state, whilst reducing the energy of the triplet state. For a given configuration (e.g. $n\text{-}\pi^*$), this has the consequence of the first singlet excited state, S_1 , nearly always being higher in energy than that of the first triplet excited state T_1 (i.e. $E_s > E_T$). The singlet-triplet energy splitting can therefore be determined by the energy difference between E_s and E_T , as shown in equation 1.14.

$$\Delta E_{\text{ST}} = E_{S_1} - E_{T_1} = [E_{\text{GAP}} + K + J] - [E_{\text{GAP}} + K - J] \quad \text{Eqn. 1.14}$$

$$\Delta E_{\text{ST}} = 2J > 0 \quad \text{Eqn. 1.15}$$

From equation 1.15, we can see that the ΔE_{ST} is found to depend on only the exchange energy, which is shown schematically in figure 1.11. The exchange energy (and therefore the ΔE_{ST}) is found to exponentially scale with the overlap between the ground state and excited state wavefunction orbitals, as shown in equation 1.16.

$$J = J_0 e^{-r} \quad \text{Eqn. 1.16}$$

Where J_0 is the coupling matrix and r is the separation between the two orbitals. Equation 1.16 states that J will decrease exponentially as the separation between the orbitals increases. In organic materials the electron wave function is found to be localised, which gives rise to large exchange energies with concomitant large ΔE_{ST} . For small molecules the exchange energy is found to be dependent upon the size of the molecule, whereas in conjugated polymers the exchange energy is determined by the oligomeric chain length. This is because the additional delocalisation into the π -backbone permits greater separation between the electron and hole involved in the exciton, thereby reducing the exchange energy. It is been found however, that there is a limit to the reduction of the exchange energy achieved in conjugated polymers, where for polymeric lengths greater than 25 Å the ΔE_{ST} is systematically found to be

around 0.7 eV.¹²³ This limit has been overcome in some cases through careful molecular design, where the donor and acceptor units in the polymer have been spatially separated via orthogonal placement on the polymer backbone. This leads to an accompanying spatial separation of the HOMO and LUMO molecular orbitals with a reduction in the exchange energy, leading to $\Delta E_{ST} < 0.1$ eV (this will be discussed further in chapter 5).⁷¹ The exchange energy also offers some insight into the binding energy of excitons. A large exchange energy suggests a small spatial separation between the HOMO and LUMO orbitals, which implies that the electron and hole comprising the exciton, will be situated close to one another, with an associated large binding energy. Conversely, a small exchange energy is indicative of strongly separated HOMO and LUMO orbitals, with the consequence of the electron and hole being found further apart from one another and concomitantly exhibiting a lower binding energy.

1.8.2 Intersystem Crossing, Spin-orbit Coupling and the Heavy Atom Effect

Intersystem crossing (ISC) plays a key role in the operation of organic solar cell materials as it often dictates the population of triplet species generated. ISC is a non-radiative, adiabatic process that allows transitions between states of different multiplicity. It should be noted that typically ISC is used to refer to crossing from the singlet to the triplet manifold, whereas reverse intersystem crossing (rISC) implies the reverse process.^{148,149} These transitions are governed by the spin-selection rule, which states that during an electronic transition the total angular momentum must be conserved and if a spin-change does occur it must be compensated by a change in orbital angular momentum.

This has the effect of ISC between the singlet and triplet states being formally spin forbidden, as there is no change in orbital angular momentum (e.g. $^1(\pi-\pi^*) \rightarrow ^3(\pi-\pi^*)$ $\Delta S = 0$). However, in some cases where a singlet to triplet transition involves a change in orbital angular momentum (e.g. $^1(\pi-\pi^*) \rightarrow ^3(n-\pi^*)$ $\Delta S = 1$) the rate of ISC may be relatively large (known as El-Sayed's rule).

One method for inducing transitions between spin states is through spin-orbit coupling (SOC), which is the coupling of the orbital angular momentum and electron spin. The strength (or alternatively energy) of SOC is directly proportional to the magnitude of the magnetic moment, which is derived from the electron orbital motion and as such is variable (unlike spin which is fixed). The magnetic field generated by the movement of a negatively charged electron (or any charged particle) is proportional to its velocity,

Chapter 1

which in turn is dependent upon the electrons distance from the nucleus. As an electron approaches the nucleus it experiences an accelerating force from the electrostatic attraction felt between the negative electron and positive nuclei. This has the effect of the magnetic moment being greatest when an electron in an orbital is found near the nucleus of charge Z . The magnetic moment will also be found to be greater with increasing charge on the nucleus, with the strength of SOC in atoms being proportional to Z^4 . It should be noted however, that as organic molecules are comprised of atoms of varying atomic weight, spin-orbit-coupling will therefore be a local effect. SOC will be most effective when an excited electron is found to reside near that of a heavy atom. This Z^4 dependence is known as the "heavy atom effect" and provides an explanation for the increased rates of ISC observed in molecules possessing heavy atoms. An example of the potential for the heavy atom effect is shown in figure 1.12, which approximates the π, π^* excited state in bromobenzene. A single electron in a half-filled orbital is now found to reside on the bromine atom, affording it the possibility to undergo SOC from the large Z .

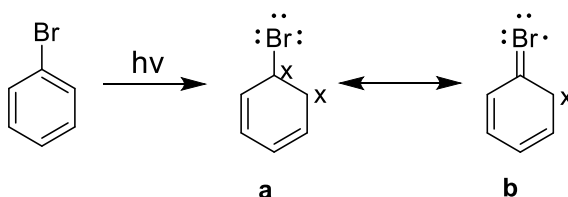


Figure 1.12 Structure of an approximate bromobenzene π - π^* generated after excitation. X denotes a π or π^* electron.

Irrespective of the strength of the SOC, for a transition between singlet and triplet states to be possible there must be a means of conserving the total angular momentum of the system. One way of conserving total angular momentum is through a transition from a p orbital of angular momentum 1 to that of angular momentum 0, corresponding to a $p_x \rightarrow p_y$ transition. This is the basis for "El-Sayed's rule" which states that the rate of intersystem crossing between singlet and triplet states is fast, provided there is a change in orbital angular momentum.¹⁵⁰ For example, the rate of ISC for a $^1(\pi-\pi^*) \rightarrow ^3(n-\pi^*)$ transition is much greater than that of a $^1(\pi-\pi^*) \rightarrow ^3(\pi-\pi^*)$ transition.

1.9 Aims of this Thesis

While many studies propose recombination to the neutral triplet exciton as one of the main loss pathways in OSCs, relatively little attention has been given to exploring methods to mitigate this. This thesis aims to rectify this issue by spectroscopically investigating several novel systems, which were designed to alter or introduce new triplet energy levels to harvest these triplet states.

Chapter 3 focuses upon the spectroscopic investigation of a novel small-molecule DPP/fullerene blend. This was for the purpose of providing a spectroscopic baseline for studies into more complex DPP-based systems. This is because small molecule DPP has been suggested to possess low triplet energy levels and as such provides a model system for studying charge generation/recombination in the presence of these deep triplet energy levels. Furthermore, this chapter provides an introduction into how these systems may be studied via transient absorption spectroscopy, the main spectroscopic technique used through this thesis.

Chapter 4 investigates the feasibility of whether covalently incorporating a sensitizer into a polymer backbone can result in a self-upconverting donor polymer. This concept was explored via spectroscopically examining a novel system, comprised of a zinc porphyrin derivative incorporated into the backbone of the well-known polymer F8BT to yield the system F8BT-HAPAPP. In this scheme, the porphyrin was intended to act as an intramolecular triplet sensitizer for the F8BT, which would then subsequently undergo upconversion to yield the F8BT singlet excited state. In the scheme of OSCs, these upconverted singlet states may then undergo electron transfer and carrier formation.

Chapter 5 aims at exploring the dynamics of a low-band gap polymer possessing a donor-orthogonal acceptor (D-oA) architecture. In this novel polymeric system Thiro, an electron rich CPDT donor backbone is used in conjunction with electron deficient dicyano substituted spirobifluorene acceptor units, which are located orthogonal along the polymer backbone. This D-oA architecture results in physical separation of the donor and acceptor orbitals, which should in turn reduce the singlet-triplet energy splitting, ΔE_{ST} . Reducing ΔE_{ST} in such systems can result in the possibility of triplet recycling back to the singlet state via reverse intersystem crossing (rISC). In the scheme of OSCs, these regenerated singlet states may then have an additional chance to undergo electron transfer and carrier formation.

1.10 Bibliography

- 1 V, Masson-Delmotte, P. Zhai, H.-O. Pörtner, D. Roberts, J. Skea, P.R. Shukla, A. Pirani, W. Moufouma-Okia, C. Péan, R. Pidcock, S. Connors, J.B.R. Matthews, Y. Chen, X. Zhou, M.I. Gomis, E. Lonnoy, T. Maycock, M. Tignor, and T. Waterfield, *Global Warming of 1.5°C. An IPCC Special Report on the impacts of global warming of 1.5°C above pre-industrial levels and related global greenhouse gas emission pathways, in the context of strengthening the global response to the threat of climate change, sustainable development, and efforts to eradicate poverty*, IPCC, 2018, <https://www.ipcc.ch/sr15/>, (accessed 28 November 2019).
- 2 UK renewable energy roadmap, <https://www.gov.uk/government/collections/uk-renewable-energy-roadmap>, (accessed December 2019).
- 3 V. Balzani, A. Credi and M. Venturi, *ChemSusChem*, 2008, **1**, 26–58.
- 4 E. Bequerel, *Comptes Rendus*, 1839, **9**, 561–567.
- 5 N. Armaroli and V. Balzani, *Energy for a Sustainable World*, Wiley-VCH Verlag GmbH & Co. KGaA, Weinheim, Germany, 2010.
- 6 D. M. Chapin, C. S. Fuller and G. L. Pearson, *J. Appl. Phys.*, 1954, **25**, 676–677.
- 7 M. A. Green, Y. Hishikawa, W. Warta, E. D. Dunlop, D. H. Levi, J. Hohl-Ebinger and A. W. H. Ho-Baillie, *Prog. Photovoltaics Res. Appl.*, 2017, **25**, 668–676.
- 8 Y. Abdelilah, U. Collier, K. Daszkiewicz, P. Feuvre, H. Kamitara and T. Rinke, *Renewables 2018*, IEA, 2018, <https://www.iea.org/reports/renewables-2018>, (accessed December 2019).
- 9 D. Gielen, F. Boshell, R. Gorini, J. Kiruja, P. Komor, T. Masuyama and B. Parthan, *Renewable Power Generation Costs in 2019*, IRENA, 2020, <https://www.irena.org/publications/2020/Jun/Renewable-Power-Costs-in-2019>, (accessed 2021).
- 10 IEA, *World Energy Outlook 2020*, IEA, 2020, <https://www.iea.org/reports/world-energy-outlook-2020>, (accessed 2021).
- 11 A. E. Brooks, *Future Energy*, Elsevier, 2nd edn., 2014, pp. 383–404.
- 12 C. Zhang, Q. Luo, H. Wu, H. Li, J. Lai, G. Ji, L. Yan, X. Wang, D. Zhang, J. Lin,

Chapter 1

- L. Chen, J. Yang and C. Ma, *Org. Electron.*, 2017, **45**, 190–197.
- 13 G. Li, R. Zhu and Y. Yang, *Nat. Photonics*, 2012, **6**, 153–161.
- 14 K. Fukuda, K. Yu and T. Someya, *Adv. Energy Mater.*, 2020, **10**, 2000765.
- 15 Y. Li, X. Guo, Z. Peng, B. Qu, H. Yan, H. Ade, M. Zhang and S. R. Forrest, *Proc. Natl. Acad. Sci.*, 2020, **117**, 21147–21154.
- 16 Ultra-Thin, Organic and Flexible Solar Energy Solution | Heliatek, <https://www.heliatek.com/product/>, (accessed 12 February 2020).
- 17 S. Rafique, S. M. Abdullah, K. Sulaiman and M. Iwamoto, *Renew. Sustain. Energy Rev.*, 2018, **84**, 43–53.
- 18 S. B. Sapkota, A. Spies, B. Zimmermann, I. Dürr and U. Würfel, *Sol. Energy Mater. Sol. Cells*, 2014, **130**, 144–150.
- 19 Q. Burlingame, X. Huang, X. Liu, C. Jeong, C. Coburn and S. R. Forrest, *Nature*, 2019, **573**, 394–397.
- 20 Q. Burlingame, X. Huang, X. Liu, C. Jeong, C. Coburn and S. R. Forrest, *Nature*, 2019, **573**, 394–397.
- 21 J. Nelson, *The Physics of Solar Cells*, Imperial College Press, London, UK, 2003
- 22 H. Ohkita, S. Cook, Y. Astuti, W. Duffy, S. Tierney, W. Zhang, M. Heeney, I. McCulloch, J. Nelson, D. D. C. Bradley and J. R. Durrant, *J. Am. Chem. Soc.*, 2008, **130**, 3030–3042.
- 23 T. M. Clarke and J. R. Durrant, *Chem. Rev.*, 2010, **110**, 6736–6767.
- 24 K. Nakano, Y. Chen, B. Xiao, W. Han, J. Huang, H. Yoshida, E. Zhou and K. Tajima, *Nat. Commun.*, 2019, **10**, 2520.
- 25 C. K. Chiang, C. R. Fincher, Y. W. Park, A. J. Heeger, H. Shirakawa, E. J. Louis, S. C. Gau and A. G. MacDiarmid, *Phys. Rev. Lett.*, 1977, **39**, 1098–1101.
- 26 C. W. Tang, *Appl. Phys. Lett.*, 1986, **48**, 183–185.
- 27 G. Yu, J. Gao, J. C. Hummelen, F. Wudl and A. J. Heeger, *Science*, 1995, **270**, 1789.
- 28 J. J. M. Halls, C. A. Walsh, N. C. Greenham, E. A. Marseglia, R. H. Friend, S. C. Moratti and A. B. Holmes, *Nature*, 1995, **376**, 498–500.

Chapter 1

- 29 Q. Liu, Y. Jiang, K. Jin, J. Qin, J. Xu, W. Li, J. Xiong, J. Liu, Z. Xiao, K. Sun, S. Yang, X. Zhang and L. Ding, *Sci. Bull.*, 2020, **65**, 272–275.
- 30 L. Meng, Y. Zhang, X. Wan, C. Li, X. Zhang, Y. Wang, X. Ke, Z. Xiao, L. Ding, R. Xia, H.-L. Yip, Y. Cao and Y. Chen, *Science*, 2018, **361**, 1094–1098.
- 31 M. A. Green, Y. Hishikawa, E. D. Dunlop, D. H. Levi, J. Hohl-Ebinger, M. Yoshita and A. W. Y. Ho-Baillie, *Prog. Photovoltaics Res. Appl.*, 2019, **27**, 3–12.
- 32 W. Shockley and H. J. Queisser, *J. Appl. Phys.*, 1961, **32**, 510–519.
- 33 S. Rühle, *Sol. Energy*, 2016, **130**, 139–147.
- 34 J. Luceño-Sánchez, A. Díez-Pascual and R. Peña Capilla, *Int. J. Mol. Sci.*, 2019, **20**, 976.
- 35 O. V Mikhnenko, P. W. M. Blom and T.-Q. Nguyen, *Energy Environ. Sci.*, 2015, **8**, 1867.
- 36 F. Laquai, Y.-S. Park, J.-J. Kim and T. Basché, *Macromol. Rapid Commun.*, 2009, **30**, 1203–1231.
- 37 F. Delijani and A. Fard, in *Lecture Notes in Electrical Engineering*, Springer Verlag, 2019, vol. 480, pp. 473–482.
- 38 S. Shoaee, PhD thesis, Imperial College London, 2010.
- 39 Y. Terao, H. Sasabe and C. Adachi, *Appl. Phys. Lett.*, 2007, **90**, 103515.
- 40 Y. Tamai, H. Ohkita, H. Benten and S. Ito, *J. Phys. Chem. Lett.*, 2015, **6**, 3417–3428.
- 41 J. Piriš, T. E. Dykstra, A. A. Bakulin, P. H. M. van Loosdrecht, W. Knulst, M. T. Trinh, J. M. Schins and L. D. A. Siebbeles, *J. Phys. Chem. C*, 2009, **113**, 14500–14506.
- 42 S. Dimitrov, B. Schroeder, C. Nielsen, H. Bronstein, Z. Fei, I. McCulloch, M. Heeney and J. Durrant, *Polymers*, 2016, **8**, 14.
- 43 K. Masuda, Y. Ikeda, M. Ogawa, H. Benten, H. Ohkita and S. Ito, *ACS Appl. Mater. Interfaces*, 2010, **2**, 236–245.
- 44 P. E. Shaw, A. Ruseckas and I. D. W. Samuel, *Adv. Mater.*, 2008, **20**, 3516–3520.
- 45 M. Streiter, D. Beer, F. Meier, C. Göhler, C. Lienert, F. Lombeck, M. Sommer

Chapter 1

- and C. Deibel, *Adv. Funct. Mater.*, 2019, **29**, 1903936.
- 46 G. Lakhwani, A. Rao and R. H. Friend, *Annu. Rev. Phys. Chem.*, 2014, **65**, 557–581.
- 47 G. D. Scholes, *Annu. Rev. Phys. Chem.*, 2003, **54**, 57–87.
- 48 Y. Kawamura, J. Brooks, J. J. Brown, H. Sasabe and C. Adachi, *Phys. Rev. Lett.*, 2006, **96**, 017404.
- 49 A. Köhler and H. Bässler, *Mater. Sci. Eng. R Reports*, 2009, **66**, 71–109.
- 50 H. Marciniak, X.-Q. Li, F. Würthner and S. Lochbrunner, *J. Phys. Chem. A*, 2011, **115**, 648–654.
- 51 S. M. Menke, W. A. Luhman and R. J. Holmes, *Nat. Mater.*, 2013, **12**, 152–157.
- 52 T. K. Mullenbach, K. A. McGarry, W. A. Luhman, C. J. Douglas and R. J. Holmes, *Adv. Mater.*, 2013, **25**, 3689–3693.
- 53 O. V. Mikhnenko, F. Cordella, A. B. Sieval, J. C. Hummelen, P. W. M. Blom and M. A. Loi, *J. Phys. Chem. B*, 2008, **112**, 11601–11604.
- 54 N. Banerji, S. Cowan, M. Leclerc, E. Vauthey and A. J. Heeger, *J. Am. Chem. Soc.*, 2010, **132**, 17459–17470.
- 55 Y. Tamai, Y. Matsuura, H. Ohkita, H. Benten and S. Ito, *J. Phys. Chem. Lett.*, 2014, **5**, 399–403.
- 56 S. Athanasopoulos, E. Hennebicq, D. Beljonne and A. B. Walker, *J. Phys. Chem. C*, 2008, **112**, 11532–11538.
- 57 D. L. Dexter, *J. Chem. Phys.*, 1953, **21**, 836–850.
- 58 C. Mongin, S. Garakyaraghi, N. Razgoniaeva, M. Zamkov and F. N. Castellano, *Science*, 2016, **351**, 369–372.
- 59 L. Sudha Devi, M. K. Al-Suti, C. Dosche, M. S. Khan, R. H. Friend and A. Köhler, *Phys. Rev. B*, 2008, **78**, 045210.
- 60 B. P. Rand, S. Schols, D. Cheyng, H. Gommans, C. Girotto, J. Genoe, P. Heremans and J. Poortmans, *Org. Electron.*, 2009, **10**, 1015–1019.
- 61 R. R. Lunt, N. C. Giebink, A. A. Belak, J. B. Benziger and S. R. Forrest, *J. Appl. Phys.*, 2009, **105**, 053711.

Chapter 1

- 62 R. Andernach, H. Utzat, S. D. Dimitrov, I. McCulloch, M. Heeney, J. R. Durrant and H. Bronstein, *J. Am. Chem. Soc.*, 2015, **137**, 10383–10390.
- 63 H.-Y. Hsu, J. H. Vella, J. D. Myers, J. Xue and K. S. Schanze, *J. Phys. Chem. C*, 2014, **118**, 24282–24289.
- 64 P. Avakian and R. E. Merrifield, *Phys. Rev. Lett.*, 1964, **13**, 541–543.
- 65 S. Arnold, J. L. Fave and M. Schott, *Chem. Phys. Lett.*, 1974, **28**, 412–417.
- 66 P. Irkhin and I. Biaggio, *Phys. Rev. Lett.*, 2011, **107**, 017402.
- 67 H. Najafov, B. Lee, Q. Zhou, L. C. Feldman and V. Podzorov, *Nat. Mater.*, 2010, **9**, 938–943.
- 68 M. Samiullah, D. Moghe, U. Scherf and S. Guha, *Phys. Rev. B - Condens. Matter Mater. Phys.*, 2010, **82**, 205211.
- 69 B. H. Wallikewitz, D. Kabra, S. Gélinas and R. H. Friend, *Phys. Rev. B - Condens. Matter Mater. Phys.*, 2012, **85**, 045209.
- 70 A. Rao and R. H. Friend, *Nat. Rev. Mater.*, 2017, **2**, 17063.
- 71 D. M. E. Freeman, A. J. Musser, J. M. Frost, H. L. Stern, A. K. Forster, K. J. Fallon, A. G. Rapisarda, F. Cacialli, I. McCulloch, T. M. Clarke, R. H. Friend and H. Bronstein, *J. Am. Chem. Soc.*, 2017, **139**, 11073–11080.
- 72 Y. H. L. Lin, M. Koch, A. N. Brigeman, D. M. E. Freeman, L. Zhao, H. Bronstein, N. C. Giebink, G. D. Scholes and B. P. Rand, *Energy Environ. Sci.*, 2017, **10**, 1465–1475.
- 73 M. B. Smith and J. Michl, *Chem. Rev.*, 2010, **110**, 6891–6936.
- 74 D. N. Congreve, J. Lee, N. J. Thompson, E. Hontz, S. R. Yost, P. D. Reusswig, M. E. Bahlke, S. Reineke, T. Van Voorhis and M. A. Baldo, *Science*, 2013, **340**, 334–337.
- 75 M. Tabachnyk, B. Ehrler, S. Bayliss, R. H. Friend and N. C. Greenham, *Appl. Phys. Lett.*, 2013, **103**, 153302.
- 76 E. Busby, J. Xia, Q. Wu, J. Z. Low, R. Song, J. R. Miller, X.-Y. Zhu, L. M. Campos and M. Y. Sfeir, *Nat. Mater.*, 2015, **14**, 426–433.
- 77 H. L. Stern, A. J. Musser, S. Gelinas, P. Parkinson, L. M. Herz, M. J. Bruzek, J. Anthony, R. H. Friend and B. J. Walker, *Proc. Natl. Acad. Sci. U.S.A.*, 2015, **112** 7656-7661.

Chapter 1

- 78 A. J. Musser, M. Maiuri, D. Brida, G. Cerullo, R. H. Friend and J. Clark, *J. Am. Chem. Soc.*, 2015, **137**, 5130–5139.
- 79 C. K. Yong, A. J. Musser, S. L. Bayliss, S. Lukman, H. Tamura, O. Bubnova, R. K. Hallani, A. Meneau, R. Resel, M. Maruyama, S. Hotta, L. M. Herz, D. Beljonne, J. E. Anthony, J. Clark and H. Sirringhaus, *Nat. Commun.*, 2017, **8**, 15953.
- 80 A. J. Musser and J. Clark, *Annu. Rev. Phys. Chem.*, 2019, **70**, 323–351.
- 81 G. D. Scholes, *J. Phys. Chem. A*, 2015, **119**, 12699–12705.
- 82 R. D. Pensack, E. E. Ostroumov, A. J. Tilley, S. Mazza, C. Grieco, K. J. Thorley, J. B. Asbury, D. S. Seferos, J. E. Anthony and G. D. Scholes, *J. Phys. Chem. Lett.*, 2016, **7**, 2370–2375.
- 83 R. A. Marcus, *J. Chem. Phys.*, 1956, **24**, 966–978.
- 84 J. R. Miller, L. T. Calcaterra and G. L. Closs, *J. Am. Chem. Soc.*, 1984, **106**, 3047–3049.
- 85 I. R. Gould, D. Ege, S. L. Mattes and S. Farid, *J. Am. Chem. Soc.*, 1987, **109**, 3794–3796.
- 86 S. S. Jayanthi and P. Ramamurthy, *J. Phys. Chem. A*, 1997, **101**, 2016–2022.
- 87 P. Sun, F. Li, Y. Chen, M. Zhang, Z. Zhang, Z. Gao and Y. Shao, *J. Am. Chem. Soc.*, 2003, **125**, 9600–9601.
- 88 D. C. Coffey, B. W. Larson, A. W. Hains, J. B. Whitaker, N. Kopidakis, O. V. Boltalina, S. H. Strauss and G. Rumbles, *J. Phys. Chem. C*, 2012, **116**, 8916–8923.
- 89 H. Ohkita, S. Cook, Y. Astuti, W. Duffy, S. Tierney, W. Zhang, M. Heeney, I. McCulloch, J. Nelson, D. D. C. Bradley and J. R. Durrant, *J. Am. Chem. Soc.*, 2008, **130**, 3030–42.
- 90 S. Shoaee, T. M. Clarke, C. Huang, S. Barlow, S. R. Marder, M. Heeney, I. McCulloch and J. R. Durrant, *J. Am. Chem. Soc.*, 2010, **132**, 12919–12926.
- 91 S. Cook, R. Katoh and A. Furube, *J. Phys. Chem. C*, 2009, **113**, 2547–2552.
- 92 J. Guo, H. Ohkita, H. Benten and S. Ito, *J. Am. Chem. Soc.*, 2009, **131**, 16869–16880.
- 93 K. Vandewal, K. Tvingstedt, A. Gadisa, O. Inganäs and J. V. Manca, *Nat.*

Chapter 1

- Mater.*, 2009, **8**, 904–909.
- 94 S. Athanasopoulos, F. Schauer, V. Nádaždy, M. Weiß, F. Kahle, U. Scherf, H. Bässler and A. Köhler, *Adv. Energy Mater.*, 2019, **9**, 1900814.
- 95 S. Albrecht, K. Vandewal, J. R. Tumbleston, F. S. U. Fischer, J. D. Douglas, J. M. J. Fréchet, S. Ludwigs, H. Ade, A. Salleo and D. Neher, *Adv. Mater.*, 2014, **26**, 2533–2539.
- 96 S. H. Park, A. Roy, S. Beaupré, S. Cho, N. Coates, J. S. Moon, D. Moses, M. Leclerc, K. Lee and A. J. Heeger, *Nat. Photonics*, 2009, **3**, 297–302.
- 97 Y. Liang, Z. Xu, J. Xia, S.-T. Tsai, Y. Wu, G. Li, C. Ray and L. Yu, *Adv. Mater.*, 2010, **22**, E135-8.
- 98 A. J. Barker, K. Chen and J. M. Hodgkiss, *J. Am. Chem. Soc.*, 2014, **136**, 12018–12026.
- 99 S. Gelinas, A. Rao, A. Kumar, S. L. Smith, A. W. Chin, J. Clark, T. S. van der Poll, G. C. Bazan and R. H. Friend, *Science*, 2014, **343**, 512–516.
- 100 M. Gerhard, A. P. Arndt, I. A. Howard, A. Rahimi-Iman, U. Lemmer and M. Koch, *J. Phys. Chem. C*, 2015, **119**, 28309–28318.
- 101 J. Kurpiers, T. Ferron, S. Roland, M. Jakoby, T. Thiede, F. Jaiser, S. Albrecht, S. Janietz, B. A. Collins, I. A. Howard and D. Neher, *Nat. Commun.*, 2018, **9**, 2038.
- 102 F. Gao, W. Tress, J. Wang and O. Inganäs, *Phys. Rev. Lett.*, 2015, **114**, 128701.
- 103 K. Vandewal, A. Gadisa, W. D. Oosterbaan, S. Bertho, F. Banishoeib, I. Van Severen, L. Lutsen, T. J. Cleij, D. Vanderzande and J. V. Manca, *Adv. Funct. Mater.*, 2008, **18**, 2064–2070.
- 104 T. Drori, C. X. Sheng, A. Ndobe, S. Singh, J. Holt and Z. V. Vardeny, *Phys. Rev. Lett.*, 2008, **101**, 037401.
- 105 P. Parkinson, J. Lloyd-Hughes, M. B. Johnston and L. M. Herz, *Phys. Rev. B*, 2008, **78**, 115321.
- 106 X.-K. Chen, V. Coropceanu and J.-L. Brédas, *Nat. Commun.*, 2018, **9**, 5295.
- 107 G. Grancini, M. Maiuri, D. Fazzi, A. Petrozza, H.-J. Egelhaaf, D. Brida, G. Cerullo and G. Lanzani, *Nat. Mater.*, 2013, **12**, 29-33

Chapter 1

- 108 A. Troisi, *Faraday Discuss.*, 2013, **163**, 377-392.
- 109 A. A. Bakulin, A. Rao, V. G. Pavelyev, P. H. M. van Loosdrecht, M. S. Pshenichnikov, D. Niedzialek, J. Cornil, D. Beljonne and R. H. Friend, *Science*, 2012, **335**, 1340–1344.
- 110 K. Vandewal, S. Albrecht, E. T. Hoke, K. R. Graham, J. Widmer, J. D. Douglas, M. Schubert, W. R. Mateker, J. T. Bloking, G. F. Burkhard, A. Sellinger, J. M. J. Fréchet, A. Amassian, M. K. Riede, M. D. McGehee, D. Neher and A. Salleo, *Nat. Mater.*, 2014, **13**, 63–68.
- 111 A. C. Jakowetz, M. L. Böhm, J. Zhang, A. Sadhanala, S. Huettnner, A. A. Bakulin, A. Rao and R. H. Friend, *J. Am. Chem. Soc.*, 2016, **138**, 11672–11679.
- 112 B. Bernardo, D. Cheyns, B. Verreert, R. D. Schaller, B. P. Rand and N. C. Giebink, *Nat. Commun.*, 2014, **5**, 3245.
- 113 B. M. Savoie, A. Rao, A. A. Bakulin, S. Gelinias, B. Movaghar, R. H. Friend, T. J. Marks and M. A. Ratner, *J. Am. Chem. Soc.*, 2014, **136**, 2876–2884.
- 114 R. A. Marsh, J. M. Hodgkiss and R. H. Friend, *Adv. Mater.*, 2010, **22**, 3672–3676.
- 115 M. Lenes, M. Morana, C. J. Brabec and P. W. M. Blom, *Adv. Funct. Mater.*, 2009, **19**, 1106–1111.
- 116 A. A. Bakulin, D. S. Martyanov, D. Y. Paraschuk, M. S. Pshenichnikov and P. H. M. Van Loosdrecht, *J. Phys. Chem. B*, 2008, **112**, 13730–13737.
- 117 S. K. Pal, T. Kesti, M. Maiti, F. Zhang, O. Inganäs, S. Hellström, M. R. Andersson, F. Oswald, F. Langa, T. Österman, T. Pascher, A. Yartsev and V. Sundström, *J. Am. Chem. Soc.*, 2010, **132**, 12440–12451.
- 118 S. Shoaee, M. P. Eng, E. Espíldora, J. L. Delgado, B. Campo, N. Martín, D. Vanderzande and J. R. Durrant, *Energy Environ. Sci.*, 2010, **3**, 971.
- 119 S. L. Bayliss, A. D. Chepelianskii, A. Sepe, B. J. Walker, B. Ehrler, M. J. Bruzek, J. E. Anthony and N. C. Greenham, *Phys. Rev. Lett.*, 2014, **112**, 238701.
- 120 K. Tvingstedt, K. Vandewal, F. Zhang and O. Inganäs, *J. Phys. Chem. C*, 2010, **114**, 21824–21832.
- 121 S. D. Dimitrov, S. Wheeler, D. Niedzialek, B. C. Schroeder, H. Utzat, J. M. Frost, J. Yao, A. Gillett, P. S. Tuladhar, I. McCulloch, J. Nelson and J. R. Durrant, *Nat. Commun.*, 2015, **6**, 6501.

Chapter 1

- 122 M. Van Landeghem, R. Lenaerts, J. Kesters, W. Maes and E. Goovaerts, *Phys. Chem. Chem. Phys.*, 2019, **21**, 22999–23008.
- 123 A. Köhler and D. Beljonne, *Adv. Funct. Mater.*, 2004, **14**, 11–18.
- 124 A. P. Monkman, H. D. Burrows, L. J. Hartwell, L. E. Horsburgh, I. Hamblett and S. Navaratnam, *Phys. Rev. Lett.*, 2001, **86**, 1358–1361.
- 125 C. G. Shuttle, B. O'Regan, A. M. Ballantyne, J. Nelson, D. D. C. Bradley and J. R. Durrant, *Phys. Rev. B*, 2008, **78**, 113201.
- 126 D. Credgington, R. Hamilton, P. Atienzar, J. Nelson and J. R. Durrant, *Adv. Funct. Mater.*, 2011, **21**, 2744–2753.
- 127 A. Pivrikas, G. Juška, A. J. Mozer, M. Scharber, K. Arlauskas, N. S. Sariciftci, H. Stubb and R. Österbacka, *Phys. Rev. Lett.*, 2005, **94**, 176806.
- 128 T. M. Clarke, D. B. Rodovsky, A. A. Herzing, J. Peet, G. Dennler, D. DeLongchamp, C. Lungenschmied and A. J. Mozer, *Adv. Energy Mater.*, 2011, **1**, 1062–1067.
- 129 L. Q. Phuong, S. M. Hosseini, C. W. Koh, H. Y. Woo and S. Shoaee, *J. Phys. Chem. C*, 2019, **123**, 27417–27422.
- 130 S. Albrecht, S. Janietz, W. Schindler, J. Frisch, J. Kurpiers, J. Kniepert, S. Inal, P. Pingel, K. Fostiropoulos, N. Koch and D. Neher, *J. Am. Chem. Soc.*, 2012, **134**, 14932–14944.
- 131 C. M. Proctor, M. Kuik and T.-Q. Nguyen, *Prog. Polym. Sci.*, 2013, **38**, 1941–1960.
- 132 S. Shoaee, A. Armin, M. Stolterfoht, S. M. Hosseini, J. Kurpiers and D. Neher, *Sol. RRL*, 2019, **3**, 1900184.
- 133 G. Juška, K. Arlauskas, J. Stuchlik and R. Österbacka, *J. Non. Cryst. Solids*, 2006, **352**, 1167–1171.
- 134 R. Hamilton, C. G. Shuttle, B. O'Regan, T. C. Hammant, J. Nelson and J. R. Durrant, *J. Phys. Chem. Lett.*, 2010, **1**, 1432–1436.
- 135 X. Yang, J. Loos, S. C. Veenstra, W. J. H. Verhees, M. M. Wienk, J. M. Kroon, M. A. J. Michels and R. A. J. Janssen, *Nano Lett.*, 2005, **5**, 579–583.
- 136 K. Tvingstedt, K. Vandewal, A. Gadisa, F. Zhang, J. Manca and O. Inganäs, *J. Am. Chem. Soc.*, 2009, **131**, 11819–11824.

Chapter 1

- 137 M. List, T. Sarkar, P. Perkhun, J. Ackermann, C. Luo and U. Würfel, *Nat. Commun.*, 2018, **9**, 3631.
- 138 S. M. Menke, A. Sadhanala, M. Nikolka, N. A. Ran, M. K. Ravva, S. Abdel-Azeim, H. L. Stern, M. Wang, H. Sirringhaus, T.-Q. Nguyen, J.-L. Brédas, G. C. Bazan and R. H. Friend, *ACS Nano*, 2016, **10**, 10736–10744.
- 139 A. Rao, P. C. Y Chow, S. Gélinas, C. W. Schlenker, C.-Z. Li, H.-L. Yip, A. K-Y Jen, D. S. Ginger and R. H. Friend, *Nature*, **500**, 435-439
- 140 A. Rao, P. C. Y. Chow, S. Gélinas, C. W. Schlenker, C.-Z. Li, H.-L. Yip, A. K.-Y. Jen, D. S. Ginger and R. H. Friend, *Nature*, 2013, **500**, 435–439.
- 141 F. C. Jamieson, E. B. Domingo, T. McCarthy-Ward, M. Heeney, N. Stingelin and J. R. Durrant, *Chem. Sci.*, 2012, **3**, 485–492.
- 142 D. Di Nuzzo, A. Aguirre, M. Shahid, V. S. Gevaerts, S. C. J. Meskers and R. A. J. Janssen, *Adv. Mater.*, 2010, **22**, 4321–4324.
- 143 A. Armin, J. R. Durrant and S. Shoaee, *J. Phys. Chem. C*, 2017, **121**, 13969–13976.
- 144 Y. C. Simon and C. Weder, *J. Mater. Chem.*, 2012, **22**, 20817-20830
- 145 F. B. Dias, T. J. Penfold and A. P. Monkman, *Methods Appl. Fluoresc.*, 2017, **5**, 012001.
- 146 M. B. Smith and J. Michl, *Chem. Rev.*, 2010, **110**, 6891–6936.
- 147 D. Veldman, S. C. J. Meskers and R. A. J. Janssen, *Adv. Funct. Mater.*, 2009, **19**, 1939–1948.
- 148 J. Gibson, A. P. Monkman and T. J. Penfold, *ChemPhysChem*, 2016, **17**, 2956–2961.
- 149 K. Goushi, K. Yoshida, K. Sato and C. Adachi, *Nat. Photonics*, 2012, **6**, 253–258.
- 150 M. A. El-Sayed, *J. Chem. Phys.*, 1963, **38**, 2834–2838.

Chapter 2

Experimental Techniques

2.1 Materials Investigated in this Thesis

All Materials (structures shown in figure 2.1) were used as received without additional modification or purification. All acceptor molecules ([6,6]-Phenyl-C61-butyric acid methyl esterPC₆₀BM, [6,6]-Phenyl-C71-butyric acid methyl esterPC70BM) were purchased from Solenne (99.9% purity). Poly(9,9-dioctylfluorene-alt-benzothiadiazole), F8BT, ($M_w = 376\ 214$ Da) was purchased from Ossila (99.9% purity). (5,15-bis((4-bromophenyl)ethynyl)-10,20-bis(3,4,5-tris(dodecyloxy)-phenyl)porphyrin), HAPAPP and Poly-2,7-(9,9-dioctylfluorene-alt-4,7-2,1,3-benzothiadiazole)-ran-2,7-(9,9dioctylfluorene-alt-4',4''-5,15-bis(phenylethynyl)-10,20-bis(3,4,5tris(dodecyloxy)phenyl)porphyrinato Zinc (II)) , F8BT-HAPAPP ($M_w = 15\ 000$ Da, PDI = 1.5), were both synthesised by David Freeman of the Bronstein group.¹ 2,5-bis(2-hexyldecyl)-3,6-di(thiophen-2-yl)-2,5-dihydropyrrolo[3,4-c]pyrrole-1,4-dione, TDPP was synthesised by Anastasia Leventis of the Bronstein group.² poly-2,6-(4,4-dihexadecyl-4H-cyclopenta[2,1-b:3,4-b']dithiophene)-alt-2,6-(spiro[cyclopenta[2,1-b:3,4-b']dithiophene-4,9'-fluorene]-2',7'-dicarbonitrile), Thiro ($M_n = 6400$ Da and $M_w = 8200$ Da), was synthesised by Alex Forster of the Bronstein group.

Chapter 2

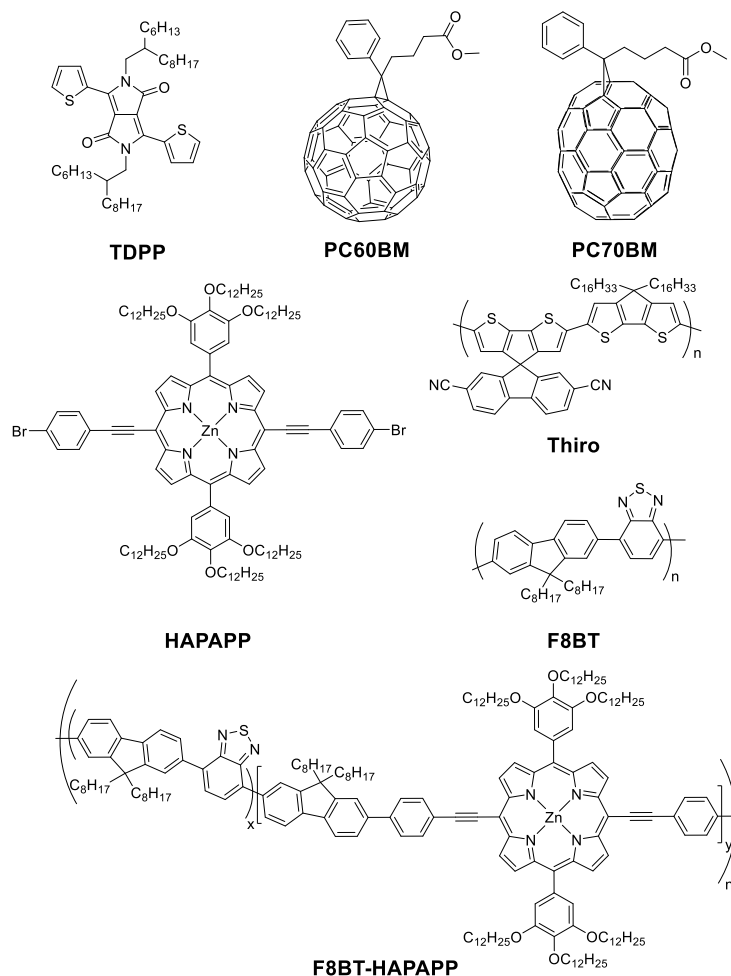


Figure 2.1 Structures of the materials used in this thesis.

2.2 Sample Preparation

A general sample preparation guide is presented in this chapter. More specific information regarding preparation of samples is presented in each chapter. Films were prepared by fully dissolving materials in chlorinated solvents (typically chlorobenzene) and stirring overnight at ~600 rpm, with heat if necessary (60-85°C). Solution concentrations employed were approximately 10 $\mu\text{g/mL}$ for the donor material as to allow for a film absorbance of <0.8 after spinning. Ultra-flat Quartz Coated glass (20 mm quartz layer) purchased from Ossila were used as substrates for film samples. Glass microscope slides purchased from VWR were also used as substrates for films by cutting the glass to approximately 1.5x1.5 cm in size. All substrates were cleaned prior to use by sonicating in water, acetone and isopropanol for 10 minutes each and left to air dry. Films were spun using an Ossila vacuum less spin coater located inside a glove box with an N_2 atmosphere. Typical spin parameters were 1600 rpm for 90 seconds. Films were kept in a N_2 filled glovebox prior to and after investigations.

Chapter 2

For solution phase-based studies, concentrations were kept <100 µg/mL. Oxygen was removed via means of freeze-pump-thaw. This was achieved by placing the solution in a Schlenk tube fitted with a Young's tap and subjecting it to three cycles of freeze pump thaw. Once completed the resulting degassed solution was transferred via cannulation to a custom made 2 mm path length cuvette fitted with a Young's tap, while under N₂.

2.3 Steady State UV-Vis Spectroscopy

Steady state UV-vis spectroscopy is a core technique for characterising the light absorption profile of a material. The absorbance of a monochromatic beam of light by a given sample is described by the Beer-Lambert law in equation 2.1.

$$I = I_0(10^{-\epsilon cl}) \quad \text{Eqn. 2.1}$$

Where I is the intensity of the transmitted light, I_0 is the intensity of the incident light, ϵ is the molar absorption coefficient (formerly called molar extinction coefficient), c is the molar concentration of the solution and l is the path length (with a 1 cm pathlength being common for solution experimental conditions). The absorbance (also historically referred to as the optical density, OD, and is used interchangeably with absorbance in this thesis) is given by equation 2.2.

$$A = \log\left(\frac{I_0}{I}\right) = \epsilon cl \quad \text{Eqn. 2.2}$$

Where A is the absorbance. In the case where a solution is comprised of a mixture of absorbers, the total absorbance at a given wavelength will be the result of a summation of the absorbances of both the individual absorbers at that wavelength. It should be noted that the Beer-Lambert law is only applicable to low concentrations of a sample, where solute-solute interactions are limited. Another important point to note is that ϵ is wavelength dependant, with units of mol⁻¹ dm³ cm⁻¹. In highly conjugated organic semiconducting materials, the main electronic transitions observed typically derive from strongly absorbing π - π^* transitions, making them ideal light absorbers.

All films and solutions were characterised initially by steady state UV-Vis spectroscopy. This allowed for observing the optical band gaps of the materials of interest and choosing the correct pump wavelength. Furthermore, for thin film samples, the absorption spectra can be used to give an indication of the relative crystallinity of a morphology. In addition, absorption values may be used to help correct photoluminescence and transient absorption data (μ s and ps) for the number of photons absorbed at the exciting wavelength.

Chapter 2

Ground state absorbance measurements were obtained with a UV-Vis spectrophotometer (Perkin Elmer, LAMDA 365). Films were recorded in air, while solution samples were recorded if possible degassed in a Young's tap cuvette. When measurements were carried out using the Young's tap cuvette the spectrometer lid would not fully close. As such, in order to reduce the impact of stray light a black cloth was used to cover the experiment chamber and in addition the room was dimmed. All samples were corrected to 100%T using either a quartz glass substrate or the corresponding path length cuvette with the corresponding solvent. UV-Vis measurements in this thesis were recorded using a double beam reference. Presented spectra have been normalised to their peaks.

When measuring UV-Vis data (particularly thin films) artefacts may arise from the presence of scattering and reflections, often manifesting itself as an increase or reduction in the background signal (thus leading to an erroneous baseline). As such, it is sometimes required that the baseline must be corrected to account for these effects. In this thesis, baseline correction was done via (sensibly) selecting a data point known to possess no or limited absorption, which was typically a point at the furthest red of the spectrum obtained (for this thesis this was typically at 850 nm). One possible methodology to help reduce the issue of scattering and reflection is through the use of an integrating sphere (which was not used for absorption measurements in this thesis).

2.4 Photoluminescence (PL) Spectroscopy

Steady state photoluminescence (PL) spectroscopy is a core experimental technique, which allows for characterisation of an emissive excited state. Although the term 'photoluminescence' encompasses both fluorescence and phosphorescence, in the literature regarding organic semiconducting materials the term PL is used interchangeably with fluorescence. A key paradigm in PL spectroscopy is that according to Kasha, fluorescence is observed from the lowest vibrational level of the S_1 state ($S_1 \rightarrow S_0$), due to the rate of internal conversion between singlet excited states being much higher than the rate of fluorescence. It should be noted however, that there are exceptions to Kasha's rule, such as in the well documented case of azulene and its derivatives. Azulene is found to have a relatively large S_2 - S_1 energy gap of ~ 1.6 eV, resulting in the rate of internal conversion being slow and with the consequence of emission being observed from the S_2 state ($S_2 \rightarrow S_0$)

Chapter 2

When a small molecule or polymer donor is excited, fluorescence will stem from the excited singlet excitonic state (S_1). However, blending with an acceptor molecule also opens up the possibility of fluorescence directly from interfacial CT states, which is typically observed as a broad, structureless emission that is found red-shifted relative to the donor exciton's fluorescence.³ In addition, provided that the absorption spectrum of the acceptor sufficiently overlaps with the exciting wavelength, direct excitation and subsequent fluorescence from the acceptor is possible. In some cases, the observed fluorescence from the acceptor may also derive from energy transfer from the donor to the acceptor.⁴

PL spectroscopy can be used to give an indication of the degree of exciton quenching in a donor-acceptor blend.³ As any observed quenching is likely to derive from electron transfer from the donor to the acceptor, the PLQ can be used to infer the morphological structure of the film and/or the energetics. The PLQ can be determined from comparing the pristine donor material with its blend with an acceptor, as shown in equation 2.3.

$$PLQ = 1 - \left(\frac{PL_{blend}}{PL_{pristine}} \right) \quad \text{Eqn. 2.3}$$

Where $PL_{pristine}$ and PL_{blend} are the emission spectrum integrated intensities of the pristine donor and blend films respectively and have been corrected for the absorbance. Blend films which exhibit a PLQ close to 100% can be considered to exhibit highly efficient donor-exciton quenching. This may be indicative that the donor and acceptor are intimately mixed and/or the exciton possesses a long diffusion lifetime.⁵ It should be noted that this conclusion relies upon the assumption that the film morphology does not change with the addition of the quencher, which is likely to not be the case. Furthermore, this methodology is only valid for materials which possess a high fluorescence quantum yield. Consequently, materials which exhibit high intersystem crossing quantum yields, or exhibit low-band gaps (which are more prone to undergo non-radiative decay processes due to the energy gap law) are less applicable to this methodology.

PL measurements were recorded on a spectrofluorometer (Horiba, FluoroMax-4). All films were carried out in air. For solution studies samples were degassed using Ar or N_2 for 30 min in a sealable cuvette. Signals if necessary were corrected for the absorbance at the exciting wavelength, unless samples possessed the same absorbance at the exciting wavelength. For presented normalised PL spectra presented in this thesis, the data has been normalised to the peak.

2.5 Quantum Yields

A quantum yield (QY) of a process or reaction is defined as the ratio of the number of excited state processes or reactions to the total number of photons absorbed. As such quantum yields give a quantitative account of the deactivation of an excited state. The fluorescence quantum yield (ϕ_F) is a key photophysical parameter and is defined in equation 2.4 and 2.5. It should also be noted that fluorescence quantum yield is used interchangeably with photoluminescence quantum yield (PLQY).

$$\phi_F = \frac{N_F}{N_{Abs}} \quad \text{Eqn. 2.4}$$

$$\phi_F = \frac{k_F}{k_F + k_{ISC} + k_{IC}} \quad \text{Eqn. 2.5}$$

Where N_F is the number of photons emitted by fluorescence and N_{Abs} is the total number of photons absorbed. Assuming steady state excitation conditions, the quantum yield of a process is given by the ratio of the rate of the process of interest to the sum of the rates of the processes that deactivate the excited state. For example, the quantum yield of fluorescence will be the rate of fluorescence divided by the sum of the rate of fluorescence (k_F), rate of intersystem crossing (ISC) and internal conversion (IC). Several precautions should be taken prior to experimental measurements. One such precaution is the use of optically diluted solutions ($A < 0.1$), as to avoid so called 'inner filter' effects and allow for a linear relationship between the photoluminescence intensity and absorbance. A second precaution to make is that all solvents used should be measured prior to use, to assess their purity, as spurious bands may result from contamination and contribute to error. It should also be noted that QY measurements typically possess an error of ~10%.

Quantum yields in chapter 4 were determined with the use of an integrating sphere (Horiba Jobin Yvon, F3018) in air, on a spectrofluorometer (Horiba, FluoroMax-4). The integrating sphere allows for quantification of the PLQY, without the need for a comparative known standard. This is achieved via determining the PLQY relative to the depletion of the excitation intensity (i.e. the absorption), using the methodology established by Beeby et al.⁶

2.6 Transient Absorption Spectroscopy (TAS)

Transient absorption spectroscopy (TAS) is an all-optical experimental technique, used to measure the absorption and kinetic behaviour of excited species (such as singlet and triplet states) which possess relatively short lifetimes. These short-lived species cannot be observed using conventional experimental methods, which require

Chapter 2

detection times longer than the lifetime of the species of interest. This spectroscopic technique was initially developed by Manfred Eigen, Ronald Norrish and Lord George Porter in 1949, for which they received the Nobel prize in 1967.⁷ The key principle employed in TAS is termed 'pump-probe'. This involves utilising an intense pulse of light, with a short enough time duration to perturb the equilibrium of the system of interest and subsequently spectroscopically follow the evolution of the transient species generated. This is achieved via measuring the change in optical density as a function of time, as shown in equation 2.6.

$$\Delta OD_{(t)} = OD_{(t)} - OD_0 \quad \text{Eqn. 2.6}$$

Where $OD_{(t)}$ is the transient absorbance as a function of time, and OD_0 is the absorbance of the sample when not excited. The transient absorbance can then be related to the concentration of the excited species via the Beer-Lambert Law (shown in equation 2.7). After excitation, part of the sample will be placed into an excited state and as such the absorbance of the sample before and after excitation is given by equation 2.8.

$$OD_0 = \epsilon cl \quad \text{Eqn. 2.7}$$

$$OD_t = \epsilon l(c - c^*) + \epsilon^* c^* l \quad \text{Eqn. 2.8}$$

$$\Delta OD_t = \epsilon^* c^* l - \epsilon c^* l = (\epsilon^* - \epsilon) l c^* \quad \text{Eqn. 2.9}$$

Where ϵ is the molar absorption coefficient, c is the molar concentration of the sample, l is the path length, ϵ^* is the molar absorption coefficient of the excited state, c^* is the molar concentration of the excited state and ΔOD_t is the change in absorbance at time, t . Equation 2.9 shows us that the measured ΔOD_t is found to be proportional to the concentration of the excited state, c^* , which allows for calculating the lifetime of the excited state by plotting a graph of ΔOD_t against t .

The duration of the excitation pulse dictates the temporal resolution of the measurement. The original flash photolysis systems were that of discharge flash lamps, which gave light pulses with a duration of 10^{-6} s. The intense pulses of light used in modern transient absorption spectroscopic systems derive from lasers, which are capable of delivering intense enough light pulses in time periods as short as 10^{-12} s and 10^{-15} s. There are two different experimental setups used depending upon the temporal resolution required, these are nanosecond-microsecond TAS and picosecond TAS (the details of these will be discussed in the following sections). Therefore, it is important to match the experimental setup to the timescale of the species or process that is to be spectroscopically observed.

2.6.1 TAS with Nanosecond-Microsecond Resolution (μ s-TAS)

In nanosecond-microsecond TAS (herein referred to as μ s-TAS) a time domain of 10^{-9} - 10^{-2} can be covered. μ s-TAS is therefore useful for studying long-lived transient species which have derived from previous ultrafast processes of exciton migration, electron transfer and subsequent free charge generation. All TAS techniques are based upon 'pump-probe' spectroscopy, whereby an initial pulsed laser (the 'pump') excites the sample of interest, populating the excited state(s). At the same time a continuous wave (CW) broadband light beam (the 'probe') is used to take an absorption profile of the excited state. A general scheme for a μ s-TAS experimental setup is shown in figure 2.2.

In the specific case of μ s-TAS, the probe is passed through the sample, with and without the presence of the exciting pulse and enters a monochromator (which permits the selecting of the wavelength of interest). Once the transmitted light exits the monochromator it is then sent to a photodiode (which generates a potential difference upon exposure to light) and records a change in voltage on the oscilloscope. The change in probe intensity as a function of time is taken from the reference voltage prior to the exciting pulse (without excited states present) and at time, t , after the reference, when the probe may now also be absorbed by the photogenerated excited states. This observed fractional change in voltage can then be used to calculate the change in optical density at t , ΔOD_t , (used for convention in TAS instead of absorbance) using equation 2.10.

$$\Delta OD_t = OD_t - OD_0 = \log \frac{I_{o1}}{I_{o2}} \quad \text{Eqn. 2.10}$$

Where I_{o1} is the intensity of the transmitted radiation before the pump pulse, and I_{o2} is the intensity of the transmitted radiation after the sample has been excited with the pump pulse. The change in absorbance is obtained electronically during TAS measurements via measuring the voltage made across a photodiode as a function of time. The voltage generated and displayed on the oscilloscope is directly proportional to the amount of probe light transmitted through the sample. The change in voltage at time t , ΔV_t , can therefore be related to the change in optical density using equation 2.11.

$$\frac{V_t - V_0}{V_0} = \frac{10^{-OD_t} - 10^{-OD_0}}{10^{-OD_0}} = 10^{-OD_t + OD_0} - 1 \quad \text{Eqn. 2.11}$$

Where V_0 is the voltage generated by the probe beam when the sample is not excited and V_t is the voltage generated by the probe beam at time t , after the sample has been excited. During TAS measurements only a small change in the voltage will be

Chapter 2

observed upon excitation of the sample, corresponding to a small change in the optical density. This has the consequence of x being small for 10^{-x} , which results in 10^{-x} being ~ 1 , thus simplifying equation 2.11 to 2.12. Subsequent rearrangement to find ΔOD yields equation 2.13, which demonstrates that for small changes in the optical density the voltage remains linearly proportional to it.

$$\frac{\Delta V_t}{V_0} = 1 - \Delta OD \ln 10 - 1 = \Delta OD \ln 10 \quad \text{Eqn. 2.12}$$

$$\Delta OD = \frac{1}{\ln(10)} \frac{\Delta V_t}{V_0} = \frac{1}{2.303} \frac{\Delta V_t}{V_0} \quad \text{Eqn. 2.13}$$

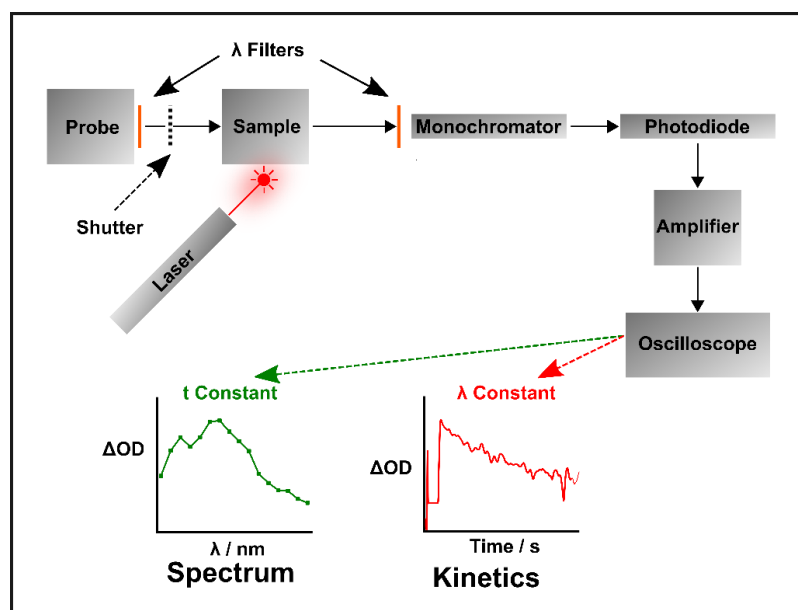


Figure 2.2 A general scheme for a μs TAS experimental setup used in this thesis. The change in the optical density (relative to the ground state absorbance) after excitation may be plotted as a function of probe wavelength, λ , yielding a transient absorption spectrum.

The μs -TAS measurements in this thesis were acquired with a bespoke setup. The pump excitation source was generated from a pulsed ND:YAG laser (Quanta-Ray INDI, Spectra Physics), with a set repetition rate of 10 Hz, a frequency of 1064 nm and a pulse width of 6 ns. The 1064 nm fundamental is frequency doubled to yield 532 nm light, which is then subsequently mixed with the 1064 nm fundamental to give an output of 355 nm. The 355 nm output beam is then used to seed a beta barium borate optical parametric oscillator (OPO) (Versascan, GWU). The OPO via means of a non-linear optical process outputs two beams, a higher energy ‘signal’ beam in the range of 410 – 709 nm and a lower energy ‘idler’ beam in the range 710-2630 nm. The signal and idler output wavelengths are related to one another by equation 2.14.

Chapter 2

$$\frac{1}{\lambda_{idler}} = \frac{1}{\lambda_{pump}} - \frac{1}{\lambda_{signal}} \quad \text{Eqn. 2.14}$$

This signal and idler are separated from one another via means of dichroic mirrors when operating with the spectral range of 400-620 nm. The signal output is used as the primary excitation source and its energy is varied through the use of neutral density filters. The probe beam is generated from a tungsten halogen lamp (Bentham, IL1) with a stabilised current power source (Bentham, 605). The probe beam is passed through the sample (either solution or thin film) in a quartz cuvette filled with an inert atmosphere (typically N₂) and into a monochromator (Cornerstone, 130), which is used to select the wavelength of interest. Optical filters, such as short pass, long pass or band pass may be used in front of the probe beam to prevent noise originating from undesired sample excitation. In addition to this, long pass filters are employed in front of the monochromator aperture to reduce noise originating from pump scatter.

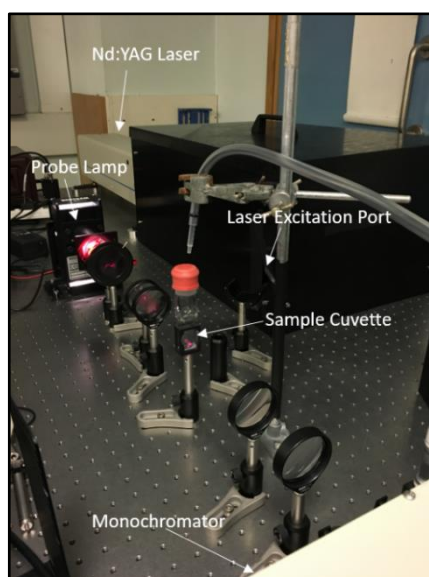


Figure 2.3 The μ s-TAS experimental setup used in this thesis. The OPO is located inside the black shroud with the laser outlet. The optical transient detectors are located after the monochromator.

The probe light is then focused onto a visible or near-infrared optical transient detector preamplifier, which is in turn connected to a main amplifier which converts the signal into a difference in voltage. The visible detector is comprised of a silicon PIN low noise photodiode (Hamamatsu, S3071) with a spectral range of 320-1060 nm (shown in figure 2.4 b)), while the infrared detector is comprised of a InGaAs PIN photodiode with a spectral detection range of 700-1700 nm (shown in figure 2.4 a)). The detectors have a rise time of \sim 80 ns, however, experimental conditions relating to pump noise from laser scatter typically limits the resolution of the μ s-TAS system to \sim 600 ns. The

Chapter 2

main amplifier (figure 5) is connected to a multichannel oscilloscope (DPO 4035B, Tetrnix) which is used to set time zero from the pump scatter using a connected silicon photodiode (Thor labs). For the main amplifier the background (DC) light level is given by the LCD screen and is expressed as a voltage that would appear at the output if the system was a pure DC amplifier. An input of 400 V represents a preamplifier output of 1 V. The preamplifier is linear up to 1.5 V (600 V on the LCD of the main amplifier), consequently the TAS optical system must be modified to keep the light input below this level via adjusting the incident probe intensity (through the use of ND filters and an iris). When looking for TAS signals generally there is a large DC component that we do not wish to amplify, and that must be removed to allow the smaller AC component to be resolved. This is possible via subtracting a DC voltage from the input, or by sending the signal through a high pass (AC coupled) stage. The box also contains additional low pass filters, allowing for the filtering of low frequency noise. The oscilloscope is connected to a computer, which completes data acquisition via commercial software (Costronics Electronics, TEKAVEUSB). Overall, this system allows for observing changes in optical density on the order of 10^{-6} .

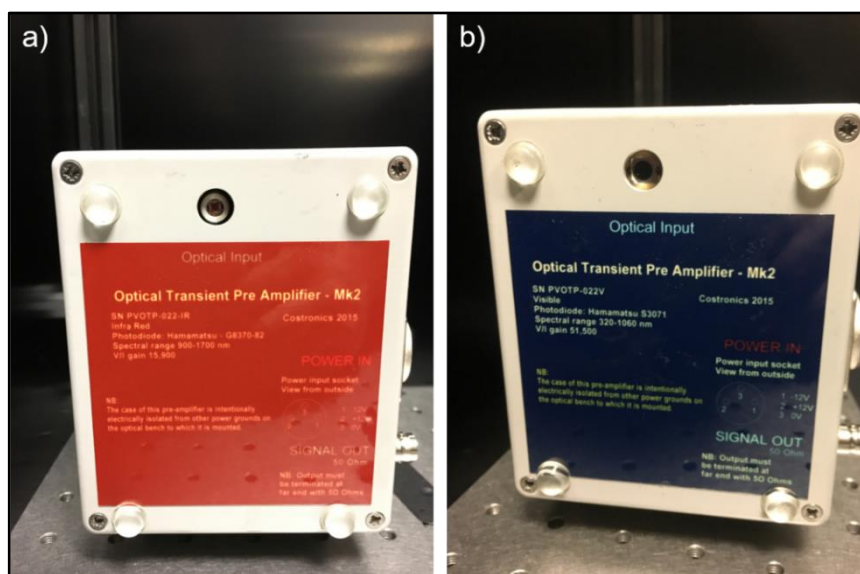


Figure 2.4 **a)** The infrared transient detector containing an InGaAs PIN photodiode with a spectral range of 700-1700 nm, **b)** The visible transient detector containing an Si PIN photodiode with a spectral range of 320-1060 nm.



Figure 2.5 Costronics transient amplifier and filtering box. The background (DC) light level is observed on the LCD screen.

2.6.2 TAS with Picosecond Resolution (ps-TAS)

When attempting to do TAS on sub-ns time scales electronic components, such as photomultipliers often lack the necessary response time and signal to noise to make accurate measurements (exceptions include that of streak cameras)⁸. In order to overcome these limitations, the same femtosecond laser source is used to generate two light pulses via means of a beam splitter or a partially reflecting mirror. The first pulse is used to excite the sample of interest and is termed the ‘pump’, whereas the second pulse is used to ‘probe’ the induced changes in the sample at a set time after excitation (this is in contrast to a μ s-TA setup, which typically uses a second light source for the probe beam). Although both pulses are generated at the same time, they are sent along different pathways so that the probe pulse arrives at the sample at a selected time after it has been excited by the pump. Prior to reaching the sample, the pump pulse is sent to an optical parametric amplifier (OPA), whereby the desired excitation wavelength is generated.

The probe pulse is initially sent through a delay stage, consisting of a mobile platform with reflector mirrors. By varying the distance between the mirrors, the time delay of the pump-probe technique is now dictated by the pathlength of the light and therefore no longer requires the use of electronics. For example, increasing the delay stage path length by 1 mm equates to a delay of 3.33 ps. The probe pulse is then used to generate ‘white light’ either in the visible or infrared range, depending upon the type of mixing crystal used. The probe then arrives at a sample at a set time, after the

Chapter 2

sample has been excited by the pump (alignment of the pump and probe beams is therefore crucial). After the probe has passed through the sample the change in its intensity (from absorption by an excited state) is then measured by an imaging detector spectrometer. Imaging spectrometers allow for the collection of an entire spectrum, as opposed to constructing one individually from the decay data obtained from probing at each individual wavelength.

The ps-TAS measurements obtained in this thesis were acquired with a commercial setup, with an instrument resolution of ~ 200 fs. The fs-TAS system is comprised of a Ti:Sapphire fs laser (Mai Tai, Spectra Physics) which is used to seed a regenerative amplifier (Solstice, Spectra Physics), which increases the output energy from 17.5 nJ to > 2.5 mJ, with a pulse duration of ~ 100 fs and a wavelength of 800 nm. The initial ~ 200 fs pulses cannot be directly amplified due to the risk of damaging the Ti:Sapphire crystal in the regenerative amplifier. In order to circumvent this problem, the ultra-short laser pulses are time stretched, amplified and then subsequently time compressed.

Using a beam splitter, part of the regenerative amplifier output is used to seed an optical parametric amplifier (Topas, Spectra Physics) to generate the exciting 'pump' pulse. The OPA uses a non-linear optical process to generate light with varying frequencies and polarisation. In addition, frequency mixers allow for extension of the wavelength range into the U.V. and IR, thus allowing for an excitation range of 285-1600 nm. The energy of this pump pulse is controlled via means of a neutral density filter wheel. In addition, the pump pulse is also passed through a depolariser, resulting in an isotropic laser pulse, thus allowing for the observed signal to be free of polarisation effects.

The rest of the amplifier output is utilised as the probe (Helios, Ultrafast Systems) via sending it to a delay stage, which allows for data to be taken up to ~ 6 ns. Once the probe pulse exits the delay stage, it then enters the spectrometer. In this section, the probe beam white light is generated, using different crystals. Either visible light (450-750 nm) or NIR (850-1450 nm) may be generated. The 800 nm fundamental (which is used to generate the probe) cannot be fully filtered from the probe, which results in a ~ 100 nm gap between the visible and NIR detectors, but nonetheless affords a large enough wavelength range for probing of the ground state bleach (GSB) region, or an excited state. The visible and IR probe lights are detected via CMOS or InGaAs detectors respectively.

The change in signal intensity is measured through reducing the repetition rate of the pump pulse relative to the probe. This is achieved via employing a chopper, which reduces the repetition rate from 1 KHz to 500 Hz (i.e. half that of the probe). This allows for the probe to be detected with and without the presence of the pump pulse. When the probe pulse is frequency-aligned with that of pump pulse, the probe will be partly absorbed by the presence of an excited state, however, when the probe pulse is not frequency aligned with that of the pump, only a ground state absorbance spectrum will be measured. The corresponding difference in the intensity of the probe pulse, in conjunction with the initial intensity, allows for determining ΔOD utilising equation 2.11. In this fs-TAS setup, in addition to the sample detector a second probe channel is utilised as a reference to increase the signal-to-noise ratio, thus allowing for a lower number of averages laser pulses to be taken. This is achieved via splitting the probe beam in two, prior to it passing through the sample. While one of the probe beams passes through the sample, the second is sent directly to a reference detector allowing for measuring any fluctuations in the probe beam intensity.

2.6.3 TAS Data Analysis in the ns-ms Regime

The preliminary step in TAS data analysis involves assignment of the observed signals/transitions. Both the visible and infrared portions (~500-1600 nm) are probed in this thesis, with both positive and negative ΔOD signals typically being observed. Negative signals generally derive from contributions from ground state bleaching effects and/or scatter from the pump laser. The ground state bleach (GSB) is found in the area of the spectrum that corresponds to the ground state absorbance of the sample. Since the ground state has been depleted by promotion to an excited state by the pump laser, the number of molecules in the ground state will therefore be less compared to the non-excited sample. This has the consequence of yielding a negative signal, that will recover to zero as the excited state decays and ground state is repopulated. Materials in this thesis predominantly absorb in the visible region, which has the effect of negative signals typically being observed on the visible detector (<1000 nm). Positive ΔOD signals correspond to absorbance of an excited state (e.g absorbance of a triplet state to an upper excited triplet state, $T_1 \rightarrow T_n$). In this thesis the main excited state products formed are either singlets, triplets or polarons. Singlet states are typically not long lived, possessing lifetimes on the order of nanoseconds or less.⁹ This results in singlet species decaying before they can be detected by the μ s-TAS setup. This infers that any positive signals observed μ s-TAS setup must derive from either that of triplets or polarons.

Chapter 2

Both triplets and polarons exhibit distinctively different kinetic behaviour at timescales typically $>1\mu\text{s}$, which has the effect of them typically being easily distinguished from one another. Provided that triplets are excited with sufficiently low excitation energies to prevent second-order effects and that they decay exclusively to the ground state, the decay of the triplet is assumed to be monomolecular. This first-order behaviour gives rise to an monoexponential decay with the corresponding non-integrated (equation 2.15) and integrated rate laws (equation 2.16):

$$-\frac{d[T]}{dt} = k[T] \quad \text{Eqn. 2.15}$$

$$[T]_t = [T]_0 e^{-t/\tau_{\text{exp}}} \quad \text{Eqn. 2.16}$$

Where τ_{exp} is the experimental lifetime for the triplet, $[T]_0$ and $[T]_t$ are the triplet concentrations at time = 0 and time = t.

A complementary way to determine whether a signal derives from that of a triplet species is through exposing a sample to oxygen. Oxygen is known to quench triplet species, provided that the triplet energy level of the species of interest is $>0.94\text{ eV}$.^{10,11} In TAS experiments, oxygen-based quenching of triplets should manifest itself as both a reduction in signal amplitude (ΔOD) and triplet lifetime.^{12,13} In solution samples, signals may also be completely quenched, as shown in figure 2.6. Particular emphasis must be placed on restoring the initial signal under an inert atmosphere. This is to confirm that any observed reduction in signal is due to triplet quenching and not oxygen-based degradation.

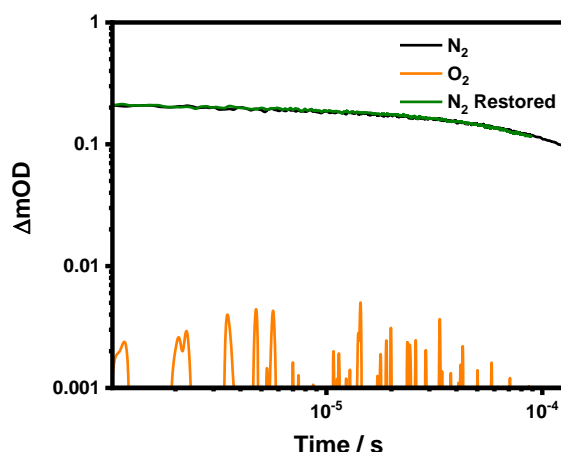


Figure 2.6 Microsecond transient absorption decay kinetics of F8BT chlorobenzene solution ($68\mu\text{g/mL}$). Bubbling O_2 through the solution results in a complete quenching of the signal. The sample was re-degassed to check that the initial signal was recoverable.

Chapter 2

Polarons, as discussed in the introduction, decay via means of recombination with their oppositely charged polaron. Polarons have been observed to undergo both geminate (monomolecular/first order) and bimolecular (second order) recombination, both with their own distinctive kinetic behaviour. Geminate recombination can be considered to take place via one of two ways. The first case involves recombination between two charges coulombically bound in a CT state (also referred to as a bound polaron pair) which have been unable to dissociate to free charge species. In the second case, the bound polaron pair is able to dissociate to free charge carriers, however, they remain trapped in their respective domains, where recombination between the electron and original positive hole is the only possibility. In both cases recombination involves the same initially excited exciton, indicating a monomolecular process and giving rise to the same kinetics previously described for that of triplet states. It should be noted however, that pure monoexponential functions are sometimes not observed experimentally, with multi or stretched exponential models often being invoked to describe experimental data. This deviation from first order decay dynamics is thought to be the consequence of the energetic disorder inherent to solids, which originate from conformational variation and polydispersity (for polymeric materials). As excitons will populate a distribution of energetic states afforded to them by the energetic disorder, the observed experimental decays will be best fitted by the function which satisfies this distribution of energies.

Bimolecular recombination, in contrast to geminate, occurs between freely separated charge species which did not originate from the same electron-hole pair. In this form of recombination, photogenerated free charges must diffuse to within the coulomb capture radius of one another. This has the effect of significantly slowing the kinetics, with bimolecular recombination often being observed in the μs -ms regime.¹⁴ This contrasts with geminate recombination which is found to typically occur on timescales of ps,¹⁵ to hundreds of ns,^{16,17} and consequently is less likely to be observed with the μs TAS experimental setup used in this thesis. It is noted, however, that there is at least one report of geminate recombination being observed on the μs timescale in a P3HT:pyrazolino fullerene derivative blend.¹⁷ As bimolecular recombination involves both a positive and negative charge, it would therefore be expected to exhibit second order kinetics, with the corresponding non-integrated (equation 2.17) and integrated rate laws (equation 2.18).

Chapter 2

$$-\frac{dn}{dt} = k(n)n^2 \quad \text{Eqn. 2.17}$$

$$n = \frac{n_0}{1 + n_0 kt} \quad \text{Eqn. 2.18}$$

Where n is the charge density in cm^{-3} at any time, and n_0 is the initial charge density after excitation. Experimental evidence for donor-acceptor blend films, however, presents much more complicated kinetics. It has been proposed that bimolecular recombination takes place in the presence of an exponential distribution of localised trap states, and that the bimolecular recombination rate constant, k , is also dependant on a power function of the charge density (shown in equation 2.19).^{18,19} Substituting equation 2.19 into 2.17 yields the rate law equation 2.20 and its integrated formed equation 2.21.

$$k(n) = k_0 n^\beta \quad \text{Eqn. 2.19}$$

$$-\frac{dn}{dt} = k_0 n^{\beta+2} \quad \text{Eqn. 2.20}$$

$$n = \frac{n_0}{(1 + k_0(\beta + 1)n_0^{\beta+1}t)^{\frac{1}{\beta+1}}} = \frac{n_0}{(1 + \mu t)^{\frac{1}{\beta+1}}} \quad \text{Eqn. 2.21}$$

Where k_0 is the bimolecular recombination constant independent of charge density and $\mu = k_0(\beta+1)n_0^{\beta+1}$. From this we can see that this function tends to n_0 as t approaches zero, which has the effect of yielding a plateau at the fastest times. In the condition where $\mu t > 1$, the dependency of charge density, n , with respect to t exhibits a power-law (equation 2.23) and is the regime where trap limited recombination dominates. This feature is particularly useful in identifying polarons, as bimolecular recombination will appear linear on a log-log plot of the μs -TAS decay kinetics.

$$n = (n_0 a^{\frac{-1}{\beta+1}})(t^{\frac{-1}{\beta+1}}) \quad \text{Eqn. 2.22}$$

$$\Delta\text{OD} \propto n = At^{-\alpha} \quad \text{Eqn. 2.23}$$

Where $A = n_0 a^{-1/\beta+1}$ and $\alpha = 1/\beta+1$. β can therefore be related to the power law exponent, α , by using the total order of the reaction $\beta+2 = 1/\alpha + 1$, therefore $\beta = 1/\alpha - 1$. As the ΔOD will be proportional to the charge density, n , the value of α may be obtained from fitting equation 2.23 to the observed the transient decay. The value of α will be a rational number, where a value of 1 indicates pure bimolecular recombination. An important point to note is that the value of α is dependent upon the distribution of energetic trap states, as such both morphology and crystallinity of a film

affect the value of α . This has been eloquently shown via annealing studies of P3HT:PCBM blend films, where annealing increases the ordering of polymer chains. This increase in crystallinity is found to reduce the depth of the energetic traps, increasing charge mobility and consequently the rate of bimolecular recombination.^{20,21} This observation indicates that this energetic trap distribution is not the result of chemical defects, but rather film morphology.

TAS can be used to experimentally find the bimolecular recombination rate constant, as has been shown by Shuttle et al.²² This is done by using the Beer-Lambert law to relate the ΔOD to the charge density, as shown in equations 2.24 and 2.25.

$$n = \frac{\Delta OD(N_A)}{\epsilon_M d 1000} \quad \text{Eqn. 2.24}$$

$$k = \frac{d\Delta OD}{dt} \frac{2d\epsilon_M}{\Delta OD^2} \frac{1000}{N_A} \quad \text{Eqn. 2.25}$$

Where d is the film thickness, N_A is Avogadro's constant and ϵ_M is the molar extinction coefficient of the polaron.

2.6.4 TAS Data Analysis in the ps-ns Regime

In ps-TAS, species which are too short-lived to be detected in μ s-TAS may be probed. This ability to probe short-lived species is afforded by the time resolution of the instrument, which spans from ~ 200 fs to 6 ns for the instrument used in this thesis. Consequently, the spectra obtained are often more complex than their μ s counterparts, containing contributions from both short and long-lived species. In ps-TAS, positive signals can now also derive from absorption by the singlet state ($S_1 \rightarrow S_n$), as well as both triplets ($T_1 \rightarrow T_n$), CT states (also known as bound polaron pairs in the context of D/A blends) and polarons. Additional photophysical processes for these long-lived species may also be observed, for example population of the triplet manifold via ISC may be monitored.²³

In addition to ground state bleaching effects (shown in figure 2.7 ii), additional contributions may now stem from stimulated emission (shown in figure 2.7 iii). This is the induced emission of a photon from an excited state, via interaction with the probe light. Stimulated emission typically manifests itself as a negative signal in the same spectral area as the observed emission, and consequently should be found red-shifted relative to the GSB. The observed negative stimulated emission signal derives from the detector measuring a higher light intensity, relative to the reference without the pump pulse, as the emitted photon will travel in the direction of the probe pulse, with both being subsequently detected.

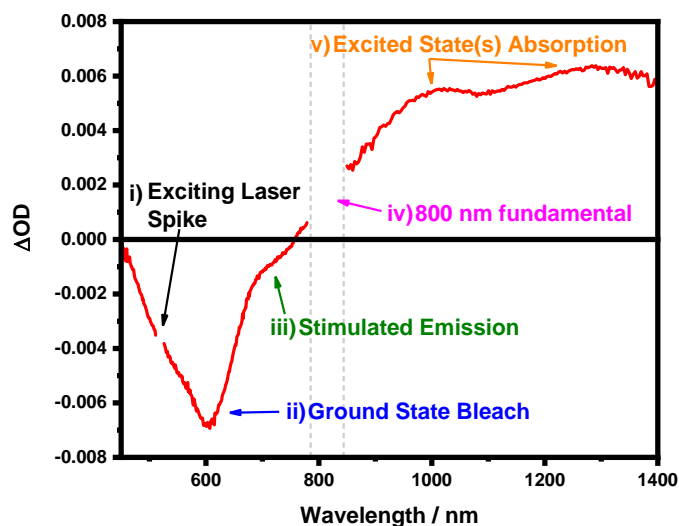


Figure 2.7 *ps-TA spectrum of a pristine Thiro film at 1 ps (taken from chapter 5), illustrating multiple signal components that may comprise the spectrum. Obtained with an excitation wavelength of 520 nm. i) The laser ‘spike’ can be observed at 520 nm. ii) The ground state bleach corresponds to depletion of the ground state and results in a negative ΔOD signal. iii) Stimulated emission can also result in a negative ΔOD signal and can be found spectrally situated in the area of emission. iv) The visible and infrared light probes do encompass the entire spectrum, and results in a ~ 100 nm spectral dead zone (represented by the grey dashed vertical lines in figure 7 v). Excited state absorption results in a positive ΔOD , but it is important to note that the obtained signals may represent contributions from different species.*

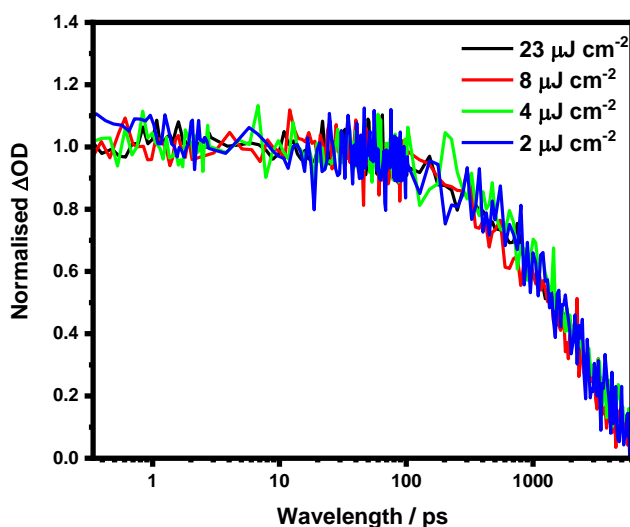


Figure 2.8 *An example of excitation energy independent ps-TA kinetics for F8BT solution (50 $\mu\text{g/mL}$).*

Chapter 2

For the studies presented in this thesis, the obtained excited state spectra are typically complex. An overarching feature for all of them, however, is the presence of a short-lived singlet state that dominates the early ps-timescale. Singlet states observed in pristine materials should elicit the same kinetic response as described for triplet species in the preceding section, exhibiting a monomolecular decay at the lowest excitation energies (shown in figure 2.8). Additional confirmation of an assignment to a singlet state can also be attained via a comparison with the stimulated emission kinetics, which should possess the same decay kinetics and therefore lifetime, which is readily apparent upon normalisation of the two decays (this is discussed in chapter 4). The singlet-state transition can also in some instances undergo a red-shift with time. This red-shifting is attributed to the singlet state undergoing energetic relaxation down the density of states (DOS).^{24,25} This relaxation process therefore indicates the presence of energetic disorder, with a large red-shift corresponding to greater energetic disorder in the material. Triplet species are typically observed upon spectral evolution, becoming spectrally evident upon the decay of the singlet state. ISC to the triplet manifold is often observed as a rise in the triplet signal amplitude, which naturally follows the decay of the singlet state. Further confirmation of a transition in the ps-TA spectrum to a triplet can be made via comparison with the corresponding μ s-TA spectrum, where the long-lived triplet species should still be evident.

Upon blending with a suitable acceptor molecule, singlet states may be quenched via electron transfer, manifesting as a reduction in both the signal amplitude and lifetime in the singlet. In addition, a commensurate reduction in the stimulated emission is also found to accompany quenching,^{24,26} as fluorescence stems from the excited singlet state (which exhibits a smaller population upon quenching). A further point to note is that ISC to the triplet manifold is often a much slower process relative to the quenching of the singlet state by the acceptor, which can take place on the sub-ps timescale. This can result in negligible triplet formation in blend films, regardless of whether triplets are formed in the pristine donor ps-TA spectrum.²⁶ In D/A blends, polarons (free charge species) are often the main product of quenching of the excited singlet state and are formed on a variety of timescales. Polarons often exhibit relatively broad transitions in the NIR (~900-1200 nm as a rule of thumb)^{24,26-29} and are often found to overlap with the singlet and triplet transitions. Furthermore, differentiation between interfacial CT states and 'free' polarons is often difficult, as they often exhibit very similar spectral profiles. Polarons often possess lifetimes that are long enough to persist into the μ s regime (like triplets) and thus a comparison between the ps and μ s-TA spectra can help confirm assignments.

2.6.5 TAS Data Processing and General Analysis

Post ps-TA data collection processing was performed using surface Xplorer and origin software packages. Surface Xplorer was used for background subtraction and chirp correction. Prior to chirp correction the data matrix on the wavelength axis was trimmed using the crop function to include only the useful data (i.e., only sensible data). Chirp correction is applied by manually selecting at least 4-time zero wavelength pairs (where time zero is defined as half the ΔOD value of the initial rise), whereby the data is then fit with a polynomial. Smoothing (e.g., adjacent averaging) and pump subtraction were not performed for the TA data presented in this thesis. When plotting ps-TA spectra, spectral data prior to absorption is included, which can show any deviation from the spectral baseline (the background offset). In this thesis this is shown via including the data at -10 ps in the ps-TA spectra. In addition, prior to plotting kinetics, time zero is checked via enhancing the region -1 to 1 ps and allows for manual correction if necessary.

Origin software was used for data fitting of both ps and μs -TA data (unless specified otherwise) instead of global fitting software. This was possible because in general the signals obtained were relatively clear and distinct from one another, thus allowing for unambiguous assignment and analysis. When fitting data, it is assumed that both singlet and triplet states decay via first order and go to zero, but this is typically not what is observed, especially when such states undergo multiple decay pathways, which often leads to multi or stretched exponential decays. For μs -TA data, the background offset is taken to be zero. Global analysis (GA) for ps-TAS data was carried out using a previously written programme based on a genetic algorithm. The genetic algorithm was provided by Dr Artem Bakulin (Imperial College London). Interested readers can get access to the code by contacting Dr Artem Bakulin or Nathaniel Gallop (Warwick University). Reference spectra (e.g. singlet or triplet) are taken from the ps-TA measurement (the raw data matrix, not the Surface Xplorer file) and used to aid as an initial "guess" for the algorithm, reducing the time needed for spectral deconvolution. For the GA carried out in chapter 5, a reference spectrum averaged between 1-6 ns was used, corresponding to the ascribed Thiro triplet. The algorithm starts with a large ensemble of randomly generated solutions and evaluates the fitness of each of them. Those solutions which possess the best fits are more likely to survive and reproduce, yielding a new generation of "children" composed of linear combinations of high-fitness parents. A degree of randomness is added to maintain the diversity of the solution ensemble. As successive generations are combined, the solution converges to an optimum/best-fitted result.³⁰

2.7 Bibliography

- 1 J. Shaikh, D. M. E. Freeman, H. Bronstein and T. M. Clarke, *J. Phys. Chem. C*, 2018, **122**, 23950–23958.
- 2 C. W. Ge, C. Y. Mei, J. Ling, F. G. Zhao, H. J. Li, L. Liang, J. T. Wang, J. C. Yu, W. Shao, Y. S. Xie and W. S. Li, *J. Polym. Sci. Part A Polym. Chem.*, 2014, **52**, 2356–2366.
- 3 K. Tvingstedt, K. Vandewal, F. Zhang and O. Inganäs, *J. Phys. Chem. C*, 2010, **114**, 21824–21832.
- 4 S. Cook, H. Ohkita, J. R. Durrant, Y. Kim, J. J. Benson-Smith, J. Nelson and D. D. C. Bradley, *Appl. Phys. Lett.*, 2006, **89**, 101128.
- 5 S. D. Dimitrov, B. C. Schroeder, C. B. Nielsen, H. Bronstein, Z. Fei, I. McCulloch, M. Heeney and J. R. Durrant, *Polymers*, 2016, **8**, 14.
- 6 L. Porrès, A. Holland, L.-O. Pålsson, A. P. Monkman, C. Kemp and A. Beeby, *J. Fluoresc.*, 2006, **16**, 267–273.
- 7 R. G. W. Norrish and G. Porter, *Nature*, 1949, **164**, 658–658.
- 8 T. Ito, M. Hiramatsu, M. Hosoda and Y. Tsuchiya, *Rev. Sci. Instrum.*, 1991, **62**, 1415–1419.
- 9 S. Dimitrov, B. Schroeder, C. Nielsen, H. Bronstein, Z. Fei, I. McCulloch, M. Heeney and J. Durrant, *Polymers*, 2016, **8**, 14.
- 10 F. Wilkinson and A. A. Abdel-Shafi, *J. Phys. Chem. A*, 1999, **103**, 5425–5435.
- 11 C. Grewer and H.-D. Brauer, *J. Phys. Chem.*, 1994, **98**, 4230–4235.
- 12 S. Shoaee and J. R. Durrant, *J. Mater. Chem. C*, 2015, **3**, 10079–10084.
- 13 Y. W. Soon, S. Shoaee, R. S. Ashraf, H. Bronstein, B. C. Schroeder, W. Zhang, Z. Fei, M. Heeney, I. McCulloch and J. R. Durrant, *Adv. Funct. Mater.*, 2014, **24**, 1474–1482.
- 14 A. F. Nogueira, I. Montanari, J. Nelson, J. R. Durrant, C. Winder, N. S. Sariciftci and C. Brabec, *J. Phys. Chem. B*, 2003, **107**, 1567–1573.
- 15 R. Sandoval-Torrientes, A. Gavrik, A. Isakova, A. Abudulimu, J. Calbo, J. Aragón, J. Santos, E. Ortí, N. Martín, V. Dyakonov and L. Lüer, *J. Mater. Chem. C*, 2019, **7**, 6641–6648.

Chapter 2

- 16 S. K. Pal, T. Kesti, M. Maiti, F. Zhang, O. Inganäs, S. Hellström, M. R. Andersson, F. Oswald, F. Langa, T. Österman, T. Pascher, A. Yartsev and V. Sundström, *J. Am. Chem. Soc.*, 2010, **132**, 12440–12451.
- 17 S. Shoaee, M. P. Eng, E. Espíldora, J. L. Delgado, B. Campo, N. Martín, D. Vanderzande and J. R. Durrant, *Energy Environ. Sci.*, 2010, **3**, 971.
- 18 J. Nelson, *Phys. Rev. B*, 2003, **67**, 155209
- 19 A. V. B. and M. Tachiya*, *J. Phys. Chem. B*, 2002, **106**, 4356–4363.
- 20 Y. Kim, S. Cook, S. M. Tuladhar, S. A. Choulis, J. Nelson, J. R. Durrant, D. D. C. Bradley, M. Giles, I. McCulloch, C.-S. Ha and M. Ree, *Nat. Mater.*, 2006, **5**, 197–203.
- 21 T. M. Clarke, F. C. Jamieson and J. R. Durrant, *J. Phys. Chem. C*, 2009, **113**, 20934–20941.
- 22 C. G. Shuttle, B. O'Regan, A. M. Ballantyne, J. Nelson, D. D. C. Bradley and J. R. Durrant, *Phys. Rev. B*, 2008, **78**, 113201.
- 23 B. Kraabel, D. Moses and A. J. Heeger, *J. Chem. Phys.*, 1995, **103**, 5102.
- 24 F. Etzold, I. A. Howard, R. Mauer, M. Meister, T. D. Kim, K. S. Lee, N. S. Baek and F. Laquai, *J. Am. Chem. Soc.*, 2011, **133**, 9469–9479.
- 25 N. Banerji, S. Cowan, M. Leclerc, E. Vauthey and A. J. Heeger, *J. Am. Chem. Soc.*, 2010, **132**, 17459–17470.
- 26 I. A. Howard, R. Mauer, M. Meister and F. Laquai, *J. Am. Chem. Soc.*, 2010, **132**, 14866–14876.
- 27 H. Ohkita, S. Cook, Y. Astuti, W. Duffy, S. Tierney, W. Zhang, M. Heeney, I. McCulloch, J. Nelson, D. D. C. Bradley and J. R. Durrant, *J. Am. Chem. Soc.*, 2008, **130**, 3030–3042.
- 28 A. Rao, P. C. Y. Chow, S. Gélinas, C. W. Schlenker, C. Z. Li, H. L. Yip, A. K. Y. Jen, D. S. Ginger and R. H. Friend, *Nature*, 2013, **500**, 435–439.
- 29 J. Liu, S. Chen, D. Qian, B. Gautam, G. Yang, J. Zhao, J. Bergqvist, F. Zhang, W. Ma, H. Ade, O. Inganäs, K. Gundogdu, F. Gao and H. Yan, *Nat. Energy*, 2016, **1**, 16089.
- 30 Y. Vaynzof, A. A. Bakulin, S. Gélinas and R. H. Friend, *Phys. Rev. Lett.*, 2012, **108**, 246605.

Chapter 3

Exploring the Photophysics of a Small-Molecule DPP/Fullerene system

3.1 Outline

In this chapter a DPP small molecule derivative, 2,5-bis(2-hexyldecyl)-3,6-di(thiophen-2-yl)-2,5-dihydropyrrolo[3,4-c]pyrrole-1,4-dione (TDPP) was spectroscopically investigated. This was for the purpose of elucidating the fundamental photophysics of a relatively simple TDPP molecule in both its pristine and PB₆₀BM/PC₇₀BM blend thin films, thus providing a foundation for spectroscopic investigations into more complex DPP-based systems. This is because DPP-based polymers and small molecules are commonplace throughout the field of organic photovoltaics primarily due to their narrow band gaps, which allows for absorbing photons in the NIR. Furthermore, the high planarity exhibited by the DPP moiety results in a propensity for these materials to form crystalline aggregates, with accompanying excellent charge transport properties.^{1,2}

In the introduction a brief overview of DPP is provided, including its advantages and current limitations. A brief description of the methodology employed is given, followed by the results of the investigation. Ground state absorbance, photoluminescence, transient electron paramagnetic resonance spectroscopy and transient absorption spectroscopy results of pristine thin film and its fullerene blends are provided. It was found that upon excitation of the pristine TDPP thin film the singlet exciton was the predominant species generated, with limited evidence of triplet species on all time scales. In contrast to this, upon addition of PC₆₀BM or PC₇₀BM, a much more complex spectrum was obtained, with three species being observed. These species were that of the TDPP singlet-exciton, the TDPP triplet-exciton and the fullerene radical anion. The appearance of the TDPP triplet in only the blend films indicated a mechanism in which triplet formation was mediated via that of the fullerene CT state. Moreover, the assigned triplet was found not to be quenched by the presence of oxygen, indicating a triplet level <0.98 eV. Finally, the proposed mechanism was confirmed through the use of transient-EPR spectroscopy.

3.2 Introduction

The diketopyrrolopyrrole (DPP) moiety (figure 3.1) is ubiquitous throughout the field of organic electronics for its synthetic versatility, thermal and photostability and high fluorescence quantum yield.^{3,4} DPP polymers have been extensively used in bulk heterojunction organic cells,⁵ attaining efficiencies in excess of 9%.⁶ Additionally, organic solar cells have also been produced using small molecule DPP, achieving efficiencies of over 7% when using a PC70BM acceptor,⁷ or 9% when coupled with a non-fullerene acceptor.⁸ One of the main attributes of DPP is that it possesses a low optical band-gap (<1.5 eV), allowing for extending absorption up to 1000 nm, thus allowing for increased short-circuit current (J_{sc}) from increased spectral coverage. This potential for semitransparency also allows for the possibility for inclusion of DPP materials into tandem organic solar cells.⁹ This low-band gap observed in DPP materials is in part attributed to its relatively low-lying LUMO, which has the consequence of reducing the donor-acceptor LUMO offset. This reduction in energy offset reduces the driving force for charge generation, with DPP organic solar cells often yielding external quantum efficiencies (EQE) of ~50%,¹ which is much lower than the >80% exhibited by the state of the art.¹⁰⁻¹²

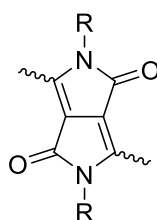


Figure 3.1 *The basic diketopyrrolopyrrole, DPP, moiety used in small molecules and polymers.*

In addition to possessing deep LUMO levels, DPP materials have been speculated to possess low-lying triplet energy levels. This has been shown to be the case for some small molecule DPP thin films, which have been found to undergo singlet fission.^{13,14} Singlet fission is a photophysical process whereby an excited singlet state is split into two triplet states on nearby molecules, and offers the prospect of being able to increase the efficiency of a photovoltaic device beyond the Shockley-Queisser limit to above 46%.^{15,16} In order for singlet fission to be energetically favourable the energy of the excited singlet state must be greater than or equal to twice the excited triplet state energy.¹⁷ It should be noted however, that singlet fission may proceed endothermically, as is the case observed for derivatives of tetracene.¹⁸ If DPP derivatives do indeed possess low-lying triplet levels, this presents a potential loss pathway in organic solar cells. This is because if the triplet level of the donor material

Chapter 3

is less than that of the CT state, this may afford an efficient CT state deactivation channel. However, to our knowledge, no time-resolved spectroscopic studies have been performed upon simple DPP monomers in bulk heterojunction films blended with fullerenes. Furthermore, previous TAS investigations have typically focused predominantly on spectral features situated in the visible region of the spectrum only.

The aim of this chapter is to build upon previous literature work by spectroscopically examining a relatively simple small molecule DPP derivative, TDPP (structure shown in figure 3.2), in bulk heterojunction blend films with PC₆₀BM and PC₇₀BM fullerene acceptors, with a particular emphasis on transient absorption features in the near-infrared region. This was for the purpose of providing a spectroscopic baseline for investigations into more complex DPP-based systems. Importantly, TR-EPR is also used to complement and validate the results provided by TAS, thus providing insight into the photophysical mechanisms present.

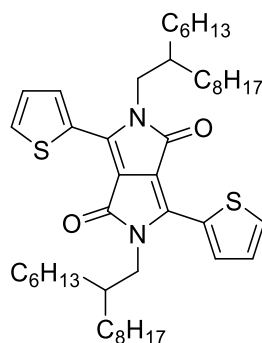


Figure 3.2 Structure of small molecule 2,5-bis(2-hexyldecyl)-3,6-di(thiophen-2-yl)-2,5-dihydropyrrolo[3,4-c]pyrrole-1,4-dione, TDPP.

3.3 Experimental

TDPP was synthesised by Anastasia Leventis of the Bronstein group using a known literature procedure.¹⁹ Thin films were prepared via spin-coating from solutions of (~5 mg/mL with respect to TDPP) of chloroform/o-dichlorobenzene (94:6) onto glass, using a spin speed of 1600 rpm, for a duration of 90 s. All films were spin coated in air, then stored in a glove box with a nitrogen atmosphere. Glass substrates were cleaned prior to spin coating via sonication for 15 min in both acetone and isopropanol.

TR-EPR thin films were prepared via drop casting onto ultra-flat quartz films (1 mm thickness) and placing into EPR tubes and sealing under vacuum. PC₇₀BM solution used in EPR experiments was prepared by dissolving in toluene (100 μ m). The solution was placed into an EPR tube and sealed under vacuum after three cycles of

freeze pump thaw. AFM films were prepared via via spin-coating from solutions onto ultraflat quartz films (1 mm thickness).

For ps-TA measurements, all thin films were excited with the same pump wavelength of 510 nm. An excitation density range of 11-91 $\mu\text{J cm}^{-2}$ was used.

For μs -TA measurements, the pristine TDPP thin film and its PC₆₀BM/PC₇₀BM blends were excited with a pump wavelength of 500 and 510 nm respectively. The pristine TDPP thin film was excited with an excitation density of 128 $\mu\text{J cm}^{-2}$. The TDPP:PCBM blend films were excited with excitation density ranges of 0.5-33 $\mu\text{J cm}^{-2}$ for the PC₆₀BM and PC₇₀BM blend films. Transient absorption results were collected with the aid of Nathaniel Luke.

3.4 Ground State Absorbance, Fluorescence and Atomic Force Microscopy (AFM)

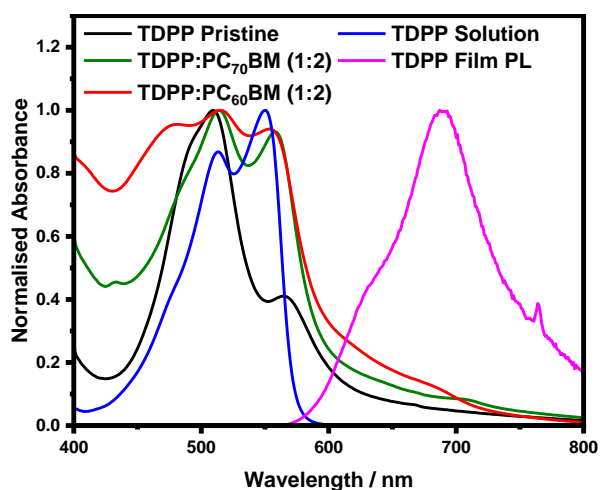


Figure 3.3 Normalised ground state absorbance spectra of a pristine TDPP film, pristine TDPP chloroform solution ($\sim 10 \mu\text{g/mL}$), TDPP:PC₆₀BM (1:2) and TDPP:PC₇₀BM blend films and normalised photoluminescence spectrum of a pristine TDPP film. Pristine TDPP film photoluminescence spectrum was collected with an excitation wavelength of 510 nm. Spectra have been normalised to their respective peak maxima.

Figure 3.3 shows the absorbance spectra for pristine TDPP thin film and its 1:2 blends (by weight) with PC₆₀BM and PC₇₀BM. A 1:2 blend ratio was chosen on the basis that other DPP-based fullerene systems obtained their highest power conversion efficiencies using this ratio.²⁰ The pristine TDPP thin film exhibits a peak maximum at 510 nm, with an additional peak found at 490 nm. A less intense peak can also be found situated at 565 nm and is assigned to the lowest vibronic 0-0 peak. The peak at 565 nm is found to increase in relative amplitude upon blending with either fullerene

acceptor. This behaviour has previously been observed in DPP polymer/fullerene blends,²¹ and has been attributed to an enhancement in film crystallinity, afforded via the high planarity exhibited by the DPP core. This enhancement in crystallinity in turn promotes π - π stacking with a concomitant increased intermolecular overlap, which manifests as an increase in the intensity of the interchain transition.²² If this hypothesis can be extended to DPP based small molecule films, this is suggestive that the presence of the fullerene imparts a degree of ordering on the TDPP molecules.

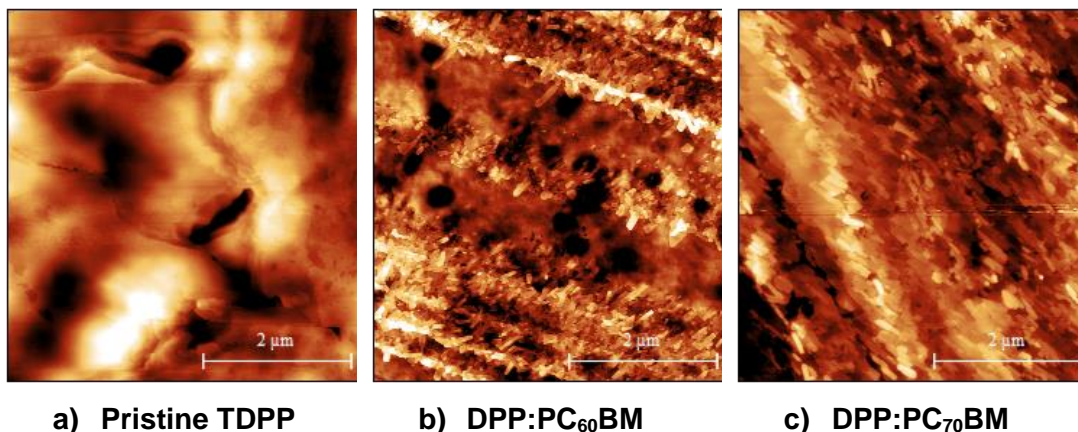


Figure 3.4 AFM images for a) pristine TDPP, b) TDPP:PC₆₀BM (1:2) and c) TDPP:PC₇₀BM films. AFM data was provided by Caroline Nowicka-Dyag. AFM images were taken with peak force tapping mode, using a ScanAsyst-Air cantilever with a nominal tip radius of 2 nm and Al coated on the back side. Images were processed in Gwyddion 2.47.

To provide further evidence that the addition of fullerenes enhanced the crystallinity of the film, atomic force microscopy (AFM) images were collected by Caroline Nowicka-Dyag and are displayed in figure 3.4. The pristine film (figure 3.4 a)) is found to exhibit an amorphous morphology, showing little evidence of order. In contrast to this, addition of either PC₆₀BM or PC₇₀BM (figure 3.4 b) and c) respectively) results in the formation of large crystallites with parallel structured domains, with the PC₇₀BM blend exhibiting larger crystal domains (~0.6 μ m in width) than that of the PC₆₀BM blend (~0.3 μ m in width). This increase in crystallisation upon blending is consistent with the increased amplitude of the 565 nm peak, which was observed in the ground state absorbance spectrum and ascribed to the presence of an interchain transition.

The pristine thin film is found to exhibit a fluorescence peak maximum at 690 nm (shown in figure 3.3), with a less intense vibronic shoulder at 635 nm. The sharp peaks at 750-760 nm is a spurious feature associated with the instrument. Using the respective fluorescence maxims (corrected for the absorbance at the exciting wavelength), quenching rates of 97 % were obtained for the 1:2 by weight

TDPP:fullerene blend films (shown in figure 3.5). This observed reduction in fluorescence is generally ascribed to quenching of the donor exciton via electron or energy transfer to the fullerene acceptor.

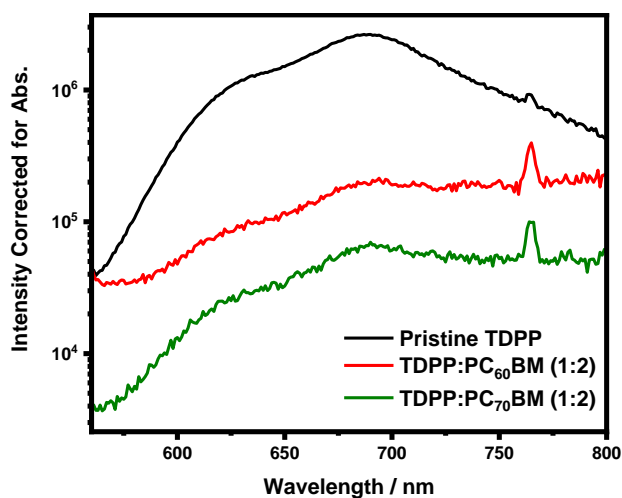


Figure 3.5 Photoluminescence spectra of a pristine TDPP thin film and TDPP:PC₆₀BM/PC₇₀BM (1:2 by weight) blend films. Spectra were obtained with an excitation wavelength of 510 nm and the data has been corrected for the absorbance at the exciting wavelength.

3.5 Picosecond Transient Absorption Spectroscopy

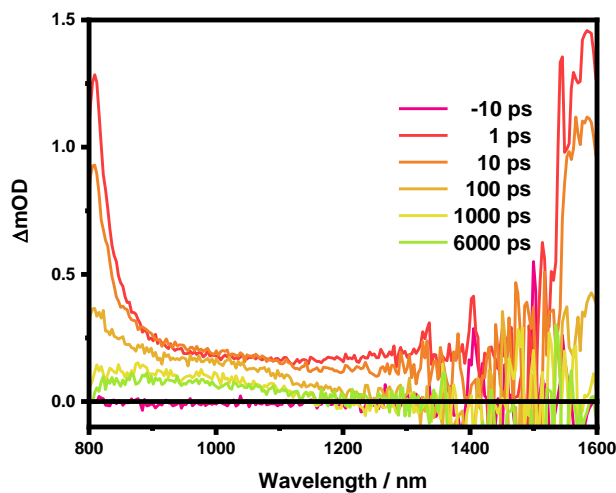


Figure 3.6 Picosecond transient absorption spectrum of a pristine TDPP thin film. The film was excited at 510 nm with an excitation density of $2.7 \mu\text{J cm}^{-2}$.

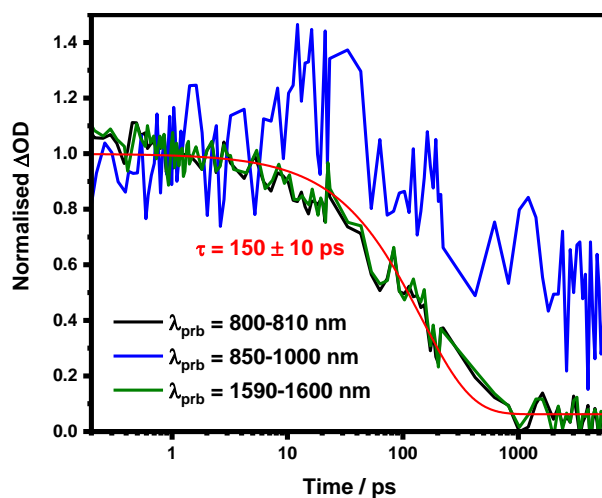


Figure 3.7 Picosecond transient absorption decay kinetics of a pristine TDPP thin film. Sample was excited with a pump wavelength 510 nm, with an excitation density of $11 \mu\text{J cm}^{-2}$. Kinetics were obtained through averaging the kinetic data in the spectral regions of 800-810 nm, 850-1000 nm and 1590-1600 nm. The red line is a monoexponential fit.

Following on from the steady state characterisation, picosecond transient absorption (ps-TA) data was collected for both the pristine TDPP and its PC₆₀BM/PC₇₀BM blend films. Figure 3.6 shows the picosecond transient absorption spectrum obtained for a pristine TDPP film when exciting at 510 nm. Two transitions from species generated on sub picosecond timescales can be seen situated at ca. 800 nm and ca. 1600 nm and dominate the early spectrum. By 1000 ps, the peaks at 800 and 1600 nm have completely decayed, revealing the presence of an additional absorption feature at 800-1100 nm that is still present at 6 ns, indicating that it is not related to either of the features found at 800 and 1600 nm. The kinetics of the transitions at 800 nm and 1600 nm were probed by averaging the decay data in the wavelength regions of 800-810 nm and 1590-1600 nm respectively. As shown in figure 3.7, the kinetics of both the transitions at 800 and 1600 nm exhibit near-identical monomolecular decay profiles, thus indicating that both transitions likely belong to a single species. As shown in figure 3.8 a) and b), both features at 800 and 1600 nm exhibit the same excitation dependence, which points to a significant bimolecular decay pathway at energies $>11 \mu\text{J cm}^{-2}$. Fitting the lowest energy kinetic decays to a monoexponential function yields the same lifetime (within error) of $\tau = 140 \pm 10$ ps and $\tau = 150 \pm 10$ ps (where the error is from fitting) for the 800 and 1600 nm transitions respectively. The sub-picosecond generation of the peaks at 800 and 1600 nm, coupled with the observed first order decay kinetics at low excitation energies and relatively short lifetime of ~ 150 ps is strongly indicative that the species responsible for these transitions is that of a singlet state ($S_1 \rightarrow S_n$). The observed loss of first order kinetics

Chapter 3

at higher excitation densities is therefore likely to derive from singlet-singlet annihilation. Furthermore, the relatively short lifetime of ~150 ps is also consistent with that of singlet excitons reported in other conjugated donor materials.^{23,24,25,26} The transition at 800 and 1600 nm are also highly unlikely to be the consequence of triplet species in a pristine organic material, which can possess lifetimes orders of magnitude greater.^{27,4} Further evidence for this singlet exciton assignment is found in previous ps-TAS studies of DPP derivatives, which also identified the presence of a singlet transition situated at 800 nm,²⁸ or the edge of it when only studying the visible region.^{29,30} As previously mentioned, a weaker broad absorption feature can be also observed at 800-1100 nm once the stronger singlet transitions at 800 and 1600 nm have sufficiently decayed. The dynamics of this feature were probed by averaging the kinetics in the region 1000-1100 nm, and show that the species obtains a maximum ΔOD at approximately 30 ps. This is in contrast to the ascribed singlet exciton, which is found generated on the sub-picosecond timescale. Extrapolating this decay (under the assumption that it remains constant) reveals that it will have completely decayed by ~500 ns, which explains its absence in the pristine TDPP μ s-TA spectrum (which will be discussed later). From the ps-TA data alone, however, it is hard to discern the identity of the species responsible for this 800-1100 nm long-lived species. Nonetheless, on the basis that the species responsible for this transition is populated on timescales much later than the singlet (which is formed on ultrafast, instrumented-limited timescales) the transition at 800-1100 nm is tentatively ascribed to the presence of short-lived triplet states, which have been generated inefficiently via direct ISC from the TDPP singlet state.

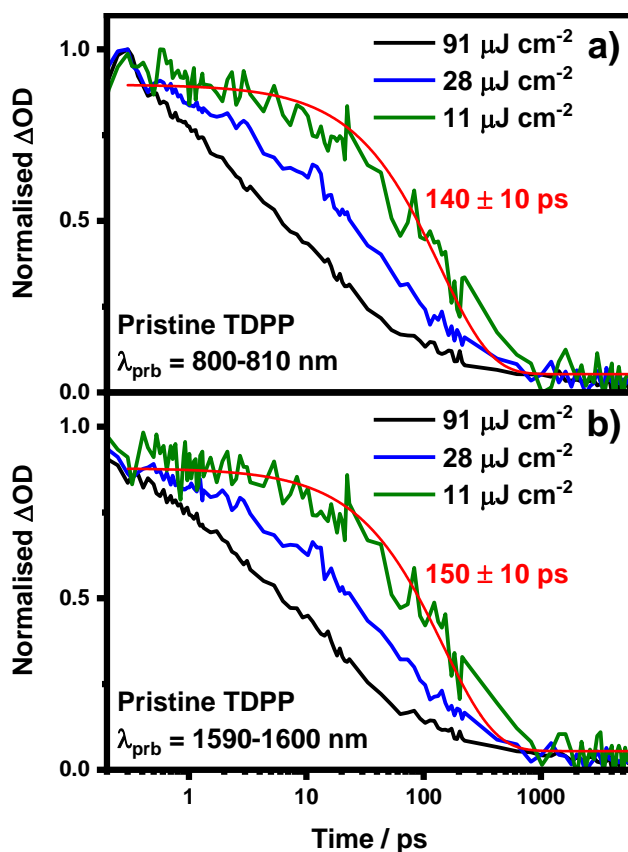


Figure 3.8 Normalised picosecond transient absorption decay kinetics of a pristine TDPP thin film. Obtained with a pump wavelength of 510 nm and at a probe wavelength (where the kinetic data has been averaged in the spectral range) of a) 800-810 nm and b) 1590-1600 nm. Both the transitions at 800-810 nm and 1590-1600 nm exhibit near-identical decays, exhibiting the same excitation dependence. Fitting the lowest energy decay of $11 \mu\text{J cm}^{-2}$ to a monoexponential function (red line) yields lifetime of $\tau = 140 \pm 10 \text{ ps}$ and $\tau = 150 \pm 10 \text{ ps}$ for the 800-810 and 1590-1600 nm transitions respectively, the same lifetime within error.

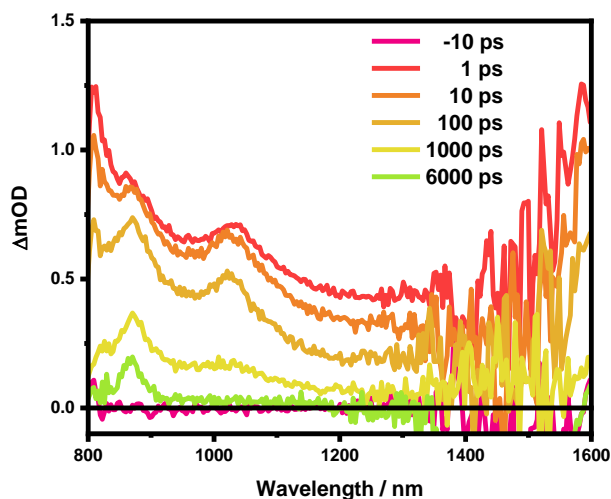


Figure 3.9 Picosecond transient absorption spectrum of a TDPP:PC₆₀BM (1:2 by weight) thin film. Sample was excited with a pump wavelength of 510 nm, with an excitation density of 2.7 $\mu\text{J cm}^{-2}$.

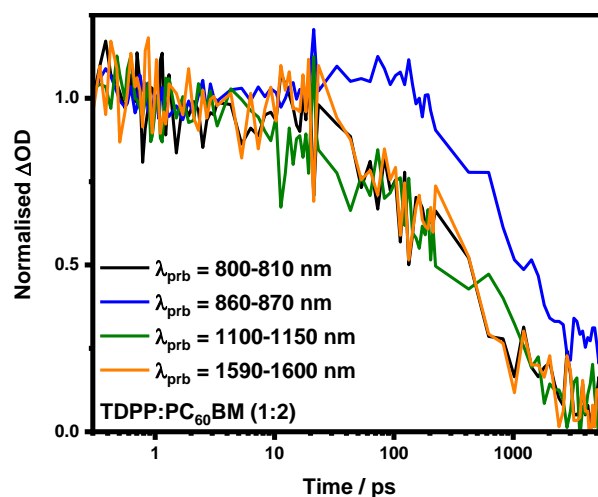


Figure 3.10 Picosecond transient absorption decay kinetics of a TDPP:PC₆₀BM (1:2 by weight) thin film. Sample was excited with a pump wavelength of 510 nm, with an excitation density of 11 $\mu\text{J cm}^{-2}$. Kinetics were obtained through averaging the kinetic data in the spectral regions of 800-810 nm, 860-870 nm, 1110-1150 nm and 1590-1600 nm.

Figure 3.9 shows the ps-TAS spectrum obtained for a TDPP:PC₆₀BM (1:2) blend film excited with 510 nm. From the spectrum, it is clear that the two singlet transitions found previously at 800 nm and 1600 nm in the pristine TDPP film are present in the blend. The kinetics of the transitions at 800 nm and 1600 nm were probed by averaging the decay data in the wavelength regions of 800-810 nm and 1590-1600 nm respectively. As shown in figure 3.10, the kinetics of both the transitions at 800 and 1600 nm exhibit near-identical monomolecular decay profiles, consistent with

what was observed for the analogous pristine TDPP transitions. Furthermore, the 800 nm transition (shown in figure 3.11 a)) is found to exhibit a similar excitation dependant behaviour that was observed in the pristine film. Fitting of the lowest energy decay ($11 \mu\text{J cm}^{-2}$) to a monoexponential function yields a lifetime of $\tau = 350 \pm 40$ ps (where the error is from fitting), which is more than double the lifetime of the pristine singlet exciton. This increase in lifetime of the 800 nm singlet exciton is not a consequence of signal contamination from the 870 nm transition, which can be demonstrated with the identical decay of the 1600 nm transition which does not overlap with the 870 nm transition. This is a counterintuitive observation, as one would expect the singlet lifetime to be reduced following quenching of the singlet exciton via electron transfer to the fullerene acceptor.

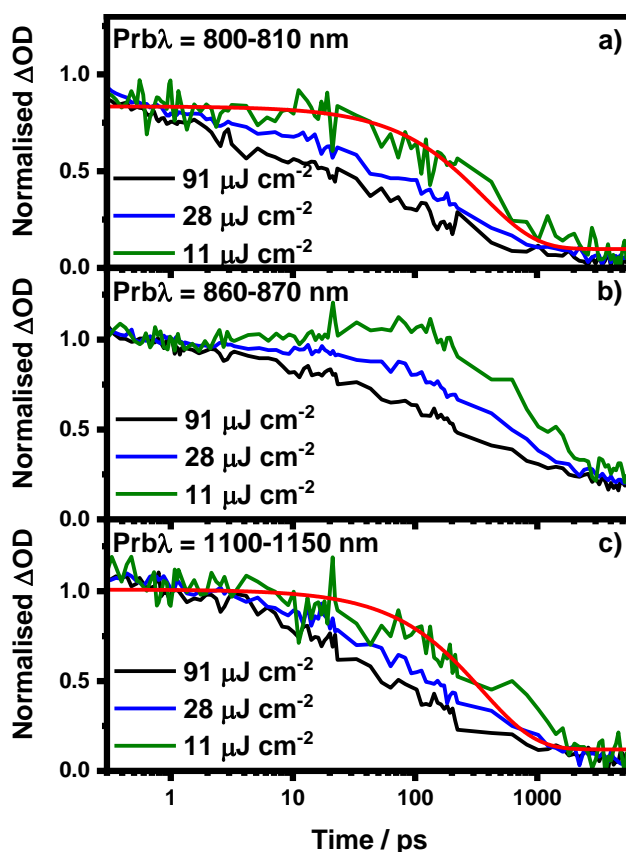


Figure 3.11 Normalised picosecond transient absorption decay kinetics of TDPP:PC₆₀BM (1:2 by weight) thin film. Obtained with a pump wavelength of 510 nm and at a probe wavelength (where the kinetic data has been averaged in the spectral range of **a**) 800-810 nm, **b**) 860-870 nm and **c**) 1100-1150 nm. The red lines are monoexponential fits.

Chapter 3

In addition to the TDPP singlet exciton transitions, two new peaks can be observed situated at 870 nm and 1030 nm and do not correspond to known fullerene singlet and triplet transitions.³¹ Although both peaks are observed at the earliest of timescales, the one located at 1030 nm has already reached its maximum amplitude on the sub-picosecond regime, whereas a clear growth can be seen in the 870 nm peak until ~50 ps (shown in figure 3.10). Interestingly, as shown in figure 3.11 b) the growth of the 870 nm peak is not observable at higher excitation densities ($>11 \mu\text{J cm}^{-2}$), which may indicate that the transient species present may be quenched via higher order processes. It is possible that the 870 nm transition observed is that of the TDPP triplet state, as it occurs in the same spectral region as the 'weak' absorption band in the pristine TDPP film, which outlives the assigned TDPP singlet state.

The peak at 1030 nm is also found to have decayed by 6 ns, whereas the one at 870 nm is still found to persist beyond this time, indicating that these transitions must derive from different species. The peak at 1030 nm is a characteristic transition of the PC₆₀BM radical anion,³² and subsequent fitting of the decay (shown in figure 3.11 c)) obtained from averaging the region 1100-1150 (so as to minimise signal contamination from the peak at 870 nm) yields a lifetime of 350 ± 40 ps. The monomolecular decay profile, in addition to the lifetime of hundreds of picoseconds, is highly indicative that recombination is occurring geminately at the interface, as opposed to recombining from free charge carriers, which typically takes place on much longer timescales.³³ It is also noted that the lifetime obtained for this 1030 nm transition is identical to that obtained for the blend's singlet exciton, which itself is much longer-lived when compared to its pristine analogue. The origin of this extended singlet lifetime may plausibly derive from repopulation of the singlet state from geminate recombination of the proposed PC₆₀BM radical anion. This recombination mechanism to yield the singlet state is typically not observed in OPV blend films but is however a prevalent feature in OLED materials, where recombination of electrically injected free charges leads to a spin-statistical 1:3 population of the singlet and triplet states.³⁴

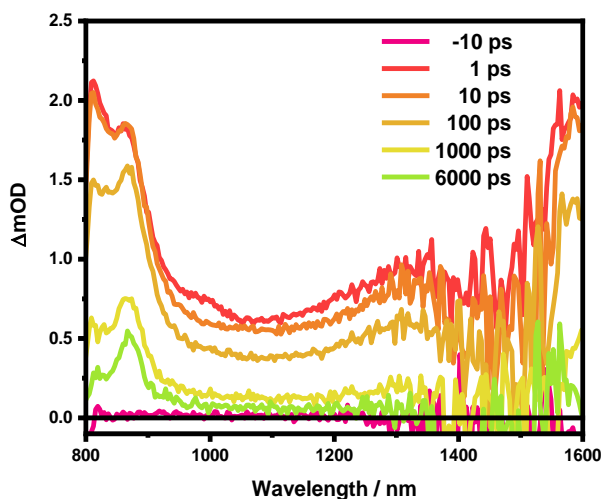


Figure 3.12 Picosecond transient absorption spectrum of a TDPP:PC₇₀BM (1:2 by weight) thin film. The film was excited at 510 nm with an excitation density of 2.7 $\mu\text{J cm}^{-2}$.

Altering the fullerene acceptor from PC₆₀BM to PC₇₀BM allows for the confirmation of previous spectral assignments. This is because the HOMO and LUMO of PC₆₀BM and PC₇₀BM differ by only ~ 0.2 eV, and as such, an analogous TDPP:PC₇₀BM blend should elicit similar photophysics to that of the previously measured PC₆₀BM blend. For example, the previously ascribed CT transition (observed at 1020 nm in the TDPP:PC₆₀BM blend) should still be present in a TDPP:PC₇₀BM ps-TA spectrum, albeit at a different, transition energy. Figure 3.12 shows the ps-TAS spectrum obtained for the TDPP:PC₇₀BM (1:2) blend film when exciting with a wavelength of 510 nm. The spectrum observed retains certain spectral features of the pristine TDPP and PC₆₀BM blend, with the TDPP singlet exciton transitions still found at 800 nm and 1600 nm, with both transitions exhibiting near identical decays (shown in figure 3.13). Once again, the singlet transition at 800 nm is shown to exhibit an excitation dependent decay (figure 3.14 a)) and fitting of the lowest energy decay (11 $\mu\text{J cm}^{-2}$) to a monoexponential function yields a lifetime of $\tau = 520 \pm 30$ ps (where the error is from fitting). This singlet state lifetime is found to be increased when compared to the pristine TDPP film, which is consistent with the same observation in the analogous TDPP:PC₆₀BM blend.

Furthermore, the unidentified transition at 870 nm is still found to be present. Interestingly, the peak seen at 1030 nm is now found to be absent and in its place a transition at ca. 1320 nm is observed. This transition at 1320 nm correlates well with literature values for the PC₇₀BM radical anion.^{35,36} The PC₇₀BM radical anion kinetics were probed (shown in figure 3.14 c)) by averaging the region 1250-1300 nm, and could be fit with a monoexponential decay to yield a lifetime of $\tau = 500 \pm 30$ ps. This

recombination lifetime is longer than that observed for the PC₆₀BM radical anion ($\tau = \sim 350$ ps), which may be a consequence of the slightly different morphological environments, as shown in the AFM. Like that of the previous PC₆₀BM blend, the relatively short lifetime in conjunction with the first order decay kinetics is suggestive of a recombination pathway that is geminate in nature. Furthermore, the lifetime of the PC₇₀BM radical anion is also found to be identical within error to that of the singlet exciton, consistent with the same behaviour for the corresponding TDPP:PC₆₀BM singlet.

The peak observed at 870 nm was found to exhibit no spectral shift when altering the fullerene in the blend film, thus indicating that the species responsible for the transition is derived from the TDPP donor. The species responsible for the peak at 870 nm is therefore likely to be either the TDPP triplet or TDPP radical cation (as the TDPP is the electron donor). If the transition at 870 nm belonged to the TDPP radical cation, one would expect it to possess identical kinetics to the ascribed fullerene radical anion if they were decaying geminately. This is because as discussed in section 1.7.1, geminate recombination implies that both the original positive and negative species must recombine with one another.

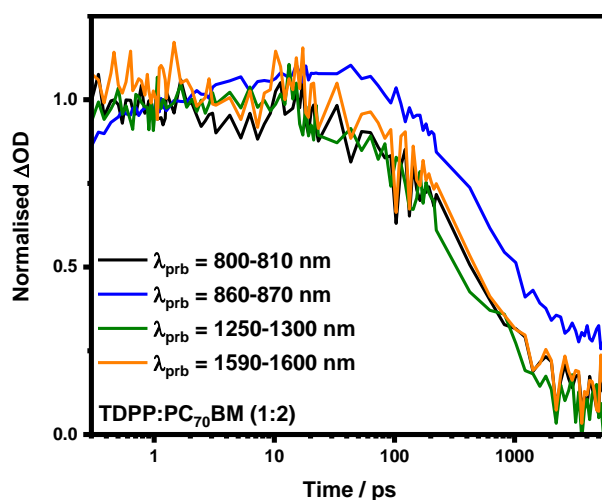


Figure 3.13 Picosecond transient absorption decay kinetics of a TDPP:PC₇₀BM (1:2 by weight) thin film. The film was excited at 510 nm with an excitation density of $11 \mu\text{J cm}^{-2}$. Kinetics were obtained through averaging in the wavelength regions 860-870 nm and 1250-1300 nm. The red line is a monoexponential fit.

The decay kinetics of the 870 nm transition (shown in figure 3.13) show a clear growth in the population until ~ 50 ps, similar to what was observed for the same transition in the PC₆₀BM blend. Furthermore, the 870 nm transition is found to exhibit an excitation dependant decay (figure 3.14 b)), with the growth of the species becoming less

prominent with increasing excitation density, the same behaviour as what was observed for the analogous PC₆₀BM blend. Although the decay at 1320 nm also appears to be sensitive to the excitation energy employed, it clearly exhibits substantially different kinetic behaviour when compared to the transition at 870 nm. This is best illustrated in figure 3.13, where a comparison between the normalised decay kinetics of the 870 and 1320 nm transitions illustrates that the PC₇₀BM radical anion is fully populated on an instrument limited timescale, whereas the 870 nm species only reaches its maximum amplitude on the tens of picosecond timescale. This points to the 870 nm not deriving from that of the TDPP radical cation, but rather the TDPP triplet state and as such the observed excitation dependence is likely attributable to the presence of triplet-triplet annihilation. It is noted, however, that small molecule DPP exhibits a radical cation transition at 750 nm when in toluene solution, spectrally close to the observed 870 nm transition. As such, assignment to the DPP radical cation cannot be completely ruled out on the basis of the ps decay kinetics presented here.³⁷

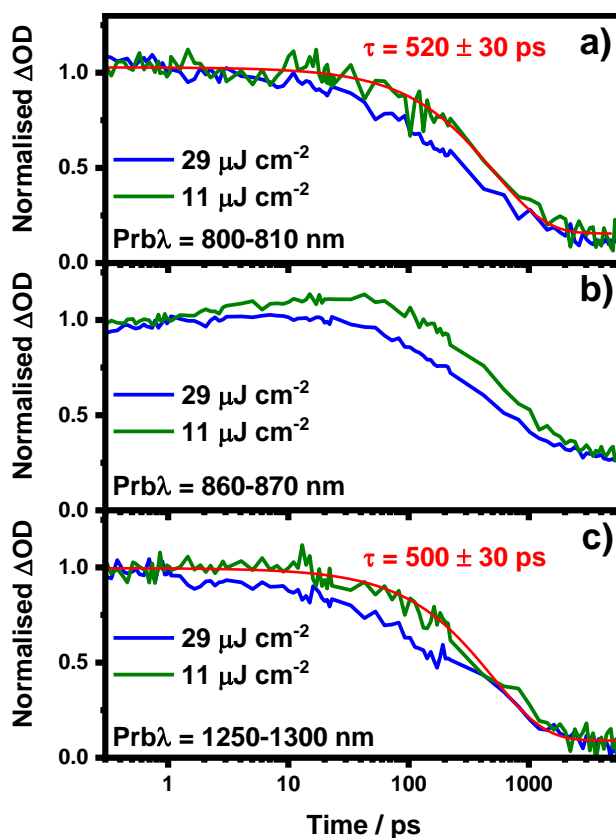


Figure 3.14 Normalised picosecond transient absorption decay kinetics of TDPP:PC₇₀BM (1:2 by weight) thin film. Obtained with a pump wavelength of 510 nm and at a probe wavelength (where the kinetic data has been averaged in the spectral range) of **a)** 800-810 nm, **b)** 860-870 nm and **c)** 1250-1150 nm.

Chapter 3

Continuing on the basis that the 870 nm band does indeed derive from that of the TDPP triplet state, allows for several important conclusions to be made. It is clear from the ps-TA data that the TDPP triplet is significantly more prevalent in the blend film when compared to the pristine TDPP film, and moreover, the triplet in the blend films appears more longer-lived than the corresponding pristine TDPP triplet. This observation is suggestive that triplet formation is enhanced via the addition of the fullerene acceptor, which in and of itself, should not lead to an increased rate of ISC from the donor TDPP singlet state. A plausible alternative explanation is that the initial TDPP singlet state is quenched via an electron transfer reaction on ultrafast timescales, yielding the TDPP/fullerene CT state. This CT state then undergoes spin mixing, resulting in the triplet CT state (i.e. $^1\text{CT} \rightarrow ^3\text{CT}$). This triplet CT state then undergoes geminate recombination to generate the TDPP triplet state, which is the lowest energy state of the system. The observed fullerene anion transitions at 1020 and 1320 nm, can therefore be attributed to the bound CT state as opposed to free fullerene anions, since the growth in the TDPP triplet population is found to concurrently follow the decay of the fullerene anion. Further evidence for this CT spin-mixing hypothesis is provided by the rise in the TDPP state population from the earliest measurable (ultrafast) timescales, until the maximum ΔOD is obtained on the tens of picoseconds, which is in stark contrast to direct ISC which is usually a much slower process that takes place on the $>\text{ns}$ regime. As such, the invoking of a direct ISC crossing mechanism cannot explain the rapid formation of the triplet species. The plausibility of the proposed CT spin-mixing mechanism is supported by numerous reports in the literature regarding the existence of DPP:fullerene CT states.^{38,39,40,41} Importantly, the proposed CT spin-mixing, followed by back recombination to yield the donor/acceptor triplet species, is now a well-established microscopic phenomena in organic solar cell blends.^{23,42}

3.6 Microsecond Transient Absorption Spectroscopy

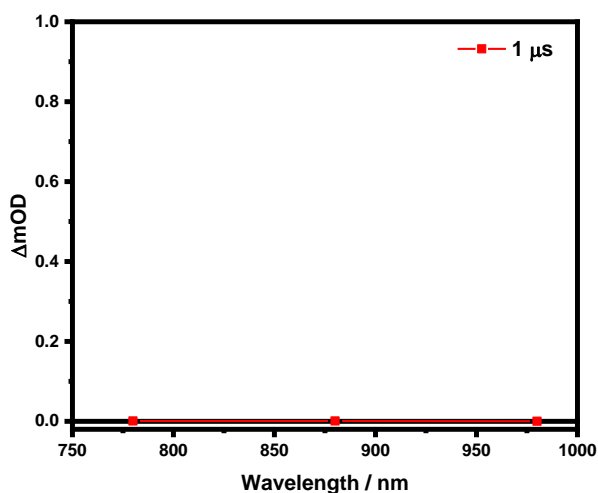


Figure 3.15 Microsecond transient absorption spectrum of a pristine TDPP thin film. The film was excited at 500 nm with an excitation density of $128 \mu\text{J cm}^{-2}$. No spectral response is observed, illustrating that no long-lived species (triplets or polarons) are generated.

A μs -TAS investigation was carried out to help provide further evidence that the observed peak at 870 nm belonged to that of a triplet state transition ($T_1 \rightarrow T_n$). This is because the long-lived triplet state should still be evident on the longest timescales, long after the ascribed TDPP singlet and PCBM radical anion have decayed.

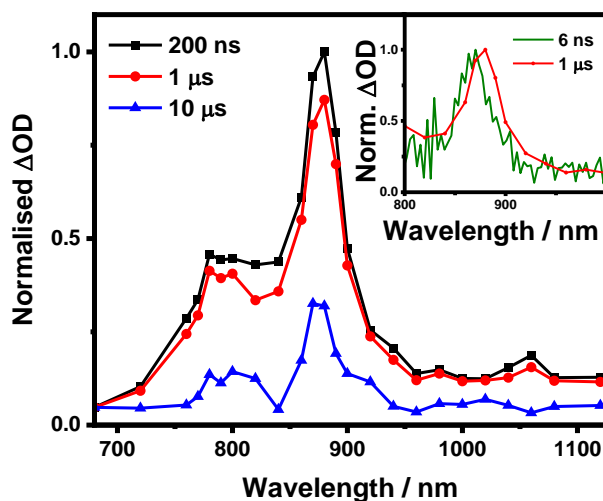


Figure 3.16 Normalised microsecond transient absorption spectrum of a TDPP:PC₆₀BM (1:2 by weight) thin film. The film was excited at 500 nm with an excitation density of $36 \mu\text{J cm}^{-2}$. Inset: Normalised ps-TA and μs -TA spectra of TDPP:PC₆₀BM (1:2 by weight) thin film. Films have been normalised to their respective peak maxima at times of 6 ns and 1 μs respectively.

Excitation of the pristine TDPP resulted in no detectable signal on the timescales of this experiment ($\sim 1 - 360 \mu\text{s}$), as shown in figure 3.15. This suggests that no triplet or polarons are formed in the pristine thin film, or that their lifetimes are too short to be detected on the μs -TA setup. This is in agreement with the lack of long-lived features in the respective pristine TDPP film ps-TA spectrum. In contrast to the pristine film, the TDPP:PC₆₀BM (1:2) blend exhibits a large spectral response when pumped with the same excitation wavelength (shown in figure 3.16). A strong narrow transition can be seen situated at 880 nm, with a second weaker transition observed at 780 nm. This 880 nm transition is unlikely to derive from either the PC₆₀BM triplet or radical anion, as their respective spectral shapes and positions are well established, exhibiting transitions at 720 and 1020 nm respectively.^{43,44} Interestingly, the peak at 880 nm bears a spectral similarity to the tentatively ascribed TDPP triplet transition seen at 870 nm in the ps-TAS. This similarity is exemplified in the inset of figure 16, which displays the normalised TA spectra obtained at 6 ns and 1 μs . The main difference between the two spectra, is that of a 10 nm (0.017 eV) red shift for the maximum peak and may be attributed to energetic relaxation of the triplet state, but it is also plausible that the peak shift is a consequence of calibration error. The transition observed at 780 nm decays at the same rate as the 880 nm transition. Furthermore, a peak energy difference of 1460 cm^{-1} is found, and as such, the weaker transition at 780 nm is likely to originate from a higher vibrational excitation of the 880 nm TDPP triplet transition.

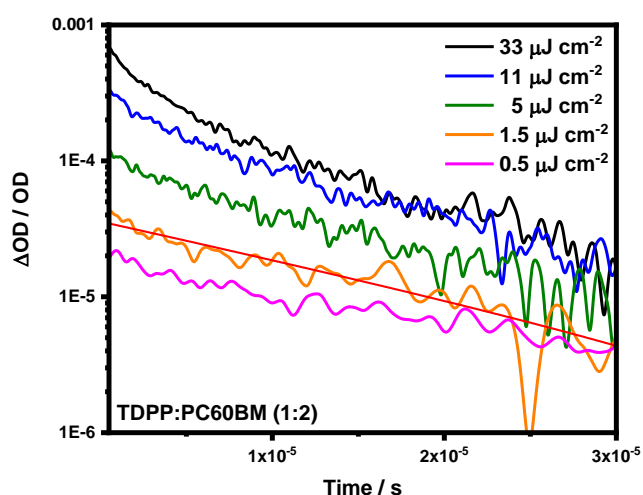


Figure 3.17 Microsecond transient absorption kinetics of a TDPP:PC₆₀BM 1:2 by weight film. Obtained with a pump wavelength of 510 nm and a probe wavelength of 875 nm. The red line is a monoexponential fit of the type $y_0 + A_1 \cdot \exp(-t/\tau)$.

The kinetics of the tentatively assigned TDPP triplet state were examined via probing the peak at 880 nm (as shown in figure 3.17). The kinetics obtained were found to exhibit an intensity dependant decay at energies $> 9 \mu\text{J cm}^{-2}$. At the lowest excitation densities measured ($\sim 9 \mu\text{J cm}^{-2}$), a first order decay is observed, and fitting a monoexponential decay to the data, yielded a lifetime of $\tau = 14 \pm 1 \mu\text{s}$ (where the error is from fitting). Such first order decay behaviour is typical of triplet decay or charge carrier geminate recombination (as discussed in section 2.9). Assignment of this decay to a TDPP triplet state, however, seems more plausible than that of the TDPP radical cation (as also discussed for the ps-TA data), given that geminate recombination in both polymer and small molecule fullerene blends typically does not persist beyond $\sim 1 \mu\text{s}$.^{45,46,47} The observed second-order behaviour at higher excitation densities is therefore likely attributed to the presence of triplet-triplet annihilation. It is noted that no long-lived polaron species are observed, which typically manifest as a power-law decay, thus providing further evidence that the fullerene radical anion observed in the ps-TA spectra decayed geminately. This is suggestive that geminate recombination is a major loss mechanism in this system.

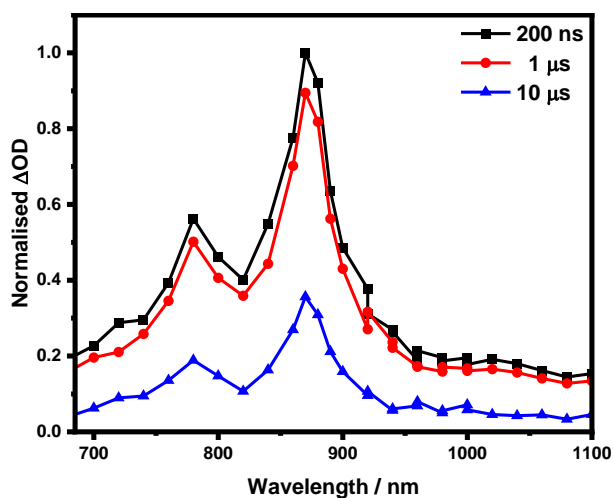


Figure 3.18 Microsecond transient absorption spectrum of a TDPP:PC₇₀BM (1:2 by weight) thin film. The film was excited at 510 nm with an excitation density of $36 \mu\text{J cm}^{-2}$.

Figure 3.18 shows the μs -TAS spectrum of TDPP:PC₇₀BM (1:2) blend. The spectrum observed is near identical to that of the one obtained for the PC₆₀BM blend. This is further evidence that the transient species responsible for the peaks at 880 nm and 780 nm are derived from the TDPP, as the spectrum does not change when altering the fullerene acceptor. If the transient species did derive from a fullerene, it would be expected that the spectrum would exhibit a red-shift upon changing the acceptor in the blend. This is because literature studies have shown that both the PC₇₀BM triplet

and radical anions are distinctively red-shifted relative to their PC₆₀BM counterparts.^{31,36} The TDPP:PC₇₀BM blend, like that of its PC₆₀BM analogue exhibits a first order decay at low excitation densities (shown in figure 3.19). Fitting a monoexponential to the decay obtained by probing at 880 nm (5.5 $\mu\text{J cm}^{-2}$) yields a lifetime of $20 \pm 1 \mu\text{s}$, slightly longer than the one obtained for the PC₆₀BM blend. Once again, the observed spectrum can be assigned to that of the TDPP triplet. Further evidence of this correct assignment is provided by a study by Karsten et al,³⁰ in which a fullerene-DPP-fullerene triad solution (o-DCB) was used to sensitise the formation of the TDPP triplet. The photoinduced transient absorption spectra obtained for the TDPP triplet, indicated transitions at 775 nm and 860 nm, correlating well with the 780 and 880 nm transitions observed in the TDPP blend films. It is noted, however, that the DPP possessed a slightly different molecular structure and was in the solution phase, but nonetheless the correlation is apparent.

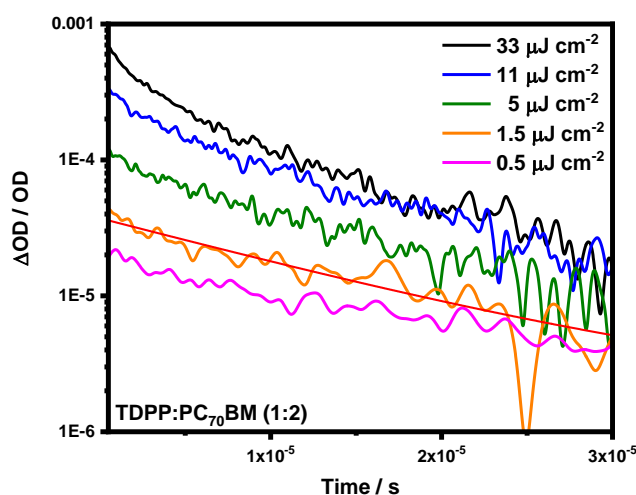


Figure 3.19 Microsecond transient absorption kinetics of a TDPP:PC₇₀BM 1:2 by weight film. Obtained with a pump wavelength of 510 nm and a probe wavelength of 880 nm. The red line is a monoexponential fit of the type $y_0 + A_1 \cdot \exp(-t/\tau)$.

To help confirm that the 880 nm peak belonged to that of the TDPP triplet, the decay kinetics of both blend films were also measured under a pure oxygen atmosphere. As stated in section 2.9, the presence of ground state oxygen should selectively quench excited triplets to the ground state, manifesting as a reduction in both triplet lifetime and signal amplitude (ΔOD). As is shown in figure 3.20 a) and b), no quenching is observed suggesting that either the 880 nm peak belongs to that of the TDPP radical cation, or that the triplet energy level of TDPP is lower than the 0.98 eV threshold required for oxygen quenching to take place. Previous studies have conjectured that DPP-based polymers have a very low-lying T₁ state,^{13,4} with the consequence of it

possibly residing below the 0.98 eV quenching limit. This might account for the perceived lack of triplet quenching.

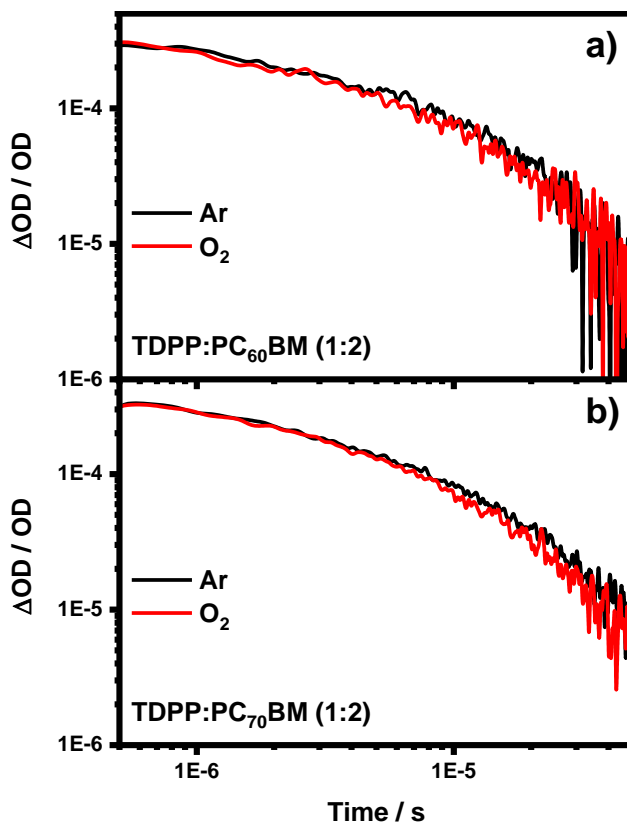


Figure 3.20 Microsecond transient absorption kinetics of **a)** TDPP:PC₆₀BM 1:2 by weight film and **b)** TDPP:PC₇₀BM 1:2 by weight film. Obtained with a pump wavelength of 510 nm, a probe wavelength of 875 nm and an excitation density of $11 \mu\text{J cm}^{-2}$. The measurement was carried out in both Ar and O₂ atmospheres, illustrating an O₂ independent decay for both blend films.

From the results attained thus far, it is likely that the long-lived transient observed in both blend films is either that of the TDPP triplet, as opposed to the radical cation. The μs lifetime, paired with the first-order decay kinetics and spectral correlation with literature, is highly indicative of a triplet state. If the transient generated is indeed the TDPP triplet state this also raises a question as to its formation, due to it not being generated in significant quantities in the pristine thin film spectra. This implies that a simple direct intersystem crossing (ISC) mechanism does not contribute measurably, and that TDPP triplet formation must predominantly be the result of addition of the fullerene. This would seem to indicate that the TDPP triplet generated is mediated via CT state spin mixing, followed by back transfer, as suggested in the ps-TAS results. In lieu of the ability to quench the observed signal with oxygen, time-resolved electron

paramagnetic resonance (TR-EPR) was carried out to help confirm the proposed mechanism.

3.7 Time-resolved electron paramagnetic resonance spectroscopy (TR-EPR)

TR-EPR was carried out by Dr Enrico Salvadori at UCL and a description of his findings are included in this thesis for completion. TR-EPR was performed on thin films of pristine TDPP and TDPP:PC₇₀BM (1:2) and on a toluene solution of PC₇₀BM (100 μ M), with spectra shown in figure 3.21. The pristine TDPP exhibited no signal response on the timescales of the experiment, thus indicating that ISC was inefficient and that no photoinduced radicals were formed, which is consistent with the TAS results. In contrast to this, the neat PC₇₀BM solution exhibited a signal that was characteristic of a triplet formed via ISC and decaying within 2 μ s. The signal obtained yields an electron spin polarisation pattern of AAEE (where E is emission and A is enhanced absorption) and can be simulated with zero field splitting (ZFS) parameters $|D| = 337$ MHz and $E = 0$ MHz and zero-field relative populations $P_x:P_y:P_z = 0 : 1 : 1$, consistent with previously reported data for C₇₀ monoadducts.⁴⁸

Excitation of the TDPP:PC₇₀BM (1:2 by weight) blend film yields a significantly more complicated EPR signal relative to the neat PC₇₀BM control. At early time scales (400-600 ns after excitation) the EPR signal of the blend contains contributions from two components. The first component is that of PC₇₀BM triplet states, populated via ISC, and this is evident when comparing the signal with the PC₇₀BM control. Based on the zero field ZFS and electron spin polarisation pattern respectively, the second broader component can be ascribed to that of a TDPP triplet formation via radical pair recombination in high magnetic field. The TDPP triplet signal becomes more pronounced after ~ 2 μ s, once the PC₇₀BM triplet has sufficiently decayed. The TR-EPR spectrum at later times (1800-2800 ns) presents an electron spin polarisation pattern of AEEAAE, which is characteristic hallmark of selective population of the T₀ sublevel (S-T₀ mixing) by recombination in the singlet-born weakly coupled radical pair at all orientations due to conservation of the spin angular momentum in the recombination process. The polarization pattern is indicative of a positive ZFS parameter D, which from simulation can be estimated to be $D = +1550$ MHz, together with $|E| = 340$ MHz. The EPR results are therefore entirely consistent with the proposed mechanism involving a TDPP:PC₆₀BM charge transfer state that undergoes ultrafast spin-mixing and recombination to yield the TDPP triplet state.

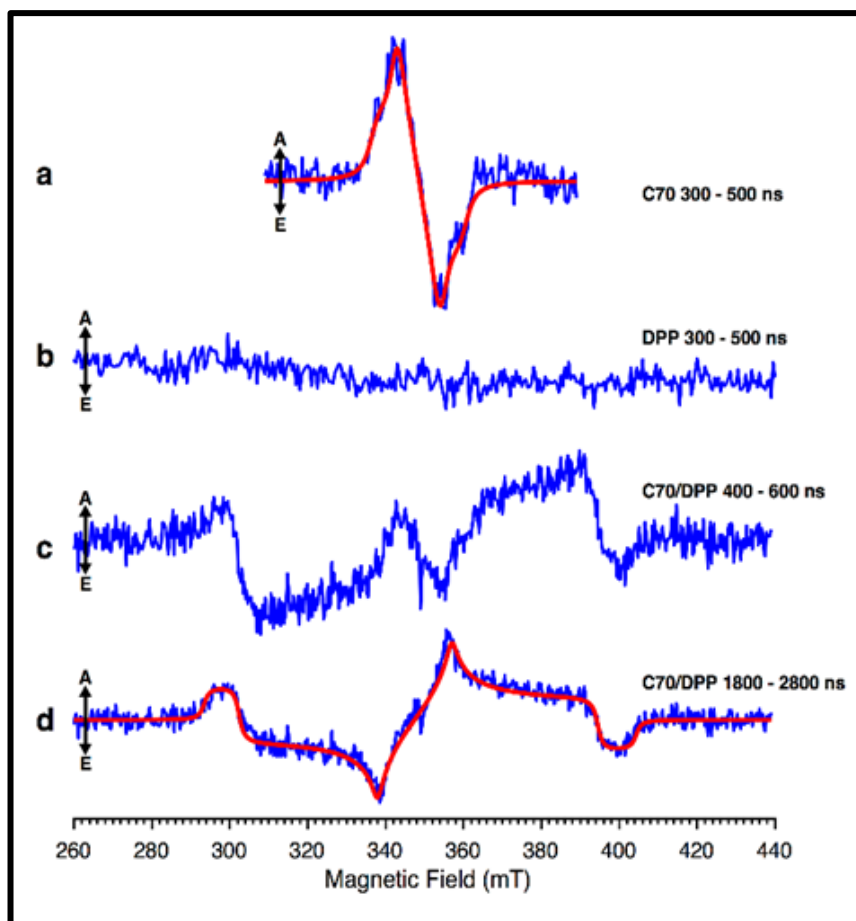


Figure 3.21 a) 50 K TR-EPR spectrum of $PC_{70}BM$ (blue line) in toluene solution recorded after 300-500 ns after excitation. The $PC_{70}BM$ spectrum can be simulated with ZFS parameters $D = 337$ MHz, $|E| = 0$ and relative populations $P_x:P_y:P_z = 0:1:1$ (red line). **b)** 50 K TR-EPR spectrum of a pristine TDPP film recorded after 300-500 ns after excitation. **c)** 50 K TR-EPR spectrum for the TDPP: $PC_{70}BM$ 1:2 blend film at early times (300-500 ns after excitation), where two contributions are distinguishable: a broad triplet and a narrower feature reminiscent of the $PC_{70}BM$ triplet. **d)** 50 K TR-EPR spectrum for the TDPP: $PC_{70}BM$ 1:2 blend film at later times (1800-2800 after excitation): only the recombination triplet on TDPP is visible. The TDPP: $PC_{70}BM$ spectrum can be simulated with ZFS parameters $D = +1550$ MHz, $|E| = 340$ MHz and assuming that only the T_0 sublevel. Data was collected by Dr Enrico Salvidori.

3.8 Discussion

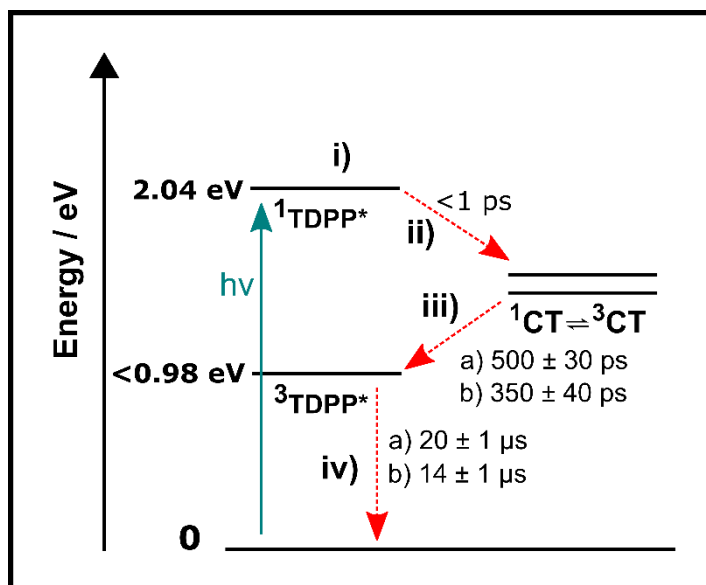


Figure 3.22 State diagram for the proposed model of TDDP triplet generation in TDPP:fullerene film. For the lifetimes given a) is for the blend containing PC₆₀BM and b) for PC₇₀BM.

The proposed mechanism for the population of the TDPP triplet state by back recombination (in a TDPP fullerene blend film) is presented in figure 3.22. Initial excitation of the TDPP generates a singlet exciton (i), which is subsequently transferred to the PC₆₀BM/PC₇₀BM acceptor to generate a charge transfer (CT) state possessing singlet character (ii). The resulting singlet CT state is then able to undergo facile intersystem crossing to the triplet manifold. This ³CT* then undergoes geminate recombination (iii) to form the ³TDPP*, which is then free to undergo radiative and non-radiative recombination (iv) back to the ground state.

Interestingly, the growth of the TDPP triplet state in the blend films is found to occur on the picosecond time scale, attaining a maximum population at 30-40 ps. This is in stark contrast to other blend systems, such as SiIDT-2FBT.PC₇₀BM, which exhibits spin-mixing on the early nanosecond timescale.²³ This disparity in triplet population times is unlikely to derive from greater spin-orbit coupling (SOC), which is suggested to play little role in CT state intersystem crossing. This is because SOC is a short-range interaction, requiring the electron to ‘see’ the positive nucleus in order to induce transitions between different spin states (see chapter 1.8.2). It has been suggested that intersystem crossing in CT states derives from hyperfine interactions (HFI),⁴⁹ which is the interaction between the polaron electron spins and the surrounding nuclear spin (electron spin-nuclear spin hyperfine interaction). The HFI is distance independent, unlike that of SOC, but possesses a much weaker interaction on the

Chapter 3

order of 10^{-7} eV (for comparison light atoms such as H,C, O, N and F elicit SOC interactions on the order of 10^{-4} - 10^{-3} eV). This therefore requires the spin states to be near isoenergetic to allow for spin-mixing. CT spin states have been suggested to be near degenerate in energy, satisfying the energetic requirements of HFI.⁵⁰ This is a consequence of an exponential dependence of the exchange energy (which determines $\Delta S-T$) on the orbital overlap between the electron and hole, where bound CT states are able to delocalise within their coulombic attraction field minimising the exchange energy as they move further apart. This mechanism implies that the TDPP:fullerene CT state is strongly separated.⁵¹ Another possible mechanism that induces efficient ISC in the CT state is via coupling to a close lying triplet level of the donor or acceptor,^{52,53} which allows for efficiency spin-flipping due to a change in orbital angular momentum.

Triplet formation in the pristine film was not observed in both the TAS and EPR results, suggesting that singlet fission is not operative in this material. This is in spite of the apparent energetic feasibility (i.e. $E_{S1} > 2T_1$). An important consideration to take into account, however, is that the TDPP studied here possesses a different side chain to the one reported to undergo singlet fission. This would seem to indicate that side chain sterics may play a significant role in the electronic coupling necessary for singlet fission in small molecules.⁵⁴

The appearance of the TDPP triplet after photoexcitation in in the TDPP:fullerene blend films is highly indicative that it is the lowest lying excited state in the system (i.e. below that of the spin-mixing CT state). Indeed, the absence of O_2 induced signal quenching infers that the TDPP triplet energy level is around or below 0.98 eV. This observation lends credence to previous conjecture that DPP-based polymers may possess energetically low lying triplet states.^{4,55} Although spin-mixing appears to be an ubiquitous feature of donor:fullerene systems, they do not necessarily constitute a loss mechanism, provided there are no triplet states lower in energy. These results presented here, therefore have important ramifications in regard to molecular design, as the formation of low-lying triplet states must be avoided to eliminate a significant loss mechanism. Regardless of this, the direct observation of a small molecule/fullerene CT state via the participating fullerene anion is very rare, which affords the possibility to further study this elusive excited state in greater detail in the future.

3.9 Conclusion

In this investigation, a small molecule DPP derivative, TDPP, was blended with both PC₆₀BM and PC₇₀BM to create bulk heterojunction thin films. This was for the purpose of establishing reference photophysical data for study into more complex DPP derivatives. A combination of transient absorption and transient electron paramagnetic resonance spectroscopy was used to help elucidate the photophysics of both pristine TDPP and its blends. It was observed that upon excitation of a pristine TDPP film only the singlet exciton was generated in sufficient yield. Upon blending with either PC₆₀BM/PC₇₀BM, however, much richer photophysics were observed. In addition to the TDPP singlet, a fullerene CT state was directly observed and found to be generated on ultrafast time scales, shorter than the instrument resolution (<200 fs). This CT state was found to undergo unusually fast spin mixing, with subsequent geminate recombination to yield the TDPP triplet state. The direct spectroscopic observation of a small molecule/fullerene CT state via the participating fullerene anion is also of relevance to the field, as it provides a model system for further studies into a rarely observed excited state.

3.10 Bibliography

1. W. Li, K. H. Hendriks, M. M. Wienk and A. J. Janssen, *Acc. Chem. Res.*, 2016, **49**, 78-85.
2. E. C. Fregoso, PhD Thesis, Imperial College London, 2015.
3. M. Kaur and D. H. Choi, *Chem. Soc. Rev.*, 2015, **44**, 58–77.
4. Y. W. Soon, H. Cho, J. Low, H. Bronstein, I. McCulloch and J. R. Durrant, *Chem. Commun.*, 2013, **49**, 1291.
5. W. Li, K. H. Hendriks, M. M. Wienk and R. A. J. Janssen, *Acc. Chem. Res.*, 2016, **49**, 78–85.
6. H. Choi, S.-J. Ko, T. Kim, P.-O. Morin, B. Walker, B. H. Lee, M. Leclerc, J. Y. Kim and A. J. Heeger, *Adv. Mater.*, 2015, **27**, 3318–3324.
7. Y. Kan, C. Liu, L. Zhang, K. Gao, F. Liu, J. Chen and Y. Cao, *J. Mater. Chem. A*, 2016, **4**, 14720–14728.
8. X. Song, N. Gasparini, M. M. Nahid, S. H. K. Paleti, C. Li, W. Li, H. Ade and D. Baran, *Adv. Funct. Mater.*, 2019, **29**, 1902441.
9. L. Dou, J. You, J. Yang, C.-C. Chen, Y. He, S. Murase, T. Moriarty, K. Emery,

Chapter 3

- G. Li and Y. Yang, *Nat. Photonics*, 2012, **6**, 180–185.
- 10 Q. Liu, Y. Jiang, K. Jin, J. Qin, J. Xu, W. Li, J. Xiong, J. Liu, Z. Xiao, K. Sun, S. Yang, X. Zhang and L. Ding, *Sci. Bull.*, 2020, **65**, 272–275.
- 11 Y. Lin, B. Adilbekova, Y. Firdaus, E. Yengel, H. Faber, M. Sajjad, X. Zheng, E. Yarali, A. Seitkhan, O. M. Bakr, A. El-Labban, U. Schwingenschlögl, V. Tung, I. McCulloch, F. Laquai and T. D. Anthopoulos, *Adv. Mater.*, 2019, **31**, 1902965.
- 12 Y. Cui, H. Yao, J. Zhang, T. Zhang, Y. Wang, L. Hong, K. Xian, B. Xu, S. Zhang, J. Peng, Z. Wei, F. Gao and J. Hou, *Nat. Commun.*, 2019, **10**, 2515.
- 13 P. E. Hartnett, E. A. Margulies, C. M. Mauck, S. A. Miller, Y. Wu, Y.-L. Wu, T. J. Marks and M. R. Wasielewski, *J. Phys. Chem. B*, 2016, **120**, 1357–1366.
- 14 A. M. Levine, C. Schierl, B. S. Basel, M. Ahmed, B. A. Camargo, D. M. Guldi and A. B. Braunschweig, *J. Phys. Chem. C*, 2019, **123**, 1587–1595.
- 15 M. C. Hanna and A. J. Nozik, *J. Appl. Phys.*, 2006, **100**, 074510.
- 16 M. B. Smith and J. Michl, *Chem. Rev.*, 2010, **110**, 6891–6936.
- 17 V. K. Thorsmølle, R. D. Averitt, J. Demsar, D. L. Smith, S. Tretiak, R. L. Martin, X. Chi, B. K. Crone, A. P. Ramirez and A. J. Taylor, *Phys. Rev. Lett.*, 2009, **102**, 017401.
- 18 P. M. Zimmerman, F. Bell, D. Casanova and M. Head-Gordon, *J. Am. Chem. Soc.*, 2011, **133**, 19944–19952.
- 19 C.-W. Ge, C.-Y. Mei, J. Ling, F.-G. Zhao, H.-J. Li, L. Liang, J.-T. Wang, J.-C. Yu, W. Shao, Y.-S. Xie and W.-S. Li, *J. Polym. Sci. Part A Polym. Chem.*, 2014, **52**, 2356–2366.
- 20 R. S. Ashraf, I. Meager, M. Nikolka, M. Kirkus, M. Planells, B. C. Schroeder, S. Holliday, M. Hurhangee, C. B. Nielsen, H. Sirringhaus and I. McCulloch, *J. Am. Chem. Soc.*, 2015, **137**, 1314–1321.
- 21 E. Collado-Fregoso, F. Deledalle, H. Utzat, P. S. Tuladhar, S. D. Dimitrov, A. Gillett, C.-H. Tan, W. Zhang, I. McCulloch and J. R. Durrant, *Adv. Funct. Mater.*, 2017, **27**, 1604426.
- 22 C. Kästner, D. A. M. Egbe and H. Hoppe, *J. Mater. Chem. A*, 2015, **3**, 395–403.

Chapter 3

- 23 S. D. Dimitrov, S. Wheeler, D. Niedzialek, B. C. Schroeder, H. Utzat, J. M. Frost, J. Yao, A. Gillett, P. S. Tuladhar, I. McCulloch, J. Nelson and J. R. Durrant, *Nat. Commun.*, 2015, **6**, 6501.
- 24 H. Ohkita, J. Kosaka, J. Guo, h. Benten and S. Ito, *J. Photonics Energy*, 2011, **1**, 011118.
- 25 S. Yamamoto, H. Ohkita, H. Benten and S. Ito, *J. Phys. Chem. C*, 2012, **116**, 14804–14810.
- 26 A. A. Paraecattil, S. Beaupré, M. Leclerc, J.-E. Moser and N. Banerji, *J. Phys. Chem. Lett.*, 2012, **3**, 2952–2958.
- 27 A. Köhler and H. Bässler, *Mater. Sci. Eng. R Reports*, 2009, **66**, 71–109.
- 28 H. Liu, H. Jia, L. Wang, Y. Wu, C. Zhan, H. Fu and J. Yao, *Phys. Chem. Chem. Phys.*, 2012, **14**, 14262.
- 29 N. Banerji, M. Wang, J. Fan, E. S. Chesnut, F. Wudl and J.-E. Moser, *J. Mater. Chem.*, 2012, **22**, 13286.
- 30 B. P. Karsten, R. K. M. Bouwer, J. C. Hummelen, R. M. Williams and R. A. J. Janssen, *Photochem. Photobiol. Sci.*, 2010, **9**, 1055–1065.
- 31 P. C. Y. Chow, S. Albert-Seifried, S. Gélinas and R. H. Friend, *Adv. Mater.*, 2014, **26**, 4851–4854.
- 32 H. Ohkita and S. Ito, *Polymer*, 2011, **52**, 4397–4417.
- 33 T. M. Clarke and J. R. Durrant, *Chem. Rev.*, 2010, **110**, 6736–6767.
- 34 H. Uoyama, K. Goushi, K. Shizu, H. Nomura and C. Adachi, *Nature*, 2012, **492**, 234-238
- 35 A. Sperlich, M. Liedtke, J. Kern, H. Kraus, C. Deibel, S. Filippone, J. L. Delgado, N. Martín and V. Dyakonov, *Phys. status solidi - Rapid Res. Lett.*, 2011, **5**, 128–130.
- 36 D. R. Lawson, D. L. Feldhiem, C. A. Foss, P. K. Dorhout, C. M. Elliott, C. R. Martin and B. Parkinson, *J. Phys. Chem.*, 1992, **96**, 7175–7177.
- 37 P. E. Hartnett, S. M. Dyar, E. A. Margulies, L. E. Shoer, A. W. Cook, S. W. Eaton, T. J. Marks and M. R. Wasielewski, *Chem. Sci.*, 2015, **6**, 402–411.
- 38 D. Moghe, P. Yu, C. Kanimozhi, S. Patil and S. Guha, *Appl. Phys. Lett.*, 2011, **99**, 233307.

Chapter 3

- 39 T. Hahn, S. Tscheuschner, C. Saller, P. Strohriegl, P. Boregowda, T. Mukhopadhyay, S. Patil, D. Neher, H. Bässler and A. Köhler, *J. Phys. Chem. C*, 2016, **120**, 25083–25091.
- 40 S. Few, J. M. Frost, J. Kirkpatrick and J. Nelson, *J. Phys. Chem. C*, 2014, **118**, 8253–8261.
- 41 M.-F. Falzon, A. P. Zoombelt, M. M. Wienk and R. A. J. Janssen, *Phys. Chem. Chem. Phys.*, 2011, **13**, 8931.
- 42 M. Van Landeghem, R. Lenaerts, J. Kesters, W. Maes and E. Goovaerts, *Phys. Chem. Chem. Phys.*, 2019, **21**, 22999–23008.
- 43 S. Cook, H. Ohkita, J. R. Durrant, Y. Kim, J. J. Benson-Smith, J. Nelson and D. D. C. Bradley, *Appl. Phys. Lett.*, 2006, **89**, 101128.
- 44 H. Ohkita and S. Ito, *Polymer*, 2011, **52**, 4397–4417.
- 45 S. K. Pal, T. Kesti, M. Maiti, F. Zhang, O. Inganäs, S. Hellström, M. R. Andersson, F. Oswald, F. Langa, T. Österman, T. Pascher, A. Yartsev and V. Sundström, *J. Am. Chem. Soc.*, 2010, **132**, 12440–12451.
- 46 S. Shoaee, M. P. Eng, E. Espíldora, J. L. Delgado, B. Campo, N. Martín, D. Vanderzande and J. R. Durrant, *Energy Environ. Sci.*, 2010, **3**, 971–976.
- 47 D. Credginton, F. C. Jamieson, B. Walker, T.-Q. Nguyen and J. R. Durrant, *Adv. Mater.*, 2012, **24**, 2135–2141.
- 48 L. Franco, A. Toffoletti and M. Maggini, *Phys. Chem. Chem. Phys.*, 2012, **14**, 14358.
- 49 R. Haberkorn, M. E. Michel-Beyerle and R. A. Marcus, *Proc. Natl. Acad. Sci.*, 1979, **76**, 4185–4188.
- 50 B. Hu, L. Yan and M. Shao, *Adv. Mater.*, 2009, **21**, 1500–1516.
- 51 W. Chang, D. N. Congreve, E. Hontz, M. E. Bahlke, D. P. McMahon, S. Reineke, T. C. Wu, V. Bulović, T. Van Voorhis and M. A. Baldo, *Nat. Commun.*, 2015, **6**, 6415.
- 52 M. K. Etherington, J. Gibson, H. F. Higginbotham, T. J. Penfold and A. P. Monkman, *Nat. Commun.*, 2016, **7**, 13680.
- 53 F. B. Dias, J. Santos, D. R. Graves, P. Data, R. S. Nobuyasu, M. A. Fox, A. S. Batsanov, T. Palmeira, M. N. Berberan-Santos, M. R. Bryce and A. P.

Chapter 3

- Monkman, *Adv. Sci.*, 2016, **3**, 1600080.
- 54 R. D. Pensack, A. J. Tilley, C. Grieco, G. E. Purdum, E. E. Ostroumov, D. B. Granger, D. G. Oblinsky, J. C. Dean, G. S. Doucette, J. B. Asbury, Y.-L. Loo, D. S. Seferos, J. E. Anthony and G. D. Scholes, *Chem. Sci.*, 2018, **9**, 6240–6259.
- 55 J. R. Ochsmann, D. Chandran, D. W. Gehrig, H. Anwar, P. K. Madathil, K.-S. Lee and F. Laquai, *Macromol. Rapid Commun.*, 2015, **36**, 1122–1128.

Chapter 4

Investigation into Energy-Transfer Pathways in a Zinc Porphyrin/F8BT Hybrid Polymer

4.1 Outline

Triplet species are ubiquitous throughout the area of organic optoelectronics. Triplet states have long been found to be a loss mechanism by virtue of them being energetically low lying relative to CT states and consequently acting as energetic trap states. Recently however, the intrinsic properties of triplet states are being exploited to enhance device efficiencies. In spite of their ubiquity, key fundamental aspects of triplets are not yet fully elucidated, predominantly as a consequence of them being generated indirectly. Important properties such as triplet diffusion length, absorbance cross-sections and population density remain largely unknown, and so further research is critical to establish these fundamental characteristics before the full advantage of triplet enhanced devices can be exploited. The synthesis and study of rationally designed triplet sensitised systems is therefore of crucial interest to the field of organic electronics.

In this chapter a well-known conjugated polymer, F8BT, copolymerised with a zinc tetraphenyl porphyrin derivative, HAPAPP, was spectroscopically investigated. This was for the purpose of exploring the feasibility of an intramolecular triplet-triplet annihilation self-upconverting donor polymer material. In the introduction a brief overview is given on the principles behind the harvesting of the solar spectrum with photovoltaic materials, including the current limitations of organic donor polymers. This is followed by a description of triplet-triplet annihilation upconversion (TTA-UC), its application to improving solar spectral harvesting, including examples from the literature. A brief description of the methodology employed is given, followed by the results of the investigation. Ground state absorbance, photoluminescence and transient absorption spectroscopic results of F8BT-HAPAPP in chlorobenzene solution are provided. It was found that F8BT-HAPAPP did not undergo the desired TTA-UC process, due to the zinc porphyrin possessing a lower energy triplet state compared to the F8BT. In spite of this a rich photophysical mechanism was elucidated, whereby a dual singlet/triplet energy transfer process was observed from the F8BT to the HAPAPP moiety.

4.2 Introduction

The solar spectrum encompasses wavelengths from 280-4000 nm, however most energy is found situated in the visible and near-infrared (NIR) regions,¹ as shown in figure 4.1. In order to efficiently harvest solar output, one must ensure sufficient spectral overlap between the light absorbing material and that of the solar spectrum. While many conjugated donor polymers absorb in the visible region, significantly fewer do so in the NIR. A good example of this is P3HT, which possesses a band gap of 1.9 eV, and at most can absorb 27% of the solar spectrum available. This is illustrated in figure 4.1, where the normalised P3HT absorbance and solar emission spectrum are overlaid. Shockley and Queisser demonstrated that any photons with an energy less than the bandgap do not contribute to photocurrent, and in addition proposed that the optimal band-gap of a light harvesting material should be 1.3-1.4 eV.² Shifting the absorption spectrum of the polymer to longer wavelengths (i.e. reducing the bandgap) would therefore allow for greater efficiency in harvesting solar output. This has the effect of increasing the short circuit photocurrent, J_{sc} , as a greater number of above band gap photons can now be absorbed.³ However, it should be noted that a decrease in the band gap is often accompanied by a reduction in the U.V.-blue spectral region, limiting potential solar harvesting gains. In order to counteract this one must simultaneously obtain a broad absorption range whilst obtaining a reduction in the band-gap. Another issue found is that the open circuit voltage, V_{oc} , is found to decrease linearly with decreasing bandgap (provided the acceptor molecule is kept the same).⁴ This is because the V_{oc} is correlated with the difference between the HOMO of the donor polymer and the LUMO of the acceptor. This has the effect of reducing the photoconversion efficiency of a device, which as previously stated is a product of the V_{oc} , J_{sc} , and FF divided by the input power.

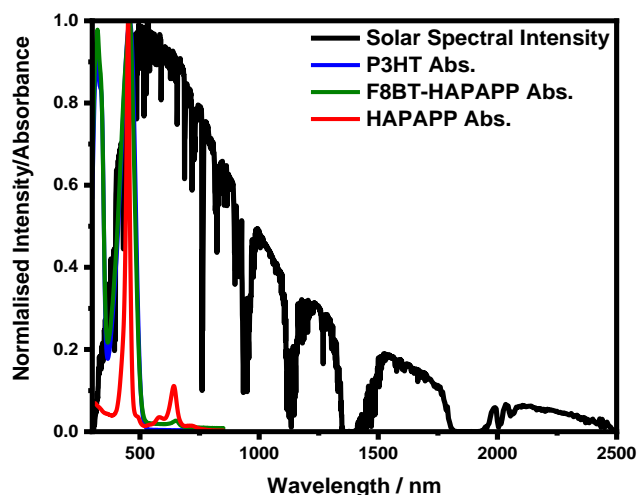


Figure 4.1 Normalised AM1.5 solar emission spectrum overlaid with the normalised absorbance spectra of P3HT thin film and chlorobenzene solutions of F8BT-HAPAPP and HAPAPP.

An alternate method for attaining broad band solar absorption, without having to reduce the bandgap, is through the inclusion of an additional NIR absorbing triplet sensitiser species. The intention of the NIR absorber would be to sensitise triplet formation on the donor conjugated polymer and allow for the increased possibility of triplet-triplet annihilation upconversion, TTA-UC. In the general case of triplet-triplet annihilation, TTA (as shown in figure 4.2), two lower energy triplet excited states undergo an electron exchange interaction to form a higher energy excited singlet state, and an additional singlet ground state. The newly formed S_1 state can then undergo subsequent deactivation via a long-lived fluorescence (provided the system is fluorescent), with a lifetime on the order of that of the triplet state. This process is therefore only possible if twice the energy of the triplet state is greater than that of the singlet state ($2x E_{T1} > E_{S1}$).⁵ Delayed fluorescence stemming from triplet-triplet annihilation was first observed in pyrene, and consequently is now referred to as 'p-type' fluorescence.⁶ It is important to also note that TTA has additional nomenclature in the literature, which includes triplet fusion.⁷

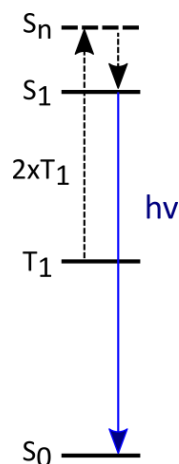


Figure 4.2 Schematic representation of the general case of triplet-triplet annihilation upconversion. Note: the presence of a second molecule has been omitted for simplicity.

TTA is a bimolecular collisional process and therefore depends upon the concentration of available triplets. A NIR absorbing triplet sensitizer can be used to generate the necessary triplet populations to incur TTA in the donor polymer via triplet-triplet energy transfer (as shown in figure 4.3). The initial step in sensitised TTA-UC involves the absorption of a photon by the sensitizer molecule, generating a singlet state. Crucially the absorbed photon has an energy smaller than that of the donor polymer's band gap, which would otherwise not contribute to the photocurrent of the photovoltaic device. The sensitizer singlet state subsequently undergoes intersystem crossing (ISC) to the triplet manifold, followed by triplet energy transfer to the conjugated polymer. This is ensured by making the triplet energy of the sensitizer higher than that of the upconverting polymer's by at least 0.08-0.12 eV.⁸ Two sensitised polymer triplet states then undergo the standard triplet-triplet annihilation (TTA) mechanism (subject to the same energetic requirements) to yield a higher energy singlet state and a singlet ground state. In an OPV device, this higher energy singlet state can then be quenched by an electron acceptor to generate the charge carriers required for operation. A salient point is that generation of potential charge carriers from otherwise unused sub-bandgap photons would allow for overcoming the Shockley-Queisser limit.⁹

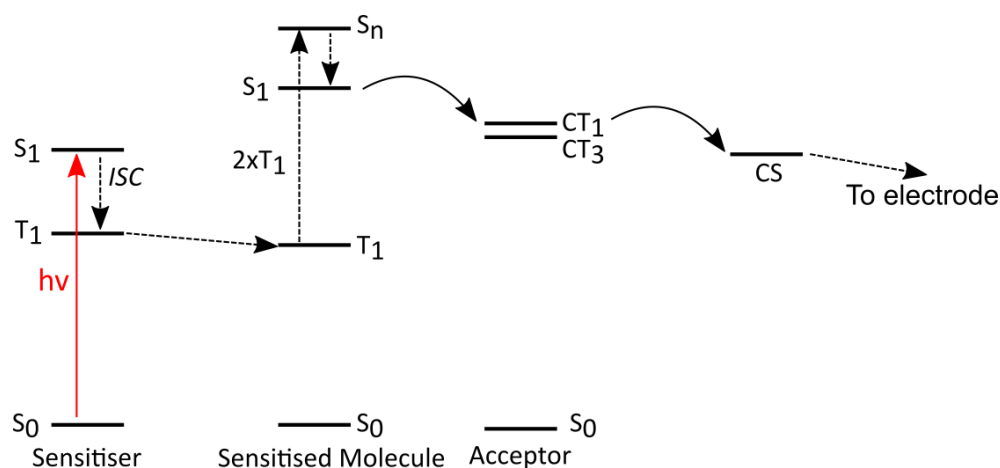


Figure 4.3 Schematic representation of sensitised triplet-triplet annihilation upconversion and resulting charge separation. The presence of the acceptor molecule quenches the 'delayed' fluorescence. Note: the presence of a second sensitised molecule has been omitted for simplicity.

At first glance the annihilation of two triplets to yield one singlet state appears to be a violation of spin conservation rules, which state that there must be no overall net change in spin orientation. However, a consideration of the spin statistics reveals that there are three different permutations in which two triplets may combine, as shown in table 4.1. For the type 1 triplet encounter complex ((T₊(↑↑) T₋(↓↓)) spin can be conserved, thus allowing the formation of a singlet state. From this simple spin statistical analysis, encounter complexes of triplets will have a possible 9 states from the multiplicity (1+3+5 = 9), and as such will form 5/9 quintets, 3/9 triplets and 1/9 singlets. Taking account that each annihilation process will require two photons to generate a singlet, the overall annihilation efficiency of TTA-UC will be 5.5%. However, this analysis is purely predicated upon the basis that any quintet and triplet encounter complexes will quench directly to the ground state. Experimental evidence indicates that this may not necessarily be the case. Schmidt et al.¹⁰ reported an efficiency of 12.5% using a Pd porphyrin and rubrene solution, while Kondakov extended these findings to OLEDs, establishing an efficiency of 20%.^{11,12} Both of these values were attributed to the potential of triplet encounter complexes not quenching the available energy, and subsequently repopulating the triplet state (which can then go on and react again). In addition to this, the formation of quintet states by TTA has been calculated to be an endothermic process in a number of organic systems,^{13,14} as such rendering this triplet deactivation channel inoperative.

Table 4.1 Spin statistics for the interaction of two triplet states. The type 1 interaction permits spin conservation.

Type	Spin Configuration	Total Spin	Arrow Notation	Multiplicity = (2S+1)	Overall State
1	T ₊ (↑↑) T ₋ (↓↓)	0	↑↑↓↓	1	Singlet
2	T ₊ (↑↑) T ₀ (↓↑)	+1	↑↑↓↑	3	Triplet
3	T ₊ (↑↑) T ₊ (↑↑)	+2	↑↑↑↑	5	Quintet

In the absence of an electron acceptor the photoluminescence intensity derived from TTA-UC is typically reported to exhibit a quadratic power dependence, attributed to the bimolecular annihilation process.^{15,16} This has been shown not necessarily to be the case, where a linear regime can be accessed, provided the experimental conditions are correct.^{17,18,19} Through rigorous removal of triplet quenching oxygen via freeze pump thaw, or increasing the concentration of the sensitiser, sufficiently high concentrations of sensitised triplets are present such that a new linear kinetic regime is attained. In this linear regime the rate of TTA-UC is much higher than that of the unimolecular or pseudo first order decay of the triplet.^{20,21}

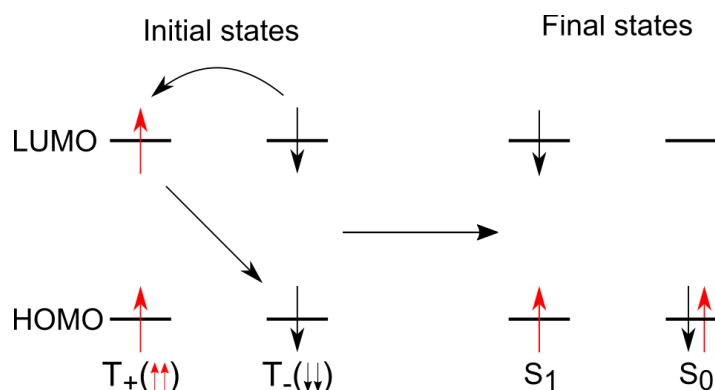


Figure 4.4 Schematic representation of the electron exchange mechanism of TTA to yield a singlet excited state and singlet ground state.

Parker and Hatchard first discovered TTA-UC phenomena in 1962 using a solution of phenanthrene with a trace amount of anthracene.²² They observed a long-lived fluorescence spectrum identical to that of anthracene when the much higher in concentration phenanthrene was excited. They conjectured that the long-lived decay was the consequence of TTA-UC stemming from triplet sensitisation from the phenanthrene, and not from an excited singlet dimer of anthracene. Since then there have been many other reports of solution based TTA-UC systems such as [Ru(dmb)₃]²⁺ with anthracene,²³ Ir(ppy)₃ with pyrene,²⁴ and Pd/PtOEP coupled with DPA becoming commonplace for investigating TTA-UC fundamentals.^{25,26} Unfortunately the design and implementation of TTA-UC systems applicable to the

Chapter 4

solid state have been less successful. This has predominantly been attributed due to the lack of translational mobility needed to form encounter complexes, or poor diffusion. Most systems employed have focused predominantly on the use of an inert polymeric matrix. Jankus et al successfully demonstrated that doping of super yellow PPV thin films with a Pd porphyrin derivative sensitizer resulted in an upconversion efficiency of 6%.⁷ This efficiency surpasses the 5.5% limit imposed by spin statistics, but it is lower than what has been previously found in solution studies. This was attributed to crystalline porphyrin aggregates in the thin film, which were accounting for up to 99% of sensitizer triplets being quenched from annihilation effects before they could diffuse to a polymer unit and undergo triplet transfer. This quenching process was observed in time-resolved emission experiments, manifesting itself as a power-law at early decay times. It was therefore concluded that if the sensitizer can be prevented from quenching in the solid phase, then a significant increase in TTA-UC might be attained. One method of achieving this is by incorporating the sensitizer into the same polymer backbone, thus potentially removing concerns of phase segregation associated with processing typically amorphous polymers with highly crystalline metal complex sensitizers.

The aim of this chapter is to test the hypothesis of whether covalently incorporating a sensitizer into a polymer backbone can result in efficient TTA-UC. A zinc porphyrin derivative (5,15-bis((4-bromophenyl)ethynyl)-10,20-bis(3,4,5-tris(dodecyloxy)phenyl)porphyrin), HAPAPP, was copolymerised with the well-known polymer poly(9,9-dioctylfluorene-co-benzothiadiazole), F8BT. This system was rationally designed to undergo intramolecular TTA-UC, whereby the porphyrin would act as an intramolecular triplet sensitiser for F8BT. Incorporating both the sensitiser and upconverter also has the added benefit of removing the diffusional problems associated with two discrete components, allowing for the study of the intrinsic intramolecular dynamics of the system in the solution phase. Both the pure F8BT and isolated porphyrin, HAPAPP, were used as control samples. The structures of the materials involved in this study are displayed in figure 4.5.

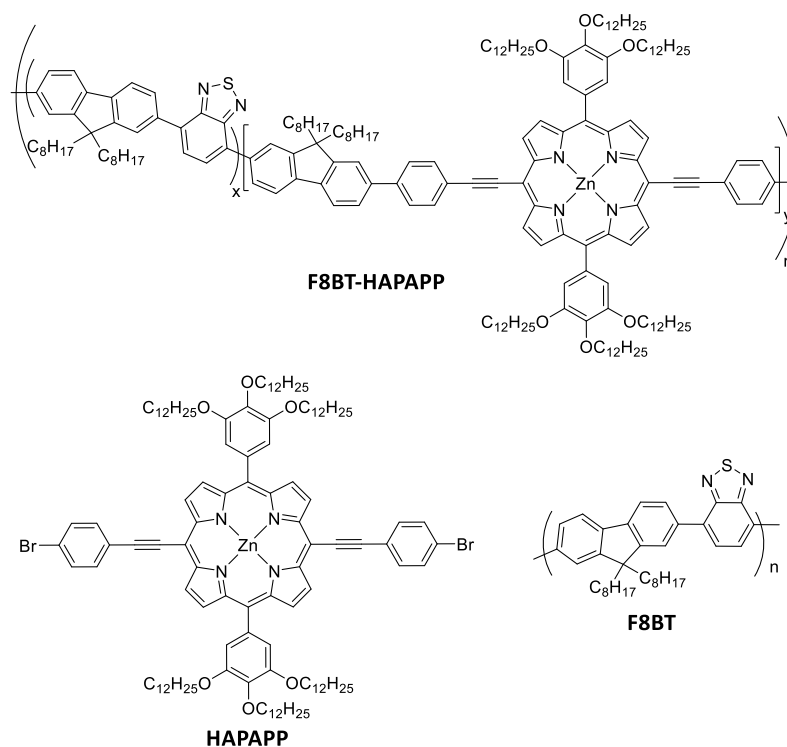


Figure 4.5 Structures of the polymer F8BT, the isolated porphyrin HAPAPP and porphyrin containing polymer, F8BT-HAPAPP. F8BT-HAPAPP was synthesised with a weight percentage of 5% porphyrin to benzothiadiazole moiety ($x:y = 19:1$).

A ZnTPP derivative was used on the basis of its narrow singlet-triplet energy gap ($\Delta E_{S-T} = 0.45$ eV), with high triplet yields ($\Phi_{ISC} = 0.84-0.88$)^{27,28} derived from the Zn centres heavy atom influence (see section 1.8.2). This heavy atom effect stems from the large nuclear charge (Z) of the Zn nucleus, which has the effect of increasing the strength of the spin orbit coupling and in turn increasing the rate of intersystem crossing (k_{ST}). One of the most important features the Zn porphyrin possesses however, is a set of spectral transitions known as Q-bands, which absorbs at longer wavelengths where the F8BT does not (this is shown in figure 4.6). The origin of this Q-band is derived from the ‘four-orbital’ model, as proposed by Gouterman.²⁹ In this model, the absorption bands observed are the result of transitions between two degenerate HOMO and two LUMOs. The energies of these transitions are dictated by the identity of the metal centre and the substituents present on the macrocyclic ring. The HOMOs have been calculated to be a_{1u} and a_{2u} , and the LUMOs were calculated to be the result of a degenerate set of e_g orbitals. Transitions between these orbitals will therefore give rise to two excited states. Orbital mixing between these states then splits the two states in energy, yielding a higher energy state with a stronger oscillator

strength (known as the Soret band), and a lower energy state with weaker oscillator strength (known as the Q-band).³⁰

F8BT was chosen as the polymer backbone as it has been shown to undergo TTA in the solid phase.^{31,32} Importantly the energetics obtained from the literature indicates that triplet energy transfer between the two systems was feasible. The triplet energy level of F8BT is found to be 1.7-1.8 eV,³³ which is situated near to that of the Zn porphyrin triplet energy of > 1.6 eV. It was therefore argued that the greater density of states available to the polymer, relative to the discrete Zn porphyrin, would entropically drive energy transfer from the porphyrin to the F8BT, even though the process was likely to be endothermic.

4.3 Experimental

F8BT was obtained from Ossila ($M_w = 376\ 214$ Da), whilst F8BT-HAPAPP ($M_w = 15\ 000$ Da, PDI = 1.5) and HAPAPP were synthesised by David Freeman of the Bronstein group. F8BT, F8BT-HAPAPP and HAPAPP were dissolved in spectroscopic grade chlorobenzene (Alfa Aesar) at differing concentrations of 68 $\mu\text{g/mL}$, 0.65 mg/mL and 34 $\mu\text{g/mL}$ respectively. These concentrations were used for transient absorption studies such that the ground state absorbance of the F8BT at 518 nm (where the F8BT would be selectively excited) was the same as that of the F8BT-HAPAPP Q-band at 650 nm. This ensured that the same number of molecules were excited in both the neat F8BT and F8BT-HAPAPP. The relatively high concentration of F8BT-HAPAPP was necessitated by the low (~10%) concentration of porphyrin incorporated into the F8BT polymer backbone, which had the effect of the porphyrin Q-band absorbance being low. Chlorobenzene was selected as the solvent for this investigation due to its excellent ability to solvate polymeric materials, such as F8BT.

All solutions were degassed by freeze pump thawing of solutions and sealing under a nitrogen atmosphere. This was achieved using a custom-made Young's tap quartz cuvette, with a pathlength of 2 mm. Films of F8BT-HAPAPP were made via drop casting.

4.4 Ground State Absorbance and Fluorescence

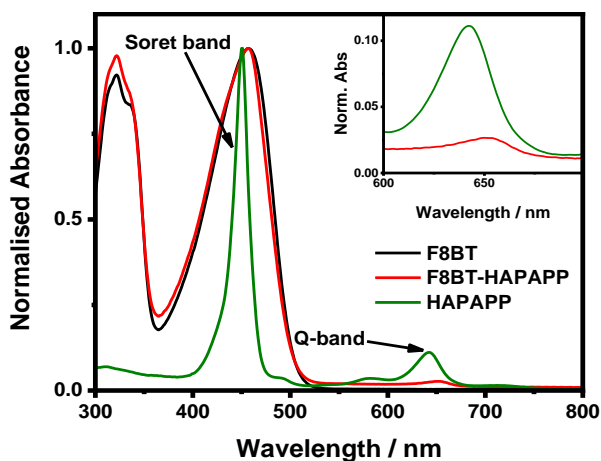


Figure 4.6 Normalised ground state absorption spectra of F8BT, F8BT-HAPAPP and HAPAPP in chlorobenzene solution. The inset enhances the spectral area of the Q-bands observed in HAPAPP and F8BT-HAPAPP. Pristine F8BT exhibits negligible absorption in the red and near infrared.

The ground state UV-Vis absorption spectrum of pristine F8BT chlorobenzene solution is shown in figure 4.6 and exhibits two absorption maxima at 322 and 457 nm, with negligible absorption in the red and near infrared. Theoretical calculations found in the literature assign the transition at 457 nm to a charge-transfer transition,³⁴ where the electron is found to reside on the acceptor benzothiazole unit, and the hole located on the fluorene unit. The shorter wavelength absorption at 322 nm is assigned to a direct π - π^* transition and is found to be delocalised across the polymer chain. The pure HAPAPP chlorobenzene solution absorption spectrum displays two prominent absorption bands at 450 and 642 nm respectively. Following the Gouterman four-orbital model the intense transition at 450 nm known as the Soret band corresponds to the strongly allowed S_0 - S_2 transition, whereas the lower energy transition at 642 nm is known as a Q-band and corresponds to the weakly allowed S_0 - S_1 transition. In a chlorobenzene solution of the porphyrin containing polymer, F8BT-HAPAPP, the absorption spectrum exhibits very little change with respect to the parent F8BT transitions at 322 and 457 nm, albeit the formation of a new weak transition at 652 nm. This new transition is assigned to a red-shifted porphyrin Q-band and can be seen in the inset of figure 4.6. It should be noted that the Soret band seen in the pure HAPAPP spectra is obscured via the presence of the broad F8BT charge transfer absorption at 457 nm. The negligible deviation from the parent F8BT transitions suggests very little electronic perturbation of the F8BT backbone upon inclusion of the porphyrin moiety into the polymer. In contrast to this the F8BT-HAPAPP Q-band is found to exhibit a 0.04 eV red shift relative to its isolated porphyrin

analogue. This observed Q-band red shift is likely to derive from the greater delocalisation of the porphyrin π system into the conjugated polymer backbone, as has been seen in other cases.³⁵ It is noted that introduction of the porphyrin into the F8BT results in a modest solar spectral coverage increase of 1%, as seen in figure 4.1, however, the purpose of this work is to help elucidate the mechanisms governing TTA-UC and provide a proof of concept system.

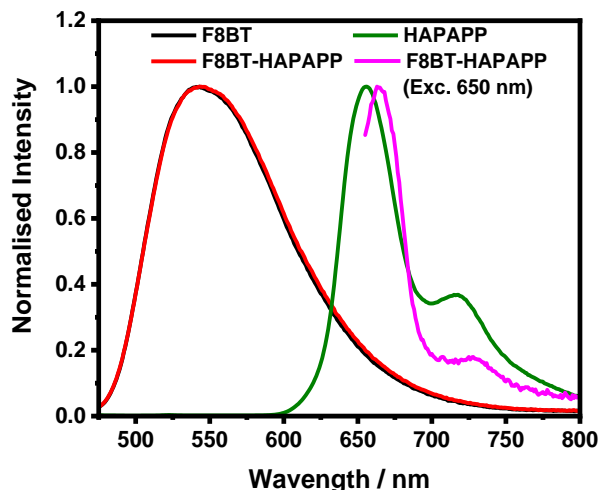


Figure 4.7 Steady state fluorescence spectra of F8BT, F8BT-HAPAPP and HAPAPP, in chlorobenzene solution (3.4 $\mu\text{g}/\text{mL}$) with an excitation wavelength of 450 nm. F8BT-HAPAPP was also excited at the porphyrin Q-band with 650 nm. F8BT and F8BT-HAPAPP exhibit near identical fluorescence spectra under the same excitation conditions.

The steady state fluorescence spectra for F8BT, F8BT-HAPAPP and HAPAPP are shown in figure 4.7. All spectra were obtained with an excitation wavelength of 450 nm, corresponding to excitation of the CT transition in F8BT, or that of the Soret band in HAPAPP. The pure F8BT exhibits a single emission peak at 544 nm, whereas excitation of the isolated porphyrin, HAPAPP, results in two emission peaks situated at 655 and 715 nm. Excitation of F8BT-HAPAPP yields a near identical emission profile to that of the pure F8BT, with the absence of any porphyrin fluorescence. This suggests that excitation with 450 nm leads to fluorescence from only the F8BT component, or that the yield of fluorescence from the porphyrin is so small it cannot be resolved above the F8BT fluorescence signal. A band gap of 2.5 eV was approximated for F8BT using the absorbance and emission spectra intersection.

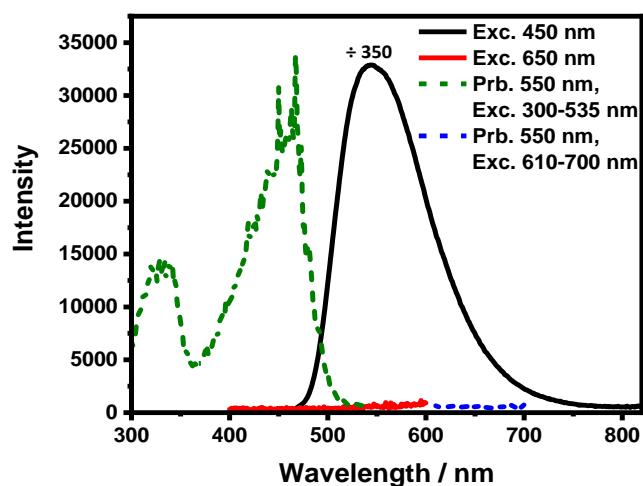


Figure 4.8 Excitation and emission spectra of F8BT-HAPAPP in chlorobenzene solution. The lack of upconverted (anti-Stokes) fluorescence, can be seen when exciting the porphyrin Q-band with 650 nm, and probing for the fluorescence of F8BT at 550 nm. Emission and excitation spectra were corrected for instrument response.

To investigate the potential presence of fluorescence upconversion, F8BT-HAPAPP was excited at the lower energy Q-band at 650 nm, where the F8BT would not absorb. This would allow for any subsequent detected F8BT fluorescence to be directly attributed to a photophysical mechanism involving the porphyrin moiety. The presence of TTA-UC would manifest itself as F8BT fluorescence in the 500-600 nm region when solely the porphyrin is excited. As previously observed in figure 4.7, exciting the F8BT backbone of F8BT-HAPAPP with 450 nm yields an emission peak at 544 nm. Under the conditions of selectively exciting the porphyrin moiety with 650 nm light, no fluorescence is observed from the F8BT (shown in figure 4.8 as the red line), only a weak porphyrin emission as shown in figure 4.7. This is indicative that TTA-UC is not occurring or is very inefficient. To further confirm these findings, excitation spectra were obtained in addition to the standard fluorescence measurements. Exciting the F8BT-HAPAPP in the range of 300-535 nm and probing at 550 nm results (shown in figure 4.8 as the green dashed line) in an excitation spectrum that possesses the same spectral structure as that of the F8BT absorbance spectra, with peaks situated at 330 and 460 nm. This indicates that the fluorescence observed is directly emitted from the S_1 state (according to Kasha's rule) of F8BT. Conversely, probing at the same wavelength 550 nm, but exciting the porphyrin Q-band in the range 610-700 nm results (shown in figure 4.8 as the blue dashed line) in no emissive response from the F8BT component.

Chapter 4

Table 4.2 Photophysical parameters obtained for F8BT-HAPAPP and its control samples F8BT and HAPAPP. F8BT-HAPAPP was selectively excited at 400 and 645 nm, corresponding to exciting of the F8BT backbone and porphyrin Q-band respectively.

Parameter	F8BT excitation		HAPAPP excitation	
	F8BT	F8BT-HAPAPP	HAPAPP	F8BT-HAPAPP
Φ_F	0.85 ^a	0.60 ^a	0.035 ^b	0.086 ^b
τ_{S1} (ns) ^c	1.9	1.9 and 0.14	1.0	0.9
τ_{T1} (μ s) ^c	180	460 and 19	1000	460

a. Excitation at 400 nm, probe 475-700 nm; b. Excitation at 645 nm, probe range 655-800 nm; c. Lifetimes were obtained from TAS data fitting.

The fluorescence quantum yields, Φ_F , for chlorobenzene solutions of F8BT, F8BT-HAPAPP and HAPAPP were also determined via a fluorimeter integrating sphere, with the results shown in table 4.2. Quantum yields represent the relative efficiencies of the various competing excited state deactivation processes. Any discrepancies between the quantum yields of the pure control samples and F8BT-HAPAPP would therefore be indicative of a newly created photophysical pathway. The pure F8BT and HAPAPP were found to have $\Phi_F = 0.85$ and 0.035 respectively. The low Φ_F found for the isolated porphyrin is a consequence of its zinc centre, which induces efficient intersystem crossing to the triplet manifold, due to the heavy atom effect. The heavy atom effect is the process by which spin-orbit coupling is increased, with increasing atom size, resulting in an increase in the rate of spin forbidden transitions.³⁶ This has the effect of increasing the rate of ISC, which in turn depletes the population of the singlet state and consequently reduces the Φ_F . When exciting the F8BT backbone of F8BT-HAPAPP and probing for F8BT emission in the range 475-700 nm a $\Phi_F = 0.60$ is obtained, which is significantly smaller compared to the pure F8BT of $\Phi_F = 0.85$. This reduction in Φ_F is indicative that introduction of the porphyrin into the F8BT backbone introduces a new singlet decay pathway(s) that can compete effectively on the timescales of F8BT fluorescence. When directly exciting the porphyrin in F8BT-HAPAPP with a pump wavelength of 645 nm and probing for HAPAPP fluorescence in the range 655-800 nm, a $\Phi_F = 0.086$ is acquired, which is slightly higher than the pure porphyrin's $\Phi_F = 0.035$. This change is likely to be attributed to a reduction in solution aggregation (the change in Φ_F is much smaller relative to the change from F8BT to F8BT-HAPAPP), therefore leading to a reduction in self-quenching effects. It is noted, however, that it is also possible that the measured difference in porphyrin Φ_F is the result of error, especially considering that the values reported are low.

4.5 Picosecond Transient Absorption Spectroscopy

Fluorescence studies indicated that TTA-UC was likely to not be operative in F8BT-HAPAPP, as evidenced by a lack of anti-Stokes fluorescence from F8BT, when exciting the lower energy porphyrin Q-band at 650 nm. Although this seemed to suggest that the F8BT-HAPAPP system underwent the standard photophysics of both the polymer and porphyrin constituents, analysis of the Φ_F for F8BT fluorescence in F8BT-HAPAPP revealed a Φ_F reduction relative to pure F8BT. This is indicative of a newly introduced photophysical mechanism that quenches the F8BT singlet state and may offer some potential insight into why TTA-UC is precluded. It is also possible, however, that excitation of the porphyrin Q-band is still resulting in TTA-UC, albeit with some additional deactivation process potentially quenching any formed $^1\text{F8BT}^*$ formed from annihilation events, preventing significant emission. In theory, as any upconverted $^1\text{F8BT}^*$ are derived from corresponding porphyrin triplet states ($^3\text{HAPAPP}^*$) they should therefore be formed at later timescales relative to $^1\text{F8BT}^*$ generated from direct excitation of the F8BT component. Picosecond transient absorption spectroscopy affords the time resolution with which to probe singlet state dynamics, and so provides an experimental technique with which to elucidate why F8BT-HAPAPP does not appear to yield an upconverted fluorescence signal.

The dynamics of F8BT-HAPAPP were probed by selectively exciting either its F8BT backbone at 518 nm, or its porphyrin Q-band at 650 nm. Excitation of the F8BT component should provide information on the reduction in Φ_F experienced when introducing the porphyrin into the polymer. Selective excitation at 518 and 650 nm ensures that any differences in spectral dynamics could be directly assigned to the local photophysics of either the F8BT or porphyrin. The pure F8BT and HAPAPP were used as controls to provide reference data with which to compare F8BT-HAPAPP against. Neat spectra of F8BT, HAPAPP and F8BT-HAPAPP in chlorobenzene are presented, with a subsequent description of their relevant decay dynamics.

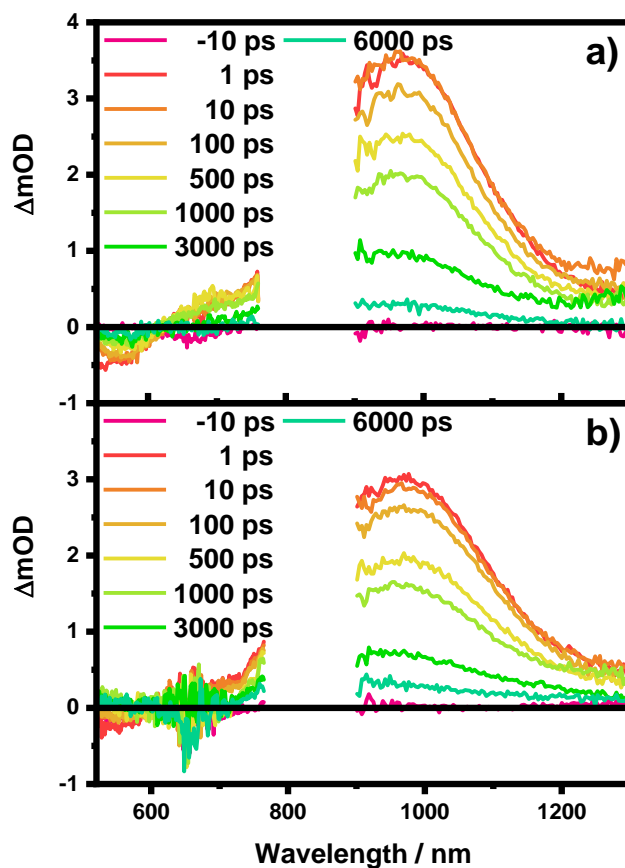


Figure 4.9 Picosecond transient absorption spectra of chlorobenzene solutions **a)** F8BT **b)** F8BT-HAPAPP excited at 518 nm with an excitation energy of $23 \mu\text{J cm}^{-2}$. Samples were degassed with argon for 30 min. Solution concentrations were 3.4 mg/mL for both F8BT and F8BT-HAPAPP. The gap at $\sim 770\text{-}900$ nm is from the fundamental pulse that is used to generate the probe.

When pristine F8BT is excited with an excitation wavelength of 518 nm, the ps-TAS spectrum is dominated by a broad peak at 975 nm, as shown in figure 4.9 a). The transient decay obtained from averaging in the range of 900-1000 nm (shown in figure 4.10) can be well fit with that of a monoexponential function to yield a lifetime of 1.9 ± 0.1 ns (where the error is the standard deviation). The species responsible for this decay is too short-lived to be ascribed to that of a triplet state, which for solution based polymers are typically found to possess lifetimes in the microsecond regime.^{37,38} On the other hand it is of the same order of what has been reported for solution based donor polymer singlet states.³⁸ Literature values for F8BT thin film suggest a singlet lifetime of 0.5 ns,^{39,40} less than that of the 1.9 ns obtained for the chlorobenzene solution. However, an increased excited state lifetime is often observed in solutions of a conjugated polymer relative to its thin film, and is rationalised on the basis that there are fewer interchain interactions in the solution phase that may provide

additional decay pathways to the singlet state, with the consequence of reducing the singlet state lifetime.⁴¹ Interestingly, no subsequent spectral evolution is observed, even though F8BT is known to form triplet states from ISC.^{42,43} This could possibly be attributed to the intense transition at 975 nm obscuring any underlying signal.

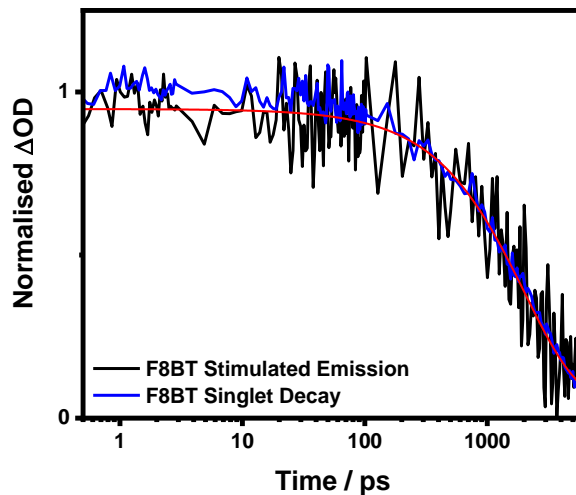


Figure 4.10 Picosecond transient absorption decay kinetics of pristine F8BT chlorobenzene solution (3.4 mg/mL) obtained with an excitation wavelength of 518 nm. Kinetics traces of the stimulated emission and singlet decay were obtained via averaging the regions of 550-600 nm and 900-1000 nm respectively. Kinetics have been normalised at 1 ps to illustrate the similarity of the F8BT stimulated emission and singlet decay.

Analysis of the ascribed F8BT singlet state dynamics as a function of excitation intensity (figure 4.11) showed that they were invariant within the energy regimes employed (2-23 $\mu\text{J cm}^{-2}$). This is also exemplified by the signal amplitude at 1 ps, as shown in the inset of figure 4.11, which demonstrates a linear response to increasing excitation intensity, as expected for a first order decay process. This observation is consistent with the assignment of the peak at 975 nm to a transition belonging to that of a singlet state.

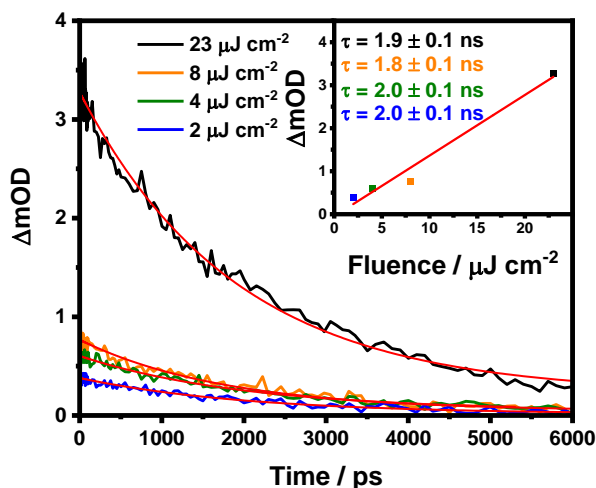


Figure 4.11 Picosecond transient absorption decay kinetics of neat F8BT chlorobenzene solution (3.4 mg/mL) obtained with an excitation wavelength of 518 nm. Kinetics were obtained through averaging decays in the wavelength region of 900-1000 nm. Sample was degassed with argon. The red lines are monoexponential fits. Inset: The transient signal amplitude at 1 ps as a function of energy density, illustrating the linear signal response. The red line is a linear fit for the eye.

In addition to the intense absorption located at 975 nm in figure 4.9 a), a weak negative feature is also found situated below 600 nm, correlating well with the spectral emission region of F8BT (seen previously in figure 4.7). This is indicative of stimulated emission, which is the induced emission of a photon from an excited state by the probe pulse. As the emitted photon will travel in the direction of the probe pulse both will subsequently be detected, resulting in a higher light intensity on the detector and manifesting itself as a negative absorption signal. The kinetics of the stimulated F8BT emission signal should consequently yield the same decay profile (albeit negative in signal) and therefore lifetime of the singlet state (assuming emission from the lowest excited, S_1), which can be used to confirm the ascribed $^1F8BT^*$ at 975 nm. Indeed, the kinetics obtained from averaging the stimulated emission from 550-600 nm are near identical to that obtained from the 975 nm transition, as observed in the normalised kinetics shown in figure 4.10. To further illustrate this, fitting of the stimulated emission decay results in a lifetime of $\tau = 2.0 \pm 0.2$ ns (where the error is from fitting), the same lifetime within error of that obtained for the 975 nm species. We can therefore confirm that the broad transition at 975 nm is likely to derive from that of a $^1F8BT^*$ transition ($S_1 \rightarrow S_n$).

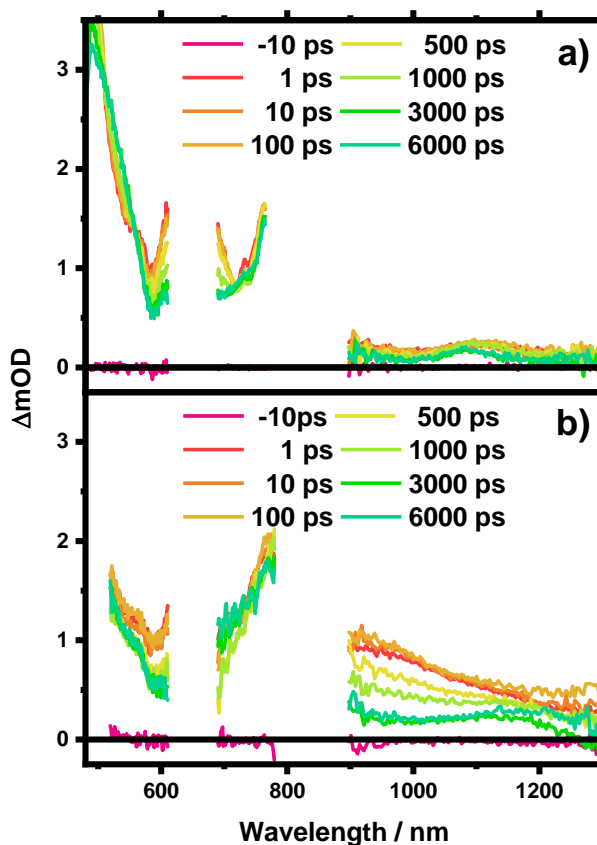


Figure 4.12 Picosecond transient absorption spectra of chlorobenzene solutions **a)** HAPAPP **b)** F8BT-HAPAPP excited at 650 nm with an excitation energy of $23 \mu\text{J cm}^{-2}$. Samples were degassed with argon for 30 min. Solution concentrations were $34 \mu\text{g/mL}$ for HAPAPP and 3.4 mg/mL for F8BT-HAPAPP. The gap at $\sim 770\text{-}900 \text{ nm}$ is from the fundamental pulse that is used to generate the probe, whereas the one at 650 nm derives from the exciting 650 nm pulse.

We now turn our attention to investigating the dynamics of the control ‘free’ porphyrin, HAPAPP. As shown in figure 4.12 a), excitation of the pristine HAPAPP’s Q-band with a pump wavelength of 650 nm results in the formation of a distinctively different spectrum to that of the pure F8BT. Focusing in on the visible portion of the spectrum, a transition band seen situated at the spectral limit of the detector at 480 nm is found to have been generated on ultrafast time scales ($<1 \text{ ps}$), with the absorption band extending to 560 nm. The peak of an additional ultrafast generated transition is also found directly inside the laser spike/ground state bleach spectral dark region of 610-690 nm, as evidenced by absorption on either side of the dark zone. In addition to this, the growth of a new more longer-lived species can also be observed in the region between the isosbestic points of 518 and 558 nm at later time scales ($>1000 \text{ ps}$), with its growth initially obscured by the presence of absorption by the ultrafast generated species. This longer-lived species can be seen most prominently in the region of 730-

760 nm, where the side of a transition can be observed extending into the detector gap (caused by the 800 nm fundamental, see section 2.6.4 for more details).

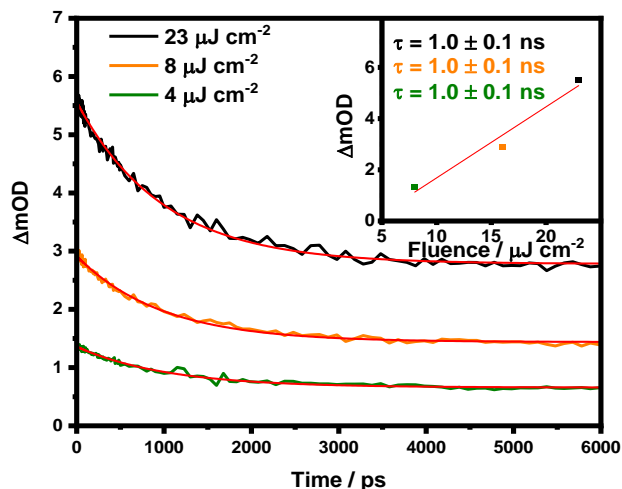


Figure 4.13 Picosecond transient absorption decay kinetics of pristine HAPAPP chlorobenzene solution (34 $\mu\text{g}/\text{mL}$) obtained with an excitation wavelength of 650 nm. Kinetics were obtained through averaging the decays from averaging decays in the wavelength region of 480-485 nm. Sample was degassed with argon. The red lines are monoexponential fits. Inset shows the transient signal amplitude at 1 ps as a function of energy density, illustrating the linear signal response. The red line is a linear fit for the eye.

The kinetics of the porphyrin's ultrafast generated species were probed by averaging the spectral area of 480-485 nm, where overlapping with transition bands from the later species was minimal, and as such the lifetime of the early species can be more easily assessed. Fitting to a monoexponential decay yielded a lifetime of $\tau = 1.0 \pm 0.1$ ns, with the inset of figure 4.13 illustrates that the lifetime is independent of the excitation energies utilised (8-23 $\mu\text{J cm}^{-2}$). This lifetime of 1.0 ns is far too short to be ascribed to that of Zn porphyrin triplet species, which have been found to have lifetimes on the order of milliseconds.²⁷ The ultrafast generated species responsible for the transition at 480 nm is therefore likely to be that of the porphyrin singlet state ($S_1 \rightarrow S_n$), $^1\text{HAPAPP}^*$. The transition located in the laser spike region was also investigated by averaging the kinetics in the region 600-610 nm. The kinetic decay obtained (shown in figure 4.14) is near identical to that of the one obtained averaging 480-485 nm, yielding a $\tau = 0.9 \pm 0.1$ ns, and so this transition is assigned to a lower energy $^1\text{HAPAPP}^*$ transition. These assignments are in agreement with previous ps transient absorption studies of near structurally identical ZnTPP, which exhibits a singlet lifetime of 2.0-2.5 ns,^{44,45} close to that obtained for $^1\text{HAPAPP}^*$. The species that appears later in time is therefore likely to be that of the $^3\text{HAPAPP}^*$, which is

expected to be formed owing to metalated porphyrin's ability to undergo facile intersystem crossing to the triplet manifold.

Investigating the near-infrared portion of the spectrum (>900 nm) reveals the presence of a transition at 1115 nm, which is generated on the same ultrafast timescales as that of the previously ascribed singlet transition. This feature is therefore likely to belong to a lower energy $^1\text{HAPAPP}^*$ transition. It should also be noted that an additional singlet transition appears to be located within the detector blind spot, as indicated by the signal rise in the region of 900-1000 nm. Interestingly, as the spectrum evolves in time, the decay of the singlet transition reveals the presence of an additional, more longer-lived species at 1080 nm. Once again, this long-lived species is likely to be that of the triplet state. A previous ps TAS study of ZnTPP that placed emphasis on the infrared also found a porphyrin singlet transition at 1258 nm,⁴⁴ however, a second triplet transition was not observed.

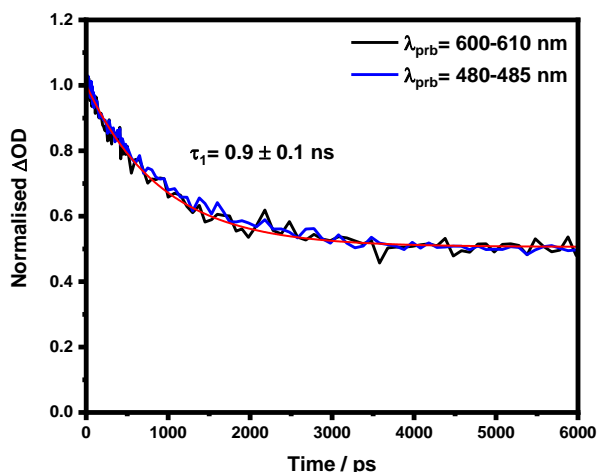


Figure 4.14 Picosecond transient absorption decay kinetics of pristine HAPAPP chlorobenzene solution (34 $\mu\text{g}/\text{mL}$) obtained with an excitation wavelength of 650 nm and an excitation energy of 23 $\mu\text{J cm}^{-2}$. Kinetics were obtained through averaging in the probe wavelength regions of 600-610 nm and 480-485 nm. The red line is a monoexponential fit.

Now that we have established the baseline dynamics of the pristine control samples, we will now focus upon the F8BT-HAPAPP. We will start with excitation of the porphyrin component as shown in figure 4.12 b). Selectively exciting the porphyrin Q-band with an excitation wavelength of 650 nm yields a spectrum that is similar in structure to that of the control isolated porphyrin, albeit with some differences. The prominent visible singlet transition at 485 nm is also found in the F8BT-HAPAPP spectrum, however, it appears red-shifted with respect to the isolated porphyrin. Quantifying the extent of this red-shift, however, is difficult, owing to the F8BT-

HAPAPP porphyrin transition peak residing below the detector's limit. In addition to this, the spectral range of the detector of has been reduced from 480 to 510 nm, due to ground state bleaching effects from the edge of the F8BT absorbance. The porphyrin triplet transition at 760 nm is still found to be present, but once again appears red-shifted relative to the isolated porphyrin. Exploring the NIR reveals the presence of a transition that spans across the entire IR region that was probed and can be most prominently observed in the region 900-1000 nm. This absorption was previously observed in the isolated porphyrin, albeit less intense. By 3 ns the 900-1000 nm transition has sufficiently decayed to reveal the presence of a long-lived feature at 1150 nm. This feature was previously observed in the neat HAPAPP spectrum at 1080 nm and was assigned to that of a $^3\text{HAPAPP}^*$ transition. This 0.07 eV reduction in transition energy is consistent with the redshift of 0.04 eV observed in the ground state absorbance spectra for the porphyrin Q-band upon inclusion into the F8BT backbone.

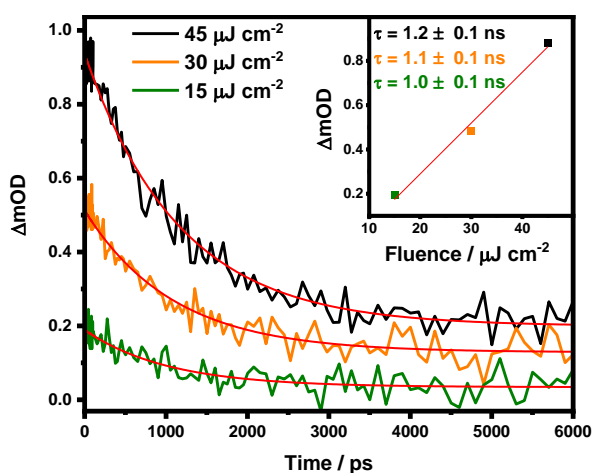


Figure 4.15 Picosecond transient absorption decay kinetics of F8BT-HAPAPP chlorobenzene solution (3.4 mg/mL) obtained with an excitation wavelength of 650 nm. Kinetics were obtained through averaging the decays in the wavelength region of 900-1000 nm. Sample was degassed with argon. The red lines are monoexponential fits. Inset shows the transient signal amplitude at 1 ps as a function of energy density, illustrating the linear signal response. The red line is a linear fit for the eye.

To determine the origin of the broad transition that extends from 900 out to 1300 nm, the kinetics were probed by averaging the decays between 900-1000 nm (figure 4.15), where spectral contamination from the tentatively assigned triplet transition at 1150 nm would be minimal. Fitting of the early decay component to a monoexponential yielded a lifetime of $\tau = 1.0 \pm 0.1 \text{ ns}$, which is the same (within error) exhibited for the

pure porphyrin singlet state. The transition at 900 nm is therefore likely to belong $^1\text{HAPAPP}^*$ state, as even though the $^1\text{F8BT}^*$ transition absorbs in the same spectral region, it exhibits approximately double the lifetime.

Considering the evidence thus far, exciting the porphyrin component of F8BT-HAPAPP appears to result in little deviation from the isolated porphyrin's photophysics, with only an apparent red shifting of singlet and triplet transitions being the predominant difference. Importantly, the lack of the 975 nm $^1\text{F8BT}^*$ transition confirms that TTA-UC is not operative upon exciting the HAPAPP component, which agrees with the observed absence of anti-Stokes fluorescence. Furthermore, there is no evidence for the formation of the $^3\text{F8BT}^*$ state in the F8BT-HAPAPP spectra (which would precede the formation of the $^1\text{F8BT}^*$ via TTA), which strongly indicates that energy transfer from the $^3\text{HAPAPP}^*$ to the $^3\text{F8BT}^*$ is not occurring, thus precluding any possibility of TTA to form the $^1\text{F8BT}^*$ state. This observation is consistent with the $^3\text{F8BT}^*$ energy level residing below that of the $^3\text{HAPAPP}^*$ state, as such the TTA mechanism can be considered to 'fail' once the porphyrin triplet state is formed.

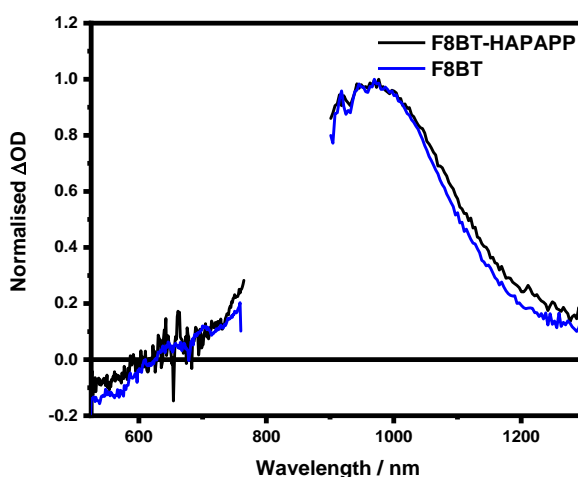


Figure 4.16 Normalised picosecond transient absorption spectra take at 1 ps of F8BT and F8BT-HAPAPP chlorobenzene solution (3.4 mg/mL) obtained with an excitation wavelength of 518 nm ($23 \mu\text{J cm}^{-2}$). Spectra have been normalised to their respective peak maxim.

Now that the F8BT-HAPAPP has been shown to undergo the standard porphyrin photophysics when excited at the Q-band, we will now assess the dynamics obtained from exciting the F8BT component. Exciting the F8BT backbone of F8BT-HAPAPP with 518 nm results in the formation of a near-identical transient absorption profile to that of the F8BT control polymer. This is best shown in figure 4.16 which displays the normalised spectra of F8BT and F8BT-HAPAPP taken at 1 ps. The dominating $^1\text{F8BT}^*$ singlet transition ($S_1 \rightarrow S_n$) is still found identically situated at 975 nm. In

addition to this, the F8BT stimulated emission is still observed below 600 nm. However, the stimulated emission is found to be less intense when compared to the pristine F8BT. By integrating the stimulated emission in the region of 534-580 nm at 1 ps we calculate an observed reduction in intensity of 42%. It is noted that this 42% reduction in stimulated emission intensity is greater than the 30% reduction in Φ_F when comparing F8BT ($\Phi_F = 0.85$) to F8BT-HAPAPP ($\Phi_F = 0.60$), and possible reasons for this difference will be discussed later.

Although the spectra of F8BT and F8BT-HAPAPP appear near identical, analysis of the kinetics at 975 nm, however, reveals that the monoexponential behaviour previously observed in the pristine F8BT has been replaced by a decay that is multiexponential in nature. Indeed, the decay data obtained from averaging the spectral region of 900-1000 nm can be well fitted to a biexponential function of the type shown in equation 4.1.

$$\Delta OD(t) = A_1 * e\left(\frac{-t}{\tau_1}\right) + A_2 * e\left(\frac{-t}{\tau_2}\right) \quad \text{Eqn. 4.1}$$

The first decay component is found to have a lifetime of $\tau_1 = 140 \pm 20$ ps, significantly faster than the second component, which possesses the same $^1\text{F8BT}^*$ lifetime of $\tau_2 = 1.9 \pm 0.1$ ns. The contribution from each component was assessed from their corresponding fit amplitudes, yielding contributions of $\tau_1 = 19\%$ and of $\tau_2 = 81\%$.

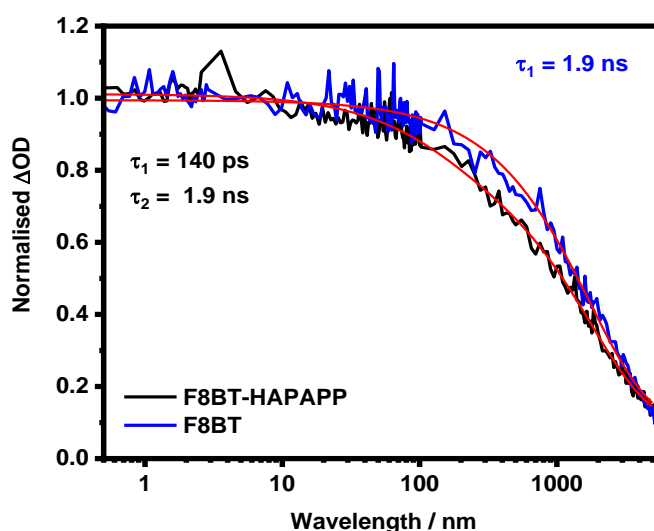


Figure 4.17 Kinetic decays of F8BT and F8BT-HAPAPP, excited with a pump wavelength of 518 nm. Kinetic decays obtained from averaging the probe wavelengths 900-1000 nm. Decays have been normalised to 1 ps to illustrate the additional decay phase present in F8BT-HAPAPP. The red lines are mono and biexponential fits for F8BT and F8BT-HAPAPP respectively.

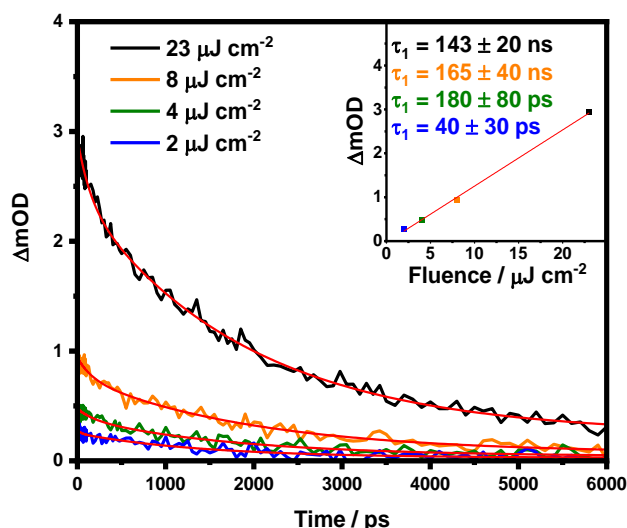


Figure 4.18 Picosecond transient absorption decay kinetics of F8BT-HAPAPP in chlorobenzene solution (3.4 mg/mL) obtained with an excitation wavelength of 518 nm. Kinetics were obtained through averaging decays in the wavelength region of 900-1000 nm. Sample was degassed with argon. Red lines are biexponential fits of the type $y_0 + A_1 \cdot \exp(-t/\tau_1) + A_2 \cdot \exp(-t/\tau_2)$. Inset: the transient signal amplitude at 1 ps as a function of energy density, illustrating the linear signal response. The red line is a linear fit for the eye. The values for τ_1 and τ_2 are given in table 4.3.

To ensure that this additional decay pathway was not the result of a laser induced second order effects, the F8BT-HAPAPP dynamics were analysed as a function of excitation energy, as shown in figure 18. The amplitude at 1 ps corresponds to the kinetics of the fast phase and showed a linear signal amplitude increase with respect to increasing excitation energy, with the lifetimes observed for both features being within error (inset of figure 4.18). It is noted that the lowest energy data set provides anomalous τ_1 and τ_2 lifetimes (which may be a consequence of excessive signal to noise in the data), however, it is discounted on the basis that all higher energies exhibit the same lifetimes within error. The discounting of annihilation effects therefore provides evidence that the introduction of the porphyrin moiety into the F8BT backbone introduces a new decay channel. It is possible that the fast phase derives from a singlet-singlet energy transfer process (SET), from the F8BT to the HAPAPP, which can alternatively be considered as an IC process (i.e. $S_{n(F8BT)} \rightarrow S_{1(HAPAPP)}$). This hypothesis would explain why there is an observed reduction in Φ_F , as ~19% (established from the contribution of the fast phase) of the photogenerated $^1F8BT^*$ are quenched by the porphyrin moieties. This raises the question as to why no $^1HAPAPP^*$ spectral features are observed in the ps TAS spectrum after energy

transfer from F8BT has taken place. This can be rationalised on the basis that the more intense $^1\text{F8BT}^*$ transition at 975 nm will obscure any underlying $^1\text{HAPAPP}^*$ signals observed at 900-1000 nm and 1115 nm, which will be generated in much lower concentrations. This will have the effect of the $^1\text{F8BT}^*$ dominating the F8BT-HAPAPP spectrum. It should be noted that the $^1\text{HAPAPP}^*$ transition seen previously below 600 nm sits in the region where the F8BT stimulated emission is present. As such, this may also account for the previously mentioned 42% reduction in stimulated emission compared to the 30% observed in the Φ_F . This is because in addition to the quenched F8BT fluorescence the positive gain from the $^1\text{HAPAPP}^*$ transition signal will partially cancel out the negative signal originating from the F8BT emission. If this SET theory is correct any porphyrin singlets formed from energy transfer should efficiently intersystem cross over to the triplet manifold ($\Phi_{\text{ISC}} \leq 0.91$ assuming $\Phi_{\text{IC}} = 0$), and as such should be observable/detectable at the longest timescales. The use of μs TAS should therefore be able to confirm whether $^3\text{HAPAPP}^*$ are indeed present.

Table 4.3 *Fitting results of F8BT-HAPAPP chlorobenzene solution (3.2 mg/mL) excited with 518 nm. Decays were obtained by averaging the region 900-1000 nm. Decays were obtained from fits with a biexponential function shown in equation 4.1.*

Energy Density ($\mu\text{J cm}^{-2}$)	τ_1 (ps)	A_1	τ_2 (ns)	A_2
23	143 ± 20	5.2E-4	1.9 ± 0.1	2.1E-3
8	165 ± 40	1.7E-4	2.0 ± 0.2	6.9E-4
4	180 ± 84	8E-5	1.8 ± 0.3	3.5E-4
2	39 ± 35	3E-5	1.4 ± 0.2	2.2E-4

4.6 Microsecond Transient Absorption Spectroscopy

Picosecond transient absorption spectroscopy demonstrated that F8BT-HAPAPP underwent the standard porphyrin photophysics when exciting the HAPAPP Q-band, as opposed to $^1\text{F8BT}^*$ generation through the TTA-UC process. In addition to this, ps-TAS had also shown that excitation of the F8BT component with 518 nm revealed the presence of a new decay pathway, not previously seen in the control pristine F8BT. In both cases, however, the ultimate dynamics of the triplet states involved were not elucidated, leaving questions as to their ultimate fate. μs transient absorption spectroscopy affords the time domain to monitor these triplet states and provide a clearer photophysical picture as to why TTA-UC was being precluded.

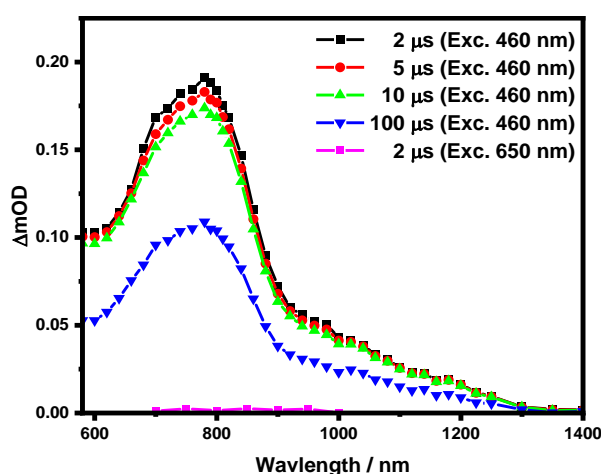


Figure 4.19 Microsecond transient absorption spectrum of neat F8BT chlorobenzene solution ($68 \mu\text{g/mL}$) excited with a pump wavelength of 460 nm and 650 nm. Obtained with excitation densities of 16 and $25 \mu\text{J cm}^{-2}$ for 460 and 650 nm respectively. Solution was degassed via three cycles of freeze pump thawing and placed under an N_2 atmosphere. Note: excitation with 650 nm results on negligible spectral response.

As with the ps study, we will initially focus upon the neat F8BT and HAPAPP. As shown in figure 4.19, excitation of the pure F8BT chlorobenzene solution at 460 nm results in the formation of a transition peak centred at 780 nm, with a tail extending out into the NIR, whereas excitation with 650 nm yields no spectral response. This feature is of a similar spectral shape to other reported photoinduced transient absorption studies of neat F8BT thin films, although the peak positions are reported red-shifted at 845 nm owing to characteristic solid state red-shifting.⁴⁶ This transition was previously assigned to that of a F8BT triplet transition ($T_1 \rightarrow T_n$) derived from intersystem crossing. To demonstrate that the transition observed at 780 nm in F8BT

belonged to the same F8BT triplet transition previously seen in literature thin film reports, the solution was bubbled with O₂. The presence of O₂ should selectively quench triplet states via triplet energy transfer, provided that the energy of the F8BT triplet was >0.94 eV.^{8,47,48} This triplet quenching process should manifest itself as a reduction in both signal amplitude and triplet lifetime. Indeed, the oxygenated solution results in the complete quenching of signal (shown in figure 4.20), suggesting that the transition at 780 nm derives from a highly oxygen sensitive ³F8BT*. The complete quenching of this signal is found to be reversible, therefore discounting the possibility of oxygen-based degradation, which would otherwise result in an unrecoverable initial signal.

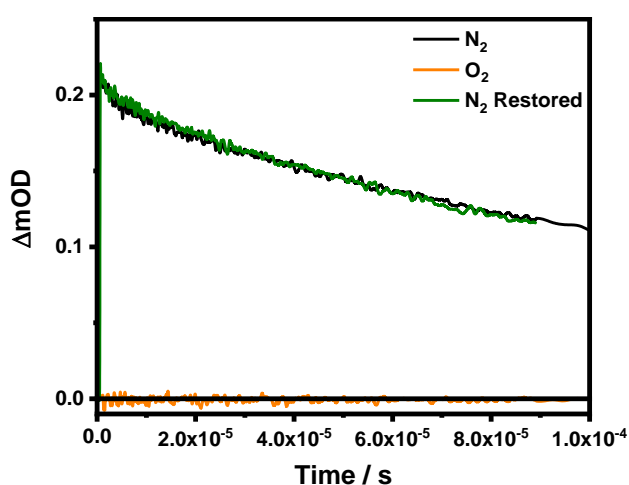


Figure 4.20 *Microsecond transient absorption decay kinetics of F8BT chlorobenzene solution (68 $\mu\text{g/mL}$) under nitrogen, oxygen and nitrogen restored atmospheres, at a probe wavelength of 800 nm. Obtained with a pump wavelength of 460 nm with an excitation density of $12.2 \mu\text{J cm}^{-2}$. Bubbling O₂ through the solution results in a complete quenching of the signal, illustrating the presence of a highly oxygen sensitive species, most likely to be that of a triplet.*

Inspection of the kinetics of the F8BT triplet (shown figure 4.21) reveals that the decay is not completely monoexponential in nature, with a small contribution (~10%) from an additional phase apparent at the earliest timescales. Interestingly, the existence of this second phase does not seem predicated upon the excitation energy employed, as demonstrated by the very similar τ_1 and τ_2 lifetimes obtained from biexponential fitting (shown in table 4.4) and consistent ~10% contribution from the initial decay phase. From biexponential fitting to the F8BT decays, average lifetimes of $\tau_1 = 12 \pm 3 \mu\text{s}$ and $\tau_2 = 214 \pm 9 \mu\text{s}$ (where the error is the standard deviation) are obtained. The origin of this early decay phase is currently not known. It should be noted, however,

that this study was conducted at room temperature and the F8BT triplet lifetime has been found to increase by approximately two orders of magnitude upon decreasing temperature (300-77 K).^{49,50} The reason for this observed temperature dependence has been suggested to derive from the deactivation of triplet decay channels, which increases the $^3\text{F8BT}^*$ lifetime.

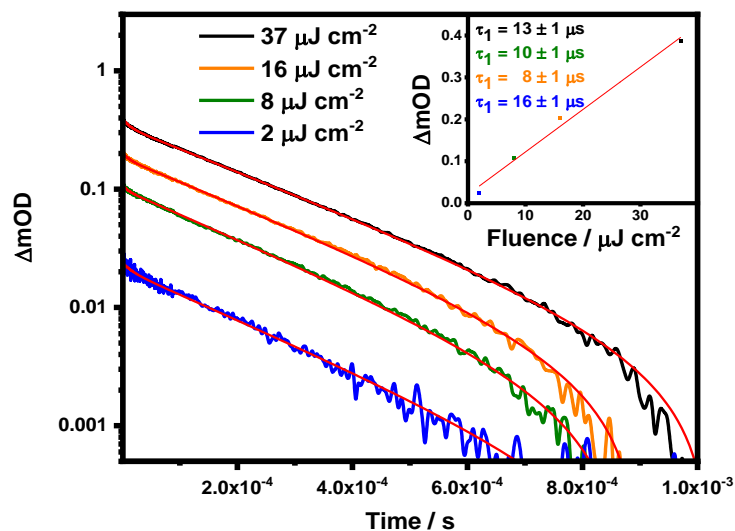


Figure 4.21 Microsecond transient absorption decay kinetics of F8BT chlorobenzene solution (68 $\mu\text{g}/\text{mL}$), excited with a pump wavelength of 460 nm and probe wavelength of 800 nm. Solution was degassed via three cycles of freeze pump thawing and placed under an N_2 atmosphere. Red lines are biexponential fits of the type $y_0 + A_1 \cdot \exp(-t/\tau_1) + A_2 \cdot \exp(-t/\tau_2)$. Inset: the transient signal amplitude at 1 μs as a function of energy density, illustrating the linear signal response. The red line is a linear fit for the eye. The values for τ_1 and τ_2 are given in table 4.4.

Table 4.4 Fitting results of F8BT chlorobenzene solution (68 $\mu\text{g}/\text{mL}$) excited with 460 nm and a probe wavelength of 800 nm. Decays were obtained from fits with a biexponential function shown in equation 4.1.

Energy Density ($\mu\text{J cm}^{-2}$)	τ_1 (ps)	A_1	τ_2 (μs)	A_2
37	13 ± 1	5E-5	226 ± 1	3.5E-4
16	10 ± 1	2E-5	219 ± 1	1.9E-4
8	8 ± 1	1E-5	207 ± 1	1.0E-4
2	16 ± 2	3E-6	205 ± 1	1.9E-5

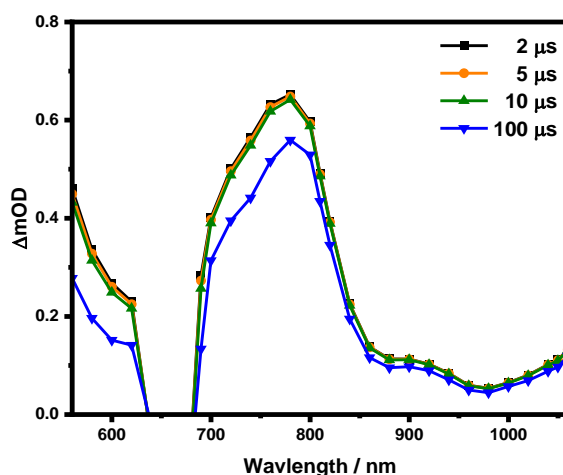


Figure 4.22 Microsecond transient absorption spectrum of neat HAPAPP chlorobenzene solution ($32 \mu\text{g/mL}$) excited with a pump wavelength of 640 nm. Obtained with an excitation energy of $10 \mu\text{J cm}^{-2}$. Solution was degassed via three cycles of freeze pump thawing and placed under an N_2 atmosphere.

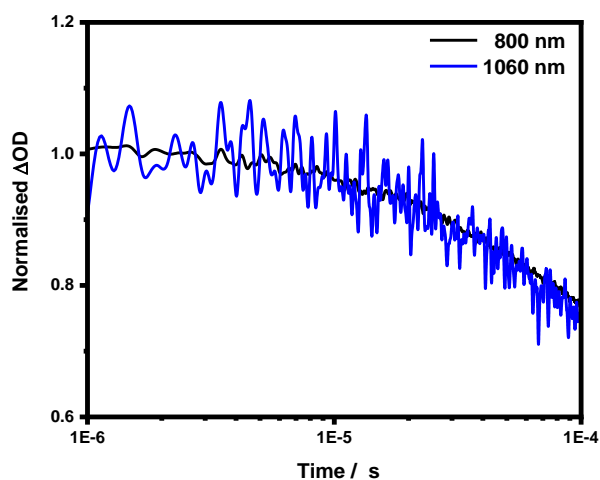


Figure 4.23 Normalised microsecond transient absorption decay kinetics of neat HAPAPP chlorobenzene solution ($32 \mu\text{g/mL}$) excited with a pump wavelength of 640 nm. Probe wavelengths of 800 and 1060 nm were used. Solution was degassed via three cycles of freeze pump thawing and placed under an N_2 atmosphere.

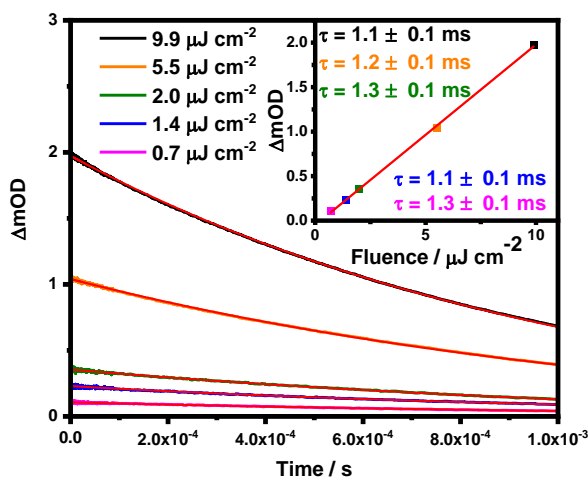


Figure 4.24 Microsecond transient absorption decay kinetics of neat HAPAPP chlorobenzene solution (32 $\mu\text{g/mL}$) excited with a pump wavelength of 640 nm and probe wavelength of 800 nm. Solution was degassed via three cycles of freeze pump thawing and placed under an N_2 atmosphere

Now that the F8BT triplet's presence has been established we will now assess the pristine HAPAPP. Exciting the Q-band of the pristine porphyrin with a pump wavelength of 640 nm results in the formation of two main transition peaks, situated at 780 and 1060 nm. It is noted that data presented in figure 4.22 only shows the edge of the transition at 1060 nm, but previous data presented in figure 4.19 shows this transition fully. These peaks were seen previously in the ps-TA spectrum of HAPAPP, with both being ascribed to $^3\text{HAPAPP}^*$ transitions. Confirmation that both the 780 and 1060 nm transitions belong to the same species can be observed in the normalised kinetics (shown in figure 4.23), which demonstrates identical decay dynamics for both transitions. Literature ns- μs transient absorption studies of ZnTPP solution also place a triplet transition in the infrared at 850 nm.⁵¹ The study did not however, identify the additional 1060 nm triplet transition, which is consistent with it also not being observed in the ZnTPP ps-TA spectrum.⁴⁴ Probing the kinetics at 800 nm as a function of excitation energy as shown in figure 4.24, reveals a decay that is invariant to the energy employed. The dynamics obtained can be well fitted to a monoexponential decay, yielding an average triplet lifetime of $\tau_1 = 1.2 \pm 0.1$ ms (where the error is the standard deviation). Overall, the ns- μs TAS spectrum of pristine HAPAPP exhibits little spectral evolution, with the only species observed being that of the $^3\text{HAPAPP}^*$. Although it was not identified, it should be noted that the ZnTPP π -cation radical transition has been seen at 500-600 nm when an electron acceptor (such as acyl chloride or quinone) is present.⁵² A further point of consideration is that both the $^3\text{F8BT}^*$ and $^3\text{HAPAPP}^*$ transition peaks (located at 800 and 780 nm respectively) are

spectrally situated close to one another, indicating that if both species are present at the same time separation of the two would be difficult.

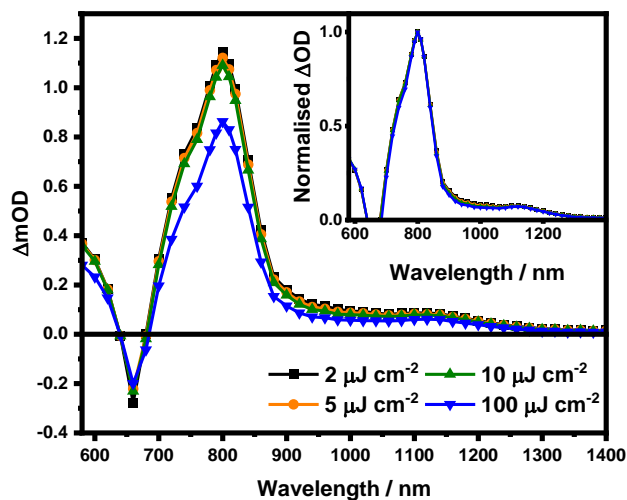


Figure 4.25 Microsecond transient absorption spectrum of F8BT-HAPAPP chlorobenzene solution (0.65 mg/mL) excited with a pump wavelength of 650 nm. Obtained with an excitation energy of $15 \mu\text{J cm}^{-2}$. Solution was degassed by three cycles of freeze pump thawing and placed under an N_2 atmosphere. Inset: the same spectral data normalised to the peak maxima, demonstrating the absence of spectral evolution.

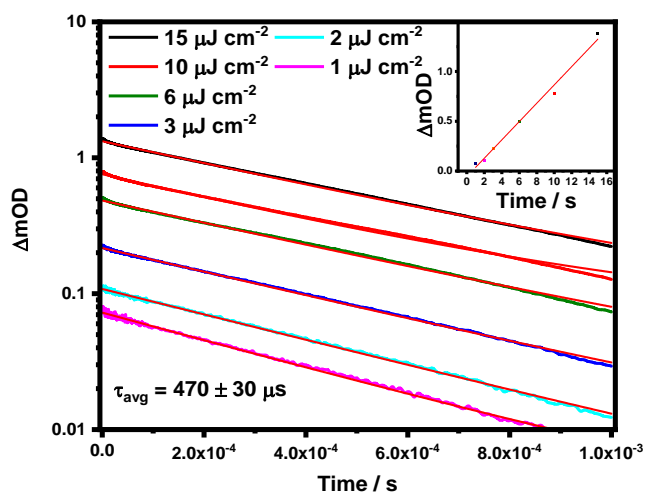


Figure 4.26 Microsecond transient absorption decay kinetics of F8BT-HAPAPP chlorobenzene solution (0.65 mg/mL) excited with a pump wavelength of 650 nm and probe wavelength of 800 nm. Solution was degassed by three cycles of freeze pump thawing and placed under an N_2 atmosphere. Inset: the transient signal amplitude at $1 \mu\text{s}$ as a function of excitation density, illustrating a linear signal response.

Chapter 4

Once again, we turn our attention to investigating what effect excitation of the Q-band has on F8BT-HAPAPP. Selectively exciting the porphyrin Q-band with 650 nm (shown in figure 4.25) results in a very similar spectrum to that of the isolated porphyrin, exhibiting little spectral evolution, as shown in the normalized TA spectrum in the inset of figure 4.25. Although the $^3\text{F8BT}^*$ transition was found to absorb in the same ~ 800 nm area, its presence can be discounted on the basis of the different spectral shapes, with F8BT-HAPAPP exhibiting a much narrower transition more akin to the spectrum of the $^3\text{HAPAPP}^*$, as shown in the normalized spectra in figure 4.27. As such the spectrum exhibited by F8BT-HAPAPP upon excitation with 650 nm is tentatively ascribed to absorption by the $^3\text{HAPAPP}^*$ state. The main porphyrin triplet transition previously found situated at 780 nm in the pristine HAPAPP μs -TA spectrum is now found red-shifted by 0.04 eV to 800 nm. Quantification of this redshift in the ps TAS spectra was previously impossible, due to both peaks lying within the spectral dead zone. This red-shift in transition energy is similar in magnitude to the ~ 0.07 eV exhibited for the lower energy NIR transition at 1115 nm as observed in the ps TAS spectra. Focusing in on the infrared region in the μs spectrum reveals that this same lower energy transition is found conserved from the ps TAS spectrum at 1120 nm. Probing the kinetics at 800 nm as a function of excitation density (shown in figure 4.26) reveals a decay that is invariant to the excitation energy employed. The kinetics obtained can be well fit to a monoexponential decay, yielding an average lifetime of $470 \pm 30 \mu\text{s}$ (where the error obtained is the standard deviation). Interestingly, this lifetime does not match either the pristine F8BT or pristine HAPAPP triplet lifetimes (214 μs and 1.2 ms respectively) and will be addressed in the discussion. From the μs TAS data we can infer that excitation of the Q-band of F8BT-HAPAPP results in similar porphyrin photophysics, as suggested by the ps TAS data and is consistent with the $^3\text{HAPAPP}^*$ being the lowest energy state of the system.

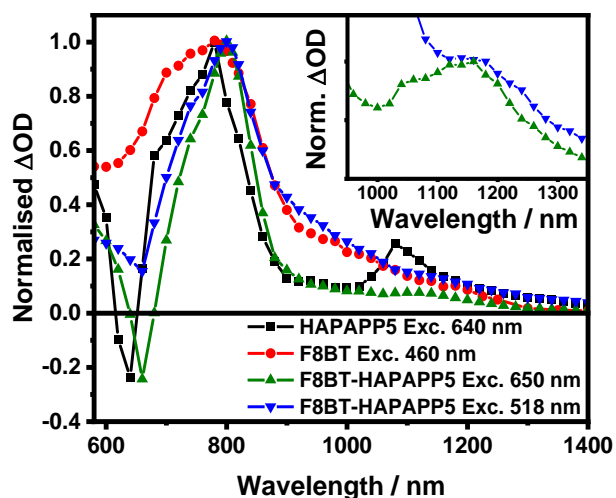


Figure 4.27 Microsecond transient absorption spectra of F8BT and F8BT-HAPAPP taken at 1 μ s. F8BT-HAPAPP was selectively excited with a pump wavelength of 518 and 650 nm, corresponding to excitation of F8BT or HAPAPP respectively. The inset enhances the region of 950-1350 nm for F8BT-HAPAPP, illustrating the characteristic porphyrin triplet peak present regardless of excitation of F8BT or the Q-band. Solutions were degassed via three cycles of freeze pump thawing and placed under an N_2 atmosphere.

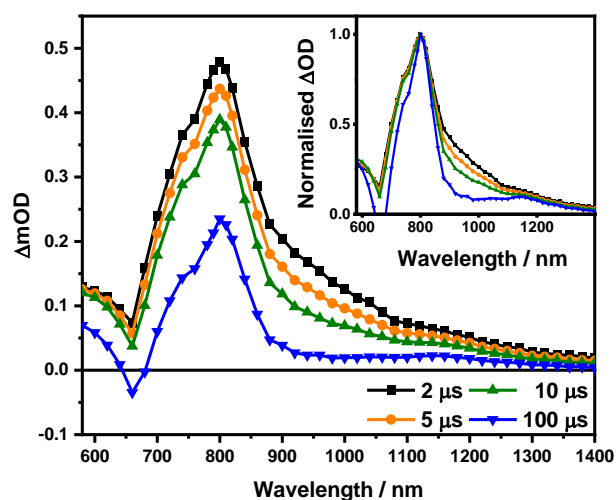


Figure 4.28 Microsecond transient absorption spectrum of F8BT-HAPAPP chlorobenzene solution (0.65 mg/mL) excited with a pump wavelength of 518 nm. Obtained with an excitation energy of 21 μ J cm^{-2} . Solution was degassed via three cycles of freeze pump thawing and placed under an N_2 atmosphere. Inset: the same spectral data normalised to the peak maxima, demonstrating the presence of spectral evolution.

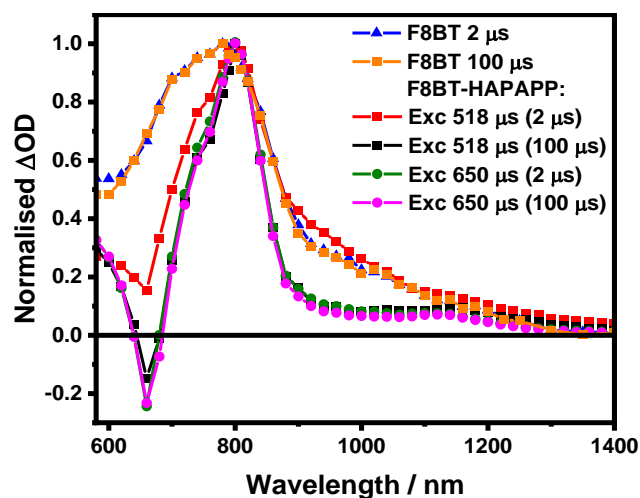


Figure 4.29 Microsecond transient absorption spectra of F8BT and F8BT-HAPAPP. F8BT-HAPAPP was selectively excited with a pump wavelength of 518 and 650 nm, corresponding to excitation of the F8BT or HAPAPP respectively. Solution was degassed via three cycles of freeze pump thawing and placed under an N_2 atmosphere. Spectra have been normalised to their respective peak maxima. For F8BT-HAPAPP spectra are taken at 2 and 100 μ s to illustrate the spectral evolution from the F8BT triplet to that of the porphyrin, HAPAPP, triplet.

Now that it has been established that excitation of the HAPAPP Q-band in F8BT-HAPAPP results in photophysics similar to the isolated porphyrin, we will now explore what happens when the F8BT backbone is excited. Selective excitation of F8BT-HAPAPP with 518 nm (figure 4.28) results in markedly different behaviour to when exciting the Q-band with 650 nm, exhibiting a spectrum that evolves over time, which can be observed in the normalised spectrum in the inset of figure 4.28. At early time scales up to 100 μ s the spectrum strongly resembles that of the F8BT triplet, with this resemblance being best observed in figure 4.30 which shows the normalised spectra of both pristine F8BT and F8BT-HAPAPP at 2 μ s. The main $^3F8BT^*$ transition of F8BT-HAPAPP can be clearly seen at 800 nm, red-shifted by 0.04 eV relative to the pristine F8BT and in line with the same red-shift seen for the $^3HAPAPP^*$ transition (as discussed previously). In addition to the transition seen at 800 nm, the F8BT absorption tail which extends out into the NIR (seen most prominently in the region of 900-1000 nm) is also found in F8BT-HAPAPP. However, when going towards the blue side of the 800 nm transition the spectrum is less of a match. This stems from a contribution from the negative porphyrin Q-band ground state bleach, manifesting itself as a reduction in signal amplitude in the region of 600-780 nm when compared to the pristine F8BT. It should be noted that this ground state bleach at 2 μ s does not

result in a negative signal like that of the pristine HAPAPP (or exciting the Q-band of F8BT-HAPAPP), suggesting contribution from the positive signal originating from the F8BT triplet. However, spectral evolution shows that by 100 μs the spectrum now clearly resembles that of the porphyrin instead: the spectrum obtained via exciting the Q-band of F8BT-HAPAPP. This is most evident at 1150 nm, where the less intense $^3\text{HAPAPP}^*$ triplet transition can be observed only at late timescales once the F8BT NIR absorption tail has sufficiently decayed. More subtle evidence can be seen in the form of a narrowing of the $^3\text{F8BT}^*$ main transition to match that of the $^3\text{HAPAPP}^*$. In addition to this, the ground state bleach at 650 nm can be seen to become negative by 100 μs . This is the consequence of a reduction in contribution from the positive signal, originating from the faster decaying/shorter lived $^3\text{F8BT}^*$.

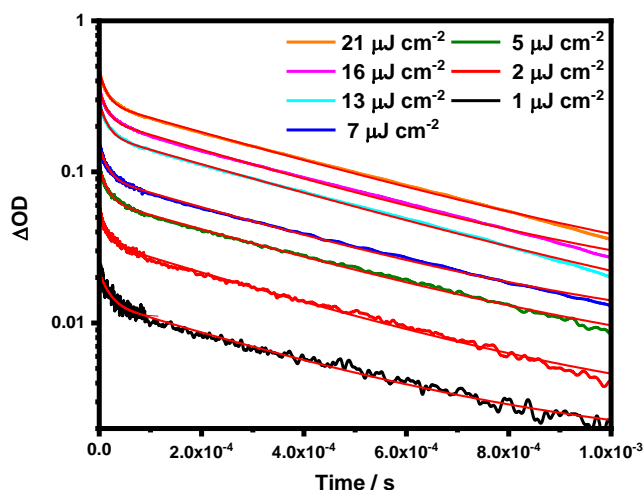


Figure 4.30 Microsecond transient absorption decay kinetics of F8BT-HAPAPP, probed at 800 nm. Obtained using a pump wavelength of 650 nm, with excitation densities ranging from 6 – 15 $\mu\text{J cm}^{-2}$.

Analysis of the decay dynamics of the tentatively ascribed $^3\text{F8BT}^*/^3\text{HAPAPP}^*$ transition at 800 nm reveals that the decay is not purely monoexponential (shown in figure 4.30), but rather possesses an early time scale fast phase and a late time scale slow phase. Indeed, the decay dynamics can be well fit to a biexponential, yielding average lifetimes of $\tau_1 = 15 \pm 3 \mu\text{s}$ and $\tau_2 = 409 \pm 19 \mu\text{s}$ (where the error is the standard deviation) and where the fast phase contributes $\sim 40\%$ to the overall decay. The fast phase is unlikely to derive from triplet-triplet annihilation, as its magnitude relative to the slow phase is found to be invariant to the excitation density. This is shown in figure 4.31, where a plot of the normalised signal amplitude at 1.2 and 120 μs (corresponding to the decays at fast and slow phases respectively) demonstrates almost identical linear signal responses to the range of excitation energies employed (2-21 $\mu\text{J cm}^{-2}$). As discussed previously, there was spectral evidence for formation of

the $^3\text{F8BT}^*$ triplet at early time scales, followed by the $^3\text{HAPAPP}^*$ at late time scales: this spectral evolution is consistent with the presence of two decay phases. This short lifetime of $\tau_1 = 15 \mu\text{s}$ does appear to be within error of the early decay phase ($\tau_1 = 12 \mu\text{s}$) for the pristine F8BT. However, the early decay phase exhibited for F8BT-HAPAPP contributes substantially more to the overall decay than that of the pristine F8BT (10 vs 40% respectively), which may suggest that they do not originate from the same photophysical process. Moreover, the F8BT triplet in F8BT-HAPAPP is found to decay faster than the one found in the corresponding pristine F8BT solution. This is readily apparent in the normalised $\mu\text{s-TA}$ spectra, where a comparison of the pristine F8BT and F8BT-HAPAPP solution spectra at $100 \mu\text{s}$ clearly demonstrates that the F8BT triplet is still present in the pristine F8BT's spectrum, whereas in F8BT-HAPAPP it is absent (as can be observed most prominently by reduced absorption in the regions 750 and 950 nm). This is suggestive that the F8BT triplet formed via ISC in F8BT-HAPAPP is being quenched. One such process that could account for this reduction in F8BT triplet lifetime is that of triplet energy transfer, whereby a F8BT triplet undergoes energy transfer to yield the porphyrin triplet. As such, the $\tau_1 = 15 \mu\text{s}$ decay phase in F8BT-HAPAPP can be ascribed to that of a triplet energy transfer (TET) process from the F8BT to the porphyrin. Probing the slow phase of the F8BT-HAPAPP decay reveals that it is excitation density independent (figure 4.31), thus ruling out contributions from any second-order processes. Interestingly, the lifetime of the longest phase ($\tau_2 = 409 \mu\text{s}$) is found to be near to that obtained for the $^3\text{HAPAPP}^*$ ($\tau_2 = 470$) when exciting the Q-band with 650 nm. This would therefore suggest that the species responsible for the spectrum observed by $100 \mu\text{s}$ does indeed derive from that of the $^3\text{HAPAPP}^*$, even though the F8BT backbone was excited. The significance of these findings will be discussed shortly.

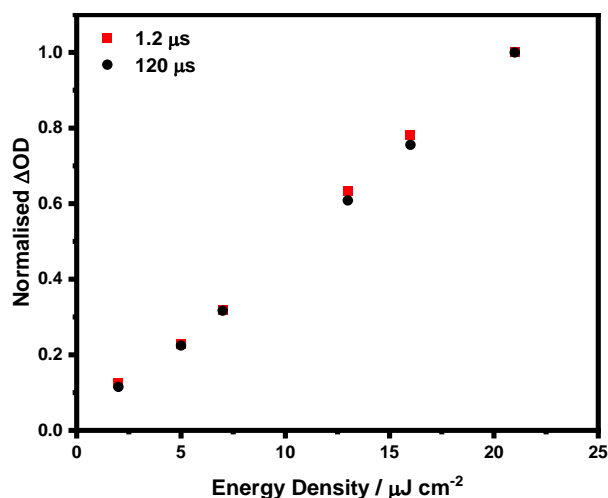


Figure 4.31 Normalised signal amplitudes obtained from the kinetic decays of F8BT-HAPAPP chlorobenzene solution (0.65 mg/mL) excited with a pump wavelength of 518 nm. Signal amplitudes were taken at 1.2 and 120 μs corresponding to the decay of the fast and slow phases respectively.

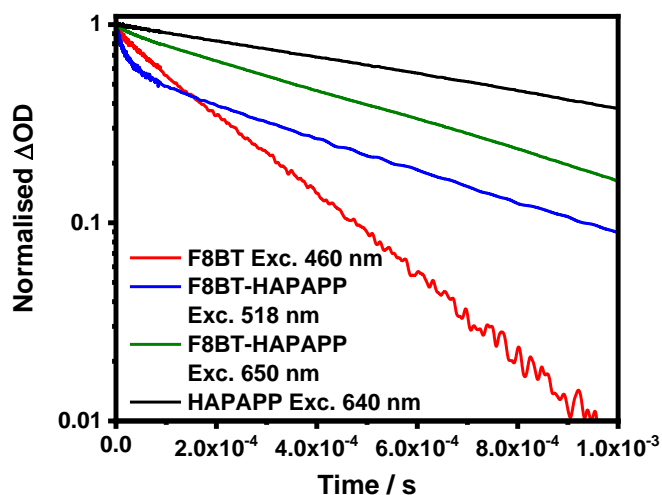


Figure 4.32 Microsecond transient absorption decay kinetics of F8BT, F8BT-HAPAPP and HAPAPP, obtained at a probe wavelength of 800 nm. Solution was degassed via three cycles of freeze pump thawing and placed under an N_2 atmosphere. Varying excitation energies were used, with excitation densities ranging from 6 – 9 $\mu J cm^{-2}$. Kinetics decays have been normalised to the value at 1 μs .

4.7 A note on Oxygen sensitivity and reproducibility

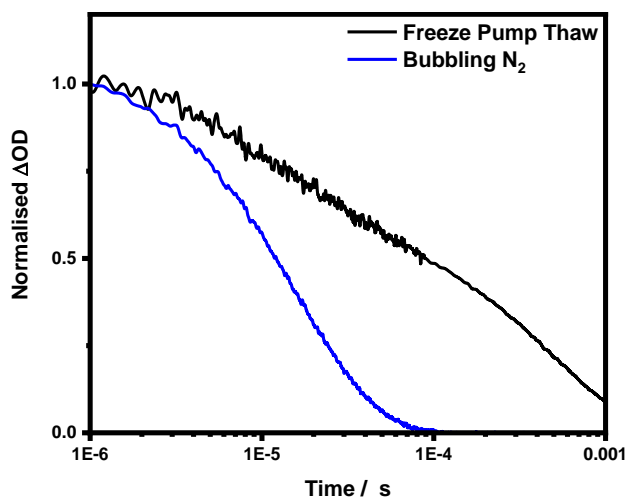


Figure 4.33 Microsecond transient absorption decay kinetics of F8BT-HAPAPP, probed at 800 nm and illustrating the difference in kinetics obtained from degassing via bubbling with N₂ or using a freeze pump thaw technique. Obtained using a pump wavelength of 518 nm, with excitation density of 7 μJ cm⁻².

Throughout the course of the solution transient absorption investigation, reproducibility was found to be a major issue (particularly for μs-TAS) which needed to be overcome. This was primarily due to the experimental technique of bubbling an inert gas through a solution in a screw top cuvette being inadequate at removing all oxygen. The F8BT and HAPAPP triplet signals were found to be extremely sensitive to the presence of oxygen and as such necessitated the development of a more rigorous and consistent methodology for removing all O₂ from the solution. The freeze pump thaw technique was chosen, in conjunction with a custom made youngs tap quartz cuvette. This allowed for better removal of oxygen, and resealing under an inert N₂ atmosphere, enhancing reproducibility. Figure 4.32 displays the kinetics of the F8BT-HAPAPP triplet obtained from either the bubbling method or freeze pump thaw. The freeze pump thaw method clearly results in a much longer decay when compared to just bubbling the solution for 30 mins, therefore allowing for determining much more accurate species (particularly triplet) lifetimes.

The initial fluorescence data of F8BT-HAPAPP suggested that TTA-UC was not operative upon excitation of the HAPAPP Q-band at 650 nm, as indicated by an absence of upconverted F8BT fluorescence, which was the initial intention of the system. The ps TAS data clearly demonstrated that only the porphyrin singlet and triplet species were generated upon photoexcitation of the Q-band. The presence of only the $^3\text{HAPAPP}^*$ was further confirmed by μs TAS, which yielded a near identical triplet spectrum to that of the control pristine HAPAPP. This $^3\text{HAPAPP}^*$ state can therefore be assumed to derive from intersystem crossing of the $^1\text{HAPAPP}^*$ state, which is a ubiquitous feature of porphyrin systems.²⁷ F8BT triplets were not identified under these conditions, suggesting triplet energy transfer (TET) was not occurring from the porphyrin moiety to the F8BT backbone, therefore removing the possibility of TTA-UC.

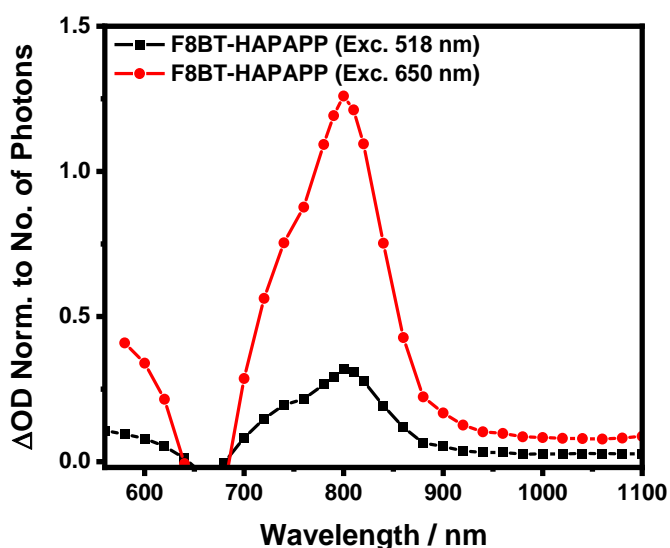


Figure 4.35 Microsecond transient absorption spectra of F8BT-HAPAPP chlorobenzene solution, excited with pump wavelengths of 518 and 650 nm. Spectra are taken at 100 μs and have been normalised to the number of photons absorbed. The porphyrin triplet peak at 800 nm when exciting at 518 nm is 25% of the value of that obtained when exciting at 650 nm.

In contrast to excitation of the Q-band with 650 nm, exciting the F8BT backbone with 518 nm results in distinctively different photophysics relative to its pristine control, with the proposed mechanism shown in figure 4.33 (including those for the pristine F8BT and HAPAPP controls). The ps-TA data obtained when exciting with 518 nm unambiguously demonstrates the formation of the $^1\text{F8BT}^*$ state, by exhibiting a near identical transition at 975 nm to that of the control pristine F8BT solution. The main difference between the F8BT-HAPAPP and that of the pristine F8BT was the introduction of an additional $^1\text{F8BT}^*$ deactivation channel in the dynamics. This

Chapter 4

elucidates why there was an observed reduction in ϕ_F from 0.85 to 0.60 (for F8BT and F8BT-HAPAPP respectively) upon inclusion of the porphyrin into the F8BT. This new decay component was ascribed to the presence of a singlet energy transfer (SET) process from the F8BT to the HAPAPP, occurring with an efficiency of $\sim 19\%$ to yield the $^1\text{HAPAPP}^*$ state. The $^1\text{HAPAPP}^*$ formed via SET was then observed to undergo intersystem crossing ($\phi_{\text{ISC}} = 0.91$) to the triplet manifold, to yield the $^3\text{HAPAPP}^*$ state. This $^3\text{HAPAPP}^*$ could then be observed in the μs -TA spectrum at long time scales ($>100 \mu\text{s}$), once the $^3\text{F8BT}^*$ signal had sufficiently decayed. In addition to the $^3\text{HAPAPP}^*$ formed via ISC from the $^1\text{HAPAPP}^*$ state, there was also evidence for triplet energy transfer (TET) from the $^3\text{F8BT}^*$ to the $^3\text{HAPAPP}^*$ state in the form of a fast decay phase, which was only observed when exciting the F8BT.

Correcting the μs -TA spectra of F8BT-HAPAPP (both excitation with 518 and 650 nm) for the number of photons absorbed (shown in figure 4.34), allows for a direct comparison of the $^3\text{HAPAPP}^*$ generation efficiency and to further assess the plausibility of the proposed energy transfer mechanisms. As expected, direct excitation of the porphyrin results in the formation of a greater population of $^3\text{HAPAPP}^*$ when compared to excitation of the F8BT component. Nonetheless, excitation of the F8BT still results in the formation of a substantial $^3\text{HAPAPP}^*$ population, suggesting that both SET and TET is relatively efficient. Assuming no losses, the quantum yield for $^3\text{HAPAPP}^*$ generated via energy transfer (ϕ_{ET}) should be the sum of ϕ_{SET} and ϕ_{TET} over the ϕ_{ISC} for HAPAPP (as shown in equation 4.2). The upper limit for ϕ_{TET} (with the assumption of zero IC) can be estimated from the previously determined $\phi_F = 0.60$ and $\phi_{\text{SET}} = 0.19$, yielding a maximum theoretical yield of $\phi_{\text{TET}} = 1 - (0.60 + 0.19) = 0.21$. This value of $\phi_{\text{TET}} \leq 0.21$ represents the maximum theoretical yield for energy transfer to produce the $^3\text{HAPAPP}^*$ state, but it is noted that the actual yield is likely to be much lower because of the expected poor intersystem crossing rate for F8BT. This relatively poor ISC is expected to stem from F8BT's large $S_1\text{-}T_1$ gap of ~ 0.7 eV, lack of heavy atoms to induce spin orbit coupling and relatively large $S_1\text{-}S_0$ gap (which is also indicative that IC will be low). Indeed, a study by Ford et al. estimated $\phi_{\text{ISC}} = 0.019$ for F8BT.⁵³

$$\phi_{\text{ET}} = \frac{\phi_{\text{SET}} + \phi_{\text{TET}}}{\phi_{\text{ISC}}} = \frac{0.19 + 0.21}{0.91} = 0.44 \quad \text{Eqn. 4.2}$$

As previously discussed, the amplitude/ ΔOD of the $^3\text{HAPAPP}^*$ obtained with 518 nm was found to be 25% of that exhibited for direct porphyrin excitation with 650 nm, which indicates that the estimated value of $\phi_{\text{ET}} = 0.44$ is too high. The ϕ_{TET} is therefore likely to be lower (given that the previous value of 0.21 was approximated as an upper

Chapter 4

limit with the assumption of no IC), with a computed value of $\phi_{\text{TET}} = 0.04$ to account for the observed 25% signal, which is close to the reported $\phi_{\text{ISC}} = \sim 0.02$ for F8BT.⁵³ This observation is indicative that SET (with subsequent efficient ISC) constitutes the main porphyrin triplet population pathway when exciting with 518 nm.

We will now further discuss the origin of both the observed SET and TET pathways in F8BT-HAPAPP. SET was found to occur on a timescale of 140 ps, much shorter than the 1.9 ns $^1\text{F8BT}^*$ fluorescence lifetime, thereby providing an effective deactivation pathway for the $^1\text{F8BT}^*$. The proposed SET mechanism is expected to be dominant when $^1\text{F8BT}^*$ states are generated within the singlet exciton diffusion distance of the HAPAPP moiety (<8 nm),⁵⁴ as intersystem crossing (ISC) is less competitive due to it being a much slower process. On the other hand, $^1\text{F8BT}^*$ which are generated beyond the exciton diffusion distance of F8BT (>8 nm) will undergo the standard F8BT radiative and non-radiative relaxation pathways. The TET pathway derives from those F8BT singlet states which undergo ISC ($\phi_{\text{ISC}} \leq 0.21$) instead of fluorescence, to yield the $^3\text{F8BT}^*$ state. This resulting $^3\text{F8BT}^*$ state possesses a diffusion length of 180 nm,³¹ which is considerably longer when compared to the ~ 8 nm diffusion length of the $^1\text{F8BT}^*$. This longer diffusion length is a consequence of the $^3\text{F8BT}^*$ longer lifetime relative to the $^1\text{F8BT}^*$. This allows for the possibility of F8BT triplets being able to diffuse to a porphyrin centre within their lifetime and subsequently undergo TET. The hypothesised photophysical mechanism taking place upon excitation of F8BT or HAPAPP in F8BT-HAPAPP is displayed in figure 4.35.

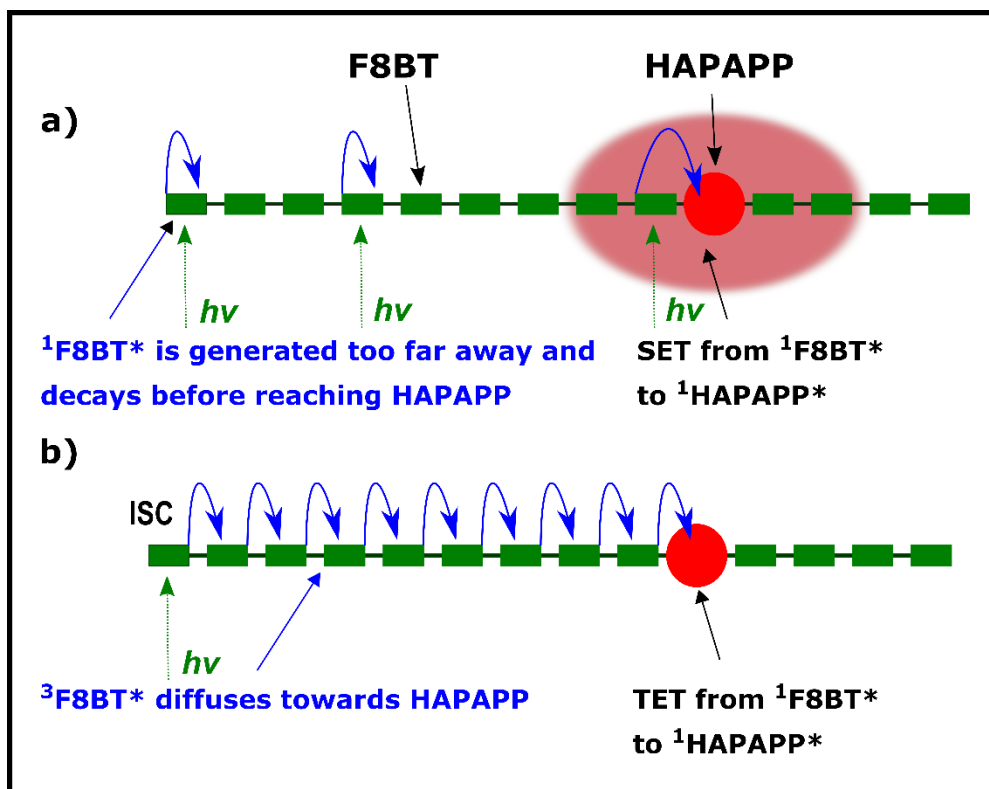


Figure 4.36 Schematic representation of a) Singlet energy transfer (SET) from the initially excited F8BT, to that of the porphyrin HAPAPP. F8BT moieties excited near the porphyrin may undergo rapid SET and subsequent IC/ISC. Those F8BT moieties excited beyond the diffusion distance of the porphyrin may undergo the standard photophysics of the control F8BT. b) Triplet energy transfer (TET) from F8BT triplets formed from ISC, to that of the porphyrin HAPAPP. ¹F8BT* states initially excited may undergo ISC to yield the ³F8BT* state. The long lifetime of the ³F8BT* permits diffusion towards the porphyrin with subsequent TET.

Interestingly, the porphyrin triplet lifetime of F8BT-HAPAPP (470 μ s) is found to be less than half of the pure porphyrin (1.2 ms), but still substantially longer than that of the F8BT (214 μ s). Such behaviour has been observed in a Pt-porphyrin-polythiophene hybrid polymer,⁵⁵ which was attributed to an energy transfer equilibrium between the porphyrin and polymer triplet populations. However, in that case no spectral evolution was observed. This is in contrast to the μ s-TA spectrum of F8BT-HAPAPP, which exhibits a clear evolution from the F8BT triplet to that of the porphyrin triplet on the early microsecond timescale, upon excitation of the F8BT component. Furthermore, the F8BT-HAPAPP porphyrin triplet decay is found to be monoexponential and thus no higher order quenching effects arising from clustering of the porphyrin units together in the polymer chain are evident.

Chapter 4

Theoretical calculations were provided by Dr Tracey Clarke (UCL) and are included for completion. DFT (B3LYP/6-31G(d)) calculations were performed on a F8BT-HAPAPP model (shown in figure 4.36) in conjunction with a Mulliken orbital composition analysis shows that the molecular orbital density of both the HOMO and LUMO partially extend across the F8BT in addition to the porphyrin (6.5 and 7.2% of the total orbital density, respectively, are located on the F8BT). This greater delocalisation of the hybrid system's frontier molecular orbitals is afforded via the additional alkyne bond, which enhances the planarity of the porphyrin relative to the polymer chain. The previously reported Pt-porphyrin hybrid polymer was found to possess a much more distorted structure, thus reducing the possibility of delocalisation of the porphyrin MOs onto the polymer chain. Another relevant observation is that the F8BT-HAPAPP is found to possess two isoenergetic benzothiadiazole-localised unoccupied MOs (LUMO +1/ +2) that are interposed between the energetically close porphyrin-based LUMO and LUMO +3 (with the latter being identical to the pristine porphyrin's LUMO +1). Given that the close proximity in energy of these benzothiadiazole and porphyrin localised unoccupied MOs, orbital mixing would be expected to be present. This hypothesis was further investigated via time dependant density functional theory (TD-DFT) calculations. It is noted that the triplet energies are unlikely to be highly accurate using this methodology, however, the transition contributions to each excited state are the parameter of most interest. As expected, the T_1 state of the porphyrin unit is calculated to involve a simple HOMO-LUMO transition. TD-DFT calculations on the F8BT-HAPAPP, however, suggest multiple transitions contribute to the T_1 state. The expected porphyrin-based HOMO-LUMO dominates, however, an appreciable contribution from the HOMO→LUMO +2 transition, which involves the F8BT's benzothiadiazole, is also present. It is known from literature that the T_1 state of F8BT is localised upon the benzothiadiazole unit. Thus, the T_1 state of F8BT-HAPAPP appears to possess dual HAPAPP/F8BT character, yielding a triplet lifetime that is intermediate between the two pristine materials.

Overall, although the main aim of achieving a self-upconverting polymer was not achieved, a rich photophysical mechanism was elucidated for F8BT-HAPAPP. The results of this investigation can therefore be used to establish several fundamental design principles for realising porphyrin containing intramolecular TTA-UC polymer materials. The first design principle involves limiting the polymeric host's band edge to <2.5 eV, assuming the 0.7 eV singlet-triplet splitting holds true.⁴² This is to ensure the polymer triplet level is lower than of the Zn porphyrin's. However, reducing the bandgap of the polymer too much will render useless the concept of a polymer that

absorbs in the visible and a sensitiser that absorbs in the NIR. One possible avenue would be to synthetically raise the triplet energy level of the ZnTPP, however, this has yet to be achieved. An alternative method involves utilising a heavier metal porphyrin congener, such as PdTPP, which possesses a higher triplet energy of 1.82 eV.⁵⁶ The use of these heavier metals unfortunately often comes with a blue shift in the porphyrin Q-band, thereby reducing its effectiveness as an NIR absorber.

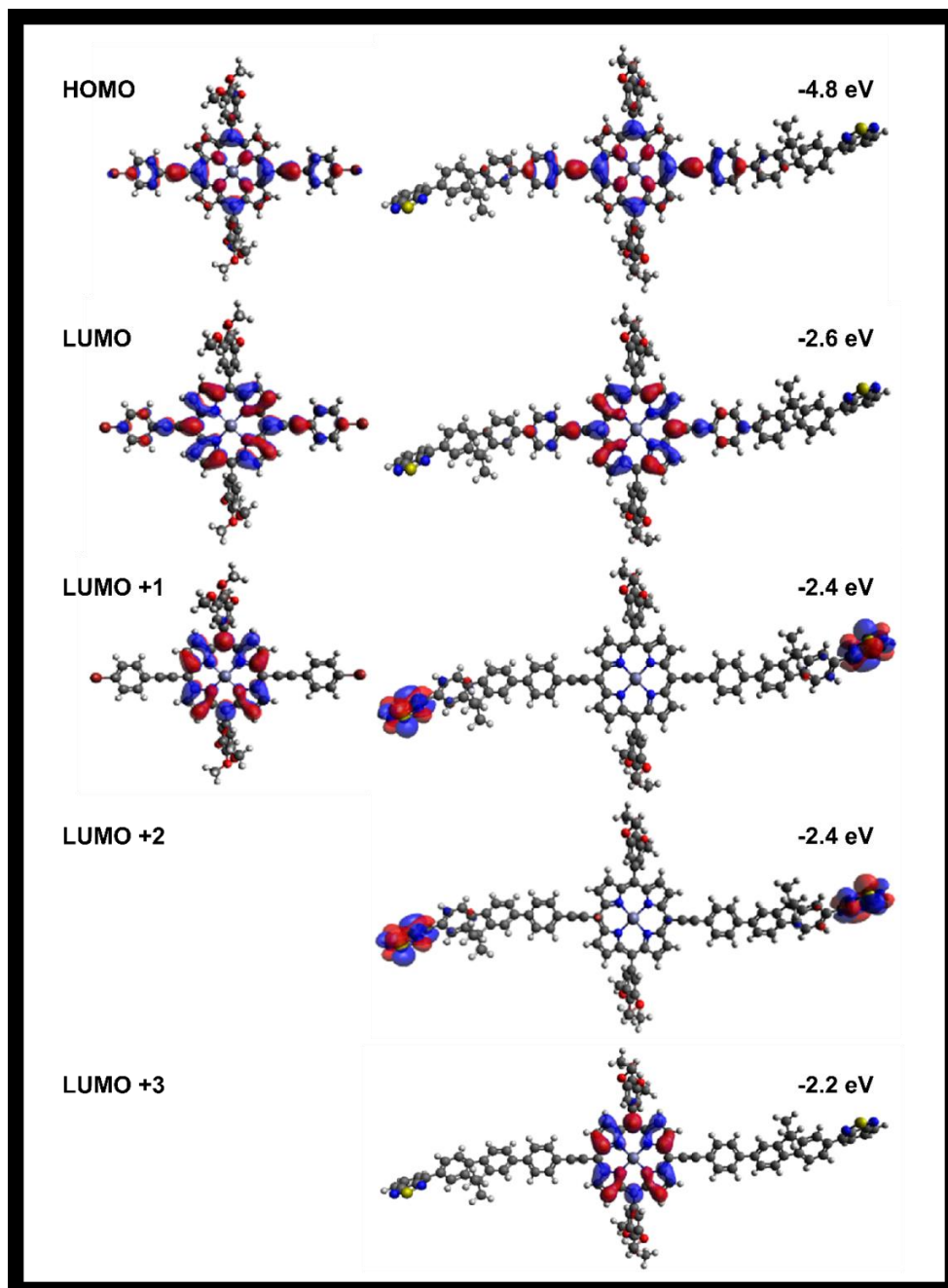


Figure 4.37 Molecular orbitals of a F8BT-HAPAPP model and HAPAPP calculated using a B3LYP/6-31G(d). Note that the LUMO +1 and LUMO +2 of F8BT-HAPAPP are isoenergetic and identical except for inversion of the wavefunction phase symmetry. Results provided by Dr Tracey Clarke.

Table 4.5 Selected TD-DFT results for HAPAPP and an F8BT-Model using B3LYP/6-31G(d). Coefficient represents the transition contribution. Results provided by Dr Tracey Clarke.

Molecule	State	Transition	Coefficient
HAPAPP	T ₁	HOMO→LUMO	0.70
F8BT-HAPAPP	T ₁	HOMO→LUMO	0.68
F8BT-HAPAPP	T ₁	HOMO→LUMO +2	-0.12

4.9 Conclusion

In this investigation, a zinc tetraphenyl porphyrin derivative was introduced (approximately 10% by weight) into the backbone of the polymer F8BT. This was for the purpose of obtaining a single polymer self-upconverting system. A combination of ps and μs transient absorption spectroscopy was used to reveal that TTA-UC was not occurring and that the porphyrin triplet was formed irrespective of whether the F8BT or HAPAPP components were excited. Upon excitation of the F8BT backbone, two triplet formation pathways were found to be present. This was a consequence of where the F8BT singlet exciton was initially formed on the polymer backbone. If the F8BT exciton was formed within the singlet exciton diffusion distance of a HAPAPP unit, it could undergo singlet energy transfer, followed by ISC to yield the porphyrin triplet. F8BT excitons which were generated within the bulk of the F8BT polymer were found to undergo the intrinsic F8BT decay pathways, with a small percentage intersystem crossing over to the triplet manifold. These F8BT triplet states could then diffuse to a porphyrin unit and undergo triplet energy transfer. The F8BT-HAPAPP triplet that resulted was found to possess a lifetime intermediate between the two control samples. This intermediate lifetime was ascribed to orbital mixing of energetically close porphyrin and benzothiadiazole-based unoccupied molecular orbitals, resulting in a mixed F8BT/porphyrin triplet state.

Although TTA-UC was not observed in F8BT-HAPAPP, the observation of triplet energy transfer from the F8BT to the porphyrin is of significance. This is because if triplet energy transfer can occur in one direction in F8BT-HAPAPP, it stands to be reasoned that with optimised energetics, triplet energy transfer could occur from the porphyrin to a host polymer, thus allowing for a TTA-UC donor polymer.

4.10 Bibliography

- 1 Y. C. Simon and C. Weder, *J. Mater. Chem.*, 2012, **22**, 20817.
- 2 W. Shockley and H. J. Queisser, *J. Appl. Phys.*, 1961, **32**, 510–519.
- 3 J. Nelson, *The Physics of Solar Cells*, Imperial College Press, London, UK, 2003.
- 4 K. Vandewal, A. Gadisa, W. D. Oosterbaan, S. Bertho, F. Banishoeib, I. Van Severen, L. Lutsen, T. J. Cleij, D. Vanderzande and J. V. Manca, *Adv. Funct. Mater.*, 2008, **18**, 2064–2070.
- 5 N. J. Turro, V. Ramamurthy and J. C. Scaiano, *Modern Molecular Photochemistry of Organic Molecules*, University Science Books, Sausalito, California, 2010, pp. 414–416.
- 6 C. A. Parker and C. G. Hatchard, *Trans. Faraday Soc.*, 1963, **59**, 284.
- 7 V. Jankus, E. W. Snedden, D. W. Bright, V. L. Whittle, J. A. G. Williams and A. Monkman, *Adv. Funct. Mater.*, 2013, **23**, 384–393.
- 8 J. S. Seixas De Melo, J. Pina, F. B. Dias and A. L. Maçanita, *Applied Photochemistry*, Springer Netherlands, Dordrecht, 2013, pp. 533–585.
- 9 M. J. Y. Tayebjee, D. R. McCamey and T. W. Schmidt, *J. Phys. Chem. Lett.*, 2015, **6**, 2367–2378.
- 10 Y. Y. Cheng, T. Khoury, R. G. C. R. Clady, M. J. Y. Tayebjee, N. J. Ekins-Daukes, M. J. Crossley and T. W. Schmidt, *Phys. Chem. Chem. Phys.*, 2010, **12**, 66–71.
- 11 D. Y. Kondakov, *J. Soc. Inf. Disp.*, 2009, **17**, 137.
- 12 D. Y. Kondakov, *Philos. Trans. R. Soc. A Math. Phys. Eng. Sci.*, 2015, **373**, 20140321–20140321.
- 13 R. D. . Froese and K. Morokuma, *Chem. Phys. Lett.*, 1999, **305**, 419–424.
- 14 B. Dick and B. Nickel, *Chem. Phys.*, 1983, **78**, 1–16.
- 15 T. N. Singh-Rachford, A. Haefele, R. Ziessel and F. N. Castellano, *J. AM. CHEM. SOC.*, 2008, **130**, 29.
- 16 T. N. Singh-Rachford and F. N. Castellano, *Coord. Chem. Rev.*, 2010, **254**, 2560–2573.

Chapter 4

- 17 A. Monguzzi, R. Tubino and F. Meinardi, *Phys. Rev. B*, 2008, **77**, 155122.
- 18 Y. Y. Cheng, T. Khoury, R. G. C. R. Clady, M. J. Y. Tayebjee, N. J. Ekins-Daukes, M. J. Crossley and T. W. Schmidt, *Phys. Chem. Chem. Phys.*, 2010, **12**, 66–71.
- 19 J. E. Auckett, Y. Y. Chen, T. Khoury, R. G. C. R. Clady, N. J. Ekins-Daukes, M. J. Crossley and T. W. Schmidt, *J. Phys. Conf. Ser.*, 2009, **185**, 012002.
- 20 S. M. Bachilo and R. B. Weisman, *J. Phys. Chem. A*, 2000, **104**, 7711–7714.
- 21 A. Haefele, J. Rg Blumhoff, R. S. Khnayzer and F. N. Castellano, *J. Phys. Chem. Lett*, 2012, **3**, 299–303.
- 22 C. A. Parker and C. G. Hatchard, *Proc. R. Soc. London. Ser. A. Math. Phys. Sci.*, 1962, **269**, 574–584.
- 23 R. R. Islangulov, D. V. Kozlov and F. N. Castellano, *Chem. Commun.*, 2005, **0**, 3776.
- 24 W. Zhao and F. N. Castellano, *J. Phys. Chem. A*, 2006, **110**, 11440–11445.
- 25 A. Monguzzi, R. Tubino and F. Meinardi, *Phys. Rev. B*, 2008, **77**, 155122.
- 26 Y. V. Aulin, M. van Seville, M. Moes and F. C. Grozema, *RSC Adv.*, 2015, **5**, 107896–107903.
- 27 J. E. Rogers, K. A. Nguyen, D. C. Hufnagle, D. G. McLean, W. Su, K. M. Gossett, A. R. Burke, S. A. Vinogradov, R. Pachter and P. A. Fleitz, *J. Phys. Chem. A*, 2003, **107**, 11331–11339.
- 28 W. A. Lee, M. Grätzel and K. Kalyanasundaram, *Chem. Phys. Lett.*, 1984, **107**, 308–313.
- 29 P. G. Seybold and M. Gouterman, *J. Mol. Spectrosc.*, 1969, **31**, 1–13.
- 30 R. Giovannetti, in *Macro To Nano Spectroscopy*, InTech, 2012, pp. 91–92.
- 31 B. H. Wallikewitz, D. Kabra, S. Gélinas and R. H. Friend, *Phys. Rev. B*, 2012, **85**, 045209.
- 32 I. A. Howard, J. M. Hodgkiss, X. Zhang, K. R. Kirov, H. A. Bronstein, C. K. Williams, R. H. Friend, S. Westenhoff and N. C. Greenham, *J. Am. Chem. Soc.*, 2010, **132**, 328–335.
- 33 A. Köhler and D. Beljonne, *Adv. Funct. Mater.*, 2004, **14**, 11–18.

Chapter 4

- 34 K. G. Jespersen, W. J. D. Beenken, Y. Zaushitsyn, A. Yartsev, M. Andersson, T. Pullerits and V. Sundström, *J. Chem. Phys.*, 2004, **121**, 12613.
- 35 M. K. Kuimova, M. Hoffmann, M. U. Winters, M. Eng, M. Balaz, I. P. Clark, H. A. Collins, S. M. Tavender, C. J. Wilson, B. Albinsson, H. L. Anderson, A. W. Parker and D. Phillips, *Photochem. Photobiol. Sci.*, 2007, **6**, 675.
- 36 J. C. Koziar and D. O. Cowan, *Acc. Chem. Res.*, 1978, **11**, 334–341.
- 37 A. P. Monkman, H. D. Burrows, L. J. Hartwell, L. E. Horsburgh, I. Hamblett and S. Navaratnam, *Phys. Rev. Lett.*, 2001, **86**, 1358–1361.
- 38 S. Cook, A. Furube and R. Kato, *Energy Environ. Sci.*, 2008, **1**, 294.
- 39 C. Yan, A. J. Cadby, A. J. Parnell, W. Tang, M. W. A. Skoda, D. Mohamad, S. P. King, L. X. Reynolds, S. A. Haque, T. Wang, S. R. Parnell, A. B. Holmes, R. A. L. Jones and D. J. Jones, *J. Polym. Sci. Part B Polym. Phys.*, 2013, **51**, 1705–1718.
- 40 S. Cook, H. Ohkita, J. R. Durrant, Y. Kim, J. J. Benson-Smith, J. Nelson and D. D. C. Bradley, *Appl. Phys. Lett.*, 2006, **89**, 101128.
- 41 N. Banerji, S. Cowan, M. Leclerc, E. Vauthey and A. J. Heeger, *J. Am. Chem. Soc.*, 2010, **132**, 17459–17470.
- 42 A. Köhler and H. Bässler, *Mater. Sci. Eng. R Reports*, 2009, **66**, 71–109.
- 43 C.-L. Lee, X. Yang and N. C. Greenham, *Phys. Rev. B*, 2007, **76**, 245201.
- 44 D. B. Moravec, B. M. Lovaasen and M. D. Hopkins, *J. Photochem. Photobiol. A Chem.*, 2013, **254**, 20–24.
- 45 J. Rodriguez, C. Kirmaier and D. Holten, *J. Am. Chem. Soc.*, 1989, **111**, 6500–6506.
- 46 C.-L. Lee, X. Yang and N. C. Greenham, *Phys. Rev. B*, 2007, **76**, 245201.
- 47 C. Grewer and H.-D. Brauer, *J. Phys. Chem.*, 1994, **98**, 4230–4235.
- 48 F. Wilkinson and A. A. Abdel-Shafi, *J. Phys. Chem. A*, 1999, **103**, 5425–5435.
- 49 A. S. Dhoot and N. C. Greenham, *Adv. Mater.*, 2002, **14**, 1834–1837.
- 50 H. Ohkita, S. Cook, T. A. Ford, N. C. Greenham and J. R. Durrant, *J. Photochem. Photobiol. A Chem.*, 2006, **182**, 225–230.
- 51 T. Nojiri, A. Watanabe and O. Ito, *J. Phys. Chem. A*, 1998, **102**, 5215–5219.

Chapter 4

- 52 Z. Gasyna, W. R. Browett and M. J. Stillman, *Inorg. Chem.*, 1985, **24**, 2440–2447.
- 53 T. A. Ford, I. Avilov, D. Beljonne and N. C. Greenham, *Phys. Rev. B*, 2005, **71**, 125212.
- 54 Y. Tamai, H. Ohkita, H. Benten and S. Ito, *J. Phys. Chem. Lett.*, 2015, **6**, 3417–3428.
- 55 R. Andernach, H. Utzat, S. D. Dimitrov, I. McCulloch, M. Heeney, J. R. Durrant and H. Bronstein, *J. Am. Chem. Soc.*, 2015, **137**, 10383–10390.
- 56 J. E. Rogers, K. A. Nguyen, D. C. Hufnagle, D. G. McLean, W. Su, K. M. Gossett, A. R. Burke, S. A. Vinogradov, R. Pachter and P. A. Fleitz, *J. Phys. Chem. A*, 2003, **107**, 11331–11339.

Chapter 5

Investigating the Impact of a Donor-orthogonal Acceptor Architecture on Reducing the Singlet-Triplet Energy Splitting in a Low-band Gap Polymer

5.1 Outline

In this chapter a novel donor-orthogonal acceptor conjugated polymer, Thiro, was spectroscopically investigated. This was for the purpose of further expanding the donor-orthogonal acceptor concept to a low band gap conjugated polymer, which better reflects materials utilised in state of art OPV devices. In a step further, Thiro was also blended with the acceptor molecule PC₆₀BM, to assess whether charge generation could take place with this unique class of donor conjugated polymers. In the introduction a brief overview is given for the photophysical processes of reverse ISC (rISC) and of thermally activated delayed fluorescence (TADF). Furthermore, recent attempts to extend these photophysical phenomena to conjugated polymeric materials, via donor-orthogonal acceptor architecture are also explored.

A brief description of the methodology employed is given, followed by the results of the investigation. Ground state absorbance, photoluminescence, time-correlated single photon counting and transient absorption (ps-ms range) results of pristine Thiro solution and its thin film are provided. Furthermore, a microsecond transient absorption study was also conducted on a bulk heterojunction thin film of Thiro:PC₆₀BM. It was found that pristine Thiro, be it in solution or thin film, yielded facile triplet formation on ultrafast timescales. This rapid triplet population was thought to derive from a spin-orbit charge transfer interaction, afforded by CT states deriving from the perpendicular substituted spirobifluorene groups. Most peculiarly, free charge formation was observed in both the solution and pristine Thiro film, as evidenced via the observation of a radical cation in the μ s-TA spectra. This assignment was further confirmed via comparison with the Thiro:PC₆₀BM in μ s-TA spectra, which is to the best of our knowledge the first time a D-oA conjugated polymer has been investigated in a bulk heterojunction .

5.2 Introduction

A theme prevalent throughout this thesis has been the role of triplet states in the field of organic photovoltaics, both as a potential to act as a loss mechanism or enhance device efficiency.¹ However, the photophysics of the triplet state are primarily dictated by its relative energy level, which itself is governed by the singlet-triplet energy splitting (see section 1.8.1 for more details).² A simplistic approach to eliminating donor triplet excitons as a potential loss pathway in OSCs would be to raise the energy of the triplet above that of the CT state. This could be achieved via reducing ΔE_{ST} . If the ΔE_{ST} becomes sufficiently small, the molecule or polymer may exhibit a photophysical phenomenon known as reverse intersystem crossing (rISC).³ In this process, photogenerated triplet excitons undergo ISC back to the singlet manifold ($T_1 \rightarrow S_1$) in a thermally activated process. In an organic solar cell architecture this would mean that triplet states formed via geminate or bimolecular recombination would not constitute a loss process, as singlets formed via rISC could have another chance at charge separation. In the absence of an acceptor molecule, singlet states formed via rISC may undergo a thermally activated delayed fluorescence (TADF),⁴ which can allow for a fluorescence internal quantum efficiency of 100%.^{5,6} Investigations into TADF have typically involved small molecules which possess a donor-acceptor (D-A),⁷ or donor-acceptor-donor structure (D-A-D),⁸ which are conducive to efficient rISC. This is because these structures allow for the formation of intramolecular CT states, whose excited state conformation breaks the conjugation between the D-A unit (and therefore results in a strong CT interaction). The CT state results in a small overlap between the HOMO and LUMO molecular orbitals, which helps to minimise the exchange energy and in turn the singlet-triplet energy gap.

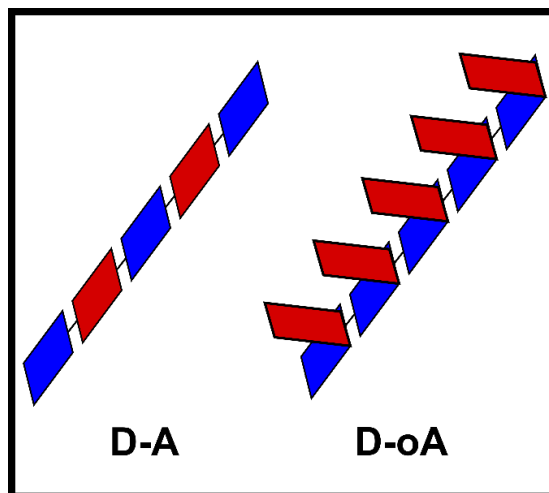


Figure 5.1 Schematic representation of a donor-acceptor (D-A) and a donor-orthogonal acceptor (D-oA) conjugated polymer. The blue and red rectangles represent donor and acceptor units respectively.

Conjugated polymeric materials possess strong absorption and emissive properties, which are largely derived from their extended system of overlapping π and π^* orbitals. These localised and overlapping wavefunctions give rise to a large exchange energy with a systematic observation of $\Delta E_{ST} = \sim 0.7$ eV,² which can result in the triplet exciton being the lowest energy state of an OSC system. In addition, the planarized backbone exhibited by conjugated polymers is in stark contrast to TADF small molecules, which exhibit highly distorted conformations. For example, the D-A-D small molecules DPTZ-DBTO2 and DMePT-TXO2 possess near-orthogonal donor acceptor units, providing an effective means to separate the HOMO and LUMO orbitals and lower the exchange energy to permit rISC.^{9,8} It should be noted, however, that merely reducing the ΔE_{ST} will not necessarily result in efficient rISC in small molecules. As revealed by Ward et al.,¹⁰ for a series of different D-A-D small molecules with very similar ΔE_{ST} a wide range of reverse intersystem crossing rates (k_{rISC}) were observed. They found that by sterically hindering the donor and acceptor group the emission obtained could be switched from TADF to that of phosphorescence. This is indicative of a mechanism that involves molecular vibrations and not just the electronic coupling. Furthermore, theoretical and experimental studies on DPTZ-DPTO2 show that rISC involves spin-orbit coupling between 1CT and 3CT , which is mediated by a local $^3\pi\pi^*$ on the donor or acceptor.^{11,12}

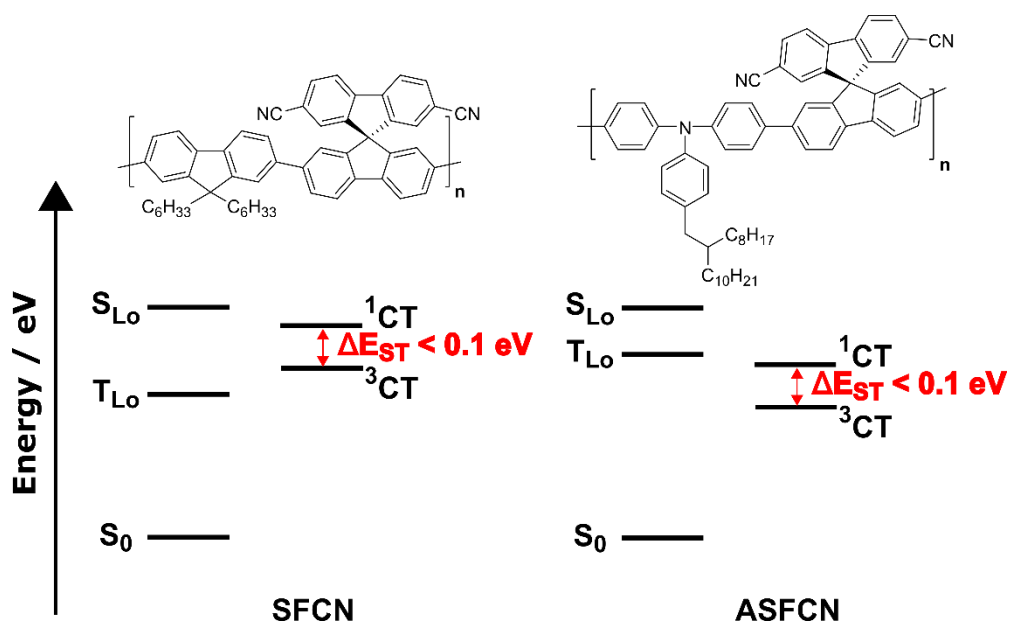


Figure 5.2 Structures of the donor-orthogonal acceptor conjugated polymers SFCN and ASFCN. Note the substituted spiro moiety located orthogonal to the backbone in SFCN and ASFCN. S_{Lo} and T_{Lo} represent local singlet and triplet states respectively.¹³

While previously it was thought that the energy manipulation exhibited in TADF small molecules were near-impossible to extend to conjugated polymers, recent breakthroughs in synthetic and structural control have managed to achieve this. Bronstein et al have recently presented a novel way to effectively reduce the ΔE_{ST} of conjugated D-A copolymers.¹³ D-A copolymers are different to homopolymers (e.g. P3HT, MDMO-PPV) in that they are comprised of one electron-rich moiety (donor) and one electron-deficient moiety (acceptor). Importantly, the HOMO and LUMO energy levels are derived from the HOMO energy of the donor and the LUMO energy of the acceptor. Thus, the energy levels of conjugated polymers may be elegantly tuned via engineering the donor and acceptor units independent from one another.¹⁴ Bronstein et al realised that by removing the electron acceptor moiety from the main chain and positioning it physically orthogonal to the donor backbone (shown schematically in figure 5.1), a significant reduction in the spatial overlap between the frontier molecular orbitals could be achieved. This donor-orthogonal acceptor (D-oA) motif therefore permits a reduction in ΔE_{ST} whilst still maintaining a conjugated backbone, thus allowing for processability and charge transport.

This D-oA effect was observed in the polymers SFCN and ASFCN, with their structures shown in figure 5.2. The presence of orthogonal -CN substituted spirobifluorene groups were found to stabilise the intramolecular CT state below that of the local singlet state located along the polymer backbone. This has the result of

localising the LUMO on the orthogonal spiro groups, thus effectively reducing the spatial overlap between the HOMO and LUMO molecular orbitals. Both SFCN and ASFCN were found to exhibit the formation of CT states below the energy of the main optically allowed π - π^* transition. In SFCN, these CT states were higher in energy than the local triplet, leading to poor rISC efficiency and facile triplet formation. In contrast, ASFCN was found to yield CT states that were lower in energy than the local triplet state, affording TADF via efficient rISC. This TADF was readily apparent via a long-lived fluorescence, which could also be quenched via reducing the temperature to 77 K. Interestingly, the ps-TA of ASFCN in both solution and thin film showed the presence of significant excited state spin-mixing, with a dynamic equilibrium between the ^1CT and $^3(\pi$ - $\pi^*)$ states being observed.

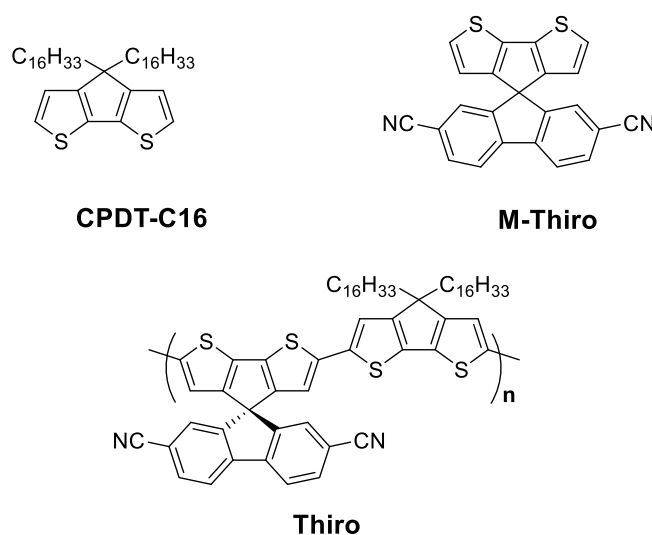


Figure 5.3 Structures of the donor-orthogonal acceptor conjugated polymer *Thiro* and its monomeric derivatives, *CPDT-C16* and *M-Thiro*. Note the substituted spiro moiety located orthogonal to the CPDT backbone on *Thiro*.

The aim of this chapter is to expand on Bronstein et al's previous work by spectroscopically investigating a novel D-oA conjugated polymer, poly-2,6-(4,4-dihexadecyl-4*H*-cyclopenta[2,1-*b*:3,4-*b'*]dithiophene)-alt-2,6-spiro[cyclopenta[2,1-*b*:3,4-*b'*]dithiophene-4,9'-fluorene]-2',7'-dicyanonitrile, referred to as *Thiro* (structure shown in figure 5.3). This is for the purpose of extending the D-oA architecture to that of a low-band gap polymer. As discussed previously (see section 4.1), to efficiently harvest solar energy the absorbing donor polymer should possess good overlap with the solar emission spectrum, which exhibits a maximum solar flux in the red and near-infrared region. As such, low band gap polymers with a broad absorption range can allow for greater efficiency in harvesting solar output. The *Thiro* D-oA polymer is comprised of an electron rich CPDT donor backbone in combination with a dicyano

substituted spirobifluorene, which is located orthogonal along the backbone. This -CN substituted spiro unit was found to be essential in lowering the CT state energies below that of the local $^1(\pi-\pi^*)$, as shown in the aforementioned study by Bronstein et al.¹³ The TFB and polyfluorene backbones used in that study have been replaced by the CPDT moiety, which is well known for its role as the donor component in the intensively studied low band gap D-A polymer PCDTBT.^{15,16} As such, the resulting Thiro polymer should be more reflective of low band gap materials utilised in state of the art devices.

Finally, a Thiro:PC₆₀BM bulk heterojunction film was also studied utilising μ s-TA, to assess whether efficient charge generation occurs for such a D-oA conjugated polymer. To our knowledge this is the first study that investigates the impact of blending an acceptor molecule with the D-oA class of conjugated polymers and as such represents an important step in further developing these unique polymeric systems.

5.3 Experimental

Thiro, including its monomeric constituents 4,4-dihexadecyl-4*H*-cyclopenta[2,1-*b*:3,4-*b'*]dithiophene, CPDT-C16, and spiro[cyclopenta[2,1-*b*:3,4-*b'*]dithiophene-4,9'-fluorene]-2',7'-dicarbonitrile, M-Thiro ($M_n = 6400$ Da and $M_w = 8200$ Da), were synthesised by Alex Forster of the Bronstein Group. PC₆₀BM (>99% purity) was purchased from Ossila. Solutions were prepared via dissolving Thiro in spectroscopic grade chlorobenzene (Alfa Aesar) and stirring overnight at 65 °C in a glovebox, with an N₂ atmosphere. Thin films were prepared via spin-coating from solution (10 μ g/mL) onto ultra-flat quartz substrates (1 mm thickness) for 90 s and at 1600 rpm. Substrates were cleaned via separately sonicating in solutions of deionised water, acetone and isopropanol for 15 min each. The pristine Thiro chlorobenzene solution was prepared with a concentration of 50 μ g/mL. The sample was also degassed by using three cycles of freeze pump thaw and sealing under a N₂ atmosphere. This was achieved using a custom-made Young's tap quartz cuvette with a pathlength of 2 mm, whereby the solution was degassed on a Schleck line and transferred to the cuvette via cannulation. Unless explicitly stated, all measurements were carried out under and inert atmosphere.

For ps-TA measurements, the pristine Thiro solution and thin film were excited with a pump wavelength of 520 nm, with an excitation density range of 5-50 μ J cm⁻². Data was processed using Surface Xplorer.

For $\mu\text{s-TA}$ measurements, the pristine Thiro solution and thin film were excited with a pump wavelength of 532 nm. Excitation density ranges of $6\text{-}81 \mu\text{J cm}^{-2}$ and $2\text{-}61 \mu\text{J cm}^{-2}$ were used for the pristine Thiro solution and thin film respectively. The Thiro:PC₆₀BM 1:1 by weight blend film was excited with a pump wavelength of 530 nm, using an excitation density range of $2\text{-}199 \mu\text{J cm}^{-2}$.

TC-SPC measurements were carried out on a Lifespec II Lifetime spectrometer (Edinburgh Instruments). Measurements for the pristine Thiro solution and thin film were obtained using a laser diode with a pump wavelength of 445 nm, a pulse width of ~ 100 ps, a repetition rate of 50 Mhz and an average power output of ~ 0.10 mW. The instrument response function (IRF) was collected using chlorobenzene solution in a 2 mm pathlength quartz cuvette from Starna scientific for the solution or using poly(methyl methacrylate) for the pristine film.

Time-resolve photoluminescence measurements were carried out at Cambridge University using an ICCD (Andor), with a Solstice Ace pulsed laser (Spectra-Physics). A pump wavelength of 525 nm was used with a power range of $1\text{-}10 \mu\text{W}$, with a 1 kHz repetition rate. A 550 nm long pass filter was used.

Global analysis (GA) was carried out using a previously written programme based on a genetic algorithm. The genetic algorithm was provided by Dr Artem Bakulin (Imperial College London).

5.4 Ground State Absorbance

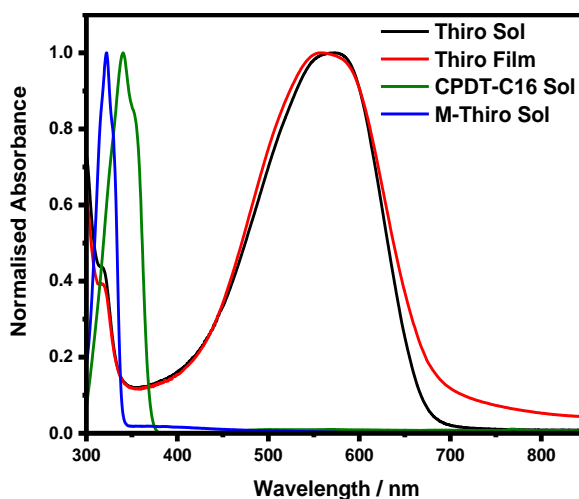


Figure 5.4 Normalised ground state absorbance spectra of pristine Thiro in chlorobenzene solution ($50 \mu\text{g/mL}$) and thin film, including its monomeric constituents *mThiro* and CPDT-C16 in chlorobenzene solution ($10 \mu\text{g/mL}$). Spectra have been normalised to their respective peak maxima.

Figure 5.4 shows the normalised ground state absorbance of both the pristine Thiro thin film and its neat chlorobenzene solution. In addition, Thiro's monomeric constituents spiro[cyclopenta[2,1-*b*:3,4-*b'*]dithiophene-4,9'-fluorene]-2',7'-dicarbonitrile, M-Thiro and 4,4-dihexadecyl-4*H*-cyclopenta[2,1-*b*:3,4-*b'*]dithiophene, CPDT-C16, in chlorobenzene solution are also shown. The orthogonal donor-acceptor copolymer, Thiro, exhibits a distinctively different spectrum to that of its monomeric constituents, with a broad peak appearing at 550 nm. Furthermore, the spectrum differs from the parent CPDT-Polyfluorene backbone spectrum.¹⁷ This new 550 nm peak is likely to derive from a new lower energy π - π^* transition, which results from an extension of the π -system upon conjugation. It is also possible that an additional charge-transfer absorption peak is found beneath or to the red of the broad peak at 550 nm, resulting from a transition from the CPDT backbone to the orthogonal dicyano fluorene unit, but this is likely to possess poor oscillator strength.¹⁸

Interestingly, the pristine Thiro is found to exhibit a very similar absorption profile irrespective of whether it is found in the solution or solid phase. This lack of delineation between the solid and solution phases is likely imparted by the presence of the orthogonal structure and the large C16 alkyl chains located on the polymer, which may inhibit π -stacking of the conjugated backbone and therefore inhibit crystallisation. This behaviour is in contrast to more crystalline systems such as P3HT and DPP, which yield greater spectral difference between the solution and film as a consequence of increased interchain transitions.^{19,20,21,22} A further point to note is that the broad transition at 550 nm does not show prominent vibronic structure, illustrating a large energetic dispersity that may indicate a broad distribution of polymer conformations. This inhomogeneous broadening is found to be more pronounced in the film, thus pointing to increased disorder in the solid phase or an increase in the refractive index, as illustrated by the broadening of the red edge of the 550 nm transition and the presence of a weakly absorbing tail that extends out to 850 nm. Nonetheless, the differences between the solution and film pristine Thiro spectra are relatively small and suggest that polymer aggregates form in solution and are similar in conformation to that of the thin film, indicating that the Thiro film morphology is amorphous in nature. This in turn allows a more direct comparison between the photophysics of the solution and solid phases.

5.5 Fluorescence

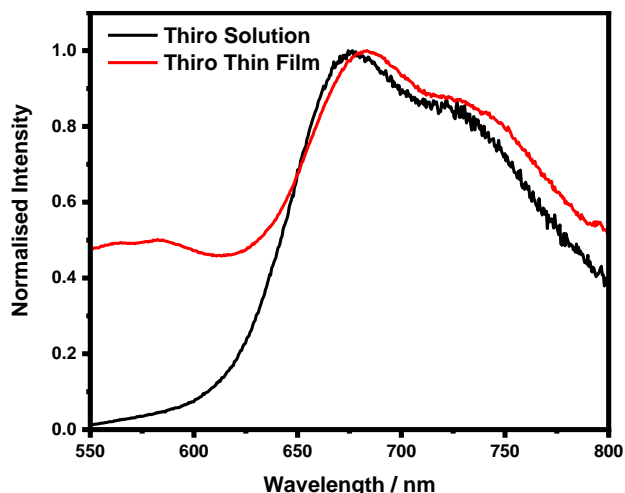


Figure 5.5 Normalised ground state photoluminescence spectra of pristine Thiro in chlorobenzene solution (50 $\mu\text{g}/\text{mL}$) and thin film. Spectra were obtained with an excitation wavelength of 532 nm and have been normalised to their respective peak maxima.

Following optical excitation with 532 nm (2.33 eV) the pristine Thiro in chlorobenzene solution was found to exhibit a relatively broad emission (figure 5.5), with a maxim situated at 680 nm (1.82 eV) and a vibronic shoulder found at ca. 720 nm (corresponding to a vibrational separation of $\sim 800\text{ cm}^{-1}$). This equates to a Stokes shift (given by the energy difference of the respective 0-0 absorption and emission spectra) of 105 nm (0.34 eV). The presence of apparent vibrational structure is suggestive that the observed fluorescence is deriving from a 'local' Thiro singlet state ($^1\text{Th}^*$) and not that of a ^1CT state, which would otherwise yield a featureless, gaussian like emission.^{9,12,13} Herein the term 'local' is used to refer to energetic states that derive from the photophysics of the donor backbone (e.g. $^1(\pi-\pi^*)$ or $^3(\pi-\pi^*)$) and not those that stem from a D to A transition. This observation would imply that if a $^1\text{CT}^*$ state is formed, radiative decay is kinetically outcompeted by intersystem crossing to a ^3CT state, or to a local Thiro triplet state ($^3\text{Th}^*$). Alternatively, this may also imply that the local singlet state is lower in energy than the CT state.

The corresponding pristine Thiro film is found to exhibit a very similar profile to the solution, albeit slightly redshifted, exhibiting a maxim at 685 nm with the additional vibrational shoulder now found at ca. 730 nm. This results in the pristine Thiro film displaying a slightly larger Stokes shift of 111 nm (0.36 eV) relative to the solution. Surprisingly, two additional weaker above-bandgap transitions, not observed in the solution can be seen at 560 and 585 nm and may help to explain the qualitative observation of white fluorescence upon excitation. It is noted, however, that these

transitions were not completely reproducible, but are not likely the result of an experimental artifact, as will be discussed in section 5.7. The optical bandgap for Thiro was approximated from the intersection of the absorption and emission edge of the transitions at 550 and 680 nm and found to be 1.86 and 1.81 eV for the solution and film respectively. It is important to note that this optical bandgap is likely to derive from the S_2 state, owing to the S_1 state likely being that of a 'dark' CT state.

5.6 Time-Correlated Single Photon Counting

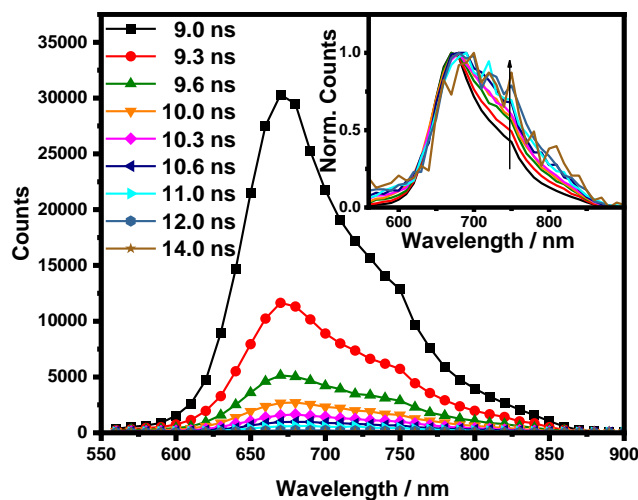


Figure 5.6 Time-correlated single photon counting obtained for pristine Thiro in chlorobenzene solution ($50 \mu\text{g/mL}$). Obtained with a pump wavelength of 467 nm and carried out under and N_2 atmosphere. Inset: The same spectral data normalised to the peak maxima, illustrating the presence of a long-lived transition to the red of the main emission. The black arrow demonstrates the spectral evolution over time. Data collected at Imperial College London.

Time correlated single photon counting (TC-SPC) measurements were carried out on both the pristine Thiro solution and thin film to investigate if an appreciable long-lived fluorescence deriving from TADF could be observed. Preliminary TC-SPC measurements were initially carried out at Imperial College London, where a time-resolved emission spectrum (TRES) was obtained for the pristine Thiro solution (shown figure 5.6). An initial prompt fluorescence is found to dominate the spectrum with the observed emission maximum at 670 nm, in approximate agreement with the emission maximum of ~ 680 nm observed in the corresponding steady state PL. Once the prompt transition has sufficiently decayed, a new much weaker longer-lived transition can be observed in the region of ca. 730 nm. This subtle spectral evolution is best observed in the normalised transient spectrum displayed in the inset of figure 5.6. It is possible that this longer-lived contribution derives from emission of a lower-

energy CT state, owing to it being found red-shifted to the main emission and possessing a much weaker transition intensity. Unfortunately, due to material and time limitations a corresponding TRES spectrum for the thin film could not be obtained.

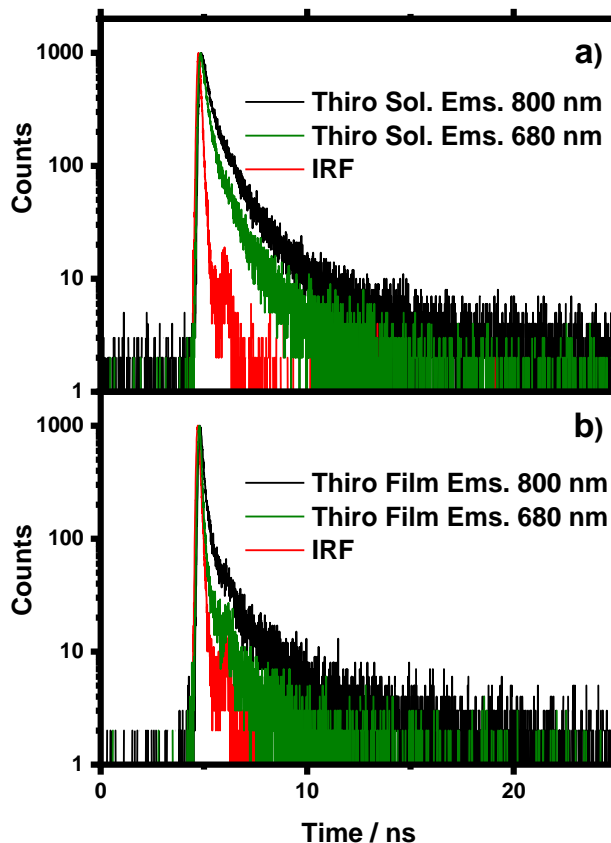


Figure 5.7 Time-correlated single photon counting obtained for a) pristine Thio in chlorobenzene solution (50 $\mu\text{g/mL}$) and b) pristine Thio thin film. Obtained with an excitation wavelength of 445 nm and at probe wavelengths of a) 680 and b) 800 nm. IRF is the instrument response function and yields a temporal resolution of ~ 5 ns. Data collected at UCL.

The PL decays obtained for the pristine solution and film are shown in figure 5.7 a) and b) respectively and illustrate a relatively short-lived decay that is multiexponential in nature. The PL decay for the pristine Thio solution at 680 nm may be fit to a biexponential function, yielding lifetimes of $\tau_1 = 0.3 \pm 0.1$ ns and $\tau_2 = 1.4 \pm 0.1$ ns (where the error is from fitting). This PL decay is also found to be faster in the pristine film when compared to its solution, which is a common occurrence due to increased non-radiative decay pathways in the solid phase.^{19,23} However, accurate fitting is difficult, due to the pristine Thio thin film PL decay possessing contributions from the IRF. Interestingly, probing to the red of the prompt emission at a wavelength of 800 nm results in an increase in the contribution from the longer lived τ_2 phase for both

the pristine solution and film. It is noted, however, that the contribution from the long-lived decay appears relatively small for both the solution and film and as such it is highly likely that TADF is not active (or is very inefficient) in the Thiro polymer. This observation is suggestive that the 'local' Thiro triplet exciton lies below that of the CT state, thus precluding efficient thermal repopulation of the ^1CT manifold.

5.7 Time-resolved Photoluminescence Spectroscopy (ICCD)

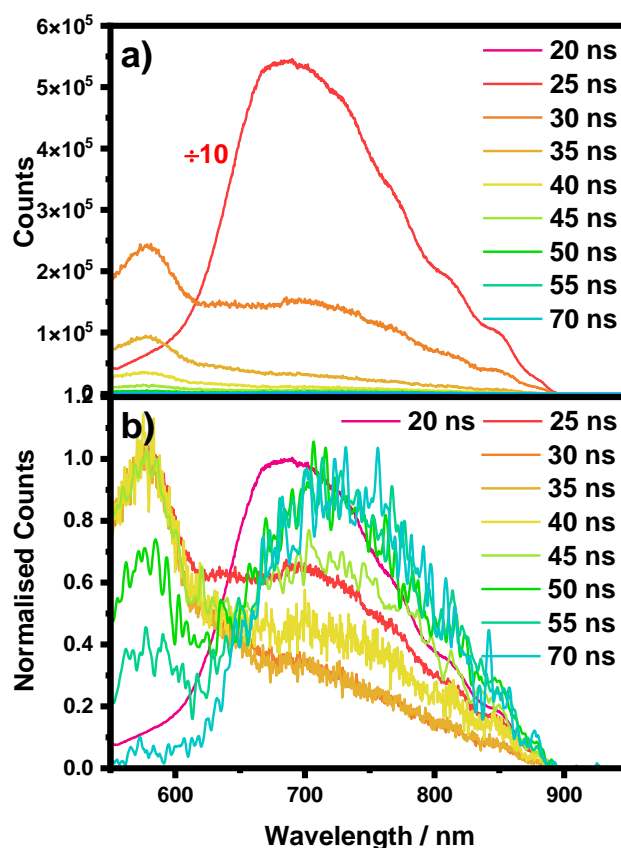


Figure 5.8 Time-resolved emission spectra of pristine Thiro solution ($50 \mu\text{g/mL}$) and **b)** the same spectral data normalised. Obtained with a ICCD camera, using an excitation wavelength of 525 nm at a power of $10 \mu\text{W}$. A 550 nm long pass filter was used. Data collected at Cambridge University with the aid of Saul Jones and Bluebell Drummond. For **b)**, the data from $45\text{-}70 \text{ ns}$ has been smoothed via adjacent averaging.

Time-resolved emission photoluminescence spectroscopy using an ICCD camera was carried out on both the pristine Thiro solution and thin film, to further investigate the long-lived photoluminescence signals. The pristine Thiro solution's time-resolved photoluminescence spectrum (shown in figure 5.8) is found to evolve over time, revealing the presence of three distinct emissive species that contribute to the overall signal. An initial prompt, vibrationally resolved emission at 680 nm is found to dominate the spectrum at the earliest timescales, which rapidly decays on an

instrument limited timescale. This observation is in agreement with the rapidly decaying photoluminescence observed in the TS-SPC. Owing to this rapidly decaying photoluminescence signal and vibrationally structured spectrum, the emission is likely to derive from that of a 'local' singlet state. Interestingly, once the prompt photoluminescence has sufficiently decayed, a new longer-lived above bandgap emissive species can be observed at 580 nm. This 580 nm emissive species is found situated in the same spectral position as the above band gap transition observed in the steady state PL spectra of the pristine Thin film. It is noted that this feature was not completely reproducible in the previous steady state spectra, nonetheless, the appearance of this additional transition on a different experimental apparatus is indicative that it is not the result of an artefact. It is possible that this transition derives from short conjugation segments that become isolated and emit at higher frequencies, or alternatively the result of emission from degradation products, but it is emphasised that these explanations are purely conjecture. The kinetic decay of the transition at 580 nm could be fit to a monoexponential function (shown in figure 5.9) to yield a lifetime of $\tau = 5.4 \pm 0.1$ ns. By 70 ns, the emission peak at 580 nm has decayed sufficiently to reveal the presence of an additional weak transition situated at 730 nm. This 730 nm emission is found to be broad and unstructured relative to 680 nm prompt photoluminescence. Fitting the long-lived decay to a monoexponential function (shown in figure 8) yields a lifetime of $\tau = 28 \pm 2$ ns. This red-shifted feature is tentatively ascribed to emission from a ^1CT state, which is weakly coupled to the ground state.

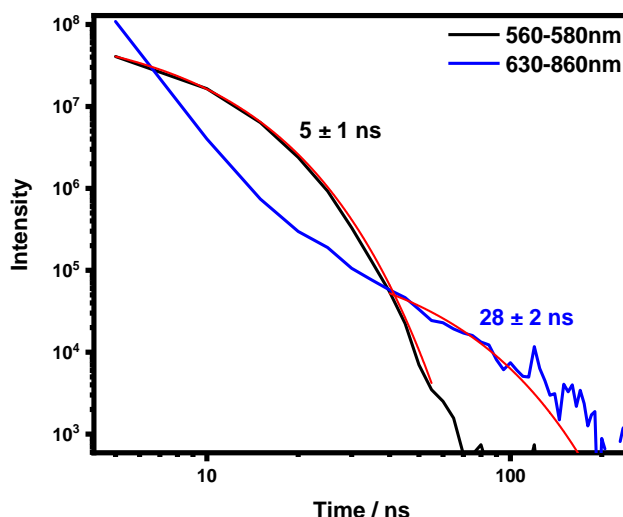


Figure 5.9 Photoluminescence decay kinetics of pristine thiro solution. Obtained with an excitation wavelength of 525 nm, at a power of 10 μw .

Moving to the pristine Thiro thin film time-resolved photoluminescence spectrum (shown in figure 5.10), the main prompt fluorescence is still found to decay rapidly. Furthermore, the main transition peak is now found red-shifted to ~ 715 nm, compared to 685 nm in the solution. Interestingly, the prompt fluorescence no longer gives way to an above bandgap, longer-lived contribution, unlike the 580 nm emission observed in the solution. This observation points towards the reproducibility issues observed with this feature and unfortunately due to time constraints any further investigation could not be carried out. Continuing, the red-shifted, unstructured emission observed in the solution is still found to be present in the thin film spectrum, albeit red-shifted from ~ 730 nm to 760 nm. This ~ 75 meV red-shift is consistent with the observed energetic difference for the solution and solid prompt fluorescence. This would seem to infer that when transitioning between the solution and solid phases the relative ordering between the 'local' singlet and ^1CT states remains essentially unchanged.

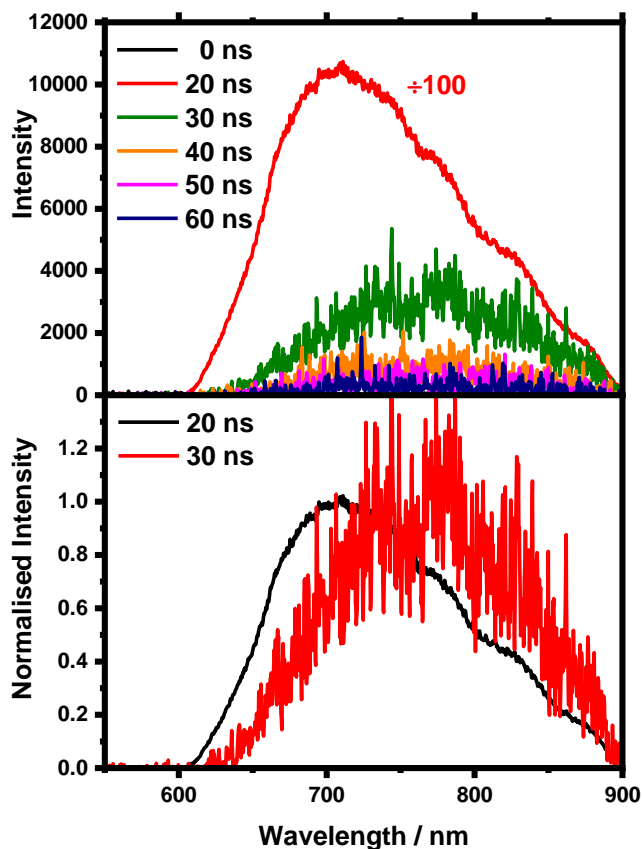


Figure 5.10 Time-resolved emission spectra of pristine Thiro thin film. Obtained with an excitation wavelength of 525 nm, at a power of 10 μW . A 550 nm long pass filter was used.

5.8 Picosecond Transient Absorption Spectroscopy

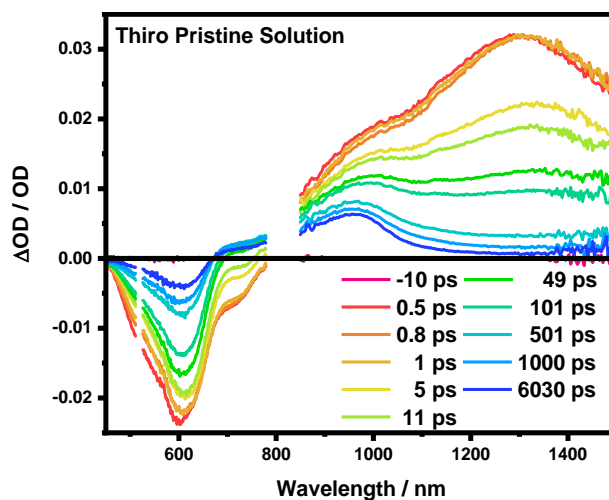


Figure 5.11 Picosecond transient absorption spectrum of Thiro in chlorobenzene solution ($50 \mu\text{g/mL}$), excited with a pump wavelength of 520 nm and an excitation density of $50 \mu\text{J cm}^{-2}$. Spectrum has been corrected for the absorbance at the exciting wavelength.

Continuing from the steady state characterisation, ps-TAS data was collected for pristine Thiro chlorobenzene solution and thin film. Figure 5.11 shows the TA spectrum obtained for Thiro in solution by exciting with a pump wavelength of 520 nm (2.38 eV). At early times, a broad transition can be observed in the NIR at 1290 nm , with an additional less intense shoulder seen at ca. 1000 nm . The transition at 1290 nm is found to undergo a red shift of $\sim 30 \text{ meV}$ to 1330 nm by 11 ps . By 6 ns the transition at 1330 nm has completely decayed, revealing the presence of a transition from a long-lived species at 960 nm . Interestingly, the species responsible for the transition at 960 nm appears to also have been fully generated on ultrafast timescales. The visible detector portion of the spectrum displays a negative signal from $450\text{--}780 \text{ nm}$ and is the result of contributions from both the ground state bleach and stimulated emission. The ground state bleach contribution can be seen in the region $450\text{--}690 \text{ nm}$, with the pump laser spike situated at 520 nm . The spectrum from $690\text{--}780 \text{ nm}$ correlates well with the spectral emission region of Thiro and as such is ascribed to stimulated emission. In this same spectral region of $690\text{--}780 \text{ nm}$ a positive signal can also be seen clearly from 100 ps and is attributed to the absorption from the species observed at 960 nm . A comparison of the pristine Thiro solution's ground state bleach and ground state absorbance spectra at 0.5 and 6000 ps (shown in figure 5.12 a)), reveals that the ground state bleach is found red shifted relative to its ground state absorbance. In addition, the spectral shape of the bleach at both timescales does not fully reproduce the steady state absorbance spectrum. It is possible that this deviation

from the ground state spectrum may be a manifestation of the Stark effect, which in donor-acceptor blend films is associated with shifting of energy levels of neighbour molecules as a consequence of the electric field generated from charge separation.²⁴ Nonetheless, any photoinduced electro absorption signals are difficult to discern, owing to contributions from both the stimulated emission and absorption from the long-lived species in the region 690-780 nm. A further possibility is that the observed absorbance shift is the result of relaxation of the ground state stemming from the disorder present.

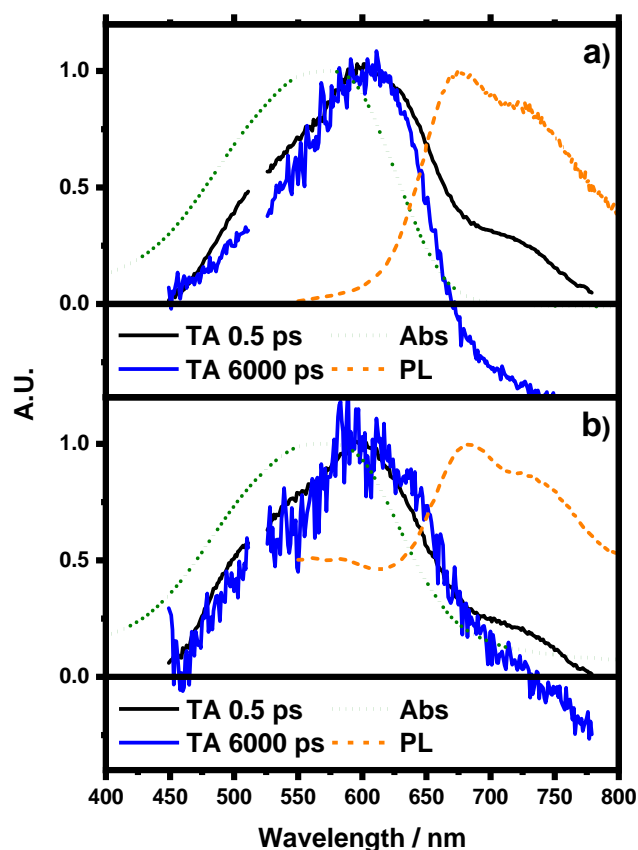


Figure 5.12 Normalised picosecond transient absorption, ground state absorbance and steady state photoluminescence spectra of **a)** pristine Thiro solution **b)** pristine Thiro film. Spectra have been normalised to their respective peak maxima.

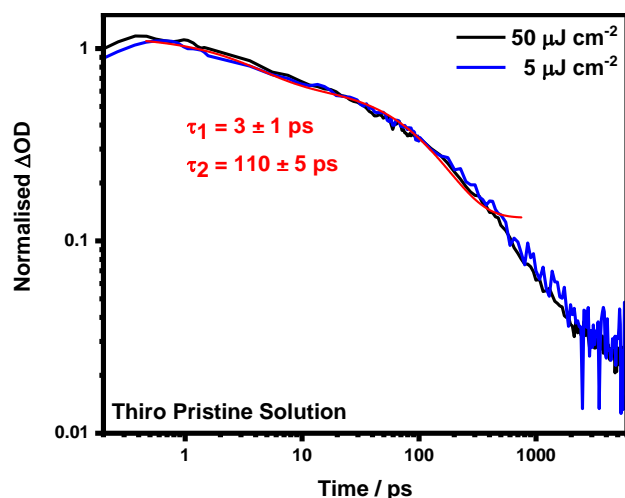


Figure 5.13 Normalised picosecond transient absorption decay kinetics of Thiro solution excited with a pump wavelength of 520 nm and excitation energies of 5 and 50 $\mu\text{J cm}^{-2}$. Dynamics were averaged using the decay data in the range of 1200-1300 nm. The red line is a biexponential fit of the type $y_0 + A_1 \cdot \exp(-t/\tau_1) + A_2 \cdot \exp(-t/\tau_2)$.

Analysis of the pristine Thiro solution kinetics (figure 5.13) obtained by averaging the spectral region of 1200-1300 nm (where contamination from the species at 960 nm was minimal) reveals a decay comprised of two phases. An initial multiexponential decay can be observed from the earliest timescales and is associated with the dynamics of the 1300 nm transition, and a second longer-lived decay observable from ~ 2 ns, which is most likely a contribution from the transition at 960 nm. The initial decay up to ~ 800 ps can be fit with a biexponential, yielding time constants of $\tau_1 = 3 \pm 1$ ps and $\tau_2 = 110 \pm 5$ ps (where the error is from fitting). Figure 5.13 shows that the decay obtained at 1200-1300 nm is invariant to the excitation energy between 5 and 50 $\mu\text{J cm}^{-2}$, therefore discounting the presence of annihilation effects in this fluence range. This allows us to attribute the observed kinetics to radiative and non-radiative decay of the Thiro singlet state ($^1\text{Th}^*$). The need for the biexponential fit for the $^1\text{Th}^*$ decay may reflect the energetic dispersity present in the solution and/or multiple decay processes. The band at 1300 nm is likely to derive from a singlet state transition ($S_1 \rightarrow S_n$) owing to the very short lifetime of the components and formation on ultrafast timescales. This assignment is consistent with the observed spectral red-shift, which can therefore be ascribed to energetic migration of the $^1\text{Th}^*$ down the density of states, afforded by the energetic disorder.¹⁶ It is possible that the transition at 960 nm belongs to that of the Thiro triplet state ($^3\text{Th}^*$), in part due to its much longer lifetime than the ascribed singlet state at 1300 nm, persisting beyond the resolution of the instrument (~ 6 ns). In addition, with the absence of an acceptor molecule, intersystem crossing

to the triplet manifold would be expected to be more prevalent. The spectral evolution of this species, however, is found to possess a contribution from the singlet transition at 1300 nm, which makes kinetic analysis of the raw data more difficult. In order to overcome this issue, a code based on a genetic algorithm was used for spectral disassembly, which provides spectra and kinetics of the individual components (i.e. the excited states) which best reproduce the original transient data set (provided by Dr Artem Bakulin, Imperial College London).^{25,26}

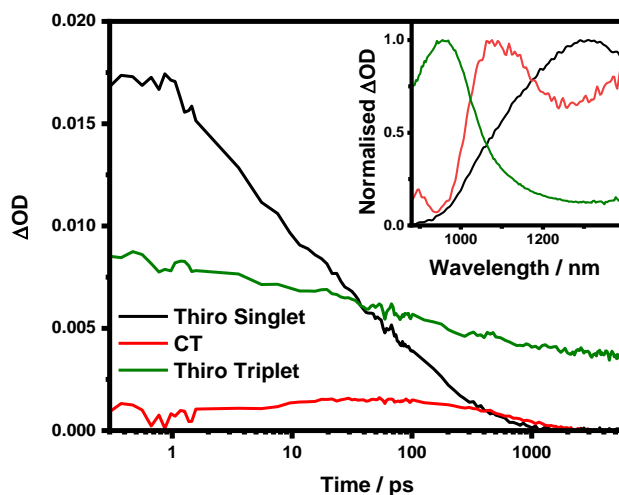


Figure 5.14 Kinetics obtained by global analysis of the picosecond transient absorption data of Thiro in chlorobenzene solution (50 $\mu\text{g/mL}$). Excited with a pump wavelength of 520 nm and an excitation density of 50 $\mu\text{J cm}^{-2}$. *Inset:* the spectral components obtained from global analysis of the same data used to obtain the kinetics.

The spectra obtained from global analyses (shown in the inset of figure 5.14) points to the presence of 3 distinct transitions, situated at 950, 1100 and 1300 nm. The transitions at 950 and 1300 nm, were observable in the raw spectral data, and tentatively ascribed to absorption by the Thiro triplet and singlet states respectively. However, a third transition is now found located at 1100 nm, which was not readily apparent from the raw spectral data (i.e. data that has not underwent spectral disassembly via GA). This is assigned to the CT state, as explained below. The singlet state is found to exhibit a multiexponential decay (shown in figure 5.15 a) that is excitation independent. The singlet decay kinetics can still be well fit to a biexponential function, yielding time constants of $\tau_1 = 5 \pm 1$ ps and $\tau_2 = 110 \pm 5$ ps (where the error is from fitting). These obtained component lifetimes are of the same within error for those obtained from fitting of the raw data, thus allowing us to be confident in the obtained GA results and the fitting parameters for the ascribed $^1\text{Th}^*$ state. As a result of the GA, the kinetics of the tentatively ascribed triplet at 950 nm (shown in figure

5.14) can be analysed without the presence of a significant contribution from additional absorbing states.

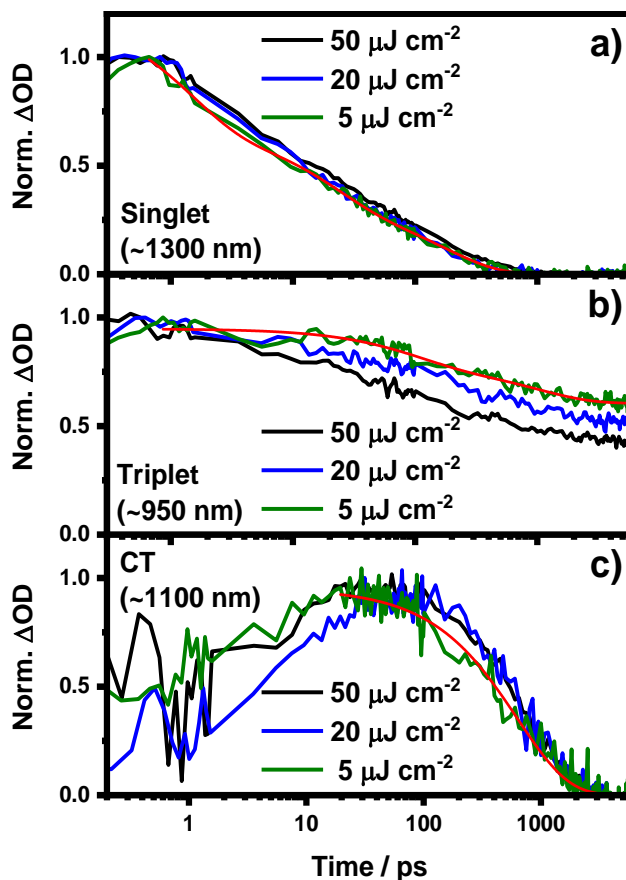


Figure 5.15 Normalised excitation dependant kinetics obtained by global analysis of the picosecond transient absorption data of Thio in chlorobenzene solution (50 $\mu\text{g/mL}$). The kinetic decays correspond to the different spectral components at **a)** 1300, **b)** 950 nm and **c)** 1100 nm. The red lines correspond to best fits. Data was obtained with a pump wavelength of 520 nm and an excitation density range of 5-50 $\mu\text{J cm}^{-2}$.

Formation of the Thio triplet state is found to occur on the sub-ps timescale, attaining its maximum population at ~ 1 ps. Furthermore, the Thio triplet exhibits an excitation dependant decay (figure 5.15 b), which plausibly, may originate from triplet-triplet annihilation. The lowest energy decay measured (5 $\mu\text{J cm}^{-2}$) may be fit to a biexponential function, yielding time constants of $\tau_1 = 100 \pm 20$ ps, $\tau_2 = 1000 \pm 200$ ps. If the transition at 950 nm does indeed derive from that of a triplet state, this would seem to imply that it is populated on instrument limited timescales (< 200 fs), which is too fast to be accounted for by an ISC process not involving heavy atoms. Furthermore, the $\tau_1 = 100$ ps decay time component suggests the presence of a rapid decay pathway for the Thio triplet, which is much faster than the typical spin forbidden

triplet decay. One possibility for the observed rapid triplet formation is that the presence of CT states energetically close to that of the local singlet state allows for the possibility of a spin orbit charge transfer ISC mechanism (this will be addressed in the discussion).

Interestingly, the kinetics show (figure 5.15 c) that the transition at 1100 nm is found to exhibit a much more pronounced population growth when compared to the Thiro triplet, including attaining its maximum amplitude at ~ 20 ps. Furthermore, the decay dynamics of the 1100 nm species is found to be excitation independent within the energy range employed, unlike that of the ascribed triplet state. The initial rise of the 1100 nm species can be well fit with a monoexponential function, yielding a time constant of $\tau_{\text{rise}} = 5 \pm 1$ ps, which interestingly, is the same as the fastest time component of for the singlet decay. This is suggestive that the transition at 1100 nm is populated via the decay of the Thiro singlet state, and the observation that both decays are excitation independent further supports this. The 1100 nm species is found to decay monomolecularly, yielding a lifetime of $\tau = 900 \pm 20$ ps. This 1100 nm transition may plausibly derive from an intramolecular CT state, formed indirectly via the decay of the initial excited local singlet state. In addition, the assignment of the 1100 nm transition to a CT state is consistent with the excitation independent, monomolecular recombination dynamics.^{27,16} In addition, the tentatively assigned CT state lifetime of $\tau = 900 \pm 20$ ps is reasonably close to that of the long-lived $\tau_2 = 1.4$ ns emission component of the corresponding TC-SPC decay, thus suggesting that the long-lived emission derives from the CT state.

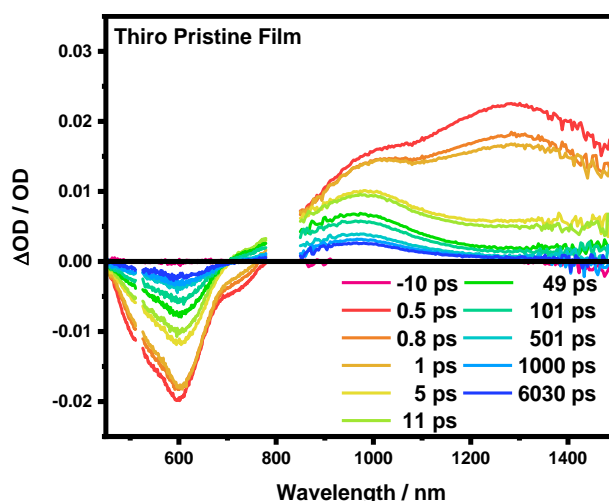


Figure 5.16 ps transient absorption spectrum of Thiro thin film, excited with a pump wavelength of 520 nm an excitation density of $50 \mu\text{J cm}^{-2}$. Spectrum has been corrected for the absorbance at the exciting wavelength.

Now that the baseline photophysics has been established for the Thiro solution, we now turn our attention to its respective thin film to ascertain any differences in the solid phase. When exciting with a pump wavelength of 520 nm the Thiro film yields a ps spectrum (figure 5.16) that is similar in appearance to that of the pristine solution. This indicates that in both the pristine solution and film, the initial excitation derives from the same transition (be it an inter or intrachain transition). At 0.5 ps a broad transition can be observed in the NIR at 1290 nm, with the less intense shoulder still found situated at ca. 1000 nm. Both of these features were observed in the solution ps spectrum as well and are ascribed to absorption by the excited $^1\text{Th}^*$ and $^3\text{Th}^*$ states respectively. The assigned $^1\text{Th}^*$ state responsible for the transition at 1290 nm is found to decay significantly faster than its solution counterpart, and in addition exhibits no spectral red shift. This contrasts with the solution phase, where the singlet responsible for the transition at 1290 nm is found to exhibit a 30 meV energetic relaxation within 11 ps. It is possible, however, that in the pristine Thiro film relaxation is a much faster process, which takes place on earlier timescales that cannot be resolved. In the pristine film, the singlet at 1290 nm has sufficiently decayed by 6 ns to reveal the presence of a new-longer lived species at 970 nm, which in the pristine solution was ascribed to that of the $^3\text{Th}^*$ state.

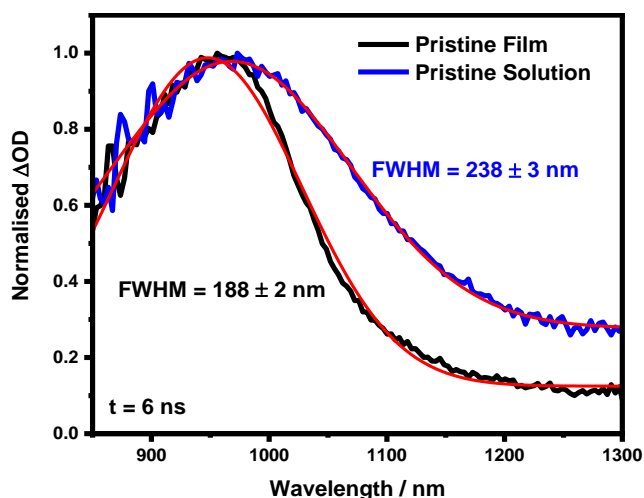


Figure 5.17 Normalised ps transient absorption spectrum of Thiro thin film and chlorobenzene solution. Obtained with a pump wavelength of 520 nm, at an excitation density of $50 \mu\text{J cm}^{-2}$. Spectra taken at 6 ns. The full width at Half Maximum were determined from a gaussian fit.

A comparison of the normalised pristine Thiro film and solution spectra at 6 ns (shown in figure 5.17) reveals that the film triplet exhibits a broader absorption profile with respect to the solution, exhibiting a $\text{FWHM} = 238 \pm 3$ and 188 ± 2 nm. This spectral broadening in the pristine film can be attributed to the greater energetic dispersity

present in the film, which is likely to originate from additional intermolecular interactions, not present in the solution phase. This greater spectral broadening in the film is also consistent with what was observed in the ground state absorbance. The raw kinetics of the ascribed singlet state were difficult to analyse, due to its short-lived nature, which quickly becomes obscured by the decay of the tentatively assigned long-lived triplet at 970 nm. In order to overcome this issue, the kinetics of the singlet were extracted using global analyses. The kinetics extracted from global analysis are shown in figure 5.18 and the corresponding spectra which they refer to are shown in the inset. All three species observed in the pristine Thiro solution GA TA spectra are still present in the pristine thin film, exhibiting transitions at 960, 1060 and 1300 nm, which were previously ascribed to the absorbance of triplet, CT and singlet states respectively.

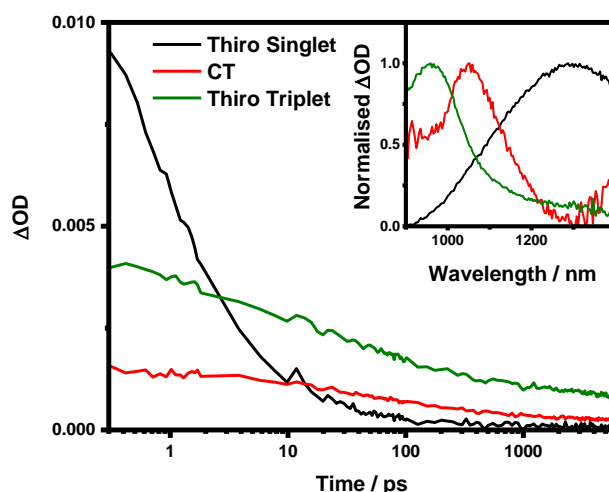


Figure 5.18 Kinetics obtained by global analysis of the picosecond transient absorption data of a pristine Thiro film. Excited with a pump wavelength of 520 nm and an excitation density of $50 \mu\text{J cm}^{-2}$. The red line is a biexponential fit of the type $y_0 + A_1 \cdot \exp(-t/\tau_1) + A_2 \cdot \exp(-t/\tau_2)$. **Inset:** the normalised spectral components obtained from global analysis of the same data used to obtain the kinetics.

The obtained GA kinetics of the singlet at 1300 nm (figure 5.18) illustrates a decay that can be well fit with a biexponential, yielding time constants of $\tau_1 = 1.2 \pm 0.1$ ps and $\tau_2 = 27 \pm 2$ ps (where the error is from fitting). A comparison between the film and solution reveals that the τ_1 and τ_2 lifetimes are ~ 4 x less than those obtained for the solution, in line with the much faster decaying film singlet exciton. It should be noted, however, that only one excitation density was acquired for the pristine thin film data, and as such, the presence of an excitation dependence contribution cannot be fully

ruled out. Nonetheless, the corresponding solution phase singlet transition at 1300 nm was found to be excitation independent.

Interestingly, the ascribed ^1CT transition at 1060 nm is found to exhibit a much less overt growth than the analogous pristine solution kinetics and is attributed to population of the CT state on much earlier timescales. Furthermore, the clear monoexponential decay in solution is now replaced in the film by a much more long-lived and complex decay phase. Previously, when analysing the pristine Thiro solution data, it was suggested that the fastest time component of $\tau_1 = 5$ ps may be related to population of the CT state at 1100 nm, as indicated by the identical CT growth time. In the pristine Thiro film the τ_1 time component exhibits a contribution of $\sim 83\%$ to the overall singlet decay, greater than that of the corresponding solution τ_1 time component, which exhibits just $\sim 55\%$. This observation would seem to indicate that the 1100 nm transition should be more prevalent in the film phase if it populated via the initial singlet decay. Indeed, this is the case as shown in the overlaid solution and film kinetics in figure 5.19.

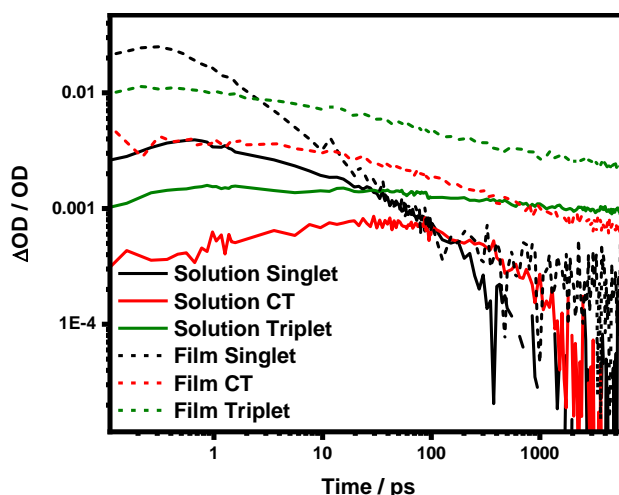


Figure 5.19 Kinetics obtained by global analysis of the picosecond transient absorption data of pristine Thiro in chlorobenzene solution and its thin film. Excited with a pump wavelength of 520 nm and an excitation density of $51 \mu\text{J cm}^{-2}$.

The kinetics of the triplet transition at 970 nm demonstrate that the Thiro triplet is fully populated on an instrument limited timescale and exhibits a multiexponential decay, like that of its solution counterpart. This decay can be fit to a triexponential function, yielding time components of $\tau_1 = 3 \pm 1$ ps, $\tau_2 = 60 \pm 5$ ps and $\tau_3 = 1200 \pm 140$ ps. The need for an additional time component when compared to the biexponential decay exhibited by the solution may be indicative of the presence of a degree of excitation dependant behaviour. However, as only one excitation energy was

obtained for the pristine film we cannot say with certainty. The most important observation, however, is still the presence of rapid triplet decay pathways on the <100 ps timescale, in line with what was observed in the solution.

From the ps-TA results several important observations were made. Firstly, an initial local singlet state can be observed at ca. 1300 nm in the ps-TA spectra, which decays within ~100 ps. Interestingly, this singlet decay is multiexponential in nature, exhibiting an initial rapid τ_1 component of 1-5 ps, followed by a longer-lived τ_2 component of 20-110 ps. This is suggestive of the presence deactivation pathways for the Thiro singlet state that are in addition to the standard radiative and non-radiative decay. Secondly, the tentatively ascribed Thiro triplet species is found rapidly generated on instrument limited timescales (>200 fs), which is too fast to be accounted for by typical direct ISC processes. Singlet fission and spin orbit charge transfer ISC are both photophysical processes that may account for the ultrafast timescales on which the Thiro triplet occurs, but a definitive assignment to either mechanism is not possible with the ps-TA data obtained here. To confirm the spectral assignment of the longest lived ps species to that of the Thiro triplet, the TA investigation was extended into the μ s-ms regime.

5.9 Microsecond Transient Absorption Spectroscopy

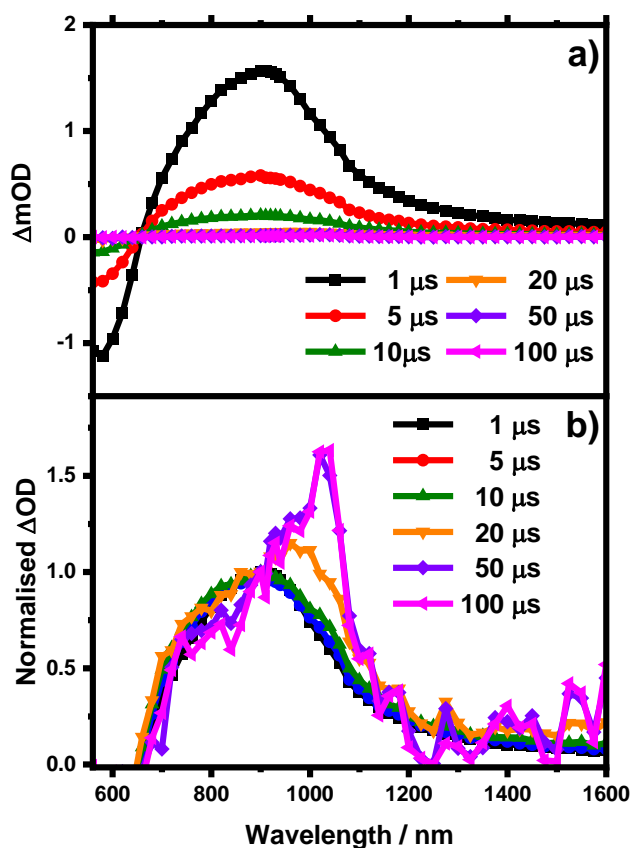


Figure 5.20 **a)** Microsecond transient absorption spectrum of Thiro in chlorobenzene solution (50 $\mu g/mL$). Obtained with an excitation wavelength of 532 nm and an excitation density of 40 $\mu J cm^{-2}$. **b)** The same spectral data normalised to 900 nm, illustrating the presence of a new species at later time scales.

Following on from the ps-TA, the investigation was extended into the μs -ms regime in order to further provide evidence for the assignment of the long-lived species to that of a triplet state. Excitation of the pristine Thiro solution results in the formation of a broad transient species in the NIR, with its peak situated at 900 nm, as shown in figure 5.20 a). Interestingly the spectral position of this peak is found blue shifted relative to the tentatively assigned triplet observed at ~ 950 nm in the ps-TAS spectrum. On the basis of the spectral similarity the transition is tentatively assigned to the same $^3Th^*$ species, with oxygen quenching evidence presented later in the results (figure 5.24). By 100 μs the pristine Thiro solution spectrum evolves to reveal the presence of a new longer-lived species, with its peak centred at 1020 nm. This spectral evolution can be readily observed in the normalised spectra in figure 5.20 b). A clear isosbestic point can be observed at 660 nm, indicating that the transition at 900 nm decays

directly back to the ground state and is not related to the growth of the later observed species at 1020 nm.¹⁶ This isosbestic feature was not observed in the ps spectrum.

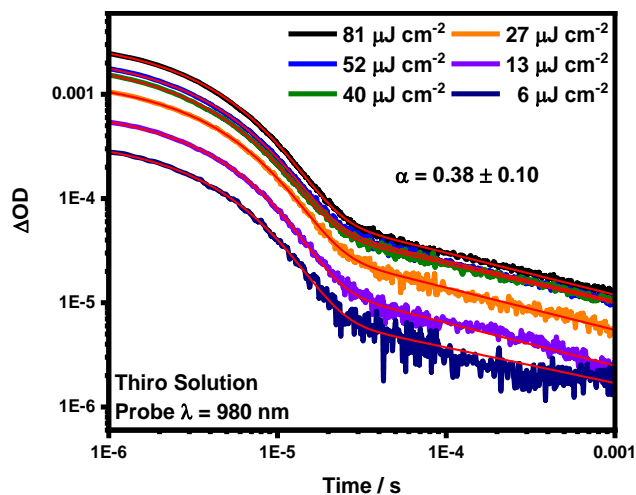


Figure 5.21 Microsecond transient absorption kinetics of pristine Thio in chlorobenzene solution (50 $\mu\text{g/mL}$). Obtained with a pump wavelength of 532 nm and a probe wavelength of 980 nm. The red line is a fit from a combination of a stretched exponential and a power law of the type $y_0 + A_1 * \exp(-(t/\tau)^\beta) + A_2 * t^\alpha$.

To help confirm the presence of the Thio triplet exciton and identify the species which appears at later timescales, a description of the kinetics is presented. Probing the pristine Thio solution kinetics obtained at 980 nm (figure 5.21) reveals a multicomponent decay, consisting of an initial exponential component until $\sim 40 \mu\text{s}$, followed by a power law decay at longer times. The presence of two phases is consistent with the observed spectral evolution with time and the close proximity of the two transitions, where the initial exponential component is related to the 900 nm band and the power law component to the 1020 nm band.

The initial exponential component derives from the species responsible for the 900 nm transition, which dominates the spectrum at early times and was analysed by subtracting the power law from the overall data, revealing the presence of a decay that could be well fit with a stretched exponential (figure 5.22). To prove that the dispersive exponential behaviour did not stem from second-order processes, such as triplet-triplet annihilation, the kinetics were probed as a function of excitation energy. Figure 5.22 displays the normalised kinetic decays obtained at 980 nm once the contribution from the power law has been subtracted. The data was fit to a stretched exponential of the type shown in equation 5.1.

$$\Delta OD(t) = A_1 * \exp(-t/\tau_1)^\beta$$

Eqn. 5.1

The lifetimes obtained from the stretched exponential fitting did not change markedly, with an average $t_{50\%} = 3.4 \pm 0.1 \mu\text{s}$ and $\beta = 0.87 \pm 0.03$ (where the error is the standard deviation) obtained from fitting. It is highly likely that the species responsible for this long-lived decay is that of the Thiro triplet, due to the close proximity of the 900 nm transition to the 950 nm triplet transition assigned in the ps-TA spectrum. It should also be noted that a bi-exponential function could also be fit to the same decays, however, the τ_1 and τ_2 lifetimes obtained were very similar and possessed near identical contributions to the overall signal amplitude. As such, it was rationalised that a bi-exponential fit was resulting in overparameterisation of the data. The requirement for a 'stretched' parameter when describing the Thiro triplet decay is indicative of the presence of a degree of energetic distribution in the Thiro solution. This is best observed in figure 5.23 a), which shows the normalised signal amplitude (ΔOD) at 1 and 100 μs , corresponding to the Thiro triplet and free charge respectively (this assignment of the 1020 nm species will be discussed shortly), as a function of excitation density. For a single decay pathway ΔOD should increase linearly with increasing excitation density, however, as can be seen for the decays at 1 μs for the pristine Thiro solution (when the contribution from the long-lived decay has been subtracted), there exists a slight sublinear relationship. This small deviation from linearity is reflected in the $\beta = 0.87$ obtained for the decay of the $^3\text{Th}^*$, where a $\beta = 1$ indicates a pure monoexponential decay. Interestingly, the long-lived power-law phase is found to start tending towards saturation with increasing excitation density, unlike that of the Thiro triplet and may be a consequence of a second order reaction such as bimolecular recombination.

In order to confirm the assignment of the transition at 900 nm to a triplet species, the neat Thiro solution was bubbled with O_2 . As shown in chapter 3 and 4, the presence of O_2 should selectively quench any Thiro triplets present, provided that their energy is $>0.94 \text{ eV}$. As shown in figure 5.24, the presence of O_2 is found to result in a $\sim 30\%$ reduction in the $t_{50\%}$ of the early decay phase, yielding $t_{50\%} = 2.8 \mu\text{s}$ and a corresponding ~ 5 times reduction in signal amplitude. Importantly, the observed oxygen quenching was found to be reversible when the sample was purged with N_2 , thus eliminating the possibility of the signal quenching deriving from oxygen-based degradation of the sample. This evidence therefore supports the assignment of the transition at 900 nm to the Thiro triplet.

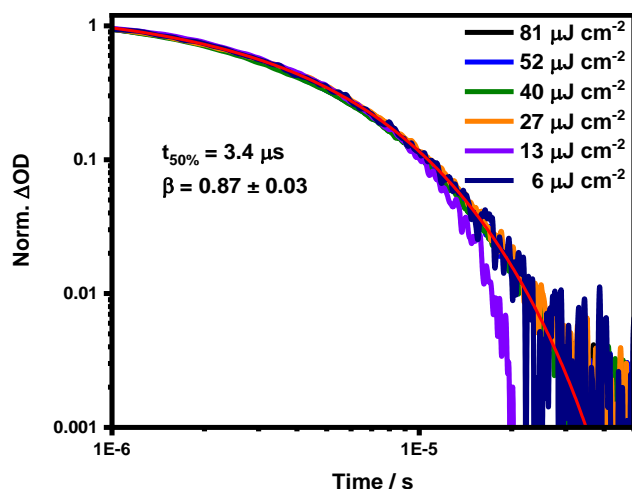


Figure 5.22 Microsecond transient absorption kinetics of neat Thiro in chlorobenzene solution (50 $\mu\text{g/mL}$). Obtained with an excitation wavelength of 532 nm and a probe wavelength of 980 nm. Decays have been obtained via subtracting a fitted power-law decay ($A t^\alpha$) from the overall decay data. The red line is a stretched exponential fit of the type $y_0 + A \exp(-(t/\tau)^\beta)$, yielding an average $\beta = 0.87 \pm 0.03$ (where the error is the standard deviation).

Interestingly, the observed transition at 1020 nm is approximately located in the same spectral area as the tentatively ascribed CT state in the GA resolved ps-TA spectrum. The transition at 1020 nm is likely to derive from a charge species (i.e. radical cation or anion) as the power-law decay exhibited at later times ($>40 \mu\text{s}$) is generally observed for bimolecular recombination of long-lived, free charges in donor/acceptor thin films.^{27,28} Interestingly, this power law behaviour implies that charge generation is occurring in a relatively dilute solution (50 $\mu\text{g/mL}$). This charge separation process may be afforded by the unique donor/orthogonal-acceptor architecture of Thiro, where an intramolecular CT state bound across the donor CPDT backbone and the orthogonal acceptor spiro unit, may afford a degree of spatial separation between the electron and hole. This increased electron and hole separation will thus result in a reduced exciton binding energy, which may then be overcome at room temperature. An alternative explanation for charge dissociation in Thiro could be an ‘inter-chain’ transition (i.e. between adjacent polymer chains), or a ‘intra-chain’ transition (i.e. between a single coiled up polymer chain). In any case, the dissolved Thiro polymer chains must be adopting aggregate configurations that loosely resemble the morphology of a thin film, as indicated by the relatively similar ground-state absorbance spectra. Owing to this fact, one would expect the pristine film phase to still possess a degree of this charge generation.

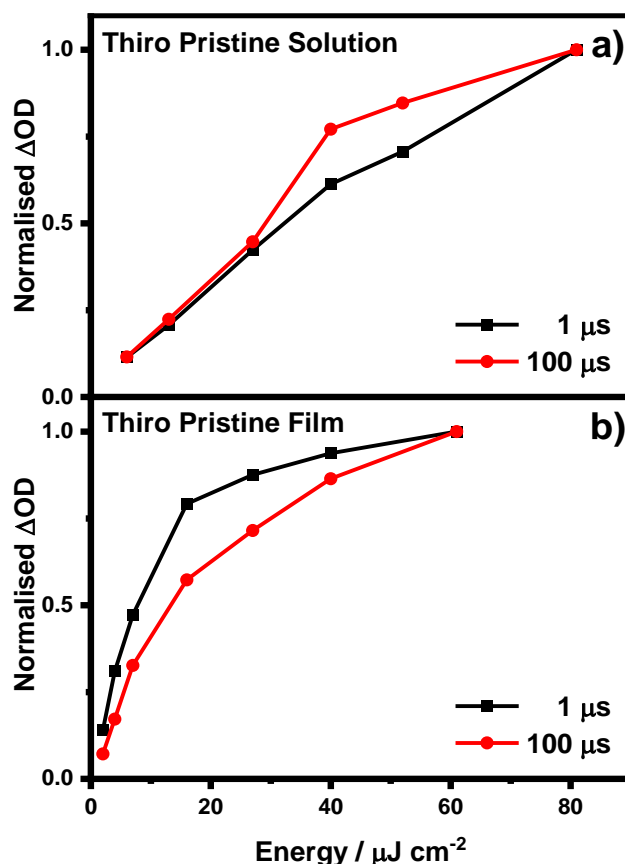


Figure 5.23 **a)** Excitation density dependant kinetics of a pristine Thio solution (50 $\mu g/mL$), **b)** pristine Thio thin film. Obtained with an excitation wavelength of 532 nm and at a probe wavelength of 980 nm. The normalised signal amplitude at 1 and 100 μs is shown as a function of excitation energy, where the ΔOD at 1 μs for both the solution and film has had the contribution from the slow phase subtracted from it.

Fitting a power-law to the long-lived component of the pristine Thio solution kinetic decays yields an average exponent of $\alpha = 0.38 \pm 0.10$ (where the error is the standard deviation), where an $\alpha = 1$ indicates trap-free bimolecular recombination. Further evidence for the assignment of the 1020 nm transition to free charges can be observed in the oxygen dependant kinetics, where the power law decay is found to exhibit indistinguishable kinetics in the presence of O_2 . In addition, the power law decay becomes visibly more pronounced in an O_2 environment due to quenching of the $^3Th^*$ signal, which allows for the underlying power law to become visible from $\sim 3 \mu s$, as opposed to $\sim 40 \mu s$ in the presence of N_2 . A salient point to note is that in addition to the expected reduction in both signal amplitude and lifetime of the $^3Th^*$ state, there is also an observed reduction in the charge carrier signal amplitude, but importantly without a change in the kinetics of the power-law. This reduction in the charge signal amplitude by $\sim 41\%$ in the presence of O_2 would seem to infer that a

significant quantity of the observed polaron is generated from a pathway that involves a triplet intermediate species that is not the ascribed $^3\text{Th}^*$ (as indicated by the isosbestic point) and the significance of these findings will be discussed later. This observed recombination behaviour has previously been observed in a study by Ohkita et al for an amorphous polythiophene derivative, P(T₁₀PhT₁₀), although it is noted that this was for a PC₆₀BM blend film and not a pristine material in solution.²⁹

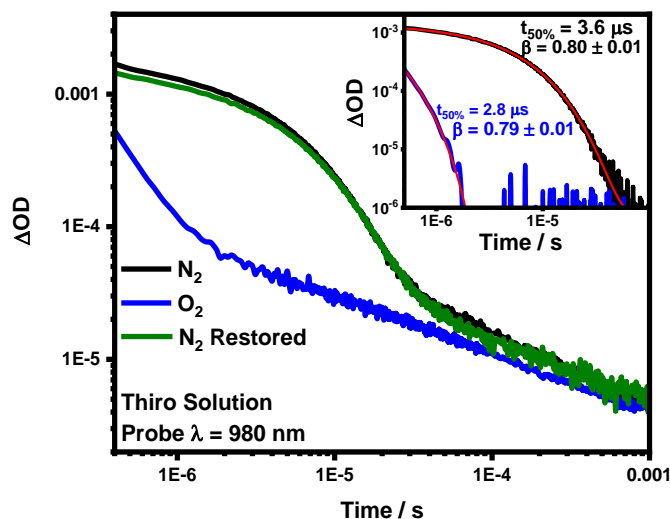


Figure 5.24 Microsecond transient absorption kinetics of pristine Thiro in chlorobenzene solution (50 $\mu\text{g}/\text{mL}$), excited with an excitation wavelength of 532 nm and at an excitation density of 20 $\mu\text{J cm}^{-2}$. The initial solution was degassed for 1h with N_2 . The solution was then bubbled with O_2 for 30 min, and then restored with N_2 by degassing for 1 h. **Inset:** the kinetic decays with the contribution from the long-lived decay removed. The red lines are stretched exponential fits type $y_0 + A \cdot \exp(-(t/\tau)^\beta)$.

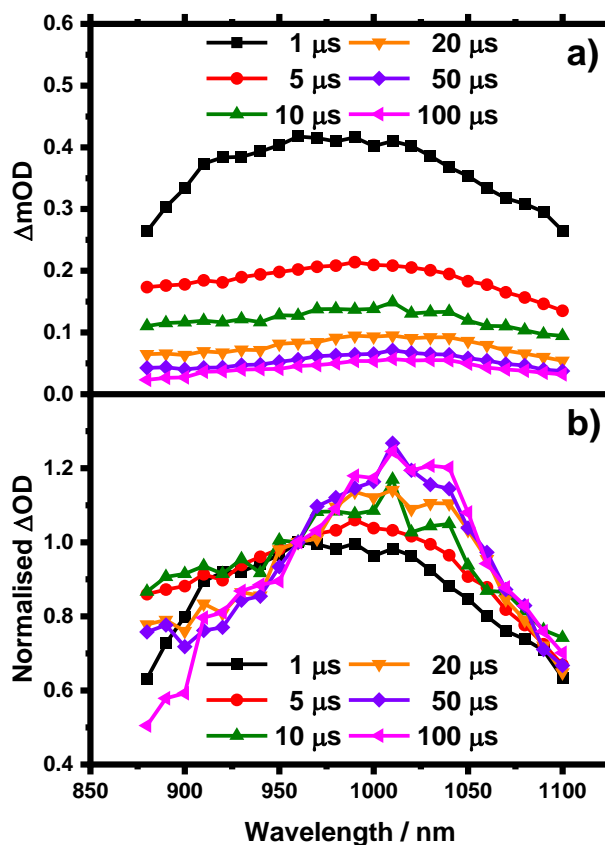


Figure 5.25 a) Microsecond transient absorption spectrum of a pristine Thiro thin film. Obtained with an excitation wavelength of 530 nm and at an excitation density of $14 \mu J cm^{-2}$. **b)** The same spectral data normalised to 960 nm, illustrating the presence of a long-lived species at later time scales.

Now that the pristine Thiro solution has been investigated, we will now elucidate the dynamics of the pristine Thiro film in the μs -ms regime. Figure 5.25 a) shows the μs -TA spectrum obtained when the Thiro film was excited with a pump wavelength of 530 nm. The Thiro film is found to exhibit a transition at 980 nm, which dominates the spectrum and an additional tail that extends out in the NIR. By 100 μs the transition at 980 nm has sufficiently decayed to reveal the presence of a more longer-lived feature at 1010 nm, which can be readily seen in the normalised spectrum presented in figure 5.25 b). As the transition at 980 nm is spectrally situated near the assigned triplet at 970 nm in the ps-TA spectrum and in addition is close to the assigned triplet in the solution, it is therefore likely to derive from the same $^3Th^*$ species. Like that of the Thiro solution, the early μs exponential decay in the pristine film is found to be oxygen dependant, as shown in figure 5.26. The initial decay can therefore be attributed to the Thiro triplet exciton. Figure 5.27 shows the kinetics obtained from probing at 980 nm, which reveals a multicomponent decay profile that is similar in nature to what was observed in the solution phase. An initial exponential decay can be observed until $\sim 30 \mu s$, followed by an additional long-lived decay that appears to

be close to a power law, but can only be fully described by a stretched-exponential type fit. Interestingly, this contrasts with the observed 'pure' power-law decay observed in the pristine solution.

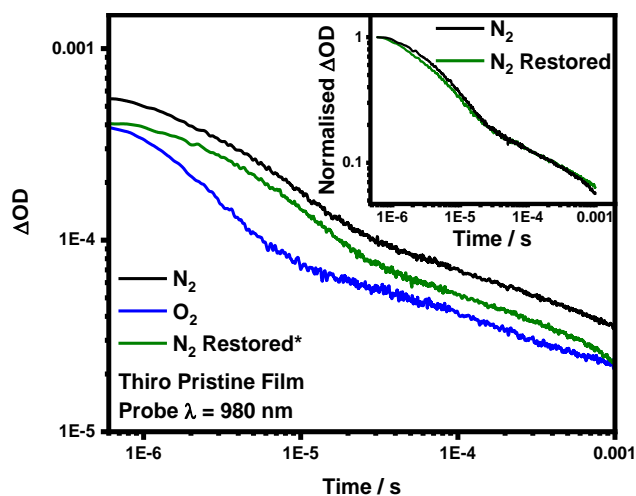


Figure 5.26 Microsecond transient absorption kinetics of pristine Thiro thin film. Obtained with a pump wavelength of 532 nm and a probe wavelength of 980 nm. Excitation energy $14 \mu\text{J cm}^{-2}$. * During the N_2 restored measurement, the power output of the laser was found to decrease, resulting in a perceived reduction in ΔOD . The normalised kinetics of the initial and restored N_2 atmospheres are provided in the inset and illustrate near identical decays.

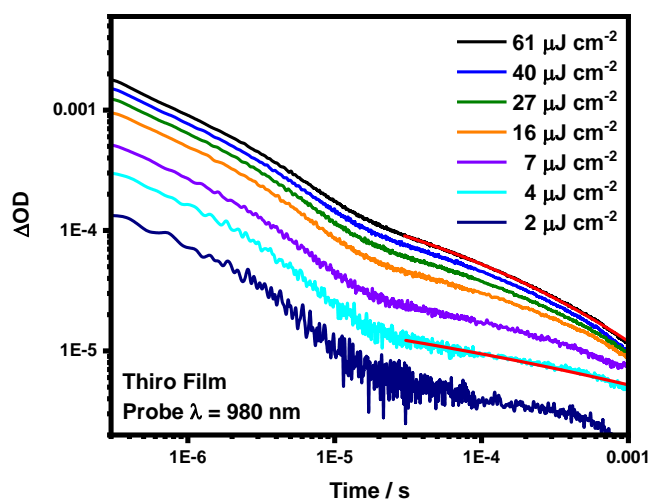


Figure 5.27 Microsecond transient absorption kinetics of a pristine Thiro thin film. Obtained with a pump wavelength of 532 nm and a probe wavelength of 980 nm. The red lines are stretched exponential fits of the type $y_0 + A \cdot \exp(- (t/\tau)^\beta)$.

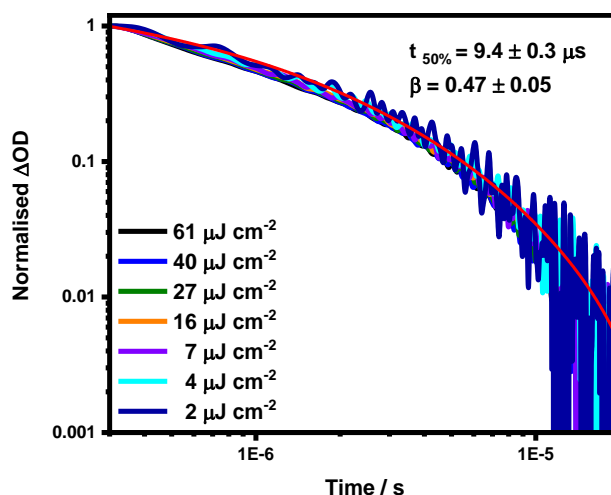


Figure 5.28 Normalised microsecond transient absorption kinetics of pristine Thiro thin film. Obtained with a pump wavelength of 532 nm and at a probe wavelength of 980 nm. Decays have been obtained via subtracting a fitted power-law decay (At^{α}) from the overall decay data. The red line is a stretched exponential fit of the type $y_0 + A \cdot \exp(-(t/\tau)^{\beta})$.

Using a similar methodology to the solution, whereby the long-lived component is subtracted from the overall data, the decay dynamics of the ‘pure’ Thiro film triplet may be extracted. Figure 5.28 shows that the decay of the Thiro triplet is excitation energy independent within the range of energies employed (2-61 $\mu\text{J cm}^{-2}$) and can be well fit with a stretched exponential to yield an average $t_{50\%} = 9.4 \pm 0.5 \mu\text{s}$ and an average exponent of $\beta = 0.47 \pm 0.05$ (where the errors are the standard deviation). The prevalence of the requirement for an additional ‘stretched’ parameter in describing both the solution and thin film triplet decays indicates the presence of a significant energetic distribution in the Thiro material. Moreover, the smaller exponent of $\beta = 0.47$ in the film compared to $\beta = 0.87$ in the solution is consistent with the expected increased disorder in the solid state, which is reflected in the broader ground state absorbance and excited triplet spectra in figures 5.4 and 5.17 respectively. The film triplet’s deviation from typical monomolecular behaviour is readily observed in the excitation density kinetics in figure 5.23 b). The normalised ΔOD at 1 μs (corresponding to the amplitude of the Thiro triplet) is found to exhibit an appreciable sublinear dependence upon the excitation energy, in contrast to the subtle deviation seen in the solution. This observation may be suggestive of multiple decay pathways being present, including a second order one.

Chapter 5

We now turn our attention to the assignment of the transition at 1020 nm and the origin of its long-lived decay. The transition at 1010 nm is likely to stem from the same polaron species assigned in the pristine Thiro solution $\mu\text{s-TA}$ spectrum, owing to its spectral proximity and similar long-lived dynamics. The long-lived polaron decay observed after $\sim 30 \mu\text{s}$ is found to exhibit an excitation dependant signal, which contrasts with the excitation independent triplet kinetics. At the lowest energies employed, the long-lived decay can be fit with that of a stretched exponential (the decay at $4 \mu\text{J cm}^{-2}$ was used instead of $2 \mu\text{J cm}^{-2}$, due to the apparent noise at the end of the $2 \mu\text{J cm}^{-2}$ decay), yielding a $\beta = 0.1$. At the highest energy employed ($61 \mu\text{J cm}^{-2}$), a stretched exponential may still be fit, however, it is found to exhibit a $\beta = 0.2$. One way to provide evidence for the assignment of the long-lived species at 1010 nm to a polaron species is to compare the pristine Thiro spectrum to that of a Thiro:PC₆₀BM blend film. This is because if the same transition is observed in both the pristine and blend film spectra, it is highly likely to derive from a Thiro positive polaron ($^+\text{Th}^*$).

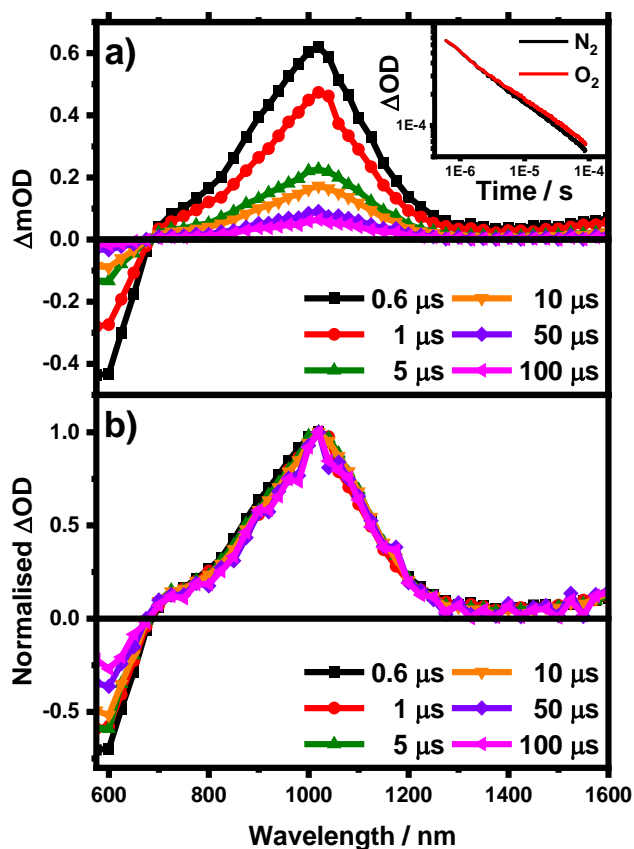


Figure 5.29 a) Microsecond transient absorption spectrum of a Thiro:PC₆₀BM 1:1 thin film. Obtained with an excitation wavelength of 530 nm and at an excitation density of 16 $\mu\text{J cm}^{-2}$. **Inset:** Microsecond transient absorption kinetics of a Thiro:PC₆₀BM 1:1 thin film under N₂ and O₂ atmospheres, illustrating an O₂ independent decay. Obtained with a pump wavelength of 530 nm, an excitation density of 18 $\mu\text{J cm}^{-2}$ and at a probe wavelength of 1020 nm. **b)** The same spectral data presented in a) normalised to 1020 nm, illustrating that new species appear at later time scales.

Figure 5.29 a) shows the μs -TA spectrum obtained for a Thiro:PC₆₀BM 1:1 blend. The spectrum at 1 μs is found to exhibit a photoinduced transition at 1020 nm, however, in contrast to the pristine Thiro solution or thin film, no additional spectral evolution over time is observed. This lack of spectral evolution with time can be readily observed in the normalised μs -TA spectrum of the blend, as shown in figure 5.29 b). This suggests that the Thiro triplet seen previously in the pristine solution and film at 900 and 960 nm respectively is no longer present. Further evidence for the absence of a triplet species is bolstered by indistinguishable decay dynamics in the presence of oxygen, as shown in the inset of figure 5.29 a). The 1020 nm transition observed in the blend film, however, bears a striking resemblance to the pristine Thiro's long-lived (>100 μs) species, which can be apparent in the normalised μs -TA spectra of the

pristine and blend film, as shown in figure 5.30. The single species observed in the Thiro:PC₆₀BM blend is likely to be that of a positive polaron, resulting from photoinduced electron transfer from the Thiro polymer (which is acting as an electron donor) to the PC₆₀BM acceptor. This helps to explain the absence of the Thiro triplet species in the blend spectrum, as it must be generated directly from the Thiro singlet, which in the blend film is likely to be quenched by the PC₆₀BM on ultrafast timescales, thus precluding ISC from taking place. Importantly, this confirms that the same 1020 nm transitions seen at later timescales in the pristine solution and thin film μ S-TA spectra, does indeed belong to that of the positive polaron.

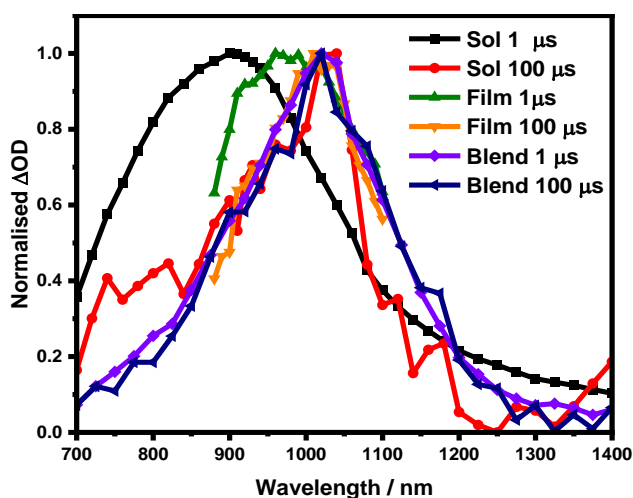


Figure 5.30 Normalised microsecond transient absorption spectra of pristine Thiro in chlorobenzene solution (50 $\mu\text{g/mL}$), pristine Thiro thin film and a Thiro:PC₆₀BM 1:1 blend. All spectra have been normalised to their respective peak maxima. At 1 μs both the pristine solution and thin film exhibit triplet transitions at 900 and 980 nm respectively. By 100 μs these triplet transitions have sufficiently decayed to reveal the presence of a new transition at 1020 nm, which is near identical to the solitary transition exhibited by the blend.

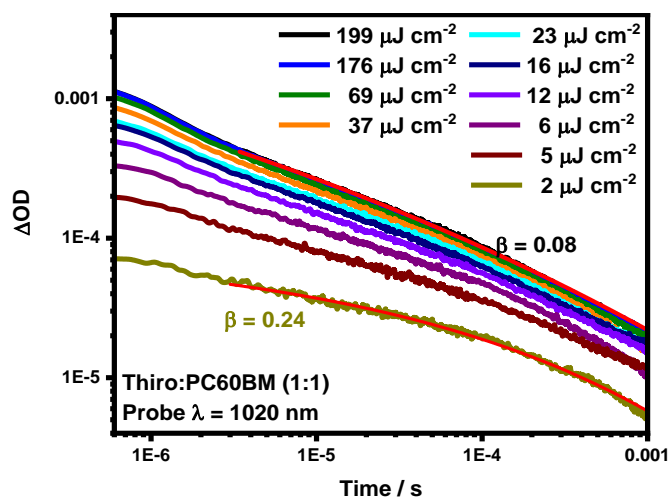


Figure 5.31 Microsecond transient absorption kinetics of a Thiro:PC₆₀BM (1:1) film. Obtained with an excitation wavelength of 530 nm and at a probe wavelength of 1020 nm. The red line is a stretched exponential fit of the type $y_0 + A \cdot \exp(-(t/\tau)^\beta)$.

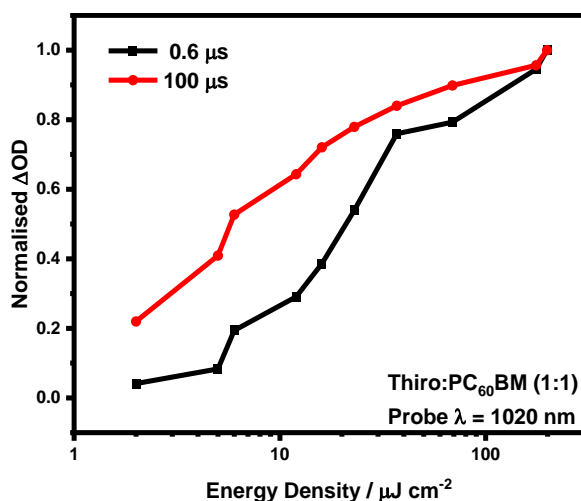


Figure 5.32 Microsecond transient absorption kinetics of a Thiro:PC₆₀BM (1:1) film. Obtained with an excitation wavelength of 530 nm and at a probe wavelength of 1020 nm. The normalised signal amplitude at 0.6 and 100 μ s is shown as a function of excitation energy, where the ΔOD at 0.6 μ s has had the contribution from the slow phase subtracted from it.

The kinetics probed at 1020 nm are shown in figure 5.31 and show a decay profile that is intensity-dependant, exhibiting both a fast phase that becomes apparent at higher excitation densities and a slower phase that persists until the ms regime. This behaviour is consistent with non-geminate recombination, as geminate recombination exhibits excitation-independent behaviour and subsequently should be observable at the lowest energies.³⁰ It should be noted however, that some degree of contribution

from geminate recombination to the overall signal cannot be ruled out. The slow phase of the lowest energy decay obtained can be well fit to a stretched exponential at the lowest excitation densities ($2 \mu\text{J cm}^{-2}$), yielding a $\beta = 0.24 \pm 0.01$ (where the error is obtained from fitting). This $\beta = 0.24$ indicates a significant deviation from monoexponential behaviour as would be expected, but nonetheless the stretched exponential fitting is in contrast to the power law decay dynamics observed in archetypal polymer blend systems, such as P3HT:PC₆₀BM and MDMO-PPV:PC₆₀BM.^{27,31} This implies that the observed Thiro polaron decay may not follow the typically observed trap-limited recombination behaviour, whereby an exponential distribution of trap states are progressively filled until a trap free recombination regime starts to dominate. Interestingly, with increasing excitation energy this slower phase is found to deviate from the stretched exponential behaviour, as illustrated by the decrease in exponent from $\beta = 0.24$ to $\beta = 0.08$. Alternatively, the decay becomes more easier to fit to a power law, with $\alpha = 0.49$. Figure 5.32 shows the normalised signal amplitude (ΔOD) as a function of excitation energy for both the fast ($0.6 \mu\text{s}$) and slow ($100 \mu\text{s}$) decay phases. Both phases are found to exhibit a sublinear dependence on the excitation energy, but a comparison of the two reveals the slow phase saturates earlier. In addition, the fast phase is apparent even at the lowest energies employed here ($2 \mu\text{J cm}^{-2}$), suggesting that the energetic distribution of trap states is 'shallow', allowing for facile thermal activation. The origin of this behaviour is currently unknown.

5.10 Discussion

Upon excitation the main photoproduct of the pristine Thiro, be it in solution or the solid phase, is that of the $^1\text{Th}^*$ state (the 'local' singlet). Evidence for this is provided by the vibrationally resolved fluorescence spectra and the strong transition observed at ca. 1300 nm in the ps-TA spectra at early times, in both the pristine Thiro solution and thin film. It should also be noted that initial excitation of the lower-lying ^1CT state is also possible, however, direct population is likely to be of low-efficiency due to the poor oscillator strengths possessed by CT states. In addition to the Thiro singlet, the $^3\text{Th}^*$ (the 'local' triplet) is also found generated on ultrafast timescales beyond the resolution of the instrument (~ 200 fs), irrespective of whether it is generated in solution or thin film and is found to persist into the μs regime. This implies that the observed rapid triplet formation is not the consequence of additional intermolecular or intramolecular interactions found in the solid phase, for example transitions that may arise from additional aggregate domains.^{32,33} The ultrafast timescales on which the Thiro triplet is found to be generated cannot be fully accounted for by the relatively slow process of direct intersystem crossing.³⁴ The two aforementioned photophysical

processes that may permit triplet population on these timescales are that of singlet fission (SF) and spin-orbit charge transfer ISC (SOCT-ISC), with the latter mechanism most likely being responsible for the observed photophysics.

One of the key features of the donor-orthogonal-acceptor architecture (D-o-A) is the prevalence of a reduced spatial overlap between the frontier molecular orbitals, which is a consequence of the physical separation of the donor and acceptor units. As discussed previously, this reduced spatial overlap has the effect of minimising the exchange energy, such that the singlet-triplet energy gap may become near degenerate.^{9,13} To observe the impact of Thiro's D-o-A structure on its energetics, theoretical calculations utilising time density functional theory (TDDFT) were carried out by Dr Tom Penfold (Newcastle University) using a dimeric unit of the Thiro Polymer, in conjunction with a CAM-B3LYP methodology with a def2-TZVP basis set. The results from the calculations are shown in figure 5.33 and do indeed show a local π - π^* singlet exciton (S_2) at higher energy than the ^1CT state (S_1). The calculations place the S_2 energy at 2.16 eV, matching well with the experimentally determined value of ~ 1.9 eV. Furthermore, the ^1CT state S_1 energy is calculated to be 2.01 eV, giving rise to a S_1 - S_2 energy gap of 0.15 eV, which is very close to 0.18 eV difference between the π - π^* and weak CT emission observed in the TC-SPC. This is a much smaller energy difference when compared to the previously mentioned SFCN and ASFCN orthogonal polymers. This difference stems from a reduction in the optical bandgap of Thiro, which substantially reduces the π - π^* energy, whereas the CT energy (which is less contingent upon the conjugation length) remains relatively unperturbed. The calculated triplet manifold indicates the T_1 state to be a local π - π^* triplet, while the T_3 state is CT in character and near isoenergetic with the S_1 (^1CT) state. This is in good agreement with the expected reduction in ΔE_{ST} stemming from the D-o-A architecture of Thiro. It is noted that calculations were performed on a dimeric unit and increasing the number of repeating units will likely increase the energy of the local triplet to an approximate maximum of $\Delta E_{S_1-T_1} \sim 0.7$ eV,^{35,36} but nonetheless it is still likely to be located below that of the ^3CT state. The presence of the ^3CT state is of particular importance as it affords the possibility of a spin-orbit charge transfer (SOCT) interaction, which may permit the population of the Thiro triplet manifold on ultrafast timescales. In the most common SOCT scheme, intersystem crossing is a second order process, whereby a $^1\text{CT}^*$ state undergoes ISC to yield the 'local' triplet state.^{12,37} This SOCT-ISC process is highly efficient, particularly in the case where the acceptor's molecular orbitals are found near perpendicular to the donor's,³⁷ as the spin-flip can be coupled to a large change in orbital angular momentum (analogous to a $n \rightarrow \pi^*$ transition) and can therefore

conserve overall system angular momentum.³⁸ This SOCT-ISC process has been observed previously in small molecule and polymeric D-o-A systems and has been invoked to describe the mechanism via which they undergo thermally activated delayed fluorescence.^{9,13,7,39} For the case of Thiro (as shown schematically in figure 5.33), the initial ISC process is likely to occur from the S_2 $^1\text{Th}^*$ to that of the energetically close- T_3 CT state, which subsequently undergoes rapid internal conversion (IC) to that of the local triplet manifold, T_1 $^3\text{Th}^*$ (i.e. $^1\text{Th}^* \rightarrow ^3\text{CT}^* \rightarrow ^3\text{Th}^*$).

Theoretical arguments were provided by Dr Tim Hele (UCL) to explain the observed Thiro photophysics in the context of an SOCT-ISC mechanism. The Thiro polymer in a thin film is expected to be amorphous in nature and as such should exhibit little symmetry. However, locally the polymer has C_{2v} symmetry, with the C_2 axis passing through the quaternary spiro carbon. This uniquely defines the z axis, which allows us to define the x axis to run along the length of the polymer (such that the thiophene π orbitals are in the xz plane) and the y axis to be perpendicular to this (such that the fluorene π system is in the yz plane). Utilising these definitions, the HOMO of the Thiro is found to transform with A_2 symmetry, the LUMO of the thiophene units as B_2 and the LUMO of the fluorene unit as B_1 . This means the $S_1(\text{CT})$ state is $A_2 \times B_1 = B_2$, which is y-polarised dipole allowed, but very weak due to poor orbital overlap. The $S_2(\text{LE})$ state is $A_2 \times B_2 = B_1$, so is x-polarised and allowed. This gives rise to the broad absorption feature observed at 550 nm in the ground state absorption spectrum of Thiro. The $T_1(\text{LE})$ state, arising from HOMO-LUMO (thiophene) will be B_1 and the $T_3(\text{CT})$ state, arising from HOMO-LUMO (fluorene) will be B_2 .

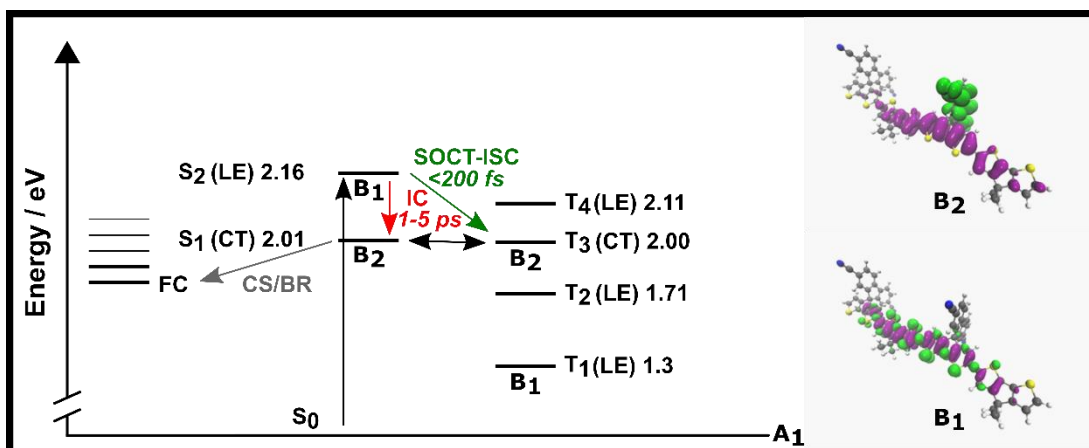


Figure 5.33 Schematic energy diagram for Thiro and density difference plots for the B_1 ($S_2(\text{LE})$ and $T_1(\text{LE})$) and B_2 ($S_1(\text{CT})$ and $T_3(\text{CT})$) symmetry states. Energies displayed were calculated by Dr Tom Penfold (Newcastle university) using a dimeric unit of the Thiro Polymer, in conjunction with a CAM-B3LYP methodology with a def2-TZVP basis set. Diagram is not to scale.

In regard to spin-orbit coupling, the spin-orbit coupling operator transforms as molecular rotations, which for C_{2v} span A_2 , B_1 and B_2 . For spin-orbit coupling between the bright $S_2(\text{LE})$ state and $T_3(\text{CT})$ state, we have $B_1 \times B_2 = A_2$, which transforms as R_z , meaning that the direct spin-orbit coupling between the S_2 and T_3 is allowed. Spin-orbit coupling between the $S_1(\text{CT})$ and $T_1(\text{LE})$ is $B_2 \times B_1 = A_2$ and is also allowed, although is predicted to have a relatively large energy gap of ~ 0.7 eV and therefore it may be slow as a consequence of the energy gap law. These results are consistent with the calculated SOC matrix elements (shown in table 5.1), which exhibit the greatest value of 2.08 cm^{-1} for the $S_2(\text{LE})$ - $T_3(\text{CT})$ transition. As such, ISC from the initially photogenerated $S_2(\text{LE})$ to the $T_3(\text{CT})$ is fully quantum mechanically allowed, thus accounting for the observed ultrafast triplet formation observed experimentally in the ps-TA data. In addition, the $S_2(\text{LE})$ and $T_3(\text{CT})$ states are separated via only 0.16 eV, which should help to facilitate a high rate of ISC. In addition, the presence of multiple triplet states that are energetically close lying to the bright $S_2(\text{LE})$ state should also promote increased ISC, as indicated by Fermi's golden rule. These multiple triplet states should also facilitate a rapid internal conversion (IC) through the triplet manifold to T_1 .

Spin-orbit coupling between the two charge transfer states $S_1(\text{CT})$ and $T_3(\text{CT})$ is $B_2 \times B_2$ and is therefore also forbidden. This then raises the question of how the singlet and triplet CT states couple, given that they have very weak direct spin-orbit coupling. However, given that these states are virtually isoenergetic (2.01 eV and 2.00 eV for the $S_1(\text{CT})$ and $T_3(\text{CT})$ respectively), virtually any perturbation can couple them. This could be vibronic coupling via any vibration except that of totally symmetric A_1 , or alternatively it could also occur via indirect coupling. For example, S_1 could couple to S_2 via the non-adiabatic coupling operator, and then S_2 to T_3 .

Table 5.1 Spin orbit couple matrix elements between the excited states calculated by Dr Tom Penfold (Newcastle university) with TDDFT using by using quasi-degenerate perturbation theory.

Computation (cm^{-1})	S_1	S_2
T1	2.00	0.00
T2	1.40	0.04
T3	0.02	2.08
T4	0.56	0.04

Chapter 5

We will now specifically consider the internal conversion between the $S_2(\text{LE})$ and $S_1(\text{CT})$, which transform as B_1 and B_2 respectively. This means that direct nonadiabatic transitions are forbidden. However, $B_1 \times B_2 = A_2$, thus indicating that non-adiabatic coupling and internal conversion between the S_2 and S_1 states could be mediated via an A_2 stretching vibration. While electronically excited molecules are commonly vibrationally excited too, generally only totally symmetric vibrations (A_1 in this instance) are excited upon photoexcitation in order to satisfy the symmetry of the transition matrix element, thus suggesting IC may be slow. An additional factor that may contribute to slow IC is that the relevant orbitals involved in the transition (π^* on the Thiro and π^* on the fluorene) are found to be spatially disjoint, thus suggesting that the transition matrix element involved is likely to be small. These predictions are consistent with the experimental results obtained, which showed a ps-timescale rise of the CT state, much slower than typical IC.

One of the most peculiar features of the Thiro system is the apparent formation of free charge species upon excitation in both the solution and solid phases, without the need for an acceptor. This is pertinent considering that while many polymers, such as P3HT and PCDTBT are found to exhibit charge generation in their neat pristine films, this behaviour is not conserved into their respective solution spectra and as such Thiro appears unique in this regard.^{15,40,41} This assignment of free charges was confirmed by comparing the pristine Thiro μs -TA spectra with that of the Thiro:PC₆₀BM (1:1) blend, which exhibited the same positive polaron transition at 1020 nm. Correcting the μs -TA data for photons absorbed of all three samples (pristine solution, film and blend) allows for a direct comparison of the efficiency of both triplet and charge generation, as shown in figure 5.34. Comparing the corrected decay data of the pristine Thiro solution and that of its thin film, reveals that the polaron concentration (measured from the ΔOD at 100 μs) is found to be 3.4 times greater in the film relative to the solution, indicating a variation in charge dissociation yield depending upon the phase. In addition, the pristine solution is found to yield a greater concentration of triplets (measured from the ΔOD at 0.6 μs) by ~ 1.7 times relative to the film. This suggests that in the pristine thin film there is an increased rate of charge dissociation from the CT state, outcompeting ISC to the Thiro triplet. This increased charge dissociation in the film may also be in part responsible for the faster singlet exciton decay in the film when compared to its solution. This is exemplified by the Thiro pristine film exhibiting a biphasic singlet exciton decay, which contrasts with the triphasic decay exhibited by the solution which also possesses an additional time constant on the order of hundreds of ps. Nonetheless, it is still noted that a reduction in the singlet exciton lifetime and fluorescence quantum yield is a commonly observed

feature when comparing a conjugated polymer's solution to its thin film, with these concentration based quenching effects typically being ascribed to an increase in non-radiative processes.^{42,43}

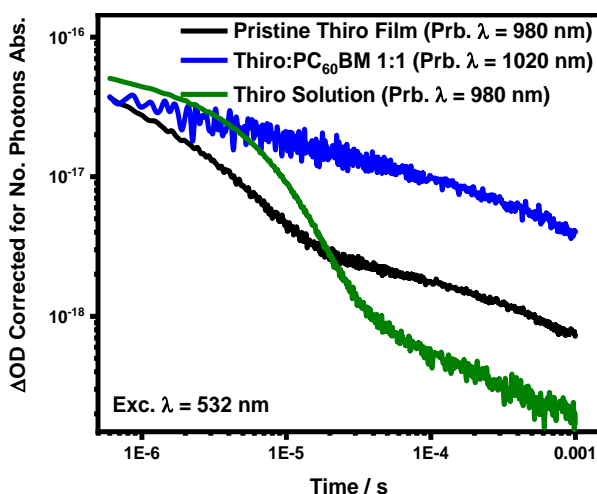


Figure 5.34 Normalised microsecond transient absorption kinetics of pristine Thiro solution (50 $\mu\text{g/mL}$), pristine Thiro film and a Thiro:PC₆₀BM 1:1 blend film. The decay data has been normalised to the number of photons absorbed at the exciting wavelength.

Spontaneous charge generation in pristine films has been observed previously in a variety of materials, such as PC₆₀BM, PC₇₀BM, MEH-PPV and P3HT,^{44,45,46,47,19} however, the exact mechanism via which charge dissociation proceeds remains controversial.⁴⁸ It should also be noted that the overwhelming evidence for charge generation in pristine polymer films derives from homopolymers, which do not necessarily reflect the intramolecular charge-transfer nature of D-A copolymers, such as Thiro. A good example of this is the copolymer PCDTBT, which in chlorobenzene solution is found to exhibit relaxed excitons with strong CT character within a timescale of ~ 200 fs.^{49,50} The strong CT character of the equilibrium excited state was suggested to aid in charge separation, due to a decreased electron-hole correlation and may provide some insight into why the formation of polarons in neat PCDTBT films is relatively efficient.⁴¹

For both the pristine Thiro solution and film, the presence of oxygen is found to result in a reduction in the polaron signal amplitude, but importantly without a change in the kinetics. This observation provides indirect evidence regarding the charge dissociation pathway in the Thiro polymer. The amplitude of the polaron signal (at 100 μs) is found to be quenched by ~ 29 and 41 % for the solution and film respectively, indicating an oxygen quenchable intermediate state that contributes significantly to

the population of the charge species. For pristine Thiro there are two possible pathways for charge dissociation in lieu of an additional acceptor molecule. The first involves autoionization upon direct excitation, which is unlikely due to the large binding energy possessed by the initially generated Thiro local singlet exciton.⁵¹ The second pathway involves charge dissociation from an intramolecular ^1CT or ^3CT dark state, formed as a result from relaxation of the initially generated $^1\text{Th}^*$ state. This generated CT state will afford a degree of intramolecular separation between the electron and hole, effectively reducing the binding energy, which is also consistent with the proposed SOCT-ISC pathway for $^3\text{Th}^*$ generation. In addition, the small spatial overlap between the HOMO and LUMO is expected to result in near degenerate $^1\text{CT}/^3\text{CT}$ state energies, as discussed previously. This presents the energetic possibility of an equilibrium between the CT states ($^1\text{CT} \rightleftharpoons ^3\text{CT}$) at room temperature, accounting for the observed reduction in polaron yield, as ^3CT states may be selectively quenched by O_2 before they can undergo charge dissociation. It is noted that some studies have indicated that transitions between ^1CT and ^3CT states are spin forbidden, as the orbital occupation does not change, therefore precluding the proposed CT spin state equilibria.^{52,38} Nonetheless, this supposition contradicts the ubiquitous reports of CT mediated geminate recombination to the local triplet state (i.e. before charge separation can occur).^{53,54} A significant implication of this $^1\text{CT}/^3\text{CT}$ equilibrium is that it must be acting as a reservoir for charge carrier formation, enabling charge carriers to generate and exist in a pristine polymer long after typically expected in standard conjugated polymers. While the existence of such a $^1\text{CT}/^3\text{CT}$ is not new, this is, to our knowledge, the first time it has been successfully combined with an orthogonal acceptor to enhance charge photogeneration. As such, this pathway may provide a promising new strategy to enhance charge carrier generation and lifetimes in organic photovoltaics.

An alternative explanation for the oxygen dependant polaron signal is that bimolecular recombination of free charges to an oxygen quenchable ^3CT state is a reversible process. This described bimolecular recombination behaviour is now a well-established feature in organic solar cell blends,^{9,55,56} with this model of re-separation of CT states being invoked to explain the origin of reduced Langevin recombination (see section 1.7.2) in donor-acceptor blends.⁵⁷ It was suggested that free charge carrier species are in equilibrium with CT states,⁵⁷ which in turn gives rise to a temperature dependence for the recombination rate and V_{OC} .^{57,58,59} Regardless of the mechanism, charge separation must be occurring via a CT state, which is shown schematically in figure 5.33.

Upon blending Thiro with PC₆₀BM, the oxygen dependency for the polaron decay is found to disappear, which can be rationalised for either of the two previously proposed mechanisms. If we take the proposed mechanisms involving an equilibrium of CT states ($^1\text{CT} \rightleftharpoons ^3\text{CT}$) prior to initial charge separation, the absence of an oxygen dependant signal can be attributed to the formation of a new dissociation pathway involving the PC₆₀BM acceptor. This is because polarons can now be generated on ultrafast timescales, without having to be involved in the intramolecular CT spin state equilibrium, thus no oxygen dependence is observed. The presence of a new ultrafast charge generation process afforded by the PC₆₀BM acceptor molecule is also consistent with the increased (~5x) polaron signal amplitude observed in the blend relative to the pristine film. This increase in polaron signal amplitude upon blending, however, is smaller than that for P3HT, which is found to exhibit an increase in signal amplitude by at least an order of magnitude for the equivalent (1:1) PC₆₀BM blend film.²⁷ Unfortunately, a direct comparison of polaron yields between Thiro and P3HT cannot be made, as the extinction coefficient for the Thiro polaron is not currently known.

Orthogonal donor-acceptor "push-pull" copolymers have previously been utilised to reduce the spatial overlap between the HOMO and LUMO orbitals.¹³ This had the intended effect of minimising the exchange energy, yielding near isoenergetic S₁ and T₁ energy levels depending upon the substituents employed and, in some cases, displaying thermally activated delayed fluorescence (TADF) effects. The effects from orthogonally positioning the acceptor moiety also now appear to extend to charge separation, via means of an intramolecular charge separation process. Direct efficient charge generation from a single polymeric system would be a major milestone in the field of organic photovoltaics. The ability to directly produce charges from a single photoactive layer alleviates the need for blending with a suitable acceptor molecule. Mixing of donor and acceptor components is normally essential to overcome the large exciton binding energy found in organic donor materials and achieve charge generation,³⁰ however, this also results in the formation of complex geometrical structures. These blend morphologies often play a critical role in dictating the device performance,⁶⁰ with additional pathways to charge generation and unwanted recombination becoming available depending upon the nanoscale geometrical structure present.^{61,62} Furthermore, the energetic offset required to initiate charge separation provides an intrinsic energy loss to any discrete donor acceptor system.^{55,63} The use of a single molecule which can overcome its own exciton coulomb binding energy inherently, instantly eliminates all the detrimental aspects of blending with an acceptor material.

5.11 Conclusion

In this investigation, the photophysics of a donor-orthogonal-acceptor (D-o-A) copolymer comprised of a CPDT backbone and a dicyanofluorene acceptor unit was spectroscopically investigated. Using ps and μ s transient absorption spectroscopy, it was shown that upon excitation the Thiro polymer readily formed local singlet and triplet excitons on ultrafast timescales. When investigated using μ s-TA, local triplet excitons in both the solution and film were found to exhibit a stretched exponential decay, indicative of a highly energetically dispersive system. This ultrafast triplet formation could not be countenanced by a relatively slow ISC process, which typically takes place on the ns timescale in lieu of heavy atom effects. Furthermore, this ultrafast triplet formation behaviour was observed in both chlorobenzene solution and thin film, thus indicating that this process was not the consequence of additional interactions found in the solid phase but as a result of the polymer's intrinsic photophysics. A spin orbit charge transfer (SOCT) ISC process was made possible by the D-o-A architecture and invoked to explain this ultrafast triplet formation, whereby the initially generated Thiro singlet exciton undergoes facile ISC to a dark $^3\text{CT}^*$ state, followed by IC to the local Thiro triplet state. Although no absolute quantitative data for the $^3\text{Th}^*$ was obtained due to limited knowledge of cross sections and quantum yields, the Thiro triplet was still thought to be generated in large concentrations, as inferred from the strong triplet signal in both the ps and μ s-TA spectrum. The most pertinent observation for the pristine Thiro polymer system was the apparent formation of free charge species in both the pristine solution and thin film, as evidenced by the appearance of a positive polaron transition at late time scales in the μ s-TA spectrum. This assignment to free charges was confirmed via blending Thiro with the acceptor molecule PC₆₀BM, which upon photoexcitation underwent ultrafast charge dissociation to yield the same positive polaron species. The Thiro polymer is unique among photovoltaic materials in that charge dissociation appears to occur in both its thin film and most importantly its solution, which points towards an intramolecular charge separation process. Although direct observation of this charge separation process was not observed, the most parsimonious explanation is that it occurs via a CT state on ultrafast timescales, beyond the resolution of the ps-TA setup. This CT state likely affords a degree of intramolecular separation between the electron and hole, thus effectively reducing the binding energy of the exciton and allowing for charge separation. The finding of a pristine polymer which undergoes charge separation has profound implications for the field of organic photovoltaics. The ability for a conjugated polymeric material to undergo intramolecular charge separation in the absence of an acceptor molecule, may in principle allow for the

circumventing of the intrinsic energy loss associated with driving electron transfer in a donor-acceptor blends.⁶⁴ In addition, the stringent morphological requirements of thin films to attain their highest efficiencies would be simplified. The observations presented in this chapter therefore demand additional investigation into D-o-A polymeric materials.

5. 12 Bibliography

- 1 A. Rao, P. C. Y. Chow, S. Gélinas, C. W. Schlenker, C. Z. Li, H. L. Yip, A. K. Y. Jen, D. S. Ginger and R. H. Friend, *Nature*, 2013, **500**, 435–439.
- 2 A. Köhler and D. Beljonne, *Adv. Funct. Mater.*, 2004, **14**, 11–18.
- 3 K. Goushi, K. Yoshida, K. Sato and C. Adachi, *Nat. Photonics*, 2012, **6**, 253–258.
- 4 H. Tanaka, K. Shizu, H. Miyazaki and C. Adachi, *Chem. Commun.*, 2012, **48**, 11392.
- 5 G. Méhes, H. Nomura, Q. Zhang, T. Nakagawa and C. Adachi, *Angew. Chemie*, 2012, **124**, 11473–11477.
- 6 F. B. Dias, K. N. Bourdakos, V. Jankus, K. C. Moss, K. T. Kamtekar, V. Bhalla, J. Santos, M. R. Bryce and A. P. Monkman, *Adv. Mater.*, 2013, **25**, 3707–3714.
- 7 R. S. Nobuyasu, Z. Ren, G. C. Griffiths, A. S. Batsanov, P. Data, S. Yan, A. P. Monkman, M. R. Bryce and F. B. Dias, *Adv. Opt. Mater.*, 2016, **4**, 597–607.
- 8 P. L. dos Santos, J. S. Ward, A. S. Batsanov, M. R. Bryce and A. P. Monkman, *J. Phys. Chem. C*, 2017, **121**, 16462–16469.
- 9 F. B. Dias, J. Santos, D. R. Graves, P. Data, R. S. Nobuyasu, M. A. Fox, A. S. Batsanov, T. Palmeira, M. N. Berberan-Santos, M. R. Bryce and A. P. Monkman, *Adv. Sci.*, 2016, **3**, 1600080.
- 10 J. S. Ward, R. S. Nobuyasu, A. S. Batsanov, P. Data, A. P. Monkman, F. B. Dias and M. R. Bryce, *Chem. Commun.*, 2016, **52**, 2612–2615.
- 11 J. Gibson, A. P. Monkman and T. J. Penfold, *ChemPhysChem*, 2016, **17**, 2956–2961.
- 12 M. K. Etherington, J. Gibson, H. F. Higginbotham, T. J. Penfold and A. P. Monkman, *Nat. Commun.*, 2016, **7**, 13680.
- 13 D. M. E. Freeman, A. J. Musser, J. M. Frost, H. L. Stern, A. K. Forster, K. J.

Chapter 5

- Fallon, A. G. Rapidis, F. Cacialli, I. McCulloch, T. M. Clarke, R. H. Friend and H. Bronstein, *J. Am. Chem. Soc.*, 2017, **139**, 11073–11080.
- 14 L. Lu, T. Zheng, Q. Wu, A. M. Schneider, D. Zhao and L. Yu, *Chem. Rev.*, 2015, **115**, 12666–12731.
- 15 N. Banerji, S. Cowan, M. Leclerc, E. Vauthey and A. J. Heeger, *J. Am. Chem. Soc.*, 2010, **132**, 17459–17470.
- 16 F. Etzold, I. A. Howard, R. Mauer, M. Meister, T. D. Kim, K. S. Lee, N. S. Baek and F. Laquai, *J. Am. Chem. Soc.*, 2011, **133**, 9469–9479.
- 17 U. Asawapirom and U. Scherf, *Macromol. Rapid Commun.*, 2001, **22**, 746–749.
- 18 X.-K. Chen, V. Coropceanu and J.-L. Brédas, *Nat. Commun.*, 2018, **9**, 5295.
- 19 S. Cook, A. Furube and R. Kato, *Energy Environ. Sci.*, 2008, **1**, 294.
- 20 J. Brazard, R. J. Ono, C. W. Bielawski, P. F. Barbara and D. A. Vanden Bout, *J. Phys. Chem. B*, 2013, **117**, 4170–4176.
- 21 L. Fan, R. Cui, X. Guo, D. Qian, B. Qiu, J. Yuan, Y. Li, W. Huang, J. Yang, W. Liu, X. Xu, L. Li and Y. Zou, *J. Mater. Chem. C*, 2014, **2**, 5651.
- 22 M. Li, P. J. Leenaers, M. M. Wienk and R. A. J. Janssen, *J. Mater. Chem. C*, 2020, **8**, 5856–5867.
- 23 N. Banerji, S. Cowan, M. Leclerc, E. Vauthey and A. J. Heeger, *J. Am. Chem. Soc.*, 2010, **132**, 17459–17470.
- 24 S. Gélinas, A. Rao, A. Kumar, S. L. Smith, A. W. Chin, J. Clark, T. S. van der Poll, G. C. Bazan and R. H. Friend, *Science*, 2014, **343**, 512–516.
- 25 M. Srinivas and L. M. Patnaik, *IEEE Trans. Syst. Man. Cybern.*, 1994, **24**, 656–667.
- 26 Y. Vaynzof, A. A. Bakulin, S. Gélinas and R. H. Friend, *Phys. Rev. Lett.*, 2012, **108**, 246605.
- 27 T. M. Clarke, F. C. Jamieson and J. R. Durrant, *J. Phys. Chem. C*, 2009, **113**, 20934–20941.
- 28 A. F. Nogueira, I. Montanari, J. Nelson, J. R. Durrant, C. Winder, N. S. Sariciftci and C. Brabec, *J. Phys. Chem. B*, 2003, **107**, 1567–1573.
- 29 H. Ohkita, S. Cook, Y. Astuti, W. Duffy, S. Tierney, W. Zhang, M. Heeney, I. McCulloch, J. Nelson, D. D. C. Bradley and J. R. Durrant, *J. Am. Chem. Soc.*,

Chapter 5

- 2008, **130**, 3030–42.
- 30 T. M. Clarke and J. R. Durrant, *Chem. Rev.*, 2010, **110**, 6736–6767.
- 31 I. Montanari, A. F. Nogueira, J. Nelson, J. R. Durrant, C. Winder, M. A. Loi, N. S. Sariciftci and C. Brabec, *Appl. Phys. Lett.*, 2002, **81**, 3001–3003.
- 32 A. K. Thomas, H. A. Brown, B. D. Datko, J. A. Garcia-Galvez and J. K. Grey, *J. Phys. Chem. C*, 2016, **120**, 23230–23238.
- 33 A. K. Thomas, J. A. Garcia, J. Ulibarri-Sanchez, J. Gao and J. K. Grey, *ACS Nano*, 2014, **8**, 10559–10568.
- 34 S. R. Yost, J. Lee, M. W. B. Wilson, T. Wu, D. P. McMahon, R. R. Parkhurst, N. J. Thompson, D. N. Congreve, A. Rao, K. Johnson, M. Y. Sfeir, M. G. Bawendi, T. M. Swager, R. H. Friend, M. A. Baldo and T. Van Voorhis, *Nat. Chem.*, 2014, **6**, 492–497.
- 35 H. Haberkern, K. R. Asmis, M. Allan and P. Swiderek, *Phys. Chem. Chem. Phys.*, 2003, **5**, 827–833.
- 36 A. Köhler and H. Bässler, *Mater. Sci. Eng. R Reports*, 2009, **66**, 71–109.
- 37 M. T. Colvin, A. B. Ricks, A. M. Scott, D. T. Co and M. R. Wasielewski, *J. Phys. Chem. A*, 2012, **116**, 1923–1930.
- 38 C. M. Marian, *J. Phys. Chem. C*, 2016, **120**, 3715–3721.
- 39 M. Lv, Y. Yu, M. E. Sandoval-Salinas, J. Xu, Z. Lei, D. Casanova, Y. Yang and J. Chen, *Angew. Chemie Int. Ed.*, 2020, **59**, 22179–22184
- 40 S. Cook, A. Furube and R. Katoh, *Energy Environ. Sci.*, 2008, **1**, 294.
- 41 M. Tong, N. E. Coates, D. Moses, A. J. Heeger, S. Beaupré and M. Leclerc, *Phys. Rev. B - Condens. Matter Mater. Phys.*, 2010, **81**, 125210.
- 42 S. Cook, A. Furube and R. Katoh, *Energy Environ. Sci.*, 2008, **1**, 294.
- 43 M. M.-L. Grage, T. Pullerits, A. Ruseckas, M. Theander, O. Inganäs and V. Sundström, *Chem. Phys. Lett.*, 2001, **339**, 96–102.
- 44 C. Keiderling, S. Dimitrov and J. R. Durrant, *J. Phys. Chem. C*, 2017, **121**, 14470–14475.
- 45 C. Keiderling, S. Dimitrov and J. R. Durrant, *J. Phys. Chem. C*, 2017, **121**, 14470–14475.

Chapter 5

- 46 J. Gorenflot, M. C. Heiber, A. Baumann, J. Lorrmann, M. Gunz, A. Kämpgen, V. Dyakonov and C. Deibel, *J. Appl. Phys.*, 2014, **115**, 144502.
- 47 D. Rana, P. Donfack, V. Jovanov, V. Wagner and A. Materny, *Phys. Chem. Chem. Phys.*, 2019, **21**, 21236–21248.
- 48 O. G. Reid, R. D. Pensack, Y. Song, G. D. Scholes and G. Rumbles, *Chem. Mater.*, 2014, **26**, 561-575
- 49 I. Hwang, S. Beaupré, M. Leclerc and G. D. Scholes, *Chem. Sci.*, 2012, **3**, 2270–2277.
- 50 M. Scarongella, A. Laktionov, U. Rothlisberger and N. Banerji, *J. Mater. Chem. C*, 2013, **1**, 2308.
- 51 S. Shoaee, PhD Thesis, Imperial College London, 2010.
- 52 B. T. Lim, S. Okajima, A. K. Chandra and E. C. Lim, *Chem. Phys. Lett.*, 1981, **79**, 22–27.
- 53 H. Ohkita, S. Cook, Y. Astuti, W. Duffy, M. Heeney, S. Tierney, I. McCulloch, D. D. C. Bradley and J. R. Durrant, *Chem. Commun.*, 2006, 3939–3941.
- 54 C. Dyer-Smith, L. X. Reynolds, A. Bruno, D. D. C. Bradley, S. A. Haque and J. Nelson, *Adv. Funct. Mater.*, 2010, **20**, 2701–2708.
- 55 S. M. Menke, A. Sadhanala, M. Nikolka, N. A. Ran, M. K. Ravva, S. Abdel-Azeim, H. L. Stern, M. Wang, H. Sirringhaus, T.-Q. Nguyen, J.-L. Brédas, G. C. Bazan and R. H. Friend, *ACS Nano*, 2016, **10**, 10736–10744.
- 56 A. Armin, J. R. Durrant and S. Shoaee, *J. Phys. Chem. C*, 2017, **121**, 13969–13976.
- 57 T. M. Burke, S. Sweetnam, K. Vandewal and M. D. McGehee, *Adv. Energy Mater.*, 2015, **5**, 1500123.
- 58 M. Hilczler and M. Tachiya, *J. Phys. Chem. C*, 2010, **114**, 6808–6813.
- 59 U. Hörmann, J. Kraus, M. Gruber, C. Schuhmair, T. Linderl, S. Grob, S. Kapfinger, K. Klein, M. Stutzman, H. J. Krenner and W. Brütting, *Phys. Rev. B*, 2013, **88**, 235307.
- 60 Y. Liu, J. Zhao, Z. Li, C. Mu, W. Ma, H. Hu, K. Jiang, H. Lin, H. Ade and H. Yan, *Nat. Commun.*, 2014, **5**, 5293.
- 61 S. Shoaee, M. P. Eng, E. Espíldora, J. L. Delgado, B. Campo, N. Martín, D.

Chapter 5

- Vanderzande and J. R. Durrant, *Energy Environ. Sci.*, 2010, **3**, 971.
- 62 I. A. Howard, R. Mauer, M. Meister and F. Laquai, *J. Am. Chem. Soc.*, 2010, **132**, 14866–14876.
- 63 K. Nakano, Y. Chen, B. Xiao, W. Han, J. Huang, H. Yoshida, E. Zhou and K. Tajima, *Nat. Commun.*, 2019, **10**, 2520.
- 64 D. H. K. Murthy, A. Melianas, Z. Tang, G. Juška, K. Arlauskas, F. Zhang, L. D. A. Siebbeles, O. Inganäs and T. J. Savenije, *Adv. Funct. Mater.*, 2013, **23**, 4262–4268.

Chapter 6

Conclusions and Future Work

6.1 Conclusions

An overarching theme throughout this thesis has been the ubiquitous presence of triplet species in organic solar cell materials, and how they can potentially decrease OSC device efficiency via acting as a loss channel. Chapter 3 elegantly demonstrated this point by presenting a study into a small molecule DPP derivative blended with the prototypical acceptor molecules PC₆₀BM and PC₇₀BM. It was shown that ultrafast - spin mixing in a CT state, followed by subsequent geminate recombination, yielded the donor-triplet exciton, the lowest energy excited state of the system.

Chapter 4 represents a significant first attempt to create a single 'self' triplet upconverting polymer, through the inclusion of a NIR absorbing porphyrin into an F8BT backbone. Although the desired TTA-UC was not observed, the F8BT-HAPAPP copolymer presented a fascinating insight into the dynamics of such systems, including their ability to manipulate triplet state lifetimes. Furthermore, several fundamental design principles were established for realising self-upconverting donor polymers utilising metal porphyrin sensitizers. One principle involves limiting the polymeric host's band edge to <2.5 eV, under the assumption that the 0.7 eV singlet-triplet splitting for polymers holds true, thus allowing triplet energy transfer from the porphyrin to that of the host polymer to be energetically favourable.

Chapter 5 explored the concept of a donor-orthogonal acceptor copolymer and its impact on triplet dynamics. It was found that the D-oA structure promoted ultrafast (<200 fs) triplet formation, which can only be accounted for by the processes of singlet fission or SOCT-ISC mechanisms. The experimental data and subsequent theoretical work pointed towards SOCT-ISC being the most probable mechanism for ultrafast triplet formation. Although this form of triplet manipulation has been observed in small molecules and existing D-oA polymers (and attributed to the SOCT-ISC process), here it is extended toward to a low-band gap polymer, which is more reflective of state-of-the-art OSC donor materials. Moreover, it was shown that this type of D-oA polymer readily underwent charge separation upon blending with the acceptor PC₆₀BM, the first time this has been achieved to our knowledge. This observation is indicative that this class of D-oA copolymers may be readily used in organic solar cell devices. The most important observation, however, was the apparent formation of charge species, in both the pristine solution and neat thin film. This was conjectured

to be a function of the orthogonal position of the acceptor moiety, which affords a degree of intramolecular separation, thus eliminating the need for an additional acceptor molecule.

6.2 Further Work

While the main aim of chapter 5 was to explore the triplet dynamics of D-oA systems, the most interesting observation made was that of charge generation in the pristine Thiro film and importantly also its solution. This points towards an intramolecular charge separation process, which is afforded via the unique D-oA architecture. It was proposed that the CT state originating from the orthogonal donor and acceptor units, most likely affords a degree of intramolecular separation between the electron and hole, thus effectively reducing the binding energy of the exciton and allowing for charge separation. The finding of a pristine polymer which undergoes charge separation has significant implications for the field of organic photovoltaics. This is because if a single photoactive material can both absorb and generate free charge species independent of an acceptor molecule, one can in principle circumvent the intrinsic energy loss associated with driving electron transfer in donor-acceptor blends. Furthermore, the stringent morphological requirements needed for thin films to attain their highest efficiencies would not be needed, thus in theory simplifying device fabrication. Since this charge generation process appears specific to Thiro, it also brings with it a host of questions. Can charge generation be observed in other D-oA polymer systems? What is the impact of macroscopic electric fields on the charge generation process? What is the mobility of free charge species in the film? Do pristine Thiro deliver non-negligible efficiencies? Many intriguing questions remain regarding this unique class of polymer, and as such it demands additional investigation.